THE UNIVERSITY OF CHICAGO

CONSEQUENCES OF MOLECULAR-SCALE NON-EQUILIBRIUM ACTIVITY ON THE DYNAMICS AND MECHANICS OF SELF-ASSEMBLED ACTIN-BASED STRUCTURES AND MATERIALS

A DISSERTATION SUBMITTED TO

THE FACULTY OF THE DIVISION OF THE PHYSICAL SCIENCES

IN CANDIDACY FOR THE DEGREE OF

DOCTOR OF PHILOSOPHY

DEPARTMENT OF PHYSICS

BY

PATRICK MARSHALL MCCALL

CHICAGO, ILLINOIS

AUGUST 2017

TABLE OF CONTENTS

LIST OF FIGURES

LIST OF TABLES

ACKNOWLEDGEMENTS

I thank my advisor, Prof. Margaret Gardel for the enormous intellectual freedom she gave me, enabling my development as a scientist. I thank Prof. David Kovar for his support, insightful recommendations, and constant mentoring. Together, I thank my committee, Profs. Gardel, Witten, Wakely, and Kovar, for there extraordinary patience while this thesis was written. Thank you for your support.

I thank the many members of the Gardel and Kovar laboratories from whom I have had the distinct pleasure of learning most of what I know about biology. You have made my time at the University of Chicago more productive and enjoyable than I could have imagined.

I thank my parents for boundless love, encouragement, and support, biased or not. You laid the essential foundations for me to do anything and everything.

Finally, I thank my wife, Tessa, and our two daughters, Hazel and Audrey. Thank you for accepting me for the flawed person I am. Every day you make me better that I have any reason to expect to be.

ABSTRACT

Living cells are hierarchically self-organized forms of active soft matter: molecules on the nanometer scale form functional structures and organelles on the micron scale, which then compose cells on the scale of 10s of microns. While the biological functions of intracellular organelles are defined by the composition and properties of the structures themselves, how those bulk properties emerge from the properties and interactions of individual molecules remains poorly understood. Actin, a globular protein which self-assembles into dynamic semi-flexible polymers, is the basic structural material of cells and the major component of many functional organelles. In this thesis, I have used purified actin as a model system to explore the interplay between molecular-scale dynamics and organelle-scale functionality, with particular focus on the role of molecular-scale non-equilibrium activity.

One of the most canonical forms of molecular-scale non-equilibrium activity is that of mechanoenzymes, also called motor proteins. These proteins utilized the free energy liberated by hydrolysis of ATP to perform mechanical work, thereby introducing non-equilibrium "active" stresses on the molecular scale. Combining experiments with mathematical modeling, we demonstrate in this thesis that non-equilibrium motor activity is sufficient to drive self-organization and pattern formation of the multimeric actin-binding motor protein Myosin II on 1D reconstituted actomyosin bundles.

Like myosin, actin is itself an ATPase. However, nono-equilibrium ATP hydrolysis on actin is known to regulate the stability and assembly kinetics of actin filaments rather than generate active stresses per se. At the level of single actin filaments, the inhomogeneous nucleotide composition generated along the filament length by hydrolysis directs binding of regulatory proteins like cofilin, which mediate filament disassembly and thereby accelerate actin filament

turnover. The concequences of this non-equilibrium turnover on the steady-state properties of collections of filaments remained unclear. Here, I reconstituted tunable, non-equilibrium actin turnover dynamics in entangled solutions of actin filaments as a model of the actin cortex of living cells. We found that this non-equilibrium turnover decouples solution mechanics from microstructure, enabling structurally indistinguishable materials to behave effectively as either viscous fluids or elastic gels. Additionally, we employed computer simulations to identify the dynamical regime in which actin turnover controls the effective viscosity of 2D cross-linked actin networks in the presence of motors.

Additionally, I examine in this thesis the localization and self-assembly of actin filaments in condensed liquid phases called polyelectrolyte coacervates as a model membrane-less organelle. We find that concentration of actin through spontaneous partitioning preferentially to the coacervate phase accelerates the assembly of filaments. These filaments then localize to the coacervate-bulk interface, generating particles with visco-elastic shells surrounding liquid cores. In this case, the properties of the condensed phase enable regulation of actin assembly dynamics.

PREFACE

This thesis is a compilation of individual documents, including three pre-prints (two of which are under review at peer-reviewed journals as of the time of writing) and one published article. The contents of Chapter 2 are from Stachowiak, M.R., **McCall, P.M.**, Thoresen, T., Balcioglu, H.E., Kasiewicz, L., Gardel, M.L., and O'Shaughnessy, B. (2012). Self-Organization of Myosin II in Reconstituted Actomyosin Bundles. Biophys. J. *103*, 1265–1274. The contents of Chapter 3 are from a draft of **McCall, P.M.**, MacKintosh, F.C., Kovar, D.R., and Gardel, M.L. (2017). Cofilin Drives Rapid Turnover and Fluidization of Entangled F-actin. bioRxiv 156224. The contents of Chapter 4 are from a revised draft of McFadden, W.M., **McCall, P.M.**, and Munro, E.M. (2016). Filament turnover is essential for continuous long range contractile flow in a model actomyosin cortex. ArXiv 1612.07430. The contents of Chapter 5 are from a draft of **McCall, P.M.***, Srivastava, S.*, Perry, S.L., Kovar, D.R., Gardel, M.L., and Tirrell, M.V. (2017). Partitioning and Enhanced Self-Assembly of Actin in Polypeptide Coacervates. bioRxiv 152025, where * denotes co-first author. In the subsequent prefaces to each chapter, I will explain my contribution to each of these multi-author works.

CHAPTER 1: INTRODUCTION

Section 1.1 CELLULAR ORGANIZATION

Eukaryotic cells are organized in space by micron-scale assemblies called organelles. Organelles serve many functions, including compartmentalization, energy production, mechanics, sensing, and motility. Three broad classes of organelles include membrane-bound structures, cytoskeletal structures, and membrane-less organelles. Canonical examples of membrane-bound organelles are mitochondria, the Golgi apparatus and lysozomes, essential for energy production, protein sorting and trafficking, and protein degredation, respectively (Alberts et al., 2007). Cytoskeletal organelles include characteristic structures formed from actin filaments, such as the contractile ring and actin cortex, important for cell division and mechanics, as well as structures formed from the other two main families of cytoskeletal filaments, microtubules and intermediate filaments, which compose the mitotic spindle and anchor desmosomes, respectively (Alberts et al., 2007; Phillips et al., 2008). Finally, membrane-less organelles include such structures as P-granules, stress-granules, and nucleoli, which are involved in germ-line fate determination, cellular stress response, and ribosome synthesis, and all of which are thought to form via liquid-liquid phase separation (Mitrea and Kriwacki, 2016).

Common features of each of these structures are that their typical dimensions are on the micron lengthscale, and that they are composed of molecules (typically proteins, RNAs, and lipids) on the nanometer scale. Another common feature is that the organelles are typically not in equilibrium, but typically in some dynamic steady-state, where the drive comes from either internal ATP hydrolysis, or a chemical/mechanical potential gradient sustained within the cell.

Understanding how biological functionality emerges from collections of molecules through self-organization into organelles is an exciting area of active research.

I invite the reader to consider subcellular organelles from the distinct perspectives of a biologist, physicist, and a materials scientist. A biologist might quite reasonably concern themselves with the complete composition and structure of a given organelle, with an eye towards its biological function in its is proper in vivo context. They could argue that anything less is a simplification of the true biological complexity of the system. In contrast, a physicist might wish to understand what properties, structures, and functionality are permissible by the physical laws of the universe for subsets of organellar components on the basis of their molecular-scale interactions, and with an eye towards the emergence of new behavior as compositional complexity increases. Such an approach defines the space of what is possible, with the specific motivating organelle representing a particular realization of a discrete point in this space.

Finally, a materials scientist might seek the minimal ingredients sufficient to achieve a particular function or structure, with an eye towards design principles for relating the ingredients to the output. Importantly, these ingredients are abstract and could bear little resemblance to the biological molecules of the true organelle. For instance, there are many ways to realize an attractive interaction between a pair of molecules, and the existence of the interaction may be the ingredient, rather than the specific identities of the molecules themselves. These design principles allow for comparison of actual biological structures with the simplest functional equivalent in the space identified by physics, offering both biological and technological insights.

Though distinct, these three vantage points are interrelated, and all hold substantial value. During my graduate studies, I have examined how the structural, mechanical, and enzymatic

properties of several self-organized materials, all based on the protein polymer actin, emerge from a minimal set of abstract components, like non-equilibrium activity. This work required working across the traditional disciplines of physics, cell biology, biochemistry, and materials science, applying the techniques and adopting the vantage points of each as necessary. In the following, I will endeavor to present the findings of my research in the light of these different perspectives, in order that insights from each might shine through.

Section 1.2 THESIS ORGANIZATION

I am interested in the very general problem of how the microscopic features of the molecular components of complex materials give rise to particular properties on the micron length scale. As indicated above, this is motivated by the sub-cellular organelles of living cells, which are themselves complex, self-organized materials composed of biomolecules. In particular, this thesis focuses on the structural, mechanical, and dynamical properties of materials based on actin, with particular attention to the role of non-equilibrium activity at the molecular scale. Chapter 2 explores the emergence of banded patterns in self-organized bundles composed of actin filaments and myosin motors both experimentally and theoretically. In this case, non-equilibrium activity enters through the molecular motor protein myosin II, and is essential for the pattern formation.

Chapter 3 examines experimentally the influence of actin turnover on the mechanical response of entangled actin filament solutions. Here, coupling of turnover to the non-equilibrium hydrolysis of ATP on actin filaments enables decoupling of solution mechanics from solution structure. Chapter 4 investigates the mechanical response of cross-linked actin networks driven by myosin motors in the presence of actin turnover using computer simulations and analytic

theory. In this case, non-equilibrium turnover is required for a stable network density under applied stress. Additionally, non-equilibrium motor activity generates mechanical stresses within the network which can only be sustained in the presence of turnover.

Chapter 5 probes experimentally the regulation of the actin self-assembly reaction in polyelectrolyte-complex coacervates as a model for biochemical reactions in membrane-less organelles. Although actin assembly is properly a non-equilibrium reaction, the focus here is on the impact of compartmentalization on a self-assembly reaction, rather than consequences of its non-equilibrium nature. Here, spontaneous partitioning of actin to coacervates enhances the rate of filament assembly primarily by increasing the local reagent concentration. Additionally, the reaction products are long filaments which localize preferentially to the interface of the coacervate phase. Finally, Chapter 6 provides a discussion of these results, which indicate that biochemical activity, and non-equilibrium activity in particular, can play important roles in regulating material properties and functionality, as well as the converse, that material properties can regulate biochemical activity.

The breadth of molecules, systems and (emergent) properties examined in this thesis necessitate the introduction of a number of concepts and, in some cases, whole fields of study. These essential prerequisites compose the remainder of the present chapter. Actin is a central component of each system studied in this thesis, and Section 1.3 outlines the fundamental properties of this important protein. Many of these properties can be thought of as "abstract ingredients" from the perspective of a materials scientist. Section 1.4 then introduces how these properties, or abstract ingredients, are regulated by the actin cytoskeleton to achieve desired cellular functions.

The viscoelastic mechanical response of materials composed of actin filaments is a prominent focus of this thesis. In particular, Chapter 3 pertains to entangled solutions of actin filaments, while cross-linked actin filament networks are discussed in Chapter 4. Accordingly, Section 1.5 introduces the study of material deformations (rheology) and the concept of viscoelasticity. Also included in Section 1.6 are physical descriptions of the major viscoelastic features of entangled actin filament solutions as well as cross-linked networks, with an emphasis on mechanisms of stress relaxation on long timescales.

Section 1.6 introduces the fundamental role of liquid-liquid phase separation in biological organization, as this is relevant to the motivation for the work with complex coacervates in Chapter 5. Finally, a discussion of my conceptual approach to framing the scientific problems examined in Chapters 2-5 is presented in Section 1.7 and concludes Chapter 1.

Section 1.3 FUNDAMENTAL PROPERTIES OF ACTIN

Actin is an abundant and highly conserved protein, with three isoforms (α, β, and γ) in humans. The exceptional degree of conservation is apparent from the identical sequences of, for instance, the alpha isoforms (expressed in skeletal muscle tissue) of actin in chickens and humans (UniProt accession numbers P68139 and P68133, respectively, (ProtParam)). Indeed, the coding regions of actin genes in algae, fungi, and humanrs differ by only a few residues out of 375 (Pollard, 2016), and organisms from all branches of life contain actin homologs of similar structure (Pollard, 2016). Such strong conservation is indicative of strong selective pressure to maintain the structure and functionality of this important protein. Fundamental properties of actin include its capacity to self-assemble into non-covalent supramolecular filaments, the semi-flexibility and asymmetric compliance of those filaments, enzymatic activity in the form of ATP

hydrolysis, allosteric conformational changes, and a non-equilibrium effect termed treadmilling. These will each be discussed in more detail presently.

Physically, actin is an ~42 kDa globular protein (G-actin) with a 2.45-nm radius of gyration (Matsudaira et al., 1987) and carries a net negative charge in solution at neutral pH. Its structure is canonically broken up into four subdomains (S1-S4), which are organized into lobes around a bound nucleotide, much like clover leaves around a stem (Fig 1.2A). The groove between subdomains S1 and S3 is referred to as the barbed face of the protein, while the groove on the opposite side, between subdomains S2 and S4, is called the nucleotide binding cleft, or the pointed face.

Actin reversibly binds adenosine nucleotides complexed with divalent cations. Given the mM concentrations of ATP and Mg^{2+} in cells, G-actin actin is thought to bind predominantly to Mg-ATP (Pollard, 2016) under physiological conditions. However, purified actin is stored in buffer with Ca-ATP. Cleavage of the covalent bond between the β- and γ-phosphates occurs very slowly on ATP molecules bound to G-actin (Rould et al., 2006), though exchange of nucleotide between G-actin and solution occurs readily in all cases (Pollard et al., 1992). The equilibrium dissociation constant, K_D, for the binding reaction of G-actin and nucleotide is on the order of ~1 nM for Mg- and Ca-ATP (De La Cruz and Pollard, 1995), and higher for Mg- and Ca-ADP (Kinosian et al., 1993). Thus G-actin is essentially always bound to nucleotide at the > 100 nM concentrations used in all experiments presented in this thesis, and is actually unstable to misfolding in dilute aqueous solution in the absence of soluble nucleotide, though stabilization is possible at high sucrose concentrations (48 % (w/v), (De La Cruz and Pollard, 1995)). In addition to nucleotide, actin also contains two binding sites for divalent cations, one in the D-

loop of subdomain S2, termed the stiffness site, and a second shared between subdomains S3 S4 of adjacent actin subunits in a filament, termed the polymerization site (Kang et al., 2012).

Perhaps the most striking feature of G-actin is its capacity to polymerize (Fig 1.1). Actin filaments are helical polymers composed of two linear, intertwined strands of actin subunits, termed protofilaments. The structure of these filamentous actin polymers (F-actin) are stabilized by binding interactions between each interior actin subunit and four neighbors; two intra-strand and two inter-strand. Importantly, these binding interactions are non-covalent and readily reversible at room temperature. Like all reversible self-assembly reactions (Israelachvili, 2011), there is a minimum monomer concentration in solution above which actin filaments are thermodynamically stable. This threshold monomer concentration is termed the actin critical concentration, c*, and reflects the balance of association and dissociation reactions at filament ends. It has a value of slightly over 0.1 μM in the presence of Mg-ATP (Fujiwara et al., 2007).

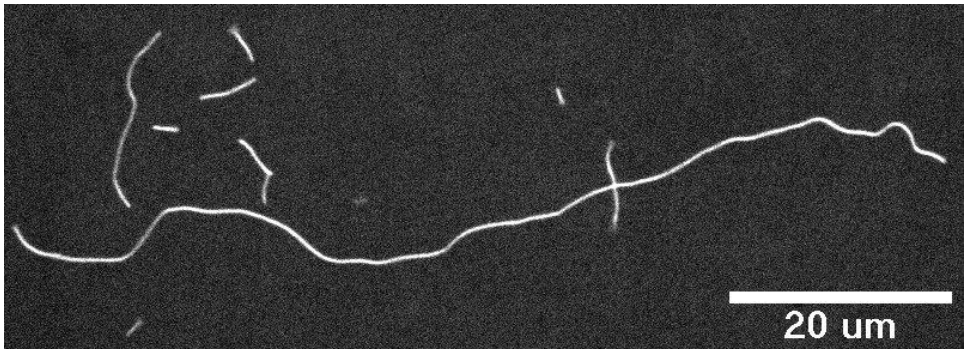

Figure. 1.1 Fluorescence micrograph of individual actin filaments

Section 1.4 THE ACTIN CYTOSKELETON

The actin cytoskeleton refers to the protein actin and all proteins which bind to either globular actin monomers (G-actin) or the helical filaments assembled from actin monomers (F-actin). In

mammalian cells, this set is quite large, including on the order of 100 actin binding proteins (wikipedia page), though when taking protein isoforms into account, the number of distinct proteins is even larger. Indeed, when counting all isoforms and alternative splice variants, one finds 40 myosins (Foth et al., 2006), > 40 tropomyosins (Gunning et al., 2008), and 15 formins (Goode and Eck, 2007) in humans, for a total of nearly 100 distinct actin binding proteins after considering only three protein families. Regardless of the exact number, however, it is convenient to conceptually group actin binding proteins on the basis of their biochemical interactions with actin, with the understanding that many proteins have activities across multiple groups. Such groupings of actin binding proteins include proteins that (1) regulate assembly of actin filaments, (2) regulate actin filament disassembly, (3) physically cross-link filaments together, (4) regulate the binding of other proteins to actin filaments (5) act as scaffolds or adaptors to physically connect actin filaments to other cellular structures, (6) are mechanochemical motors, (7) are members of cellular signaling pathways, and (8) localize to the nucleus. While I've listed all of these groups in the interest of completeness, we will restrict our attention to groups 1, 2, 3, and 6.

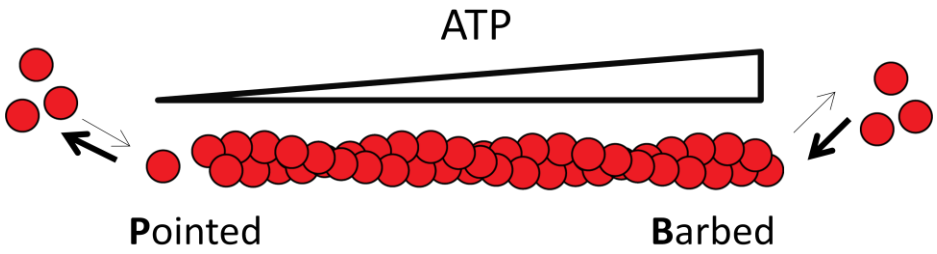

Figure 1.2 Schematic of actin filament assembly and disassembly reactions

Section 1.4.1 Regulation of actin assembly

The assembly of actin into filaments involves two distinct processes: the nucleation of new filaments, and the addition of monomers to the ends of existing filaments, termed elongation. Both are tightly controlled in cells by a host of actin assembly factors. Nucleation promoting factors like formins and the Actin related protein (Arp)2/3-complex nucleate new filaments, either de novo from monomers, in the case of formins, or by generating branches from the sides of pre-existing filaments, in the case of Arp2/3 (Pollard, 2007). In contrast, sequestering proteins like thymosin-β4 suppress filament nucleation by binding stoichiometrically to actin monomers in regions required for intra-filament contacts and inducing conformational changes in the monomer unfavorable to polymerization (Xue et al., 2014), thereby reducing the concentration of assembly-competent actin monomers. This combination of steric and allosteric effects render thymosin-β4:actin complexes unable to participate in either filament nucleation or elongation. A different binding interface and more minimal binding-induced conformational changes relative to thymosin-β4 allow monomers complexed with profilin, another protein which binds actin monomers stoichiometrically and is sometimes referred to as a sequestering protein (Xue et al., 2014), to participate in elongation reactions at one filament end (termed the barbed end), while preventing nucleation and elongation from the other filament end (termed the pointed end). Thus, the binding of regulatory proteins to actin monomers can differentially inhibit nucleation and elongation.

Filament elongation is a bimolecular reaction between a filament end and an actin monomer, and we have just seen this reaction can be regulated by proteins which bind to monomers. The other primary mode of elongation regulation is by proteins which bind filament ends. For instance, tropomodulin (Rao et al., 2014), Arp2/3 (Mullins et al., 1998) , and adenomatous

polyposis coli (APC) (Breitsprecher et al., 2012) bind to the pointed ends of filaments and prevent pointed-end elongation. Such activity is commonly referred to as capping. Similarly, the proteins gelsolin (Burtnick et al., 1997) and CapZ (Yamashita et al., 2003) (also called "capping protein") bind tightly to and inhibit the elongation of actin filament barbed ends. Not all end-binding proteins exhibit capping activity, however. Members of the Enabled/Vasodilator-stimulated phosphoprotein (Ena/VASP) (Winkelman et al., 2014) and formin (Kovar et al., 2006) families of proteins, for example, bind and track barbed ends as they elongate, an activity called processivity. Furthermore, the rate constant describing the elongation reaction of Ena-bound barbed ends is increased 2-3-fold relative to unbound ends (Winkelman et al., 2014), demonstrating that the elongation reactions are also subject to positive regulation, in addition to negative regulation by capping. Thus, while there are intrinsic values for rate constants describing actin filament nucleation (Sept and McCammon, 2001) and elongation reactions (Pollard, 1986) in aqueous solution under specified conditions (e.g. temperature, pH, ionic strength), the reaction rates for both nucleation and elongation can be tuned up and down, with the actively elongating ends differentially specified, by actin regulatory proteins.

Section 1.4.2 Regulation of actin disassembly

Opposing actin filament assembly is disassembly. The elongation reactions by which monomers can add to each filament end also have back-reactions, by which monomers dissociate from filament ends. The ratio of the off-rate and on-rate constants gives the critical concentration for actin assembly,

$$\frac{k_{off}}{k_{on}} = c_{crit} \tag{1}$$

which defines the actin monomer concentration threshold for the coexistence of polymerized and monomeric actin. At monomer concentrations above c_{crit}, elongation is favored, while depolymerization is favored below c_{crit}. As with assembly reactions, disassembly is highly regulated by actin binding proteins. For instance, monomer dissociation is inhibited at capped ends (both barbed and pointed). Notably, at least some formins are able to retain association with a filament and track depolymerizing barbed ends as well (Jégou et al., 2013), so not all end-binding proteins fully inhibit monomer exchange dynamics.

In addition to end-binding proteins, several proteins which bind to the side of actin filaments regulate disassembly dynamics, either directly, or indirectly via synergistic or antagonistic interactions with other proteins. Principle among these are members of the Actin Depolymerizing Factor (ADF)/Cofilin family, severing proteins which bind cooperatively to the sides of filaments and break them, exposing new barbed and pointed ends (De La Cruz, 2009a). Tropomyosin also binds cooperatively to filaments and inhibits severing indirectly by competing with cofilin for overlapping binding sites along actin filaments (Maciver et al., 1991). Though some disagreements remain, recent work has demonstrated that coronin can recruit cofilin (Jansen et al., 2015), and that Actin interacting protein 1 (Aip1) (Nadkarni and Brieher, 2014) and cyclase-associated protein Srv2/CAP (Chaudhry et al., 2012) each enhance cofilin-mediated severing. Aip1 may enhance depolymerization of newly exposed barbed ends (Nadkarni and Brieher, 2014) or cap them (Jansen et al., 2015). Additionally, enhancements in both barbed-end and pointed-end depolymerization rates have been reported in the presence of Srv2/CAP and twinfilin, a protein composed of two tandem ADF-homology domains (Johnston et al., 2015). Thus, the number of depolymerizing ends and the rate constants governing disassembly reactions are specified by the particular suite of disassembly factors present.

Section 1.4.3 Actin cross-linking proteins

Cross-linking proteins constitute another group of F-actin side-binding proteins and, along with the Arp2/3 complex, are responsible for organizing actin filaments into higher-ordered networks of distinct architecture. Some of the most important distinguishing properties of actin cross-linking proteins are their preference for filament orientation and size (mechanical compliance and unbinding characteristics will be touched on later). With their structurally distinct barbed and pointed ends, actin filaments are polar objects that may be cross-linked at an angle, or bundled in parallel or anti-parallel configurations. While many cross-linkers, such as α-actinin, are promiscuous and agnostic with regard to the angle between cross-linked filaments, others are much more selective. Most notably, fascin is a cross-linking protein which bundles only filaments with parallel orientations (Courson and Rock, 2010). Additionally, it was recently demonstrated that cross-linking proteins will segregate on the basis of the filament spacing dictated by cross-linker size: small cross-linkers like fascin, fimbrin and espin sort to common domains separate from those formed by larger cross-linkers like α-actinin (Winkelman et al., 2016). Control of actin network architectural features like filament orientation, bundling, and spacing often helps make cross-linking proteins defining components of distinct actin-based organelles and structures, as with fascin in filopodia (Svitkina et al., 2003), fascin and espin in stereocilia (Sekerková et al., 2011), and α-actinin in stress fibers (Tojkander et al., 2012).

Section 1.5 MECHANICS OF ACTIN NETWORKS

Section 1.5.1 Introduction to rheology

The most intuitive manner to probe the mechanical response of a material is to apply a force *F* and observe how the material deforms or flows. The systematic study of material deformation

and flow in response to applied force (or stress, $\sigma \equiv F/A$, force per unit area) is called rheology. Fig. 1.3A-B depicts the deformation of an elastic material in response to an applied shear stress. The lateral displacement averaged vertically gives the dimensionless shear strain, $\gamma \equiv \Delta x/h$, which characterizes the deformation. The reader's intuitive notion that the extent of material deformation, or strain, depends on the applied stress is captured mathematically by a constitutive relationship (Fig. 1.3C). While constitutive relationships can differ between any two materials, a relatively small number of such relationships effectively characterize the (linear) mechanical response of a relatively large number of materials.

Of particular note are the constitutive relationships for ideal elastic solids, such as a spring, $\sigma = G\gamma$, for which the strain is linear in the applied stress and G is the shear modulus, and that for ideal Newtonian fluids, $\sigma = \eta\dot{\gamma}$, for which the strain *rate* is linear in applied stress, and η is the fluid viscosity. An important difference between these two relationships is that while the former is conservative, the latter is not. That is, deformations to an ideal elastic solid can be described by a conservative potential field, therefore resulting in a restoring force capable of fully reversing the deformation upon release of the applied stress. This is the basis of the ability to store elastic stress energy. In contrast, no conservative potential is present in ideal fluids, resulting in the dissipation of stress energy and un-recovered strain following release of the applied stress.

Although written as scalar relations here, these constitutive relations are properly tensor equations, encoding directional information as well as magnitudes. Because most materials deform in the direction of the applied force, symmetry requires a that the stress be an odd function of the strain in order to capture sign changes. Since the lowest-order odd functions are linear, linear constitutive relationships like those above apply to most solids and fluids, though

often only over a limited range of stress- and time-scales. Break-down of linear-response from large stresses is the realm of non-linear rheology, whereas break-down owing to the characteristic timescale of the applied stress is described by viscoelasticity. We will be predominantly concerned with linear viscoelasticity in this thesis.

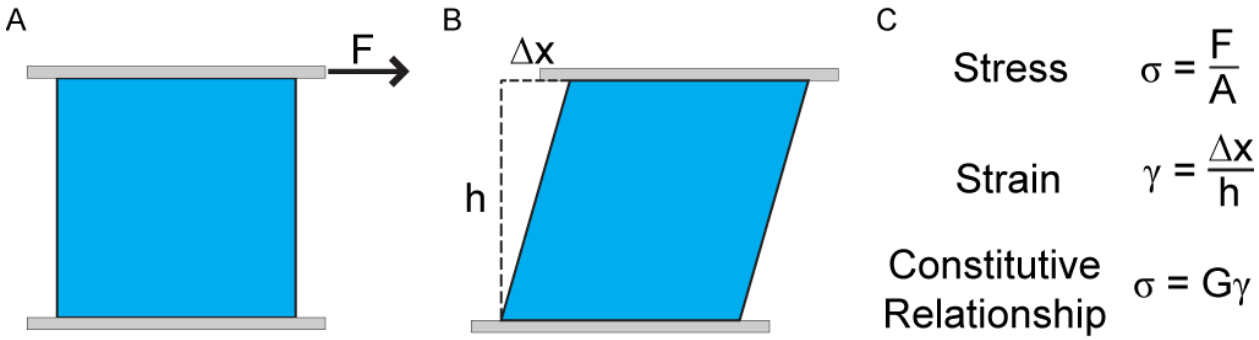

Figure 1.3 A constitutive relationship connects material deformation to applied stress.

Section 1.5.2 Viscoelasticity

The mechanical response of many real materials depends on the timescale of deformation. Silly putty, for instance, has an elastic, solid-like response on the timescale of seconds, but flows like a fluid on the timescale of minutes to hours in a gravitational field (the inquiring reader is encouraged to do the experiment). A simple toy model which captures this viscoelastic transition from elastic-like response at short times to viscous-like response at long times is the Maxwell model, and consists simply of a single ideal elastic element (spring with elastic modulus E) in series with a single viscous element (dashpot with viscosity η). The Maxwell model is analytically solvable and provides physical intuition into viscoelasticity. In particular, ratio of the dashpot viscosity to the elastic modulus of the spring has the units of a timescale, $\tau = \eta / E$. We will call this the viscoelastic relaxation time, for reasons that will become apparent shortly.

Now imagine the response of the model to an extensional stress σ. The strain from the dashpot at time *t*, $\Delta\gamma_\eta$, is related to the stress approximately by $\sigma = \eta\dot{\gamma} \approx \eta\left(\Delta\gamma_\eta / t\right)$, giving $\Delta\gamma_\eta = \sigma t / \eta$, which grows linearly with time. In contrast, the strain from the ideal spring is instantaneously $\Delta\gamma_E = \sigma / E$, independent of time. The ratio

$$\frac{\Delta\gamma_\eta}{\Delta\gamma_E} = \frac{\sigma t / \eta}{\sigma / E} = \frac{t}{\eta / E} = \frac{t}{\tau} \tag{2}$$

gives the relative contribution of the dashpot to the total strain. Thus, on timescales much shorter than the relaxation time, $t \ll \tau$, the contribution from the dashpot is dwarfed by that of the spring, and the material response is approximately elastic. However, on timescales much larger than the relaxation time, $t \gg \tau$, strain from the dashpot dominates, and the material flows like a fluid with viscosity η. Thus, a combination of viscous and elastic elements in series is sufficient to reproduce elasticity on short time-scales and viscous responses on long timescales. It is worth noting, however, that while useful for mechanical reasoning and developing intuition, real viscoelastic materials are not build from microscopic dashpots and springs connected in circuits, as in the Maxwell model. It is therefore necessary to go beyond such mechanical engineering models to explain the physical origins of the frequency-dependent viscoelasticity of real materials.

Section 1.5.3 Measuring viscoelasticity

The mechanical response of real materials to shear deformation, and the linear viscoelasticity in particular, is traditionally measured with a rheometer. The material of interest is placed between two parallel plates (e.g. Fig 1.9A-B, though other geometries are possible as well). In a stress-

controlled rheometer, for instance, the top plate then rotates in response to an applied torque and transmits a shear stress to the sample. Frequency-dependent viscoelasticity can then be measured by application of oscillatory torque at different frequencies. Such bulk rheological measurements report on the global mechanical response.

Another technique is called microrheology, and uses micron-sized particles to probe the mechanical response of the material. This can be done by actively driving the particles (active microrheology), for instance with optical or magnetic tweezers (Chen et al., 2010). An alternative approach relies on thermal forces to drive motion of the particles (passive microrheology). Intuitively, the Brownian motion of a micron-sized particle (or molecule) in a viscous medium is diffusive, with the diffusion coefficient D related to the medium viscosity η by the Stokes-Einstein Relation:

$$D = \frac{k_B T}{6\pi\eta a} \tag{3}$$

where k_B is the Boltzmann constant, T is temperature, and a is the characteristic size of the diffusing object (e.g. hydrodynamic radius). For systems in thermal equilibrium, the fluctuation-dissipation theorem allows for generalization of the Stokes-Einstein Relation to media with complex, frequency-dependent viscosities (Squires and Mason, 2010), essentially because detailed balance requires a strict equality between the power spectrum of probe fluctuations and the excited modes of the material, both of which are thermally driven. Since the response of real materials is causal (i.e. there is no deformation prior to application of stress), the real and imaginary components of the complex viscosity are not independent, but are related by Kramers-Kronig integrals (Squires and Mason, 2010). Thus, measurement of a single real-valued quantity

(e.g. particle mobility) is sufficient to extract both the real and imaginary components of the complex viscosity.

Two important caveats for passive microrheology are that the Stokes-component, which relates the hydrodynamic drag experienced by the particle to the medium viscosity, can break-down in two predictable ways (Squires and Mason, 2010). In inhomogeneous materials, probes in different regions experience different local environments and thus give conflicting impressions of global mechanics. However, cross-correlations between probes separated at different distances give mechanical moduli which agree with bulk-rheology measurements in soft inhomogeneous materials (Crocker et al., 2000), a technique referred to as two-point passive microrheology.

Second, interactions of the probe with the medium can also cause the Stokes component of the Generalized Stokes-Einstein Relation to break-down. For instance, strong attractive interactions between the probe and, for instance, a polymers in an entangled solution, could dramatically suppress the particle mobility and lead to aggregation, which changes the material under investigation and skews mechanical inferences. This can be overcome experimentally with appropriate passivation of probe. Additionally, in materials described by a mesh, such including hydrogels and entangled polymer solutions, probes smaller than the mesh display a hop-diffusion (Wong et al., 2004), which also does not report on the mechanics of the material. It is thus critical that the probe size be large enough for the particle to be well embedded in the material under investigation.

Section 1.5.4 Entangled solutions of semiflexible polymers

In preparation for the examination of the influence of turnover on the mechanics of entangled solutions of semi-flexible actin filaments in Chapter 3, I will briefly discuss the mechanics of entangled solutions in the absence of polymer dynamics. Elasticity emerges in polymer solutions once in the "semi-dilute" regime, characterized by a threshold polymer density which decreases with increases in either filament length or stiffness (Morse, 1998a). Only above this overlap concentration do polymers begin to entangle. The inability of the polymers to pass through the steric constraint posed by other nearby filaments hinders the rotational diffusion, and at higher densities, filament bending fluctuations, leading to stress storage.

To first order, the frequency-dependent mechanical response (i.e. the viscoelasticity) of entangled solutions of semiflexible polymers has three regimes (Fig. 1.4). At high frequencies, bending fluctuations of filaments give rise to anomalous 3/4 scaling of both the real (elastic, storage) and imaginary (viscous, loss) components of the shear modulus (Morse, 1998a, 1998b). At intermediate frequencies, there is a gel-like regime, and at low frequencies, fluid-like behavior is observed/expected. The viscoelasticity is controlled quantitatively by three essentially independent parameters: the plateau modulus (equivalently, the energy scale of deformations), the entanglement timescale, and the terminal relaxation timescale. The plateau modulus can be thought of as an energy density. For entangled solutions, the energy scale is thermal energy (k_BT), and the volume element is the volume per entanglement length (Isambert and Maggs, 1996) ($l_e\xi^2$), where ξ is the mesh size, giving a modulus of $k_BT/l_e\xi^2$ ~50 mPa for entangled F-actin at 0.5 mg/ml. The entanglement time sets the timescale at which bending fluctuations are localized along the polymer backbone by the meshwork, inhibiting their relaxation, and defining the high-frequency onset of the elastic plateau (Morse, 1998a, 1998b).

The viscoelastic relaxation time is understood in terms of curvilinear filament diffusion, termed reptation, and the Doi-Edwards tube model (Doi and Edwards, 1986; P G de Gennes and Leger, 1982). The owing to a diffusion coefficient inversely proportional to filament length, and a tube length comparable to the filament contour length L for stiff filament like F-actin, total disengagement of a filament with entanglements in its tube requires diffusion of a distance on the order of L^2 in a time that goes like L^3.

Chapter 4 strives to develop a microscopic understanding of how active turnover and stress generation by myosin motors influence the constitutive relationship for cross-linked networks of semi-flexible polymers in two dimensions. We therefore touch briefly on the mechanics of cross-linked networks.

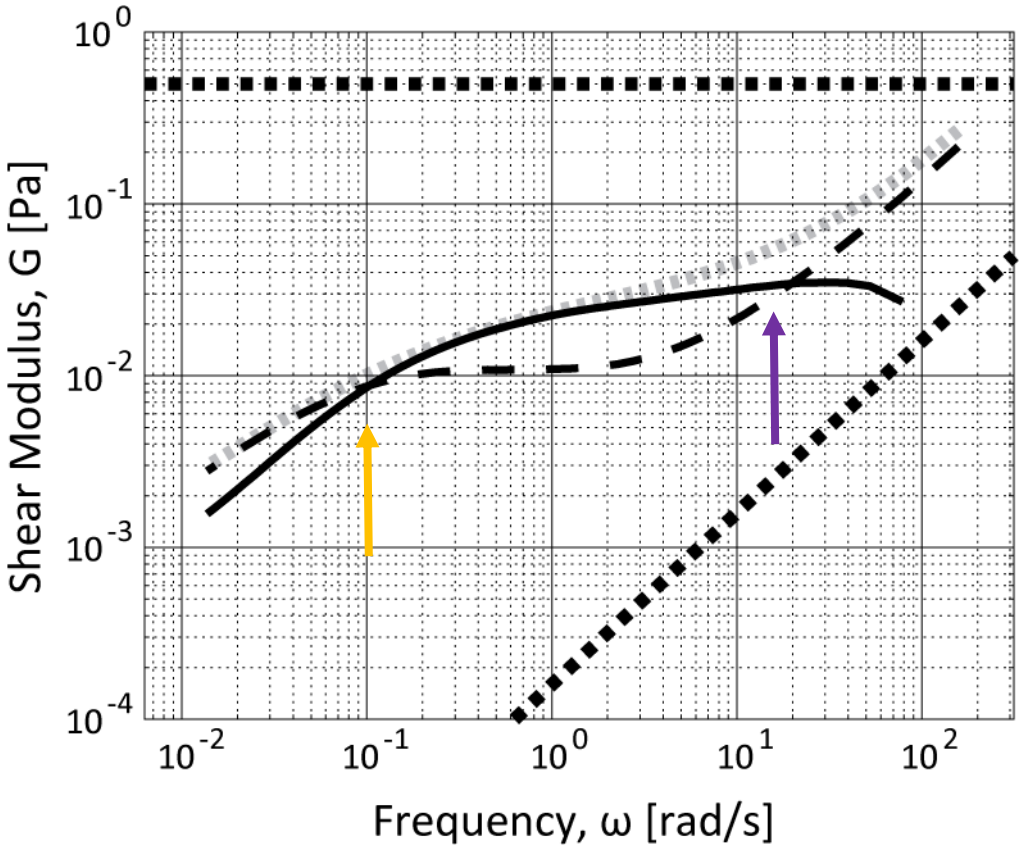

Figure 1.4 Viscoelasticity of entangled actin solutions.

Figure 1.4 Continued. Thick horizontal dashed line is elastic modulus of ideal solid. Thick dashed line with linear scaling is viscous modulus of ideal fluid. This gray dashed line is complex modulus for entangled F-actin at steady-state with minimal turnover. The solid black line is the elastic modulus of the entangled solution, and the thin dashed line is the viscous modulus. The purple arrow indicates the entanglement frequency, which demarcates the onset of the elastic plateau. The orange arrow indicates the terminal viscoelastic relaxation frequency, corresponding in this case to the inverse of the reptation time.

Section 1.5.5 Cross-linked networks and motors

Linear viscoelasticity is of cross-linked F-actin networks is qualitatively quite similar to that of entangled solutions. In particular, the three regimes characterized by $\omega^{3/4}$ scaling at high frequencies, an elastic plateau at intermediate frequencies, and pronounces relaxation at long times are all still present in networks. This is to a large degree because the mechanics of cross-linked networks, even in the presence of bundles, are representative of the mechanics of individual filaments (Gardel et al., 2004b, 2004a). Key differences between the mechanics of networks and entangled solutions are the magnitude of the modulus and character of the viscoelastic relaxation at long times. In cross-linked networks, the volume element in the modulus is now set by cross-link spacing instead of by the combination of entanglement length and mesh size, typically giving a smaller volume element and thus higher moduli (up to 100s of Pa). Also, cross-links suppress reptation as well as the relaxation of bending fluctuations. The relaxation timescale scales with the cross-link unbinding rate, but the $\omega^{1/2}$ scaling observed for both moduli at low frequencies is indicative of a broad spectrum of timescales, likely coming from the multiple sequential cross-link unbinding events necessary to equilibrate filament bending and density fluctuations (Broedersz et al., 2010).

Non-equilibrium activity introduced by myosin motors has profound effects on the mechanics and structure of crosslinked F-actin networks. First, the presence of motors stiffens

networks by pulling out the floppiest thermal bending modes (Mizuno et al., 2007). Second, at sufficiently high densities of motors, active stresses contract and reorganize the network into asters (Murrell and Gardel, 2012). Important ingredients for the preferential contraction of isotropic, disordered actin networks by myosin are the asymmetric compliance of actin filaments and dispersion in motor velocities (Lenz et al., 2012).

Section 1.6 LIQUID-LIQUID PHASE SEPARATION IN BIOLOGY

The work with polyelectrolyte complex coacervates, which are condensed polymeric liquid phases, is motivated by the discovery in 2009 that the P-granules in *C. elegans* embryos, which are responsible for specification of the germ-line during development, are condensed liquid phases (Brangwynne et al., 2009), and not the solid-like structures suggested by their name. Subsequently, 10s of other granules and cellular bodies, from the nucleoulus, PML bodies, Cajol body, and nuclear speckles in the nucleus, to stress granules, clusters of signaling proteins and balbioni bodies in the cytoplasm (Mitrea and Kriwacki, 2016; Su et al., 2016) have been reported to form (at least in part) via some form of phase separation, and mechanical properties ranging from liquids to gels to solids. These structures are referred to collectively as membrane-less organelles or, more recently, biomolecular condensates, and there is substantial interest in understanding how phase separation is harnessed to facilitate not only biological organization, but also to control the function of these membrane-less organelles.

Work with biomimetic and engineered systems has proven fruitful in this regard. Work from the Rosen lab has demonstrated that phase separation can be driven by weak multivalent binding interactions between multi-domain fusion proteins (Li et al., 2012), and that partitioning of low-valency "client" molecules into condensed phases formed by high-valency "scaffold" molecules

is consistent with expectations from mass action kinetics (Banani et al., 2016). Additionally, these results appear generic, applying to protein-protein systems, as well as protein-RNA condensates in vitro.

Another mode of phase separation is polyelectrolyte complexation and coacervation. Here, oppositely charged polymers phase separate, primarily owing to the entropic gain of counterion release (Ou and Muthukumar, 2006). Depending on the chemistry of the polyelectrolytes involved, mechanics of the coacervate can be tuned from liquid- to solid-like, with frustration of secondary-structure formation by inhomogeneities in chirality playing an especially important role in coacervates formed from polypeptide homopolymers (Perry et al., 2015). *In vitro* experiments demonstrating, reversible formation and dissolution of polypeptide-RNA coacervates upon changes in the phosphorylation of one polyelectrolyte component at a single residue (Aumiller Jr and Keating, 2016), as well as enhancements in reaction rate constants for transcription in coacervates of *E. coli* lysates (Sokolova et al., 2013) offer exciting glimpses into possible functional roles of coacervate-based phase-separated structures *in vivo*.

Open questions still remain about how generic and readily tunable many of these features are, however. In particular, recent work with polypeptide coacervates suggested that client molecules are encapsulated to coacervates (Black et al., 2014), in contrast to the dynamic partitioning observed in other biomolecular condensates (Banani et al., 2016). Additionally, the possibility that the physical or chemical properties of the condensed phase may regulate the biochemistry that occurs within them, either by controlling partitioning or altering rate constants, is tantalyzing, but lacks firm demonstration of generality. In Chapter 5, I present steps towards assessing the generality of biochemical reaction regulation and partitioning in biomolecular

condensates by examining the assembly of actin into filament in polypeptide complex coacervates.

Section 1.7 MOTIVATION AND OVERALL APPROACH

Organelles are relatively large objects composed of vey small ones. It is an observation that biological organelles often (possibly always) are composed of multiple distinct chemical species. A second observation is that many organelles are specialized for particular functions. A question is to what extent the specific composition and stoichiometry of an organelle is essential for performing the particular biological functions of the organelle.

It is of course in principle possible that the composition is fine-tuned to the point that the absence of any individual component or a slight deviation in the stoichiometry is completely deleterious, and all function (or a particular function) is lost. However, I am unaware of any examples of this. More often, an organelle (and organism) can continue to function lacking at least some components, for instance following genetic knockdown or phamacological inhibition. The lost component may be responsible for some aspect of regulatory control, but its absence doesn't completely stop the organelle from forming, or doing its job (at least partially).

Another view (perhaps more commonly held) is that components of organelles can be grouped into two (or more) categories: core components and accessory components. While core components are absolutely essential (knockdowns are often, though not necessarily lethal (PML bodies don't form without PML, but null mice develop normally and live well)), the defining characteristic of accessory components is that they are dispensable. One or more properties of the organelle may undergo a quantitative change when an accessory protein is knocked down in

a cell, but, in a binary sense, the organelle is still able to perform its functions (albeit possibly under somewhat restricted conditions).

One complication that arises in determining necessary and sufficient properties from reconstitution experiments with proteins is that that proteins are inherently complicated objects, and often do more than one thing. Just as a nail can serve both to hold two pieces of wood together or as a hook for hanging household items, proteins often have multiple activities. As outlined earlier, profilin binds to actin monomers, but also the barbed ends of actin filaments. Profilin catalyzes the exchange of ADP for ATP on monomers and thereby increases the pool of assembly-competent G-actin. Profilin-binding to monomers also inhibits the nucleation of filaments by sterically obstructing an intra-filament binding interface.

This thesis focuses less on what proteins are sufficient to reconstitute an organelle-like structure or property, but rather which molecular-scale properties / activities are sufficient. Modeling has been an important aspect of the projects worked on in this thesis, as that venue allows us to decompose the combined activities inherent in real proteins to a greater degree than is easily facilitated in experiments.

One abstraction for a cell would be a large set of coupled reaction-diffusion equations. Each equation provides a description for the factors which contribute to changes in the spatiotemporal concentration profile of a particular chemical species (ion, protein, multi-molecular complex, etc), and there is one equation for every chemical species in the cell. Clearly there are a large number of equations, and similar to how knowledge of the positions and momentum of all of the atoms in the atmosphere would likely not help one to predict the weather, it is not clear that such a description of a cell would allow one to predict a cell's next move. However, such an abstraction can help to illustrate a central aim of this thesis. In any one equation describing the

temporal evolution of the concentration of species A at a given position, there are many terms, each with at least one coefficient.

There are many, many terms to consider, but many (possibly a vast majority of) terms will likely have a similar form, for instance corresponding to mass action binding kinetics. These could be qualitatively grouped together. In my view, the important question then becomes what **types** of terms do you need? While the effect of some proteins may essentially just be to change the value of a coefficient, the effect of other activities may be to add entire terms to the equation. I'm interested in understanding how adding terms that correspond to non-equilibrium activity change the dynamics of self-assembling biological materials. The subject of this thesis is to explore how adding terms that correspond to non-equilibrium activity alter the dynamics and properties of self-assembling biological materials. This will be explored explicitly in Chapters 2, 3, and 4 through examining emergent properties of self-organization, fluidization, and stress generation resulting from non-equilibrium ATP hydrolysis in actin-based structures and materials. In Chapter 5, I will focus more on the importance of the capacity of molecules to undergo self-assembly reactions than on their equilibrium or non-equilibrium nature.

Section 1.8 REFERENCES

Alberts, B., Johnson, A., Lewis, J., Raff, M., Roberts, K., and Walter, P. (2007). Molecular Biology of the Cell (New York, NY: Garland Science).

Amblard, F., Maggs, A.C., Yurke, B., Pargellis, A.N., and Leibler, S. (1996). Subdiffusion and Anomalous Local Viscoelasticity in Actin Networks. Phys. Rev. Lett. *77*, 4470–4473.

Andelman, D., and Joanny, J.-F. (2000). Polyelectrolyte adsorption. Comptes Rendus Académie Sci. - Ser. IV - Phys. *1*, 1153–1162.

Andrianantoandro, E., and Pollard, T.D. (2006). Mechanism of actin filament turnover by severing and nucleation at different concentrations of ADF/cofilin. Mol. Cell *24*, 13–23.

Asakura, S., and Oosawa, F. (1954). On Interaction between Two Bodies Immersed in a Solution of Macromolecules. J. Chem. Phys. *22*, 1255–1256.

Aumiller Jr, W.M., and Keating, C.D. (2016). Phosphorylation-mediated RNA/peptide complex coacervation as a model for intracellular liquid organelles. Nat. Chem. *8*, 129–137.

Banani, S.F., Rice, A.M., Peeples, W.B., Lin, Y., Jain, S., Parker, R., and Rosen, M.K. (2016). Compositional Control of Phase-Separated Cellular Bodies. Cell *166*, 651–663.

Berro, J., Sirotkin, V., and Pollard, T.D. (2010). Mathematical Modeling of Endocytic Actin Patch Kinetics in Fission Yeast: Disassembly Requires Release of Actin Filament Fragments. Mol. Biol. Cell *21*, 2905–2915.

Black, K.A., Priftis, D., Perry, S.L., Yip, J., Byun, W.Y., and Tirrell, M. (2014). Protein Encapsulation via Polypeptide Complex Coacervation. ACS Macro Lett. *3*, 1088–1091.

Blair, D., and Dufresne, E. Matlab Particle Tracking.

Blanchoin, L., and Pollard, T.D. (1998). Interaction of Actin Monomers with AcanthamoebaActophorin (ADF/Cofilin) and Profilin. J. Biol. Chem. *273*, 25106–25111.

Blanchoin, L., and Pollard, T.D. (1999). Mechanism of Interaction of Acanthamoeba Actophorin (ADF/Cofilin) with Actin Filaments. J. Biol. Chem. *274*, 15538–15546.

Blanchoin, L., Boujemaa-Paterski, R., Sykes, C., and Plastino, J. (2014). Actin Dynamics, Architecture, and Mechanics in Cell Motility. Physiol. Rev. *94*, 235–263.

Bon, S.A.F. (2014). CHAPTER 1:The Phenomenon of Pickering Stabilization: A Basic Introduction. In Particle-Stabilized Emulsions and Colloids, pp. 1–7.

Brangwynne, C.P., Eckmann, C.R., Courson, D.S., Rybarska, A., Hoege, C., Gharakhani, J., Jülicher, F., and Hyman, A.A. (2009). Germline P Granules Are Liquid Droplets That Localize by Controlled Dissolution/Condensation. Science *324*, 1729–1732.

Brangwynne, C.P., Mitchison, T.J., and Hyman, A.A. (2011). Active liquid-like behavior of nucleoli determines their size and shape in Xenopus laevis oocytes. Proc. Natl. Acad. Sci. *108*, 4334–4339.

Bray, D., and White, J.G. (1988). Cortical flow in animal cells. Science *239*, 883–888.

Breitsprecher, D., Jaiswal, R., Bombardier, J.P., Gould, C.J., Gelles, J., and Goode, B.L. (2012). Rocket Launcher Mechanism of Collaborative Actin Assembly Defined by Single-Molecule Imaging. Science *336*, 1164–1168.

Brieher, W. (2013). Mechanisms of actin disassembly. Mol. Biol. Cell *24*, 2299–2302.

Broedersz, C.P., and MacKintosh, F.C. (2014). Modeling semiflexible polymer networks. Rev. Mod. Phys. *86*, 995–1036.

Broedersz, C.P., Depken, M., Yao, N.Y., Pollak, M.R., Weitz, D.A., and MacKintosh, F.C. (2010). Cross-Link-Governed Dynamics of Biopolymer Networks. Phys. Rev. Lett. *105*, 238101.

Brown, S.S., and Spudich, J.A. (1979). Nucleation of polar actin filament assembly by a positively charged surface. J. Cell Biol. *80*, 499–504.

Bubb, M.R., Govindasamy, L., Yarmola, E.G., Vorobiev, S.M., Almo, S.C., Somasundaram, T., Chapman, M.S., Agbandje-McKenna, M., and McKenna, R. (2002). Polylysine Induces an Antiparallel Actin Dimer That Nucleates Filament Assembly CRYSTAL STRUCTURE AT 3.5-Å RESOLUTION. J. Biol. Chem. *277*, 20999–21006.

Bugyi, B., and Carlier, M.-F. (2010). Control of Actin Filament Treadmilling in Cell Motility. Annu. Rev. Biophys. *39*, 449–470.

Burtnick, L.D., Koepf, E.K., Grimes, J., Jones, E.Y., Stuart, D.I., McLaughlin, P.J., and Robinson, R.C. (1997). The Crystal Structure of Plasma Gelsolin: Implications for Actin Severing, Capping, and Nucleation. Cell *90*, 661–670.

Carlier, M.-F., Laurent, V., Santolini, J., Melki, R., Didry, D., Xia, G.-X., Hong, Y., Chua, N.-H., and Pantaloni, D. (1997). Actin Depolymerizing Factor (ADF/Cofilin) Enhances the Rate of Filament Turnover: Implication in Actin-based Motility. J. Cell Biol. *136*, 1307–1322.

Cates, M.E. (1987). Reptation of living polymers: dynamics of entangled polymers in the presence of reversible chain-scission reactions. Macromolecules *20*, 2289–2296.

Chaudhry, F., Breitsprecher, D., Little, K., Sharov, G., Sokolova, O., and Goode, B.L. (2012). Srv2/CAP (cyclase-associated protein) forms hexameric shurikens that directly catalyze actin filament severing by cofilin. Mol. Biol. Cell mbc.E12-08-0589.

Chen, D.T.N., Wen, Q., Janmey, P.A., Crocker, J.C., and Yodh, A.G. (2010). Rheology of Soft Materials. Annu. Rev. Condens. Matter Phys. *1*, 301–322.

Christensen, J.R., Hocky, G.M., Homa, K.E., Morganthaler, A.N., Hitchcock-DeGregori, S.E., Voth, G.A., and Kovar, D.R. (2017). Competition between Tropomyosin, Fimbrin, and ADF/Cofilin drives their sorting to distinct actin filament networks. eLife *6*, e23152.

Cooper, J.A., Walker, S.B., and Pollard, T.D. (1983). Pyrene actin: documentation of the validity of a sensitive assay for actin polymerization. J. Muscle Res. Cell Motil. *4*, 253–262.

Courson, D.S., and Rock, R.S. (2010). Actin Cross-link Assembly and Disassembly Mechanics for α-Actinin and Fascin. J. Biol. Chem. *285*, 26350–26357.

Courtemanche, N., and Pollard, T.D. (2013). Interaction of Profilin with the Barbed End of Actin Filaments. Biochemistry (Mosc.) *52*, 6456–6466.

Crocker, J.C., and Grier, D.G. (1996). Methods of Digital Video Microscopy for Colloidal Studies. J. Colloid Interface Sci. *179*, 298–310.

Crocker, J.C., Valentine, M.T., Weeks, E.R., Gisler, T., Kaplan, P.D., Yodh, A.G., and Weitz, D.A. (2000). Two-Point Microrheology of Inhomogeneous Soft Materials. Phys. Rev. Lett. *85*, 888–891.

De La Cruz, E.M. (2005). Cofilin Binding to Muscle and Non-muscle Actin Filaments: Isoform-dependent Cooperative Interactions. J. Mol. Biol. *346*, 557–564.

De La Cruz, E.M. (2009a). How cofilin severs an actin filament. Biophys. Rev. *1*, 51–59.

De La Cruz, E.M. (2009b). How cofilin severs an actin filament. Biophys. Rev. *1*, 51–59.

De La Cruz, E.M., and Pollard, T.D. (1995). Nucleotide-Free Actin: Stabilization by Sucrose and Nucleotide Binding Kinetics. Biochemistry (Mosc.) *34*, 5452–5461.

De La Cruz, E.M., Martiel, J.-L., and Blanchoin, L. (2015). Mechanical Heterogeneity Favors Fragmentation of Strained Actin Filaments. Biophys. J. *108*, 2270–2281.

Didry, D., Carlier, M.-F., and Pantaloni, D. (1998). Synergy between Actin Depolymerizing Factor/Cofilin and Profilin in Increasing Actin Filament Turnover. J. Biol. Chem. *273*, 25602–25611.

Doi, M., and Edwards, S.F. (1986). The Theory of Polymer Dynamics (New York, NY: Oxford University Press).

Drenckhahn, D., and Pollard, T.D. (1986). Elongation of actin filaments is a diffusion-limited reaction at the barbed end and is accelerated by inert macromolecules. J. Biol. Chem. *261*, 12754–12758.

Feric, M., Vaidya, N., Harmon, T.S., Mitrea, D.M., Zhu, L., Richardson, T.M., Kriwacki, R.W., Pappu, R.V., and Brangwynne, C.P. (2016). Coexisting Liquid Phases Underlie Nucleolar Subcompartments. Cell *165*, 1686–1697.

Ferry, D.J. (1980). Viscoelastic Properties of Polymers (New York, NY: Wiley).

Foth, B.J., Goedecke, M.C., and Soldati, D. (2006). New insights into myosin evolution and classification. Proc. Natl. Acad. Sci. U. S. A. *103*, 3681–3686.

Frederick, K.B., Sept, D., and De La Cruz, E.M. (2008). Effects of Solution Crowding on Actin Polymerization Reveal the Energetic Basis for Nucleotide-Dependent Filament Stability. J. Mol. Biol. *378*, 540–550.

Fritzsche, M., Lewalle, A., Duke, T., Kruse, K., and Charras, G. (2013). Analysis of turnover dynamics of the submembranous actin cortex. Mol. Biol. Cell *24*, 757–767.

Fritzsche, M., Erlenkämper, C., Moeendarbary, E., Charras, G., and Kruse, K. (2016). Actin kinetics shapes cortical network structure and mechanics. Sci. Adv. *2*, e1501337.

Fujiwara, I., Vavylonis, D., and Pollard, T.D. (2007). Polymerization kinetics of ADP- and ADP-Pi-actin determined by fluorescence microscopy. Proc. Natl. Acad. Sci. *104*, 8827–8832.

Gardel, M.L., Valentine, M.T., Crocker, J.C., Bausch, A.R., and Weitz, D.A. (2003). Microrheology of Entangled F-Actin Solutions. Phys. Rev. Lett. *91*, 158302.

Gardel, M.L., Shin, J.H., MacKintosh, F.C., Mahadevan, L., Matsudaira, P., and Weitz, D.A. (2004b). Elastic Behavior of Cross-Linked and Bundled Actin Networks. Science *304*, 1301–1305.

Gardel, M.L., Shin, J.H., MacKintosh, F.C., Mahadevan, L., Matsudaira, P.A., and Weitz, D.A. (2004a). Scaling of F-Actin Network Rheology to Probe Single Filament Elasticity and Dynamics. Phys. Rev. Lett. *93*, 188102.

Gardel, M.L., Nakamura, F., Hartwig, J.H., Crocker, J.C., Stossel, T.P., and Weitz, D.A. (2006). Prestressed F-actin networks cross-linked by hinged filamins replicate mechanical properties of cells. Proc. Natl. Acad. Sci. U. S. A. *103*, 1762–1767.

de Gennes, P.-G. (1979). Scaling Concepts in Polymer Physics (Ithaca, NY: Cornell University Press).

Goode, B.L., and Eck, M.J. (2007). Mechanism and Function of Formins in the Control of Actin Assembly. Annu. Rev. Biochem. *76*, 593–627.

Gucht, J. van der, Spruijt, E., Lemmers, M., and Cohen Stuart, M.A. (2011). Polyelectrolyte complexes: Bulk phases and colloidal systems. J. Colloid Interface Sci. *361*, 407–422.

Gunning, P., O'Neill, G., and Hardeman, E. (2008). Tropomyosin-Based Regulation of the Actin Cytoskeleton in Time and Space. Physiol. Rev. *88*, 1–35.

Hanke, F., Serr, A., Kreuzer, H.J., and Netz, R.R. (2010). Stretching single polypeptides: The effect of rotational constraints in the backbone. EPL Europhys. Lett. *92*, 53001.

Hansen, S., Zuchero, J.B., and Mullins, R.D. (2013). Cytoplasmic Actin: Purification and Single Molecule Assembly Assays. In Adhesion Protein Protocols, A.S. Coutts, ed. (Humana Press), pp. 145–170.

Higgs, H.N., Blanchoin, L., and Pollard, T.D. (1999). Influence of the C Terminus of Wiskott-Aldrich Syndrome Protein (WASp) and the Arp2/3 Complex on Actin Polymerization. Biochemistry (Mosc.) *38*, 15212–15222.

Isambert, H., and Maggs, A.C. (1996). Dynamics and Rheology of Actin Solutions. Macromolecules *29*, 1036–1040.

Israelachvili, J.N. (2011). Intermolecular and Surface Forces (Amsterdam: Elsevier).

Jansen, S., Collins, A., Chin, S.M., Ydenberg, C.A., Gelles, J., and Goode, B.L. (2015). Single-molecule imaging of a three-component ordered actin disassembly mechanism. Nat. Commun. *6*, 7202.

Jégou, A., Niedermayer, T., Orbán, J., Didry, D., Lipowsky, R., Carlier, M.-F., and Romet-Lemonne, G. (2011). Individual Actin Filaments in a Microfluidic Flow Reveal the Mechanism of ATP Hydrolysis and Give Insight Into the Properties of Profilin. PLOS Biol. *9*, e1001161.

Jégou, A., Carlier, M.-F., and Romet-Lemonne, G. (2013). Formin mDia1 senses and generates mechanical forces on actin filaments. Nat. Commun. *4*, 1883.

Johnston, A.B., Collins, A., and Goode, B.L. (2015). High-speed depolymerization at actin filament ends jointly catalysed by Twinfilin and Srv2/CAP. Nat. Cell Biol. *17*, 1504–1511.

Jönsson, P., Jonsson, M.P., Tegenfeldt, J.O., and Höök, F. (2008). A Method Improving the Accuracy of Fluorescence Recovery after Photobleaching Analysis. Biophys. J. *95*, 5334–5348.

Kakran, M., and Antipina, M.N. (2014). Emulsion-based techniques for encapsulation in biomedicine, food and personal care. Curr. Opin. Pharmacol. *18*, 47–55.

Kang, H., Bradley, M.J., McCullough, B.R., Pierre, A., Grintsevich, E.E., Reisler, E., and Cruz, E.M.D.L. (2012). Identification of cation-binding sites on actin that drive polymerization and modulate bending stiffness. Proc. Natl. Acad. Sci. *109*, 16923–16927.

Kinosian, H.J., Selden, L.A., Estes, J.E., and Gershman, L.C. (1993). Nucleotide binding to actin. Cation dependence of nucleotide dissociation and exchange rates. J. Biol. Chem. *268*, 8683–8691.

Koestler, S.A., Rottner, K., Lai, F., Block, J., Vinzenz, M., and Small, J.V. (2009). F- and G-Actin Concentrations in Lamellipodia of Moving Cells. PLOS ONE *4*, e4810.

Koga, S., Williams, D.S., Perriman, A.W., and Mann, S. (2011). Peptide–nucleotide microdroplets as a step towards a membrane-free protocell model. Nat. Chem. *3*, 720–724.

Kovar, D.R., Kuhn, J.R., Tichy, A.L., and Pollard, T.D. (2003). The fission yeast cytokinesis formin Cdc12p is a barbed end actin filament capping protein gated by profilin. J. Cell Biol. *161*, 875–887.

Kovar, D.R., Harris, E.S., Mahaffy, R., Higgs, H.N., and Pollard, T.D. (2006). Control of the Assembly of ATP- and ADP-Actin by Formins and Profilin. Cell *124*, 423–435.

Kramer, J.R., and Deming, T.J. (2010). General Method for Purification of α-Amino acid-N-carboxyanhydrides Using Flash Chromatography. Biomacromolecules *11*, 3668–3672.

de Kruif, C.G., Weinbreck, F., and de Vries, R. (2004). Complex coacervation of proteins and anionic polysaccharides. Curr. Opin. Colloid Interface Sci. *9*, 340–349.

Kudryashov, D.S., and Reisler, E. (2003). Solution Properties of Tetramethylrhodamine-Modified G-Actin. Biophys. J. *85*, 2466–2475.

Kueh, H.Y., Brieher, W.M., and Mitchison, T.J. (2010). Quantitative Analysis of Actin Turnover in Listeria Comet Tails: Evidence for Catastrophic Filament Turnover. Biophys. J. *99*, 2153–2162.

Kuhn, J.R., and Pollard, T.D. (2005). Real-Time Measurements of Actin Filament Polymerization by Total Internal Reflection Fluorescence Microscopy. Biophys. J. *88*, 1387–1402.

Lecuit, T., Lenne, P.-F., and Munro, E. (2011). Force Generation, Transmission, and Integration during Cell and Tissue Morphogenesis. Annu. Rev. Cell Dev. Biol. *27*, 157–184.

Lenz, M., Thoresen, T., Gardel, M.L., and Dinner, A.R. (2012). Contractile Units in Disordered Actomyosin Bundles Arise from F-Actin Buckling. Phys. Rev. Lett. *108*, 238107.

Li, F., and Higgs, H.N. (2003). The Mouse Formin mDia1 Is a Potent Actin Nucleation Factor Regulated by Autoinhibition. Curr. Biol. *13*, 1335–1340.

Li, P., Banjade, S., Cheng, H.-C., Kim, S., Chen, B., Guo, L., Llaguno, M., Hollingsworth, J.V., King, D.S., Banani, S.F., et al. (2012). Phase transitions in the assembly of multivalent signalling proteins. Nature *483*, 336–340.

Lindhoud, S., and Claessens, M.M.A.E. (2015). Accumulation of small protein molecules in a macroscopic complex coacervate. Soft Matter *12*, 408–413.

Liu, J., Gardel, M.L., Kroy, K., Frey, E., Hoffman, B.D., Crocker, J.C., Bausch, A.R., and Weitz, D.A. (2006). Microrheology Probes Length Scale Dependent Rheology. Phys. Rev. Lett. *96*, 118104.

Liu, Y., Winter, H.H., and Perry, S.L. (2017). Linear viscoelasticity of complex coacervates. Adv. Colloid Interface Sci. *239*, 46–60.

Loisel, T.P., Boujemaa, R., Pantaloni, D., and Carlier, M.-F. (1999). Reconstitution of actin-based motility of Listeria and Shigella using pure proteins. Nature *401*, 613–616.

Maciver, S.K., Zot, H.G., and Pollard, T.D. (1991). Characterization of actin filament severing by actophorin from Acanthamoeba castellanii. J. Cell Biol. *115*, 1611–1620.

Matsudaira, P., Bordas, J., and Koch, M.H. (1987). Synchrotron x-ray diffraction studies of actin structure during polymerization. Proc. Natl. Acad. Sci. *84*, 3151–3155.

McCullough, B.R., Grintsevich, E.E., Chen, C.K., Kang, H., Hutchison, A.L., Henn, A., Cao, W., Suarez, C., Martiel, J.-L., Blanchoin, L., et al. (2011). Cofilin-Linked Changes in Actin Filament Flexibility Promote Severing. Biophys. J. *101*, 151–159.

Melki, R., Fievez, S., and Carlier, M.-F. (1996). Continuous Monitoring of Pi Release Following Nucleotide Hydrolysis in Actin or Tubulin Assembly Using 2-Amino-6-mercapto-7-methylpurine Ribonucleoside and Purine-Nucleoside Phosphorylase as an Enzyme-Linked Assay. Biochemistry (Mosc.) *35*, 12038–12045.

Michelot, A., Berro, J., Guérin, C., Boujemaa-Paterski, R., Staiger, C.J., Martiel, J.-L., and Blanchoin, L. (2007). Actin-Filament Stochastic Dynamics Mediated by ADF/Cofilin. Curr. Biol. *17*, 825–833.

Mitrea, D.M., and Kriwacki, R.W. (2016). Phase separation in biology; functional organization of a higher order. Cell Commun. Signal. *14*, 1.

Mizuno, D., Tardin, C., Schmidt, C.F., and MacKintosh, F.C. (2007). Nonequilibrium Mechanics of Active Cytoskeletal Networks. Science *315*, 370–373.

Molecular Probes The Molecular Probes Handbook.

Morse, D.C. (1998a). Viscoelasticity of Concentrated Isotropic Solutions of Semiflexible Polymers. 1. Model and Stress Tensor. Macromolecules *31*, 7030–7043.

Morse, D.C. (1998b). Viscoelasticity of Concentrated Isotropic Solutions of Semiflexible Polymers. 2. Linear Response. Macromolecules *31*, 7044–7067.

Mullins, R.D., Heuser, J.A., and Pollard, T.D. (1998). The interaction of Arp2/3 complex with actin: Nucleation, high affinity pointed end capping, and formation of branching networks of filaments. Proc. Natl. Acad. Sci. *95*, 6181–6186.

Murrell, M.P., and Gardel, M.L. (2012). F-actin buckling coordinates contractility and severing in a biomimetic actomyosin cortex. Proc. Natl. Acad. Sci. *109*, 20820–20825.

Nadkarni, A.V., and Brieher, W.M. (2014). Aip1 Destabilizes Cofilin-Saturated Actin Filaments by Severing and Accelerating Monomer Dissociation from Ends. Curr. Biol. *24*, 2749–2757.

Nolles, A., Westphal, A.H., de Hoop, J.A., Fokkink, R.G., Kleijn, J.M., van Berkel, W.J.H., and Borst, J.W. (2015). Encapsulation of GFP in Complex Coacervate Core Micelles. Biomacromolecules *16*, 1542–1549.

Normoyle, K.P.M., and Brieher, W.M. (2012). Cyclase-associated Protein (CAP) Acts Directly on F-actin to Accelerate Cofilin-mediated Actin Severing across the Range of Physiological pH. J. Biol. Chem. *287*, 35722–35732.

Obermeyer, A.C., Mills, C.E., Dong, X.-H., Flores, R.J., and Olsen, B.D. (2016). Complex coacervation of supercharged proteins with polyelectrolytes. Soft Matter *12*, 3570–3581.

Oriol-Audit, C. (1978). Polyamine-Induced Actin Polymerization. Eur. J. Biochem. *87*, 371–376.

Ou, Z., and Muthukumar, M. (2006). Entropy and enthalpy of polyelectrolyte complexation: Langevin dynamics simulations. J. Chem. Phys. *124*, 154902.

P G de Gennes, and Leger, and L. (1982). Dynamics of Entangled Polymer Chains. Annu. Rev. Phys. Chem. *33*, 49–61.

Pacalin, N.M., Leon, L., and Tirrell, M. (2016). Directing the phase behavior of polyelectrolyte complexes using chiral patterned peptides. Eur. Phys. J. Spec. Top. *225*, 1805–1815.

Pak, C.W., Kosno, M., Holehouse, A.S., Padrick, S.B., Mittal, A., Ali, R., Yunus, A.A., Liu, D.R., Pappu, R.V., and Rosen, M.K. (2016). Sequence Determinants of Intracellular Phase Separation by Complex Coacervation of a Disordered Protein. Mol. Cell *63*, 72–85.

Pavlov, D., Muhlrad, A., Cooper, J., Wear, M., and Reisler, E. (2007). ACTIN FILAMENT SEVERING BY COFILIN. J. Mol. Biol. *365*, 1350–1358.

Pelletier, V., Gal, N., Fournier, P., and Kilfoil, M.L. (2009). Microrheology of Microtubule Solutions and Actin-Microtubule Composite Networks. Phys. Rev. Lett. *102*, 188303.

Perry, S.L., Leon, L., Hoffmann, K.Q., Kade, M.J., Priftis, D., Black, K.A., Wong, D., Klein, R.A., Iii, C.F.P., Margossian, K.O., et al. (2015). Chirality-selected phase behaviour in ionic polypeptide complexes. Nat. Commun. *6*, 6052.

Phillips, R., Kondev, J., and Theriot, J. (2008). Physical Biology of the Cell (New York, NY: Garland Science).

Pollard, T.D. (1986). Rate constants for the reactions of ATP- and ADP-actin with the ends of actin filaments. J. Cell Biol. *103*, 2747–2754.

Pollard, T.D. (2007). Regulation of Actin Filament Assembly by Arp2/3 Complex and Formins. Annu. Rev. Biophys. Biomol. Struct. *36*, 451–477.

Pollard, T.D. (2010). Mechanics of cytokinesis in eukaryotes. Curr. Opin. Cell Biol. *22*, 50–56.

Pollard, T.D. (2016). Actin and Actin-Binding Proteins. Cold Spring Harb. Perspect. Biol. a018226.

Pollard, T.D., and Borisy, G.G. (2003). Cellular Motility Driven by Assembly and Disassembly of Actin Filaments. Cell *112*, 453–465.

Pollard, T.D., Goldberg, I., and Schwarz, W.H. (1992). Nucleotide exchange, structure, and mechanical properties of filaments assembled from ATP-actin and ADP-actin. J. Biol. Chem. *267*, 20339–20345.

Pollard, T.D., Blanchoin, L., and Mullins, R.D. (2000). Molecular Mechanisms Controlling Actin Filament Dynamics in Nonmuscle Cells. Annu. Rev. Biophys. Biomol. Struct. *29*, 545–576.

Ponti, A., Matov, A., Adams, M., Gupton, S., Waterman-Storer, C.M., and Danuser, G. (2005). Periodic Patterns of Actin Turnover in Lamellipodia and Lamellae of Migrating Epithelial Cells Analyzed by Quantitative Fluorescent Speckle Microscopy. Biophys. J. *89*, 3456–3469.

Priftis, D., Farina, R., and Tirrell, M. (2012). Interfacial Energy of Polypeptide Complex Coacervates Measured via Capillary Adhesion. Langmuir *28*, 8721–8729.

ProtParam, E. ExPASy - ProtParam tool.

Pubchem L-glutamic acid | C5H9NO4 - PubChem.

Rao, J.N., Madasu, Y., and Dominguez, R. (2014). Mechanism of actin filament pointed-end capping by tropomodulin. Science *345*, 463–467.

Reymann, A.-C., Suarez, C., Guérin, C., Martiel, J.-L., Staiger, C.J., Blanchoin, L., and Boujemaa-Paterski, R. (2011). Turnover of branched actin filament networks by stochastic fragmentation with ADF/cofilin. Mol. Biol. Cell *22*, 2541–2550.

Robin, F.B., McFadden, W.M., Yao, B., and Munro, E.M. (2014). Single-molecule analysis of cell surface dynamics in Caenorhabditis elegans embryos. Nat. Methods *11*, 677–682.

Rould, M.A., Wan, Q., Joel, P.B., Lowey, S., and Trybus, K.M. (2006). Crystal Structures of Expressed Non-polymerizable Monomeric Actin in the ADP and ATP States. J. Biol. Chem. *281*, 31909–31919.

Salbreux, G., Charras, G., and Paluch, E. (2012). Actin cortex mechanics and cellular morphogenesis. Trends Cell Biol. *22*, 536–545.

Schaus, T.E., Taylor, E.W., and Borisy, G.G. (2007). Self-organization of actin filament orientation in the dendritic-nucleation/array-treadmilling model. Proc. Natl. Acad. Sci. *104*, 7086–7091.

Schmidt, C.F., Baermann, M., Isenberg, G., and Sackmann, E. (1989). Chain dynamics, mesh size, and diffusive transport in networks of polymerized actin: a quasielastic light scattering and microfluorescence study. Macromolecules *22*, 3638–3649.

Schmoller, K.M., Semmrich, C., and Bausch, A.R. (2011). Slow down of actin depolymerization by cross-linking molecules. J. Struct. Biol. *173*, 350–357.

Sekerková, G., Richter, C.-P., and Bartles, J.R. (2011). Roles of the Espin Actin-Bundling Proteins in the Morphogenesis and Stabilization of Hair Cell Stereocilia Revealed in CBA/CaJ Congenic Jerker Mice. PLOS Genet. *7*, e1002032.

Sept, D., and McCammon, J.A. (2001). Thermodynamics and Kinetics of Actin Filament Nucleation. Biophys. J. *81*, 667–674.

Shimozawa, T., Yamagata, K., Kondo, T., Hayashi, S., Shitamukai, A., Konno, D., Matsuzaki, F., Takayama, J., Onami, S., Nakayama, H., et al. (2013). Improving spinning disk confocal microscopy by preventing pinhole cross-talk for intravital imaging. Proc. Natl. Acad. Sci. *110*, 3399–3404.

Sirotkin, V., Berro, J., Macmillan, K., Zhao, L., and Pollard, T.D. (2010). Quantitative Analysis of the Mechanism of Endocytic Actin Patch Assembly and Disassembly in Fission Yeast. Mol. Biol. Cell *21*, 2894–2904.

Skau, C.T., Neidt, E.M., and Kovar, D.R. (2009). Role of Tropomyosin in Formin-mediated Contractile Ring Assembly in Fission Yeast. Mol. Biol. Cell *20*, 2160–2173.

Sokolova, E., Spruijt, E., Hansen, M.M.K., Dubuc, E., Groen, J., Chokkalingam, V., Piruska, A., Heus, H.A., and Huck, W.T.S. (2013). Enhanced transcription rates in membrane-free protocells formed by coacervation of cell lysate. Proc. Natl. Acad. Sci. *110*, 11692–11697.

Spruijt, E., Westphal, A.H., Borst, J.W., Cohen Stuart, M.A., and van der Gucht, J. (2010). Binodal Compositions of Polyelectrolyte Complexes. Macromolecules *43*, 6476–6484.

Spudich, J.A., and Watt, S. (1971). The Regulation of Rabbit Skeletal Muscle Contraction I. BIOCHEMICAL STUDIES OF THE INTERACTION OF THE TROPOMYOSIN-TROPONIN COMPLEX WITH ACTIN AND THE PROTEOLYTIC FRAGMENTS OF MYOSIN. J. Biol. Chem. *246*, 4866–4871.

Squires, T.M., and Mason, T.G. (2010). Fluid Mechanics of Microrheology. Annu. Rev. Fluid Mech. *42*, 413–438.

Srivastava, S., and Tirrell, M.V. (2016). Polyelectrolyte Complexation. In Advances in Chemical Physics, S.A. Rice, and A.R. Dinner, eds. (Hoboken, NJ: John Wiley & Sons, Inc.), pp. 499–544.

Stuhrmann, B., Soares e Silva, M., Depken, M., MacKintosh, F.C., and Koenderink, G.H. (2012). Nonequilibrium fluctuations of a remodeling in vitro cytoskeleton. Phys. Rev. E *86*, 020901.

Su, X., Ditlev, J.A., Hui, E., Xing, W., Banjade, S., Okrut, J., King, D.S., Taunton, J., Rosen, M.K., and Vale, R.D. (2016). Phase separation of signaling molecules promotes T cell receptor signal transduction. Science *352*, 595–599.

Suarez, C., Roland, J., Boujemaa-Paterski, R., Kang, H., McCullough, B.R., Reymann, A.-C., Guérin, C., Martiel, J.-L., De La Cruz, E.M., and Blanchoin, L. (2011). Cofilin Tunes the Nucleotide State of Actin Filaments and Severs at Bare and Decorated Segment Boundaries. Curr. Biol. *21*, 862–868.

Svitkina, T.M., and Borisy, G.G. (1999). Arp2/3 Complex and Actin Depolymerizing Factor/Cofilin in Dendritic Organization and Treadmilling of Actin Filament Array in Lamellipodia. J. Cell Biol. *145*, 1009–1026.

Svitkina, T.M., Bulanova, E.A., Chaga, O.Y., Vignjevic, D.M., Kojima, S., Vasiliev, J.M., and Borisy, G.G. (2003). Mechanism of filopodia initiation by reorganization of a dendritic network. J Cell Biol *160*, 409–421.

Tang, J.X., and Janmey, P.A. (1996). The Polyelectrolyte Nature of F-actin and the Mechanism of Actin Bundle Formation. J. Biol. Chem. *271*, 8556–8563.

Theriot, J.A., and Mitchison, T.J. (1991). Actin microfilament dynamics in locomoting cells. Nature *352*, 126–131.

Theriot, J.A., and Mitchison, T.J. (1992). Comparison of actin and cell surface dynamics in motile fibroblasts. J. Cell Biol. *119*, 367–377.

Thoresen, T., Lenz, M., and Gardel, M.L. (2011). Reconstitution of Contractile Actomyosin Bundles. Biophys. J. *100*, 2698–2705.

Tinevez, J.-Y., Schulze, U., Salbreux, G., Roensch, J., Joanny, J.-F., and Paluch, E. (2009). Role of cortical tension in bleb growth. Proc. Natl. Acad. Sci. *106*, 18581–18586.

Tobolsky, A.V. (1956). Stress Relaxation Studies of the Viscoelastic Properties of Polymers. J. Appl. Phys. *27*, 673–685.

Tojkander, S., Gateva, G., and Lappalainen, P. (2012). Actin stress fibers – assembly, dynamics and biological roles. J Cell Sci *125*, 1855–1864.

Vandekerckhove, J., Deboben, A., Nassal, M., and Wieland, T. (1985). The phalloidin binding site of F-actin. EMBO J. *4*, 2815–2818.

Vieregg, J.R., and Tang, T.-Y.D. (2016). Polynucleotides in cellular mimics: Coacervates and lipid vesicles. Curr. Opin. Colloid Interface Sci. *26*, 50–57.

Vinson, V.K., De La Cruz, E.M., Higgs, H.N., and Pollard, T.D. (1998). Interactions of Acanthamoeba profilin with actin and nucleotides bound to actin. Biochemistry (Mosc.) *37*, 10871–10880.

Webb, M.R. (1992). A continuous spectrophotometric assay for inorganic phosphate and for measuring phosphate release kinetics in biological systems. Proc. Natl. Acad. Sci. *89*, 4884–4887.

Wegner, A. (1976). Head to tail polymerization of actin. J. Mol. Biol. *108*, 139–150.

Winkelman, J.D., Bilancia, C.G., Peifer, M., and Kovar, D.R. (2014). Ena/VASP Enabled is a highly processive actin polymerase tailored to self-assemble parallel-bundled F-actin networks with Fascin. Proc. Natl. Acad. Sci. *111*, 4121–4126.

Winkelman, J.D., Suarez, C., Hocky, G.M., Harker, A.J., Morganthaler, A.N., Christensen, J.R., Voth, G.A., Bartles, J.R., and Kovar, D.R. (2016). Fascin- and α-Actinin-Bundled Networks Contain Intrinsic Structural Features that Drive Protein Sorting. Curr. Biol. *26*, 2697–2706.

Wong, I.Y., Gardel, M.L., Reichman, D.R., Weeks, E.R., Valentine, M.T., Bausch, A.R., and Weitz, D.A. (2004). Anomalous Diffusion Probes Microstructure Dynamics of Entangled F-Actin Networks. Phys. Rev. Lett. *92*, 178101.

Xue, B., Leyrat, C., Grimes, J.M., and Robinson, R.C. (2014). Structural basis of thymosin-β4/profilin exchange leading to actin filament polymerization. Proc. Natl. Acad. Sci. *111*, E4596–E4605.

Yamashita, A., Maeda, K., and Maéda, Y. (2003). Crystal structure of CapZ: structural basis for actin filament barbed end capping. EMBO J. *22*, 1529–1538.

CHAPTER 2: SELF-ORGANIZATION OF MYOSIN II IN RECONSTITUTED ACTOMYOSIN BUNDLES

Section 2.1 PREFACE

The contents of this chapter are reproduced from Stachowiak, M.R., McCall, P.M., Thoresen, T., Balcioglu, H.E., Kasiewicz, L., Gardel, M.L., and O'Shaughnessy, B. (2012). Self-Organization of Myosin II in Reconstituted Actomyosin Bundles. Biophys. J. *103*, 1265–1274. (Stachowiak et al., 2012) is the result of a successful collaboration with the laboratory of Prof. Ben O'Shaughnessy at Columbia University, and focuses on the comparison of a theoretical model and simulation for stress fiber formation, developed by the first author Dr. Matt Stachowiak (then a graduate student) and Prof. O'Shaughnessy, with in vitro experiments performed Dr. Todd Thoresen (a postdoctoral researcher) and myself in Prof. Margaret Gardel's laboratory at the University of Chicago. All experimental results presented in the paper were from experiments performed by myself together with Dr. Thoresen, with the sole exception of the smooth muscle myosin II results presented in Fig. 2.9, which derived from experiments performed by Dr. Thoresen alone. All novel experimental procedures were developed by Dr. Thoresen. I performed the analysis of experimental data to determine the fraction of bundles which survived contraction, and the fraction of the surviving bundles which developed puncta of myosin II (quoted in the main text). I also measured the number of filaments per bundle, presented in Fig. 2.6, and helped with the preparation of figures containing experimental images.

The mathematical model presented in the paper and all simulations were developed and performed by our collaborators at Columbia. Additionally, measurements from experimental data of the steady-state myosin II puncta spacing distribution (Fig. 2.3E and Fig. 2.7B,C), as well as

the time-to-steady-state distribution (Fig. 2.8B) was performed by our collaborators at Columbia. In particular, Mr. Hayri Balcioglu (a graduate student) helped write code for the simulations, and Ms. Lisa Kasiewicz (an undergraduate student) measured the myosin II puncta size distribution presented in Fig. 2.2. I helped write the paper, drafting the materials and methods section and editing other sections, though the bulk of the writing was done by our collaborators at Columbia, in particular the lead author, Dr. Stachowiak. The collaboration was started by Profs. Gardel and O'Shaughnessy at the 2010 annual meeting of the American Society for Cell Biology, at which I presented a poster characterizing the emergence and dynamics of the myosin puncta observed in the experiments subsequently reported in (Stachowiak et al., 2012). I was the primary experimentalist in contact with Dr. Stachowiak, communicating with him regularly about details pertaining to experiments, the model, interpretation, analysis, and writing.

Section 2.2 ABSTRACT

Cells assemble a variety of bundled actomyosin structures in the cytoskeleton for activities such as cell shape regulation, force production and cytokinesis. While these linear structures exhibit varied architecture, two common organizational themes are a punctate distribution of myosin II and distinct patterns of actin polarity. The mechanisms that cells use to assemble and maintain these organizational features are poorly understood. To study these, we reconstituted actomyosin bundles in vitro that contained only actin filaments and myosin II. Upon addition of ATP, the bundles contracted and the uniformly distributed myosin spontaneously reorganized into discrete clusters. We developed a mathematical model in which the motion of myosin II filaments is governed by the polarities of the actin filaments with which they interact. The model showed that the assembly of myosins into clusters is driven by their tendency to migrate to locations with

zero net actin filament polarity. With no fitting parameters, the predicted distribution of myosin cluster separations was in close agreement with our experiments, including a -3/2 power law decay for intermediate length scales. Thus, without an organizing template or accessory proteins, a minimal bundle of actin and myosin has the inherent capacity to self-organize into a heterogeneous banded structure.

Section 2.3 INTRODUCTION

The actin cytoskeleton serves many purposes for cells, such as providing structural stability, guiding intracellular transport, and generating contractile force (Fletcher and Mullins, 2010). To perform these diverse functions, a variety of organizations are found in the cytoskeleton, requiring assembly and maintenance processes that can deliver components with tight spatial and temporal regulation (Chhabra and Higgs, 2007; Gardel et al., 2010; Hotulainen and Lappalainen, 2006). Cytoskeletal structures that exert contractile force are based on actin filaments, myosin II and other components. Cells assemble these components into contractile networks and bundles (Vicente-Manzanares et al., 2009) for physiological processes such as muscle contraction (Huxley, 1974), cell division (Pollard, 2010; Vavylonis et al., 2008), cell migration (Giannone et al., 2007; Vicente-Manzanares et al., 2007), and tissue morphogenesis (Martin et al., 2009; Lecuit et al., 2011).

An organizational feature in common to diverse contractile actomyosin structures is the presence of myosin II puncta. In nonmuscle cells, such puncta are aggregates of bipolar minifilaments, each containing ~10-30 nonmuscle myosin II dimers (Verkhovsky and Borisy, 1993; Svitkina et al., 1989). A second feature, demonstrated for some actomyosin organizations, is spatially organized actin filament polarity that is correlated with myosin positions. These

features are most clearly seen in the myofibrils of striated muscle whose architecture, based on the sarcomere repeat unit, exhibits spatially periodic actin filament polarity and myosin II density (Huxley, 1974). In muscle, myosin II thick filaments contract sarcomeres by pulling inward on actin filaments whose pointed ends orient toward the myosin located at the sarcomere center, while the barbed ends reside at the sarcomere boundaries. By comparison, actomyosin bundles in nonmuscle cells display a broad range of architectures. In stationary cells, stress fibers, contractile bundles of actin filaments and myosin II, display sarcomeric-like structure including alternating actin polarity and regularly spaced distinct myosin puncta with a period of ~1 μm along the bundle (Cramer et al., 1997; Peterson et al., 2004). However, stress fibers in migrating cells display both graded and mixed actin filament polarity (Cramer et al., 1997), and in fission yeast the cytokinetic contractile ring contains irregularly organized myosin puncta and apparently random actin filament polarity (Bezanilla et al., 2000; Kamasaki et al., 2007).

Recent studies have addressed the processes used by cells to assemble and organize the components that constitute these actomyosin structures. Dorsal stress fibers are assembled by formin-mediated polymerization of actin filaments from focal adhesions, following which myosin puncta appear that displace the actin filament crosslinking protein α-actinin (Hotulainen and Lappalainen, 2006). Once assembled, mature stress fibers and other actomyosin bundles undergo continuous actin polymerization from focal adhesions and insertion of nascent puncta of myosin II and α-actinin (Endlich et al., 2007; Rossier et al., 2010). However, the mechanisms that underlie these processes of organization remain poorly understood.

Two broad strategies of assembly and organization of actomyosin structures may be envisaged. (*i*) Templating. Pre-existing templates, bearing the blueprint of the structure to be assembled, could act as molecular scaffolds to direct components to specific locations. In striated

muscle the giant proteins titin, nebulin, and obscurin may assume such a role (Kontrogianni-Konstantopoulos et al., 2009), and c-titin, an isoform expressed in non-muscle cells, was identified in stress fibers but its role is unknown. (*ii*) Self-assembly. Components could spontaneously assemble themselves into organized structures. For example, fission yeast uses a dynamic "search and capture" mechanism to assemble its cytokinetic contractile ring, in which membrane-anchored components condense themselves into a tight ring by transient actin connections that myosin II pulls upon to draw the components together (Vavylonis et al., 2008).

In vitro reconstitution of minimal actomyosin structures is a powerful approach to expose mechanisms of assembly, organization and function. Some of the present authors recently reconstituted networks of actomyosin bundles tethered to substrate-bound beads (Thoresen et al., 2011). At a sufficiently high density of myosin, bundles spontaneously assembled that contained only actin filaments and smooth muscle myosin II thick filaments. Upon addition of ATP, the bundles contracted and became taut, generating ~500 pN of tension. This showed that myosin acting alone is capable of eliciting contraction of actin bundles on cellular length scales.

Here, we have reconstituted contractile bundles of actin filaments and skeletal muscle myosin II thick filaments to investigate the mechanisms of organization. In the presence of ATP, the bundles contracted and became taut over several seconds. Over a longer timescale of ~30 s skeletal muscle myosin II, initially distributed uniformly along the bundles, self-organized into distinct puncta reminiscent of those in the actomyosin cytoskeleton of living cells. This demonstrates that myosin II self-organizes into a punctate spatial arrangement without templating and without the accessory proteins found in cellular actomyosin bundles. To understand the myosin II self-organization quantitatively, we developed a mathematical model based on the forces exerted by myosin II thick filaments on actin filaments. These forces propel

myosin in the direction of local actin polarity in the bundle. The resulting motions aggregate myosin filaments at those bundle locations where the net bundle polarity vanishes. With no fitting parameters, our model successfully reproduces the broad distribution of distances d_{myo} between neighboring myosin puncta observed in our experiments. In particular, our prediction that the distribution follows a power law decay $\sim d_{\mathrm{myo}}^{-3/2}$ on intermediate scales less than the filament length is in remarkably close agreement with our measurements. Our results suggest that polarity of the local actin network is an important regulator of myosin II organization, and that cells may employ a self-assembly strategy to organize components in actomyosin assemblies.

Section 2.4 MATERIALS AND METHODS

Buffers

Spin-Down Buffer: 20 mM MOPS, pH 7.4, 500 mM KCl, 4 mM $MgCl_2$, 0.1 mM EGTA, 500 μM ATP

Wash Buffer: 20 mM MOPS, pH 7.4, 50 mM KCl, 4 mM $MgCl_2$, 0.1 mM EGTA

Assay Buffer: 20 mM MOPS, pH 7.4, 100 mM KCl, 4 mM $MgCl_2$, 0.1 mM EGTA, 0.7 % methylcellulose, 0.25 mg/ml glucose, 0.25% β-ME, 0.25 mg/ml glucose oxidase, 35 μg/mL catalase

Protein Preparations

Myosin Thick Filaments. Rabbit skeletal muscle myosin II (Cytoskeleton, Denver, CO) is fluorescently labeled with Oregon Green (OG) 488 maleimide dye (Molecular Probes, Invitrogen) as described previously (Verkhovsky and Borisy, 1993). Snap frozen aliquots of OG-

labeled and phosphorylated myosin are rapidly thawed. To isolate active myosin, myosin dimers are mixed with phalloidin-stabilized F-actin at a 1:4 myosin:actin molar ratio in Spin-Down Buffer and centrifuged for 30 min at 100,000g. The supernatant contains myosin with low affinity to F-actin in saturating ATP (presumed enzymatically active), whereas the high affinity binding fraction co-sediments with the F-actin pellet (presumed enzymatically dead). Myosin protein concentrations are determined spectroscopically. Myosin thick filaments, which we estimate are typically no more than 0.5 μm in length (Fig. 2.2), are formed by diluting myosin in Assay Buffer, thus changing the salt conditions from 500 mM to 120 mM KCl and waiting 10 min at room temperature.

Actin Filaments. Preparation of actin was described previously (Thoresen et al., 2011). G-actin is generously supplied by Dr. David Kovar (University of Chicago).

Assembly of Bundled F-actin Networks

Bead and coverslip preparation were described previously (Thoresen et al., 2011). Assembly of a network of bundles existing predominately within a single confocal plane is achieved using steps similar to those described in (Thoresen et al., 2011). First, a 10-20 μm thick polyacrylamide (PAA) gel is formed on a coverslip and biotinylated BSA is covalently attached to the top surface. This substrate is largely inert to non-specific myosin or actin binding (Sabass et al., 2008). The substrate is loaded into a flow chamber customized for imaging with high numerical aperture objectives and small (~30 μL) exchange volumes.

A dilute suspension of 3 μm diameter neutravidin-coated beads in Wash Buffer is perfused into the flow chamber and incubated for ~10 minutes to allow for the beads to sediment and bind to the biotinylated-BSA surface. Unbound beads are removed by further perfusion of Wash

Buffer. TMR-phalloidin-stabilized F-actin containing 10% biotinylated G-actin is gently sheared to a mean length of ~6.5 μm (Thoresen et al., 2011), diluted to 1 μM in Assay Buffer and perfused into the chamber. Over 30 min, F-actin binds to the avidin beads, forming asters which likely contain actin filaments of random polarity (Thoresen et al., 2011). A majority of unbound F-actin is removed by perfusion of two chamber volumes of Assay Buffer. The remaining bead-bound F-actin provides sites to template the assembly of actomyosin bundles. Upon perfusion of Assay Buffer containing myosin thick filaments in an ADP background, a bundled network forms over 30 min. The chamber is then washed with one volume of Assay Buffer, and contraction is initiated via perfusion of Assay Buffer with 100 μM ATP. We have observed myosin self-organization qualitatively in numerous experiments over several years; quantitative results in this manuscript were obtained from two independent experiments, one containing 261 total actomyosin bundles and the other containing 118 total bundles. Microscopy was described previously (Thoresen et al., 2011). All images shown are inverted contrast with low pass filtering.

Image analysis

The time scale for myosin II to reach its steady state distribution is defined relative to the first image where myosin ceases visible motion. The spacings between myosin II puncta are measured at steady state using ImageJ software (http://rsb.info.nih.gov/ij/). The myosin intensity profile along a 10-pixel (~1 μm) wide line drawn over the bundle is measured, and the separation between adjacent puncta d_{myo} is defined as the distance between adjacent fluorescence intensity peaks. Total bundle length L is determined from the length of a straight line drawn along the entire bundle, between bead attachment points or branch points with other bundles.

Section 2.5 RESULTS

Assembly and contraction of reconstituted bundles of actin and skeletal muscle myosin II

To examine mechanisms of organization in actomyosin assemblies, we reconstituted bundles of actin filaments and skeletal muscle myosin II in vitro using the technique described previously using smooth muscle myosin II (Thoresen et al., 2011). After allowing avidin-decorated beads to bind to a biotinylated coverslip, partially biotinylated F-actin filaments of length 6.5 ± 4.0 μm (mean ± SD, n = 200) (Thoresen et al., 2011) were perfused into the solution. These tetramethylrhodamine (TMR)-phalloidin-stabilized actin filaments bound to the beads to form F-actin asters (Fig. 2.1A, *i* and *ii*) which likely have random polarity (Thoresen et al., 2011). After wash steps, only a dilute F-actin background remained in solution.

Thick filaments of Oregon Green (OG)-labeled rabbit skeletal muscle myosin II, estimated to be ~0.5 μm in length (Fig. 2.2), were then perfused into the flow chamber with a concentration of 0.56 μM. Because nucleotides were absent, the myosin heads are bound with high affinity to F-actin either in rigor or with ADP (Howard, 2001). Over ~30 min, a branched network of actomyosin bundles formed that was tethered between beads (Fig. 2.1A, *iii* and 2.1B), following which myosin remaining in solution was washed out. These bundles were wavy, indicating that they lacked tension (Fig. 2.1B), and were stable over periods of more than one hour.

Upon addition of 100 μM ATP to initiate the catalytic activity of myosin II, two dramatic changes occurred. (*i*) The actomyosin bundles contracted and became taut. The only exceptions were some bundles that had length ≤ 6.5 μm, the length of the constituent actin filaments. In many cases, the bundles ruptured (41% of 379 total bundles ruptured within 8 s of ATP perfusion), apparently under their own tension (Fig. 2.1B). (*ii*) In 65% of the 222 bundles that did not rupture, myosin II, initially distributed relatively uniformly along the bundles, self-

organized into clearly distinct puncta flanked by regions with background levels of fluorescence on either side (Fig. 2.1B). The remaining 35% of bundles failed to form distinct puncta (Fig. 2.3), although some of these nevertheless developed an inhomogeneous distribution of myosin (Fig. 2.3).

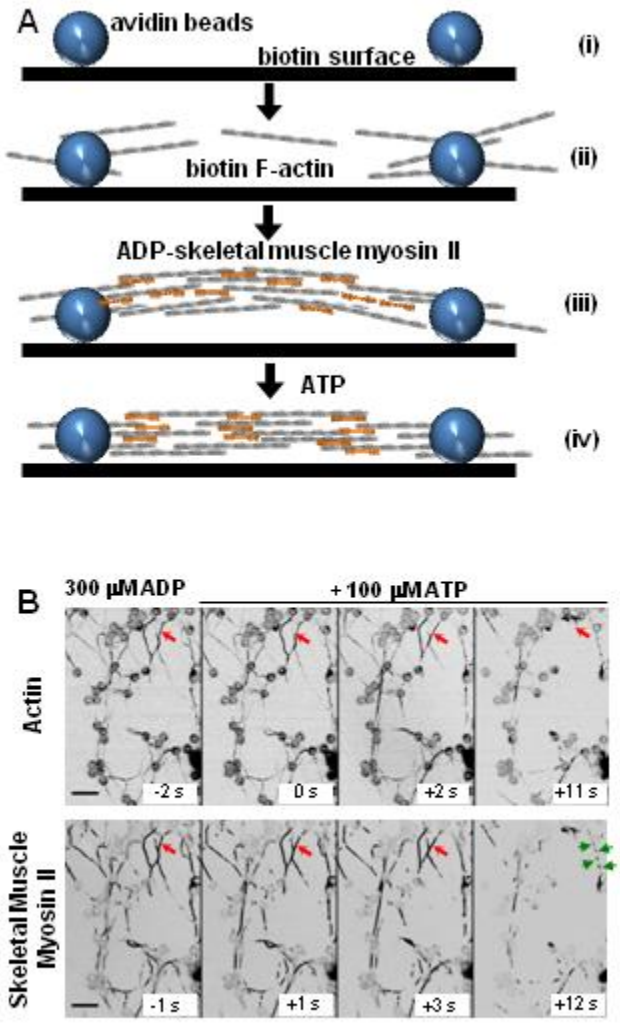

Figure 2.1 Assembly and contraction of reconstituted bundles of actin filaments and skeletal muscle myosin II. (A) Schematic illustrating bundle assembly and contraction. (i) Avidin-decorated beads (blue circles) are bound to a biotinylated surface. (ii) Biotinylated F-actin (gray) binds to beads to form F-actin asters with mixed polarity (22).

Figure 2.1 Continued. (iii) Skeletal muscle myosin II thick filaments bound to ADP are added to the actin-bead conjugate and allowed to incubate, resulting in a stable network of wavy actomyosin bundles. (iv) ATP is perfused to initiate the mechanochemical cycle of myosin II. The bundles contract and become taut. (B) Confocal, time lapse, inverted contrast images of a contracting network of bundles formed with F-actin (top, TMR-phalloidin) and skeletal muscle myosin II thick filaments (bottom, OG). Under ADP conditions the bundles are wavy, indicating a lack of tension. Upon the addition of ATP (t = 0), the bundles contract and myosin II self organizes into distinct puncta (green arrows). 41% of bundles rupture (red arrows). Scale bar: 10 μm.

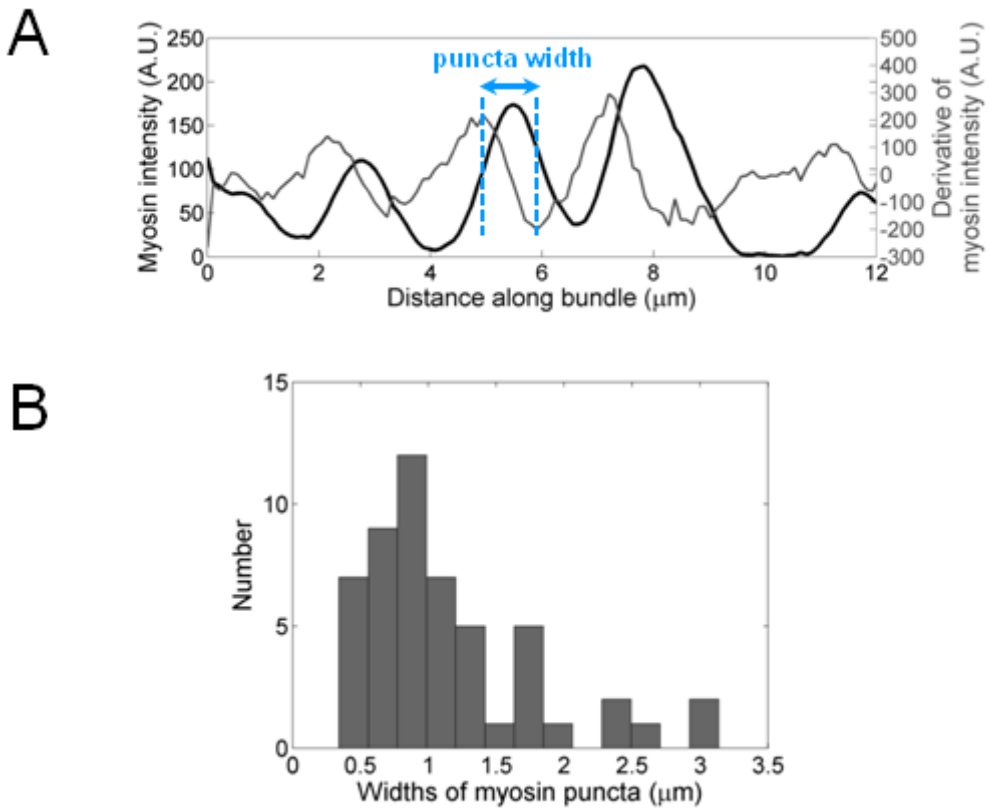

Figure 2.2 Estimation of skeletal muscle myosin II thick filament length. (A) Plot of the steady state myosin intensity (black) and its spatial derivative (gray) along the same bundle depicted in Fig. 2.4C and D. Widths of myosin puncta were defined as the distance between the positions of the maximum and minimum values of the derivative of the intensity (blue lines). (B) Histogram of myosin puncta widths (n = 52 puncta). Since the observed puncta widths define an upper bound on the thick filament length, we estimate that thick filaments have length l_{myo} = 0.5 μm, corresponding to the lower range of observed puncta widths.

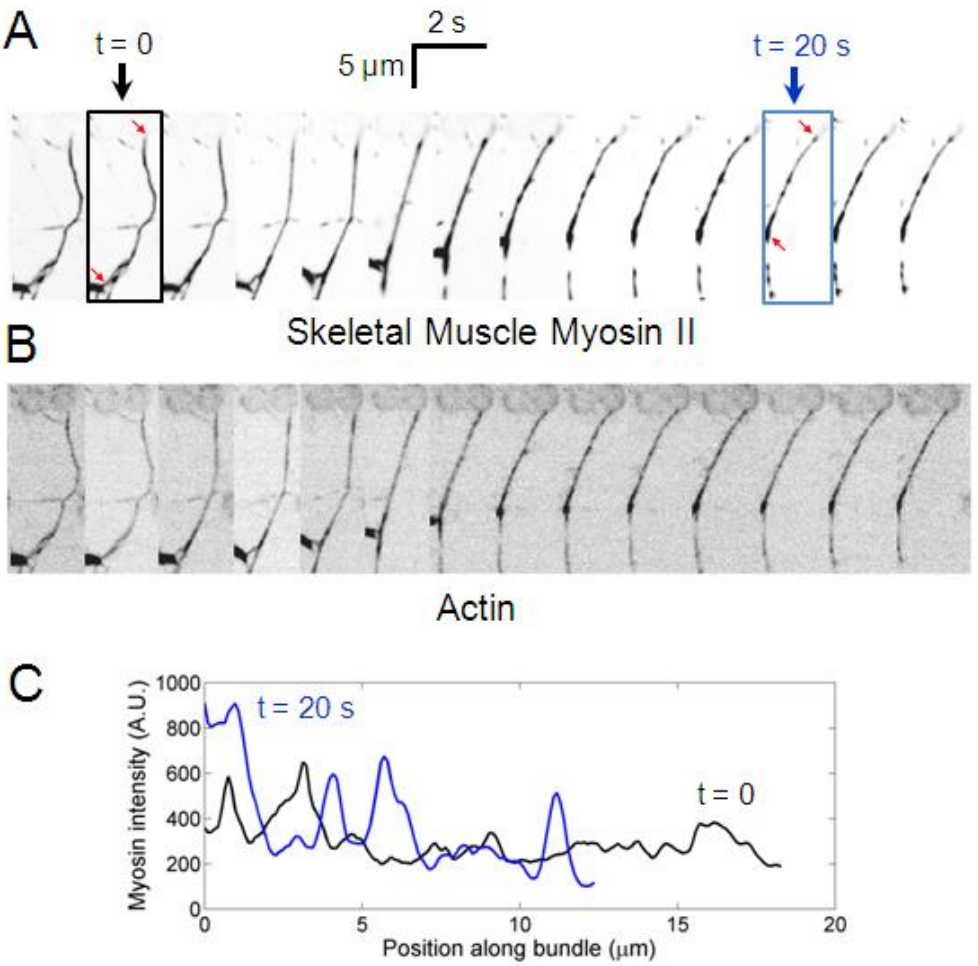

Figure 2.3. Kymograph of skeletal muscle myosin II and actin in a reconstituted actomyosin bundle that contracts but whose myosin fails to self-organize into distinct puncta. (A,B) Fluorescence images of myosin (A) and actin (B). *t* = 0 corresponds to ATP perfusion. (C) Background-subtracted line scans of myosin intensity along the bundle in panel (A) 0 and 20 s after ATP perfusion. Bundles that fail to define distinct puncta were defined as bundles in which the myosin intensity does not drop to background levels in between intensity peaks (compare to bundles that form distinct puncta in Fig. 2.4A-D).

Myosin II self-organizes into puncta after bundle contraction

We next characterized the self-organization of skeletal muscle myosin II into puncta. Prior to ATP perfusion, myosin II was distributed approximately uniformly along the bundle axis (Figs. 2.4A-D). Upon perfusion of ATP, bundles rapidly contracted and became taut over ~2-8 s (Fig. 2.4A,C). Concurrent with and following contraction, myosin evolved into distinct clusters

over ~30 s, following which the myosin distribution was stable (Figs. 2.4A,C,D and see 2.8B below). Thus, bundle contraction and myosin self-organization occur on different timescales, and the myosin motions persisted for a considerable time after the bundles had become taut. With time the actin became somewhat more concentrated at the locations of the myosin puncta, but actin remained visible along the entire bundle length throughout the episodes of contraction and myosin self-organization (Fig. 2.4A). This is as expected, given that the bundle remained intact.

The emergence of distinct myosin puncta could be caused by myosin aggregation due to translation along the bundle axis, or by selective dissociation of myosin at specific locations along the bundle. To distinguish between these possibilities, we tracked the myosin intensity profile along the bundle as a function of time after ATP perfusion (Fig. 2.4A,B). This revealed that the total amount of myosin in bundles decreased by ~30% over 14 s (Fig. 2.4A,B), consistent with measurements of bundles containing smooth muscle myosin II (Thoresen et al., 2011). Despite this net loss of myosin, the myosin concentration increased over time at the locations of emerging myosin puncta, simultaneous with depletion of myosin in flanking regions (Fig. 2.4B). Furthermore, peaks in the myosin intensity profile translated along the bundle axis (Fig. 2.4A,B). These observations argue against a selective dissociation mechanism and strongly suggest that myosin self-organization occurs by aggregation of myosin due to translation along the bundle.

To characterize the steady state organization of myosin II in the bundle after the myosin motions were complete, we measured the final distribution of separations between adjacent myosin puncta, d_{myo}, defined as the distance between adjacent peaks in the myosin II intensity profile measured along the bundle (Fig. 2.4D). In contrast to the periodic myosin distribution in

sarcomeric bundles, the spacings in reconstituted bundles were broadly distributed, with a peak at ~1.3 μm (Fig. 2.4E) and a mean value $\langle d_{myo} \rangle = 2.0 \pm 1.5$ μm (mean ± SD).

Next we examined whether the broad distribution of separations between myosin II aggregates was a consequence of the broad distribution of total bundle lengths (mean value $L = 11.5 \pm 5.0$ μm (mean ± SD), Fig. 2.4E Inset). Plotting myosin cluster separation versus bundle length revealed no such correlation (Fig. 2.4F). This strongly suggests that the statistics governing myosin location along a bundle depend only on local bundle properties rather than global properties such as total bundle length.

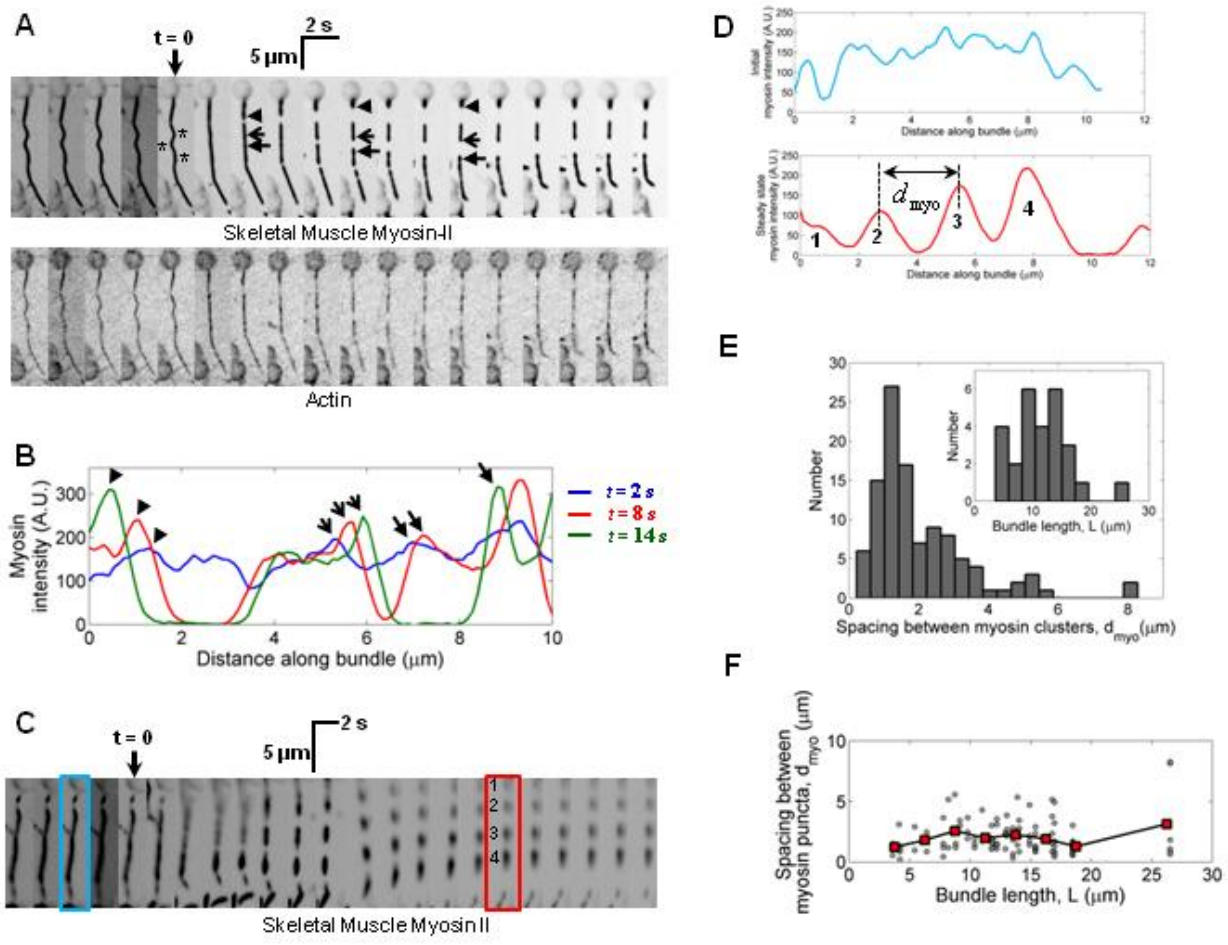

Figure 2.4 Self-organization of skeletal muscle myosin II.

Figure 2.4 Continued. (A) Kymographs of myosin (top) and actin (bottom) in a reconstituted bundle. The bundle is initially wavy (asterisks), but within 2-4 s after ATP perfusion (t = 0), the bundle has contracted and become taut. Myosin reorganizes into distinct puncta, while actin remains visible along the entire bundle. (B) Myosin intensity profiles along a portion of the bundle displayed in panel (A) at 2, 8, and 14 s after ATP perfusion. In (A) and (B), arrows track peaks in myosin intensity that develop at the boundaries of myosin puncta, suggesting that myosin movement and aggregation rather than myosin dissociation causes the development of distinct puncta. See also Movie S1. (C) Kymograph showing the evolution of the myosin II distribution along a bundle after ATP perfusion at t = 0. Four distinct myosin puncta are highlighted. (D) Profile of myosin II intensity along the bundle axis before addition of ATP (top) and after the myosin has reached steady-state (bottom). Profiles correspond to the blue and red boxes in panel (C), respectively. Myosin II self-organizes into four distinct puncta, as indicated. The distance between puncta, d_{myo}, is defined as the distance between peaks in the myosin intensity profile. (E) Measured distribution of separations between myosin puncta at steady state. The mean separation was $\langle d_{myo} \rangle = 2.0 \pm 1.5$ μm (mean ± SD; n = 108). Inset: histogram of total bundle lengths, which range between 3.6 and 26.5 μm (n = 27). (F) Measured separations between myosin II puncta as a function of total bundle length (n = 108 separations, 27 bundles). Gray circles: raw data; red squares: moving average over windows of 2.5 μm. The separation between myosin puncta is independent of bundle length, implicating a local mechanism for determining myosin II organization.

Model of self-organization dynamics of skeletal muscle myosin II in actomyosin bundles

To establish the mechanisms underlying myosin II self-organization, we developed a mathematical model based on the tendency of myosin II to migrate towards the barbed ends of actin filaments (Fig. 2.5). The model assumes that the motion of myosin II thick filaments depends only on the polarity of neighboring actin filaments. To test this hypothesis, we solved the model by evolving the positions of myosin II thick filaments in simulated bundles, and then compared the simulated results with our experimental measurements.

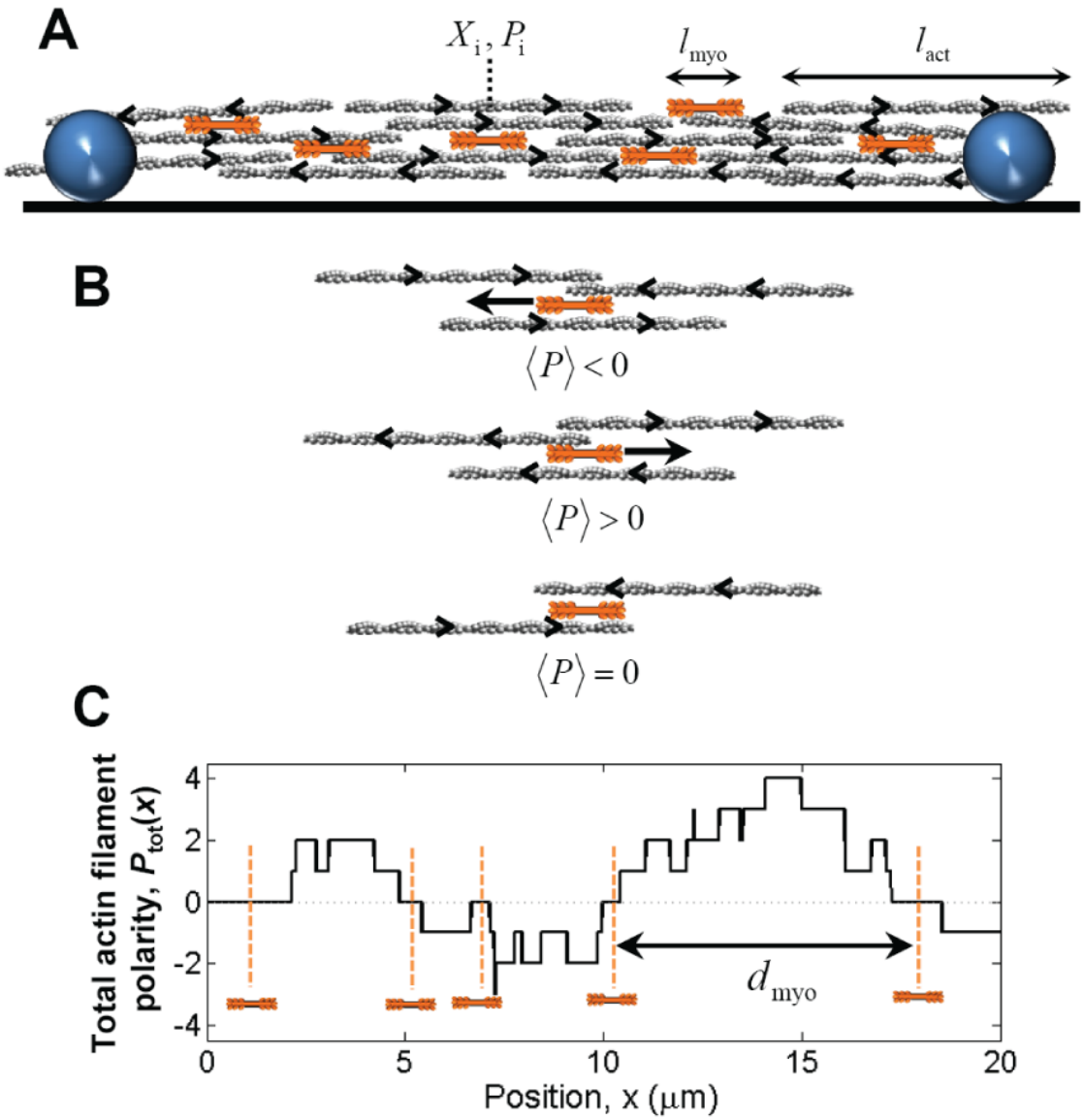

Figure 2.5 Model of myosin II self-organization in actomyosin bundles. (A) Schematic of a simulated actomyosin bundle. Actin filaments of length l_{act} have random positions and orientations, and filament *i* has position X_i and polarity P_i. Myosin II thick filaments of length l_{myo} are initially spaced uniformly along the bundle. (B) Myosin II moves toward actin filament barbed ends, and the force of the interaction is proportional to the amount of actin-myosin overlap. Thus, the velocity of each myosin thick filament is proportional to the mean polarity of overlapping actin filaments weighted by the amount of overlap, $\langle P \rangle$ (Eq. 2). Myosin thick filaments at locations where $\langle P \rangle$ is positive (negative) move to the right (left). Myosin thick filaments reach a steady state position only at locations where the mean actin filament polarity vanishes ($\langle P \rangle = 0$). (C) Example of the total actin filament polarity profile $P_{tot}(x)$ along a simulated actomyosin bundle. The polarity changes at locations of actin filament ends. Myosin II thick filaments migrate to positions where the actin filament polarity is zero (orange vertical lines).

Actin filaments in simulated bundles. Simulated bundles of length L, with ends at $x = 0$ and $x = L$, were generated by defining the positions and orientations of all actin filaments in the bundle, each of which has length l_{act}. Because the experimental bundle assembly process was unsupervised and random (Fig. 2.1A), actin filaments in simulated bundles were randomly positioned (filament i centered at location X_i) in the range $-l_{act}/2 < x < L + l_{act}/2$, and had random orientations, with polarity P_i, with $P_i = +1$ (-1) for actin filaments with barbed ends oriented in the $+x$ ($-x$) direction (Fig. 2.5A). The mean number of actin filaments in the cross section is $n_{act} \approx N_{act}l_{act}/(L + l_{act})$, where N_{act} is the total number of actin filaments in the bundle. Since we observe actin along the entire bundle and bundles become taut before myosin II self-organizes (Fig. 2.4A), we assume that the random actin organization is static during myosin II self-organization. We simulated 27,000 bundles with lengths L taken from the experimentally measured distribution (Fig. 2.4E Inset) and with values $l_{act} = 6$ μm (Thoresen et al., 2011) and $n_{act} = 5$ (Fig. 2.6), consistent with experimental measurements (Table 2.1).

Myosin II dynamics. Myosin II thick filaments of length $l_{myo} = 0.5$ μm (Fig. 2.2 and Table 2.1) were placed with an initially uniform distribution along the bundle axis (Fig. 2.5A), consistent with our experiments (Fig. 2.4A-D). The mean number of thick filaments in cross section is $n_{myo} \approx N_{myo}l_{myo}/(L + l_{myo})$, where N_{myo} is the total number of thick filaments in the bundle.

At time $t = 0$ (perfusion of ATP), the position of each thick filament begins to evolve according to the properties of its interactions with neighboring actin filaments: (*i*) Myosin exerts forces on actin filaments in the direction of their pointed ends. (*ii*) The force a thick filament exerts on an actin filament is proportional to the extent that they overlap, as observed in striated muscle (Gordon et al., 1966). For simplicity, we ignore molecular details of the myosin thick

filament, such the bare zone in the center of thick filaments that contains no myosin heads. Assuming a linear force-velocity relation, the force acting on thick filament *j* due to its interaction with actin filament *i* is

$$f_{\mathrm{myo}}^{\mathrm{ij}} = w_{\mathrm{ij}} f_{\mathrm{s}} (P_{\mathrm{i}} - v_{\mathrm{myo}}^{\mathrm{j}} / v_{\mathrm{myo}}^{0}) \,, \tag{1}$$

where w_{ij} is the length of myosin-actin overlap, f_{s} is the myosin stall force at full overlap, $v_{\mathrm{myo}}^{\mathrm{j}}$ is the velocity of thick filament *j*, and v_{myo}^{0} is the unloaded sliding velocity of skeletal muscle myosin II. As the actin bundles are thin ($n_{\mathrm{act}} \approx$ 1-6, Table 2.1), we assume that a thick filament interacts equally with all actin filaments that it overlaps and exerts a total force proportional to the number of overlapping filaments. The sum of forces actin on a given thick filament, due to interactions with all neighboring actin filaments, must vanish, $\sum_i f_{\mathrm{myo}}^{\mathrm{ij}} = 0$. Applying this condition to Eq. 1 gives the following result for the myosin thick filament velocity,

$$v_{\mathrm{myo}}^{\mathrm{j}} = v_{\mathrm{myo}}^{0} \frac{\sum_i w_{\mathrm{ij}} P_{\mathrm{i}}}{\sum_i w_{\mathrm{ij}}} = v_{\mathrm{myo}}^{0} \langle P \rangle \,. \tag{2}$$

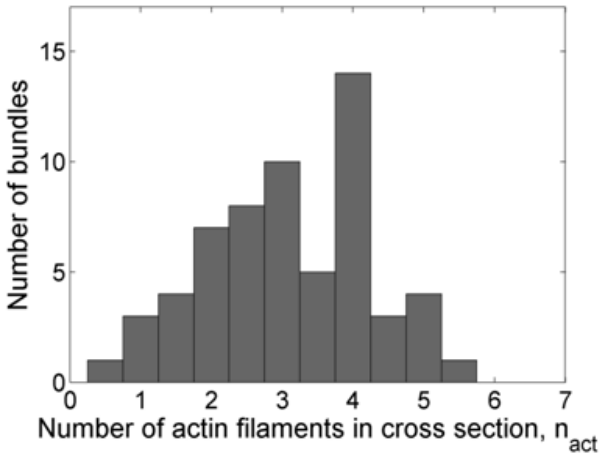

Figure 2.6 Histogram of the number of actin filaments in the bundle cross section.

Figure 2.6 Continued. Bundles typically consist of 1-6 actin filaments in parallel (n = 60 bundles). Quantitative fluorescence microscopy was used in a manner similar to (Thoresen et al., 2011) to determine n_{act}. Briefly, for a given bundle n_{act} is defined to be the ratio of the peak fluorescence intensity of the bundle, I_b, to the mean peak fluorescence intensity of single actin filaments $\langle I_f \rangle$, i.e. $n_{act} = I_b/\langle I_f \rangle$. Peak intensities of individual bundles and filaments are the maximum values of Gaussian function fits (fitting done with OriginPro 8.0) to transverse intensity linescans (acquired with ImageJ), after background correction. The analysis is performed on images of TMR-phalloidin-labeled actin taken of the same sample on the same day to minimize variability in imaging. Individual single-filament linescans (n = 20) are taken from images of actin filaments attached to beads prior to the addition of myosin, and individual bundle linescans (n = 60) are taken from images of the bundled actomyosin network in the presence of ADP.

Here, $\langle P \rangle$ denotes the mean actin polarity experienced by a myosin thick filament, weighted by the amount of overlap with each actin filament. Thus, the dynamics of each myosin II thick filament are determined only by its unloaded velocity and the polarities of neighboring actin filaments (Fig. 2.5B).

During the simulation, for each time step of duration Δt the position of each myosin thick filament was updated according to Eq. 2. We used $\Delta t = 0.067$ s, so that during one time step a myosin moves a maximum of $v_{myo}^{0} \Delta t = 75$ nm (Table 2.1), much less than the relevant simulation length scales L, l_{act}, and the mean separation between actin filament ends l_{step} (see below). The myosin II profile along the bundle was determined by calculating the number of thick filaments at each bundle location. To mimic imaging of the bundles in fluorescence microscopy (Fig. 2.4A,C), the 1D myosin density profile was then convolved with a Gaussian of standard deviation 0.15 μm to represent the point spread function.

The model predicts that myosin II migrates to zeros of actin polarity, and the steady state distribution of myosin II puncta separations is a power law

The dynamical simulations described above follow the time evolution of myosin II thick filament locations and capture the entire self-organization process. However, the final myosin II distribution generated by the self-organizing dynamics can be directly computed by noting that in steady state myosin will be located at bundle positions where the mean polarity vanishes, $\langle P \rangle = 0$, since at these locations the myosin velocity vanishes (see Eq. 2). Because myosin thick filaments are much shorter than the actin filaments ($l_{myo} << l_{act}$), the mean actin polarity $\langle P \rangle$ experienced by a myosin thick filament centered at some location x along the bundle is approximated by the mean polarity of all actin filaments that intersect the bundle cross section at x, which we name $p(x)$. Thus $p(x) = P_{tot}(x)/N_{tot}(x)$, where $P_{tot}(x)$ is the sum of the polarities of all actin filaments that cross x and $N_{tot}(x)$ is the number of such filaments. Then to determine the statistics of separation between adjacent myosin puncta in steady state we calculated the statistics of the separations of adjacent zeros of $P_{tot}(x)$ (Fig. 2.5C).

For a range of myosin cluster separations, this leads to a power law distribution with an exponent -3/2, as follows. The total bundle polarity $P_{tot}(x)$ changes only at the locations of actin filament ends. Now a bundle of n_{act} filaments in parallel contains on average $2n_{act}$ ends per length l_{act}, and the average spacing between actin filament ends is therefore $l_{step} = l_{act}/2n_{act}$ along the bundle axis, with $l_{step} = 0.6$ μm from Table 1. Thus, after each distance l_{step} along the bundle, a new filament end is encountered and the total polarity changes by ±1, depending on the polarity of the actin filament and whether the end is barbed or pointed. Because the actin filament orientation is random, the polarity changes are random and the total polarity $P_{tot}(x)$ follows a random walk as a function of x. Here x is a time-like variable, and the polarity changes randomly

after a "time step" of duration l_{step}. This random walk behavior only occurs over distances $x < l_{act}$ because the polarity changes caused by the two ends of a single filament are correlated. Thus, for length scales larger than the step size $x >> l_{step}$, the polarity variation along the bundle axis is mathematically analogous to the positional variation of a diffusing particle with diffusion constant $1/l_{step}$. Hence the probability distribution of the polarity at x, given the polarity at $x = 0$, is approximately Gaussian (Redner, 2001),

$$G\left(P_{tot}, x \mid P_{tot}(0)\right) = \frac{1}{\sqrt{4\pi x / l_{step}}} e^{-\left[P_{tot} - P_{tot}(0)\right]^2 / \left(4x / l_{step}\right)} \quad , \quad (l_{step} < x < l_{act}). \tag{3}$$

Table 2.1 Model parameter values.

Symbol	Meaning	Value	Legend
l_{act}	Length of the actin filaments	6 μm	(A)
l_{myo}	Length of reconstituted skeletal muscle myosin II thick filaments	0.5 μm	(B)
n_{act}	Mean number of actin filaments in cross section (bundle thickness)	5	(C)
n_{myo}	Mean number of myosin II thick filaments in cross section	2	(D)
L	Bundle length	3.6 - 26.5 μm	(E)
Fitting parameter			
v_{myo}^{0}	Un-loaded velocity of skeletal muscle myosin II	1.1 μm/s	(F)

Legend:
(A) Consistent with previous measurements by (Thoresen et al., 2011).

Table 2.1 Continued.
(B) Estimated from fluorescence images of myosin puncta. The lower bound of myosin puncta width sets the upper bound of thick filament length (Fig. 2.2).
(C) Quantitative fluorescent imaging shows that bundles have ~1-6 actin filaments in cross section (Fig. 2.6).
(D) Chosen to be >1 to be consistent with initial myosin staining along the entire bundle (Fig. 2.4A,C). Results are insensitive to the value of n_{myo} for $n_{myo}>1$.
(E) Measured in Fig. 2.4E, Inset. Simulations and numerical calculations were performed on simulated bundles having the measured distribution of bundle lengths.
(F) Used as fitting parameter so that the simulation matches the observed timescale for the myosin II distribution to reach steady state (Fig. 2.8B).

The distribution of separations between adjacent zeros of $P_{tot}(x)$, $f_{zero}(x)$, is the distribution of distances from one polarity zero, $P_{tot}(0) = 0$, to the next zero, $P_{tot}(x) = 0$. To obtain $f_{zero}(x)$, we first calculate the probability density $F(P_{tot}, x)$ that the polarity is P_{tot} after "time" x, given that it initially vanished, and given that the polarity was never zero during this period. This conditional probability is again the solution to a diffusion problem, but now with an absorbing boundary condition $F(0, x) = 0$. The solution is related to the Gaussian of Eq. 3, but is now the sum of one Gaussian with $P_{tot}(0) = 0^+$, and a second negative mirror image Gaussian with $P_{tot}(0) = 0^-$ to enforce the boundary condition at $P_{tot}(0) = 0$ (Redner, 2001). This amounts to taking the derivative of the Gaussian with respect to P_{tot}, evaluated at $P_{tot}(0) = 0$. Integrating this result for $F(P_{tot}, x)$ over all values of P_{tot} gives the total "survival" probability that no polarity zero is encountered after distance x. Taking minus the derivative of the survival probability with respect to x then yields the desired result, the probability density that a second polarity zero is encountered after a distance x,

$$f_{zero}(x) = \frac{C}{l_{step}}\left(\frac{x}{l_{step}}\right)^{-3/2} \qquad (l_{step} < x < l_{act}) \quad , \tag{4}$$

where the constant C fixes the normalization. This is the distribution of separations between zeros in the actin polarity. In addition to being valid only when x is much larger than the "time step" l_{step} in order that the continuous "diffusion" limit be valid, it is only valid provided x is much less than the filament length l_{act}. This is because on scales $x > l_{act}$ the free Gaussian statistics of Eq. 3 are no longer valid, as the changes in polarity that occur at the two ends of a given actin filament are correlated. Note that elsewhere we replace x with the notation d_{myo} to represent separations between mysoin puncta.

Thus, for separations less than the filament length the probability distribution of myosin separations follows a power law with exponent -3/2. This exponent is the signature of the essential mechanism proposed by our model, that myosin is driven to zeros of the total bundle polarity, and its value is independent of any model parameters. Comparison of the predicted exponent to experiment thus constitutes a stringent test of the model. To determine the complete distribution for all separations including those beyond l_{act}, and to account for finite bundle size effects and corrections due to the distribution in filament end separations (assumed above to be fixed and equal to l_{step}), we simply measured the zeros in the actin distribution of our simulated bundles (Fig. 2.5C).

Model reproduces experimentally observed steady state myosin II distributions

To compute model-predicted probability distributions of separations between adjacent myosin II puncta, we evolved our bundle simulation to steady state according to Eq. 2 and then calculated the separations between peaks in the myosin intensity profile (Fig. 2.7A), analogously to the procedure we used for our experimental measurements (Fig. 2.4D). Using the parameter values

in Table 1, model predictions were in remarkable agreement with the experimental observations, capturing the shape of the probability distribution with no fitting parameters (Fig. 2.7B, red line).

In particular, the experimental data were in close agreement with the model's predicted inverse 3/2 power law decay for myosin separations greater than the small cutoff scale l_{step} (0.6 μm, using Table 1) but smaller than the filament length l_{act} (6 μm, Table 1). To test this, we fitted a power law to the experimental data for separations d_{myo} in the range $\alpha l_{step} < d_{myo} < l_{act}/\alpha$, choosing the constant $\alpha = 1.5$ to be greater than unity as the power law is an asymptotic prediction valid, in principle, only for scales well inside the window bounded by l_{step} and l_{act} (Fig. 2.7C, thick blue line). Within this window of 0.9 μm < d_{myo} < 4 μm, we found a best fit exponent of -1.51 ± 0.14 (standard error) (Fig. 2.7C).

We then confirmed that in our simulated bundles the steady state myosin locations did indeed coincide with the zeros in total actin filament polarity (locations where $P_{tot} = 0$). We found that the distribution of separations between zeros in P_{tot} from our simulations (Fig. 2.7B, green curve) closely tracked the distribution of myosin separations in the simulation (Fig. 2.7B, red curve) as expected. The small differences between these two distributions arise because: (*i*) the simulation includes finite size myosin II thick filaments, and (*ii*) to mimic optical effects, the simulations (red curve) include a point spread function that smears the myosin distribution and obscures the smallest separations between myosin clusters.

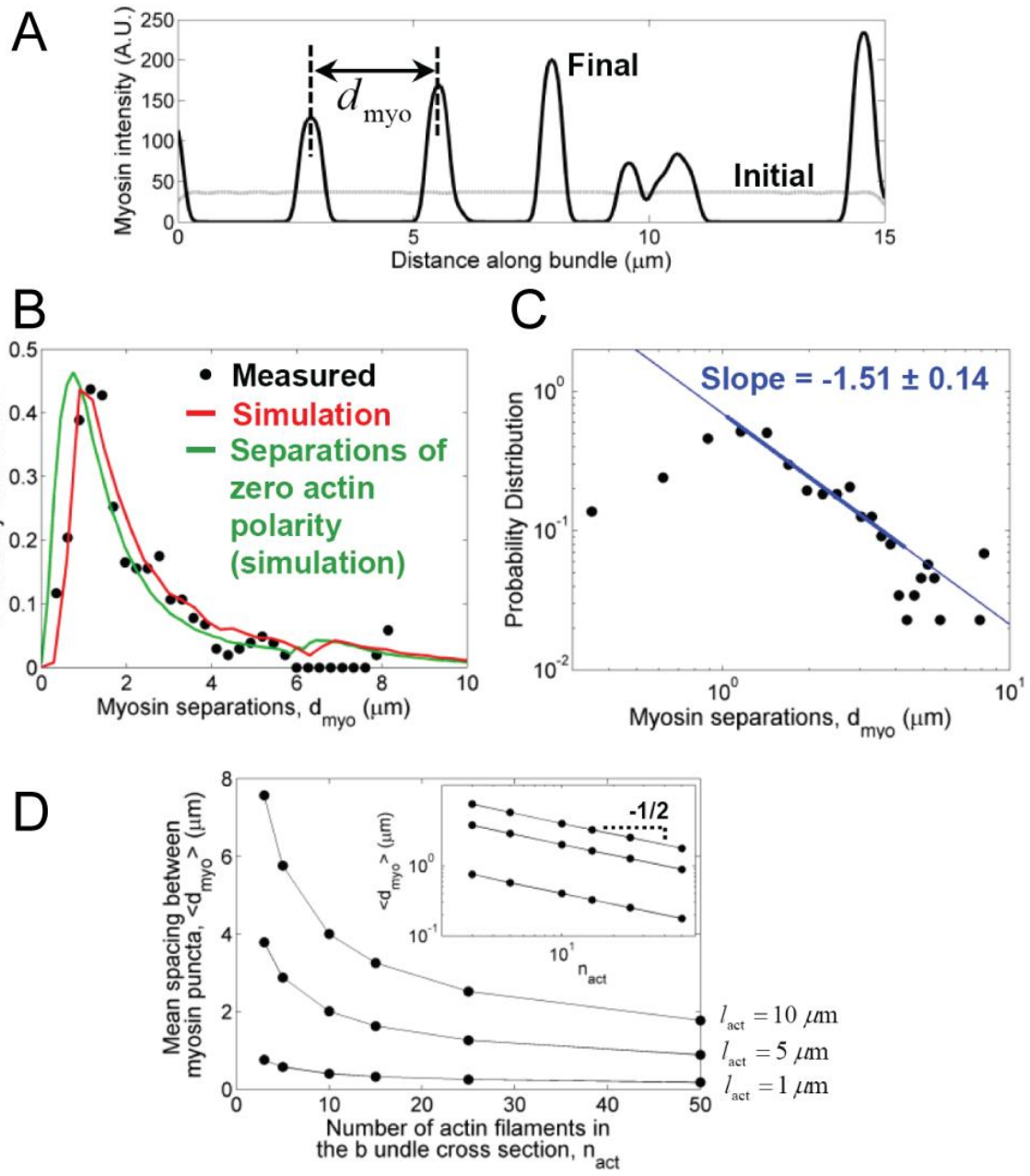

Figure 2.7 Comparison of measured and model-predicted distribution of myosin II in actomyosin bundles at steady state. (A) Initial (dotted line) and steady state (solid line) myosin distribution along a simulated bundle. Myosin puncta separations were measured peak-to-peak, as for experimentally observed bundles (Fig. 2.4D). (B) Probability distribution of steady state separations between myosin puncta. Red line: bundle simulations; green line: calculated from the positions where the total actin polarity vanishes in simulated bundles. Black circles: experimental measurements, averaged over 0.8 μm window. Vertical scaling is arbitrary for measurements because of low sample size in the distribution tail. The peak value was matched to the peak value of the simulation distribution. Parameters, as in Table 1. No fitting parameters were used in the model.

Figure 2.7 Continued. (C) Log-log plot of the steady state distribution of separations between myosin II puncta. Black circles: experimental measurement; blue line: best fit line. Fitting range is indicated by the thick portion of the line. The best fit exponent matches the predicted -3/2 power law from Eq. 4. (D) Predictions for the mean separation between myosin II puncta as a function of actin filament length and bundle thickness, calculated from the positions where the total polarity vanishes in simulated bundles. Longer actin filaments and thinner actin bundles result in larger spacing between myosin II puncta. Inset: Log-log plot confirms the predicted power law, $\langle d_{myo} \rangle \sim n_{act}^{-1/2}$ (Eq. 5).

The organization of myosin II depends on bundle thickness and actin filament length

Next we used our model to predict how the spatial distribution of myosin II clusters would vary as the properties of the actomyosin bundles are varied. We calculated the mean distance between adjacent myosin II puncta, given by locations where the net actin polarity vanishes in simulated bundles, as a function of both the mean number of actin filaments in cross section, n_{act} , and the actin filament length, l_{act} (Fig. 7D). From the distribution of myosin puncta separations that we calculated exactly, Eq. 4, the mean separation is

$$\left\langle d_{myo} \right\rangle \approx \int_{l_{step}}^{l_{act}} x f_{zero}(x) dx \sim \left(l_{step} l_{act} \right)^{1/2} \sim \frac{l_{act}}{n_{act}^{1/2}} \quad , \tag{5}$$

where we use $l_{step} << l_{act}$ and the fact that the true distribution falls off exponentially for $x > l_{act}$. Thus, the mean distance between adjacent myosin clusters increases linearly with the actin filament length, $\langle d_{myo} \rangle \sim l_{act}$, and decays with increasing numbers of actin filaments in the bundle, $\langle d_{myo} \rangle \sim n_{act}^{-1/2}$ (Fig. 7D). Both of these trends could be tested by future experiments.

Dynamics of myosin II self-organization

We next used our simulation to investigate the time course of myosin II self organization. Kymographs of the myosin distribution in simulated bundles showed evolution from an initially

uniform distribution to the final punctate distribution (Fig. 2.8A), similar to experimentally measured kymographs (Fig. 2.4A,C).

Our experiments showed that the time for the myosin distribution to reach steady state was 31.0 ± 17.2 s (mean ± SD) (Fig. 2.8B, top). In the simulations, we defined the myosin self-organization time as that by which all myosin II motion had ceased. We fitted the simulated mean self-organization time to the measured value, using the unloaded velocity of skeletal muscle myosin II as the fitting parameter. This procedure yielded $v_{myo}^{0} = 1.1$ μm/s (Fig. 2.8B, bottom), on the same order, but ~3-fold lower than, the value measured in in vitro gliding assays, ~2.8 μm/s (Lord and Pollard, 2004; Cheung et al., 2002). Simulated bundles displayed a broad distribution of myosin self-organization times, whose standard deviation of 16.3 s was in close agreement with our experimental measurements (Fig. 2.8B).

Thus, the experimental data are consistent with our model in which the velocity of a myosin II aggregate depends only on the polarities of the actin filaments in its neighborhood and the unloaded sliding velocity of the myosin.

Section 2.6 DISCUSSION

We combined mathematical modeling with quantitative measurements of reconstituted actomyosin bundles to identify a mechanism that organizes myosin II into heterogeneous clusters similar to those observed in the actomyosin cytoskeleton. Our results demonstrate that in bundles containing only actin filaments and thick filaments of skeletal muscle myosin II, myosin has the inherent ability to self-organize into puncta in the absence of a template or other components. The experimental data were consistent with our model in which the dynamics of myosin II are determined only by the polarities of nearby actin filaments (Fig. 2.5). When the total actin

polarity is non-zero the forces are proportionally unbalanced, and myosin translates along the bundle. Steady state is achieved once thick filaments have translated to locations where the net actin filament polarity vanishes and forces are balanced. With no fitting parameters, the predictions of this model were in remarkably close agreement with our experimental measurements, including a characteristic power law decay in the distribution of separations between myosin puncta at intermediate lengths. These findings suggest that in cells the actin polarity profile may be a key regulator of myosin II organization.

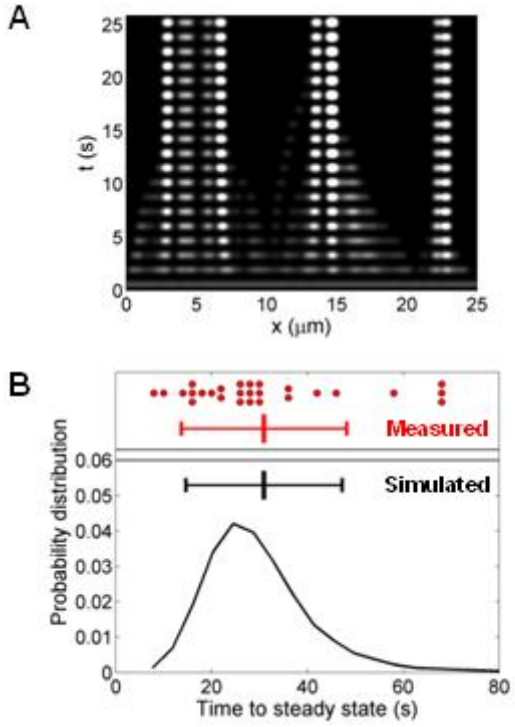

Figure 2.8 Kinetics of myosin II self-organization. (A) Kymograph from our bundle simulation showing the evolution of myosin II (white) from an initially uniform distribution along the bundle to a punctate distribution at steady state. In the simulation, ATP is added at t = 0 s and the bundle spans between x = 0 and x = 25 μm. (B) Distribution of timescales for the myosin II organization to reach steady state. In experiments (top, red), myosin II reached steady-state in 31.0 ± 17.2 s (mean ± SD, n = 27).

Figure 2.8 Continued. In simulations (bottom, black), the un-loaded sliding velocity of skeletal muscle myosin II, v_{myo}^{0} = 1.1 μm/s, was used as a fitting parameter so that the mean time to steady state matched the experimentally measured value. The standard deviation of the simulated time to steady state, 16.3 s, matched the experimentally measured standard deviation without any additional fitting. Red and black bars: mean ± SD. Parameter values, as in Table 1.

The self-organization mechanism described by our model assumed a random and static pattern of actin filament polarity in the reconstituted bundles. Random actin polarity in the bundles is likely, as the bundle assembly process was itself unsupervised and random (Fig. 2.1A). We assumed that the actin filaments responsible for the myosin motions are immobile, because bundle shortening ceased (2-8 s, Fig. 2.4A) well before myosin self-organization was complete (30 s, Fig. 2.8), and because actin was visible along the entire bundle at all times (Fig. 2.4A). These assumptions are corroborated by the ability of the model to account quantitatively for the experimentally measured separations of myosin puncta, without fitting parameters (Fig. 2.7B,C). However, in the absence of specific crosslinking molecules, it is not known how the actin filaments maintain bundle integrity. This could be due to a combination of non-specific interactions and the crosslinking activity of myosin thick filaments. In addition to a set of apparently static actin filaments that our results suggest are responsible for the myosin self-organization, we observed a dynamic component to the actin density that correlated with the myosin puncta locations (Fig. 2.4A). This presumably corresponds to a mobile fraction of uncrosslinked actin filaments; we speculate that, being free to translate, this fraction would not support force and would therefore not affect the myosin dynamics.

Here we assembled bundles containing bipolar thick filaments of skeletal muscle myosin II. Previously, some of the present authors reported contraction of reconstituted bundles containing side polar (Xu et al., 1996) smooth muscle myosin II thick filaments (Thoresen et al., 2011).

Interestingly, smooth muscle myosin in reconstituted bundles is also able to self-organize into puncta (Fig. 2.9 and see Fig. 2 of (Thoresen et al., 2011)), suggesting that the mechanisms of contraction and self-organization of reconstituted bundles do not depend on the detailed thick filament composition and structure. However, while bundles containing skeletal muscle myosin II contracted and became taut within 2-8 s after perfusion of ATP (Fig. 2.4A,C), smooth muscle myosin bundles contracted over a longer ~20 s timescale (Thoresen et al., 2011). This is consistent with the slower working velocity of the smooth muscle myosin motor, 0.2-0.4 μm/s (Warshaw et al., 1990), compared to >1 μm/s for skeletal muscle myosin II (Lord and Pollard, 2004; Cheung et al., 2002).

Similar to actomyosin bundles reconstituted in vitro, stress fibers in cells have a punctate distribution of myosin II (Peterson et al., 2004), exhibit complex myosin dynamics after stimulation (Peterson et al., 2004), and recoil after rupturing spontaneously (Smith et al., 2010) or by laser ablation (Kumar et al., 2006; Tanner et al., 2010). Several studies attempted to infer the mechanisms that underlie stress fiber kinetics from their behavior following stimulation or during recoil. These studies implicated factors, in addition to myosin contractility, such as internal and external frictional and elastic forces, and elastic stress-dependent actin depolymerization (Colombelli et al., 2009; Russell et al., 2009; Stachowiak and O'Shaughnessy, 2009, 2008).

While these previous studies addressed kinetics in already-assembled stress fibers, the present work has addressed component motions that lead to assembly of the stress fiber itself. The self-assembly mechanism described here may help cells to organize contractile actomyosin structures, as the punctate myosin distributions in reconstituted bundles are similar to those in cellular actomyosin bundles (Hotulainen and Lappalainen, 2006; Peterson et al., 2004).

Presumably templating mechanisms also contribute to organization in cells, as sarcomeric contractile structures contain scaffolding molecules such as titin (Kontrogianni-Konstantopoulos et al., 2009). The myosin distribution that we observed was more random than the tightly periodic distribution in striated muscle, with a broad distribution of spacings between myosin regions (Fig. 2.4E) that is reminiscent of more disordered bundled architectures in the cell, such as the cytokinetic ring and randomly organized stress fibers (Cramer et al., 1997; Bezanilla et al., 2000).

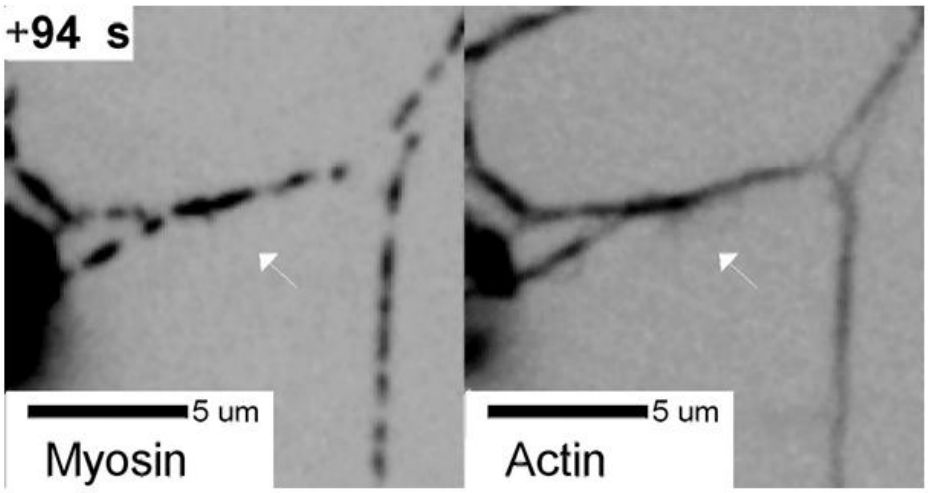

Figure 2.9 Puncta formation by smooth muscle myosin II in reconstituted actomyosin bundles. Confocal fluorescence images of reconstituted bundles containing smooth muscle myosin II thick filaments (left) and actin (right), 94 s after ATP perfusion. In these bundles, smooth muscle myosin II thick filaments self-organize into distinct clusters, similar to bundles containing skeletal muscle myosin II. Bundles containing smooth muscle myosin were prepared as described by (Thoresen et al., 2011).

Section 2.7 ACKNOWLEDGMENTS

We thank David Kovar for supplying G-actin, and Michael Murrell for supplying Oregon Green labeled myosin. This work was supported by NIH GM086731 (B.O.) and NIH DP10D00354 (M.L.G.).

Section 2.8 REFERENCES

Bezanilla, M., Wilson, J.M., and Pollard, T.D. (2000). Fission yeast myosin-II isoforms assemble into contractile rings at distinct times during mitosis. Curr. Biol. *10*, 397–400.

Cheung, A., Dantzig, J.A., Hollingworth, S., Baylor, S.M., Goldman, Y.E., Mitchison, T.J., and Straight, A.F. (2002). A small-molecule inhibitor of skeletal muscle myosin II. Nat. Cell Biol. *4*, 83–88.

Chhabra, E.S., and Higgs, H.N. (2007). The many faces of actin: matching assembly factors with cellular structures. Nat. Cell Biol. *9*, 1110–1121.

Colombelli, J., Besser, A., Kress, H., Reynaud, E.G., Girard, P., Caussinus, E., Haselmann, U., Small, J.V., Schwarz, U.S., and Stelzer, E.H.K. (2009). Mechanosensing in actin stress fibers revealed by a close correlation between force and protein localization. J. Cell Sci. *122*, 1665–1679.

Cramer, L.P., Siebert, M., and Mitchison, T.J. (1997). Identification of Novel Graded Polarity Actin Filament Bundles in Locomoting Heart Fibroblasts: Implications for the Generation of Motile Force. J. Cell Biol. *136*, 1287–1305.

Endlich, N., Otey, C.A., Kriz, W., and Endlich, K. (2007). Movement of stress fibers away from focal adhesions identifies focal adhesions as sites of stress fiber assembly in stationary cells. Cell Motil. Cytoskeleton *64*, 966–976.

Fletcher, D.A., and Mullins, R.D. (2010). Cell mechanics and the cytoskeleton. Nature *463*, 485–492.

Gardel, M.L., Schneider, I.C., Yvonne Aratyn-Schaus, and Waterman, C.M. (2010). Mechanical Integration of Actin and Adhesion Dynamics in Cell Migration. Annu. Rev. Cell Dev. Biol. *26*, 315–333.

Giannone, G., Dubin-Thaler, B.J., Rossier, O., Cai, Y., Chaga, O., Jiang, G., Beaver, W., Döbereiner, H.-G., Freund, Y., Borisy, G., et al. (2007). Lamellipodial Actin Mechanically Links Myosin Activity with Adhesion-Site Formation. Cell *128*, 561–575.

Gordon, A.M., Huxley, A.F., and Julian, F.J. (1966). The variation in isometric tension with sarcomere length in vertebrate muscle fibres. J. Physiol. *184*, 170–192.

Hotulainen, P., and Lappalainen, P. (2006). Stress fibers are generated by two distinct actin assembly mechanisms in motile cells. J. Cell Biol. *173*, 383–394.

Howard, J. (2001). Mechanics of Motor Proteins and the Cytoskeleton (Sunderland, MA: Sinauer Associates).

Huxley, A.F. (1974). Muscular contraction. J. Physiol. *243*, 1–43.

Kamasaki, T., Osumi, M., and Mabuchi, I. (2007). Three-dimensional arrangement of F-actin in the contractile ring of fission yeast. J Cell Biol *178*, 765–771.

Kontrogianni-Konstantopoulos, A., Ackermann, M.A., Bowman, A.L., Yap, S.V., and Bloch, R.J. (2009). Muscle Giants: Molecular Scaffolds in Sarcomerogenesis. Physiol. Rev. *89*, 1217–1267.

Kumar, S., Maxwell, I.Z., Heisterkamp, A., Polte, T.R., Lele, T.P., Salanga, M., Mazur, E., and Ingber, D.E. (2006). Viscoelastic Retraction of Single Living Stress Fibers and Its Impact on Cell Shape, Cytoskeletal Organization, and Extracellular Matrix Mechanics. Biophys. J. *90*, 3762–3773.

Lecuit, T., Lenne, P.-F., and Munro, E. (2011). Force Generation, Transmission, and Integration during Cell and Tissue Morphogenesis. Annu. Rev. Cell Dev. Biol. *27*, 157–184.

Lord, M., and Pollard, T.D. (2004). UCS protein Rng3p activates actin filament gliding by fission yeast myosin-II. J. Cell Biol. *167*, 315–325.

Martin, A.C., Kaschube, M., and Wieschaus, E.F. (2009). Pulsed contractions of an actin–myosin network drive apical constriction. Nature *457*, 495–499.

Peterson, L.J., Rajfur, Z., Maddox, A.S., Freel, C.D., Chen, Y., Edlund, M., Otey, C., and Burridge, K. (2004). Simultaneous Stretching and Contraction of Stress Fibers In Vivo. Mol. Biol. Cell *15*, 3497–3508.

Pollard, T.D. (2010). Mechanics of cytokinesis in eukaryotes. Curr. Opin. Cell Biol. *22*, 50–56.

Redner, S. (2001). A Guide to First-Passage Processes (Cambridge, United Kingdom: Cambridge University Press).

Rossier, O.M., Gauthier, N., Biais, N., Vonnegut, W., Fardin, M.-A., Avigan, P., Heller, E.R., Mathur, A., Ghassemi, S., Koeckert, M.S., et al. (2010). Force generated by actomyosin contraction builds bridges between adhesive contacts. EMBO J. *29*, 1055–1068.

Russell, R.J., Xia, S.-L., Dickinson, R.B., and Lele, T.P. (2009). Sarcomere Mechanics in Capillary Endothelial Cells. Biophys. J. *97*, 1578–1585.

Sabass, B., Gardel, M.L., Waterman, C.M., and Schwarz, U.S. (2008). High Resolution Traction Force Microscopy Based on Experimental and Computational Advances. Biophys. J. *94*, 207–220.

Smith, M.A., Blankman, E., Gardel, M.L., Luettjohann, L., Waterman, C.M., and Beckerle, M.C. (2010). A Zyxin-Mediated Mechanism for Actin Stress Fiber Maintenance and Repair. Dev. Cell *19*, 365–376.

Stachowiak, M.R., and O'Shaughnessy, B. (2008). Kinetics of stress fibers. New J. Phys. *10*, 025002.

Stachowiak, M.R., and O'Shaughnessy, B. (2009). Recoil after Severing Reveals Stress Fiber Contraction Mechanisms. Biophys. J. *97*, 462–471.

Stachowiak, M.R., McCall, P.M., Thoresen, T., Balcioglu, H.E., Kasiewicz, L., Gardel, M.L., and O'Shaughnessy, B. (2012). Self-Organization of Myosin II in Reconstituted Actomyosin Bundles. Biophys. J. *103*, 1265–1274.

Svitkina, T.M., Surguchova, I.G., Verkhovsky, A.B., Gelfand, V.I., Moeremans, M., and De Mey, J. (1989). Direct visualization of bipolar myosin filaments in stress fibers of cultured fibroblasts. Cell Motil. Cytoskeleton *12*, 150–156.

Tanner, K., Boudreau, A., Bissell, M.J., and Kumar, S. (2010). Dissecting Regional Variations in Stress Fiber Mechanics in Living Cells with Laser Nanosurgery. Biophys. J. *99*, 2775–2783.

Thoresen, T., Lenz, M., and Gardel, M.L. (2011). Reconstitution of Contractile Actomyosin Bundles. Biophys. J. *100*, 2698–2705.

Vavylonis, D., Wu, J.-Q., Hao, S., O'Shaughnessy, B., and Pollard, T.D. (2008). Assembly Mechanism of the Contractile Ring for Cytokinesis by Fission Yeast. Science *319*, 97–100.

Verkhovsky, A.B., and Borisy, G.G. (1993). Non-sarcomeric mode of myosin II organization in the fibroblast lamellum. J. Cell Biol. *123*, 637–652.

Vicente-Manzanares, M., Zareno, J., Whitmore, L., Choi, C.K., and Horwitz, A.F. (2007). Regulation of protrusion, adhesion dynamics, and polarity by myosins IIA and IIB in migrating cells. J. Cell Biol. *176*, 573–580.

Vicente-Manzanares, M., Ma, X., Adelstein, R.S., and Horwitz, A.R. (2009). Non-muscle myosin II takes centre stage in cell adhesion and migration. Nat. Rev. Mol. Cell Biol. *10*, 778–790.

Warshaw, D.M., Desrosiers, J.M., Work, S.S., and Trybus, K.M. (1990). Smooth muscle myosin cross-bridge interactions modulate actin filament sliding velocity in vitro. J. Cell Biol. *111*, 453–463.

Xu, J.Q., Harder, B.A., Uman, P., and Craig, R. (1996). Myosin filament structure in vertebrate smooth muscle. J. Cell Biol. *134*, 53–66.

CHAPTER 3: COFILIN DRIVES RAPID NON-EQUILIBRIUM TURNOVER AND FLUIDIZATION OF ENTANGLED F-ACTIN SOLUTIONS

Section 3.1 PREFACE

The contents of Chapter 3 are from a draft of **P.M. McCall**, F.C. MacKintosh, D.R. Kovar, M.L. Gardel, "Cofilin Drives Rapid Non-Equilibrium Turnover and Fluidization of Entangled F-actin Solutions," (in preparation). I am the sole junior scientist on this project. The idea for the project, to examine the effect of actin filament turnover on the mechanics of actin networks using microrheology, was developed by Prof. Margaret Gardel and I, in close consultation with Prof. David Kovar. I performed all experiments and analysis reported. I also extended existing experimental protocols as necessary to arrive at the procedures reported here to measure steady-state filament length distributions (both directly and from inferred nucleation rates) as well as single-filament phosphate release rates. The cofilin, profilin, and formins used in this project were purified by me from plasmids cloned by the Kovar laboratory, and using reagents from, equipment in, and protocols developed by the Kovar laboratory. I purified some of the unlabeled and pyrene-labeled actin used in this study, though most experiments were conducted with actins purified by other members of the Kovar laboratory.

While the code used for particle identification and tracking (developed by Profs. John Crocker and David Grier, and implemented in MATLAB by Profs. Daniel Blair and Eric Dufresne), as well as for calculation of shear moduli from particle trajectories (Prof. Maria Kilfoil), was developed elsewhere, I wrote the MATLAB code used to calculate the mean-squared displacements (MSDs) and step-size distributions of particles, as well as the code for subtracting particle drift. Additionally, I wrote the code used to calculate radial and averaged fluorescence recovery after photobleaching (FRAP) profiles, to account for photobleaching in

FRAP and fluorescence spectroscopy experiments, and to extract nucleation rate constant estimates from pyrene fluroescence timeseries data. Other code used in the present work include utility functions generously shared by current and former members of the Gardel lab, in particular Dr. Patrick Oakes, Dr. Thomas Caswell and Dr. Chris Harland. All text and figures in the present form of the chapter were generated by me (though the helical actin filament schematics are derived from an Adobe Illustrator file from Prof. Kovar). Profs. Gardel and Kovar provided guidance, suggestions, and advice throughout.

Prof. Gardel approached Prof. Fred MacKintosh about our data, and several conversations with him have shaped the scientific content of the present chapter in a number of ways. Most fundamentally, Prof. MacKintosh contributed the idea to employ an analog of the time-temperature superposition principle to our microrheology data. This allowed us to 1) demonstrate that the cofilin-mediated relaxation is a single-timescale process, 2) estimate, on the basis of the universal form of the single-timescale relaxation process, the terminal stress relaxation timescales from data where the viscoelastic crossover frequency is either too low to observe or not present by virtue of its proximity to the entanglement timescale, and 3) report the mechanistically informative length dependence of the cofilin-mediated relaxation time. These points form much of the content in Fig 5.

Section 3.2 ABSTRACT

The shape of most animal cells is controlled by the actin cortex, a thin, isotropic network of dynamic actin filaments (F-actin) situated just beneath the plasma membrane. The cortex is held far from equilibrium by stresses from myosin-II molecular motors, used to drive deformations required for cell division, migration, and tissue morphogenesis, in combination with turnover of

its molecular components to relax stress and facilitate network reorganization. While many aspects of F-actin network viscoelasticity are well-characterized in the presence and absence of motor activity, a mechanistic understanding of how non-equilibrium actin turnover contributes to stress relaxation is still lacking. To address this, we developed a model in vitro system wherein the steady-state length and turnover rate of F-actin in entangled solutions are controlled by the actin regulatory proteins cofilin, profilin, and formin, which sever, recycle, and nucleate filaments, respectively. Surprisingly, we find that cofilin-mediated severing accelerates F-actin turnover and spatial reorganization without substantially shortening filaments. Microrheology measurements demonstrate that cofilin-mediated severing is a single-timescale mode of stress relaxation which tunes the low-frequency viscosity over two orders of magnitude. These findings serve as the foundation for understanding the mechanics of more physiological F-actin networks with turnover, and inform an updated microscopic model of single-filament turnover in which polymer activity, in the form of ATP hydrolysis on F-actin, coupled to nucleotide-dependent cofilin binding is sufficient to generate a form of active matter wherein asymmetric filament disassembly preserves filament number in spite of sustained severing.

Section 3.3 SIGNIFICANCE STATEMENT

When an animal cell moves or divides, a disordered network of stiff actin filaments (F-actin) plays a central role in controlling the resulting changes in cell shape. While it is known that continual turnover of F-actin by cofilin-mediated severing aids F-actin network reorganization in cells, it is unclear how the turnover of structural elements alters the mechanical properties of the network. Here we show that severing of purified F-actin by cofilin results in a stress relaxation mechanism in entangled solutions characterized by a single-timescale set by the severing rate.

Additionally, we identify ATP hydrolysis and nucleotide-dependent cofilin binding as sufficient ingredients to generate a non-equilibrium steady-state in which asymmetric F-actin disassembly preserves filament number in spite of sustained severing.

Section 3.4 INTRODUCTION

The capacity of the cytoskeletal protein actin to dynamically assemble into semi-flexible filaments (F-actin) which turn over and reorganize underlies its fundamental role in cell motility (Pollard and Borisy, 2003), morphogenesis (Lecuit et al., 2011), division (Pollard, 2010), and mechanics (Blanchoin et al., 2014). More than 100 actin-binding proteins control the formation and differential regulation of actin networks, yielding architectures and turnover rates tuned for specific cellular processes (Pollard, 2016). Accordingly, the actin cortex, a thin (Clark et al., 2013) and approximately isotropic F-actin meshwork anchored just beneath the plasma membrane is thought to be the primary determinant of cell shape and mechanics (Salbreux et al., 2012). In vivo measurements place cortical actin turnover on the 10-100 s timescale (Fritzsche et al., 2013; Robin et al., 2014), and while turnover is known to modulate cortical tension (Tinevez et al., 2009) and flows (Bray and White, 1988), a mechanistic understanding of how turnover regulates cortical mechanics is currently lacking.

Rheological measurements of actin networks reconstituted with purified proteins provide significant insight into the mechanics of living cells by enabling architectural and compositional control difficult in cells, and are sufficient to capture aspects of cellular mechanical response (Gardel et al., 2006). Guided by decades of such experiments, a quantitative theoretical understanding has emerged for how static microscopic parameters like filament density, length, and stiffness contribute to the viscoelastic mechanics of entangled F-actin solutions (Morse,

1998a, 1998b) and cross-linked networks (Broedersz and MacKintosh, 2014), which in both cases reflect the mechanics of semi-flexible actin filaments themselves (Gardel et al., 2004b). Suppression of filament bending fluctuations by entanglements or cross-links transiently stores stress energy, giving rise to elasticity on the timescale of seconds. Diffusive, snake-like reptation of filaments (in entangled solutions) or cross-link unbinding (in networks) sets the timescale for stress relaxation, t_{relax}. While the response of networks on timescales longer than t_{relax} is complicated by a broad spectrum of timescales related to the unbinding of multiple cross-links (Broedersz et al., 2010), relaxation is expected to be nearly Maxwellian in entangled solutions, with response dominated by a simple viscosity (Isambert and Maggs, 1996; Morse, 1998a). The contribution of dynamic actin filament turnover to stress relaxation remains largely unknown, owing in large part to the slow turnover rate of purified actin.

Actin turnover requires sequential disassembly, nucleotide exchange, and assembly, and is limited *in vitro* primarily by slow disassembly kinetics (Brieher, 2013; Pollard, 1986). However, all of these reactions are tightly regulated in vivo, with the actin-binding proteins cofilin and profilin playing particularly important roles (Bugyi and Carlier, 2010; Pollard et al., 2000). Cofilin binds cooperatively (De La Cruz, 2005) and preferentially (Blanchoin and Pollard, 1999; Carlier et al., 1997) to ADP-F-actin, allosterically accelerates release of inorganic phosphate (Blanchoin and Pollard, 1999; Carlier et al., 1997; Suarez et al., 2011), and severs filaments at boundaries between clusters of cofilin-bound and -unbound subunits (De La Cruz, 2009b; McCullough et al., 2011; Suarez et al., 2011). Profilin, in turn, promotes disassembly of ADP-F-actin from barbed ends (Courtemanche and Pollard, 2013; Jégou et al., 2011), competes with cofilin for binding to ADP-bound monomers (Blanchoin and Pollard, 1998), catalyzes exchange of ADP for ATP (Vinson et al., 1998), and promotes assembly specifically at barbed-ends by

formin proteins (Kovar et al., 2006), which are responsible for generating the long cortical filaments important for mechanics in living cells (Fritzsche et al., 2016).

Here, we use purified cofilin, profilin, and formin to reconstitute rapid actin filament turnover at steady-state. We then combine filament-level measurements of length and turnover rate with fluorescence recovery after photobleaching (FRAP) and microrheology to systematically study the impact of non-equilibrium turnover on the dynamics and mechanics of entangled actin filament solutions *in vitro*. The choice of entangled solutions enables a quantitative assessment of possible stress relaxation mechanisms, including reptation, treadmilling, and severing. Our work lays the foundation for elucidating the influence of filament turnover on the mechanics of more physiological network architectures.

Section 3.5 RESULTS

Independent control of actin length and turnover at steady-state in vitro

Nucleotide hydrolysis is intimately coupled to actin polymer dynamics, as shown in Fig. 1A. Upon incorporation into filaments, ATP-bound globular actin (ATP-G-actin) monomers undergo a conformational change, becoming ATP-F-actin. ATP is rapidly hydrolyzed on the filament (Jégou et al., 2011), converting ATP-F-actin to ADP-Pi-F-actin (orange). The inorganic phosphate (P_i) is subsequently released on a much slower timescale (300-500 s) (Blanchoin and Pollard, 1999; Melki et al., 1996), resulting in ADP-F-actin (yellow). ADP-F-actin converts to ADP-G-actin upon dissociation from the filament, and the cycle is completed by exchange of the bound ADP nucleotide with free ATP in solution. Importantly, it is the effective irreversibility of the ATP-hydrolysis step which confers non-equilibrium dynamics to this set of coupled reactions, generating a directed turnover cycle with a steady-state flux of monomers. Monitoring

the production of P_i in solution with a coupled-enzyme reaction gives a direct measure of bulk turnover (Webb, 1992).

Actin turnover is regulated by the actin binding proteins profilin and cofilin (Fig. 1B) (Blanchoin and Pollard, 1999; Carlier et al., 1997; Didry et al., 1998). We measure turnover in solutions assembled from 1.5 μM Mg-ATP-actin alone (Fig. 1C, gray), or copolymerized with either 4.5 μM profilin (mole ratio profilin:actin = R_p = 3, blue), 0.75 μM cofilin (R_c = 0.5, purple), or 4.5 μM profilin and 0.75 μM cofilin (R_p = 3 and R_c = 0.5, red). All traces are initially non-linear as actin is assembled, but become linear once steady-state is reached (Fig. 1C, Fig. S1). Measurements of steady-state P_i production (180-240 min after initiation of polymerization) indicate that a molar excess of profilin:actin (Rp = 3) is sufficient to increase the bulk turnover rate ~3-fold over actin alone (Fig.1D). Optimal concentrations of cofilin (R_c = 0.5, determined from FRAP and microrheology, Figs 3-4) accelerate bulk turnover ~20-fold over actin alone, consistent with previous work (Carlier et al., 1997), while the combined effects of profilin and cofilin increase bulk turnover ~23-fold (red).

To extract how profilin and cofilin affect the rate of turnover for each filament, we first determine the number of filaments in solution from a seeded assembly assay (Fig. 1E-F, Methods). Consistent with its role in inhibiting spontaneous nucleation (Pollard et al., 2000), profilin (R_p = 3) reduces the filament concentration at steady-state ~5-fold (Fig. 1B,E,F). By contrast, cofilin (R_c = 0.5) increases the filament concentration ~2-fold, qualitatively consistent with its severing activity (De La Cruz, 2009b) (Fig. 1B,E,F). In the presence of both profilin and cofilin, the filament concentration is comparable to that for actin alone. By dividing the bulk phosphate release rate by the filament density, we obtain the turnover rate for individual filaments (Fig. 1G).

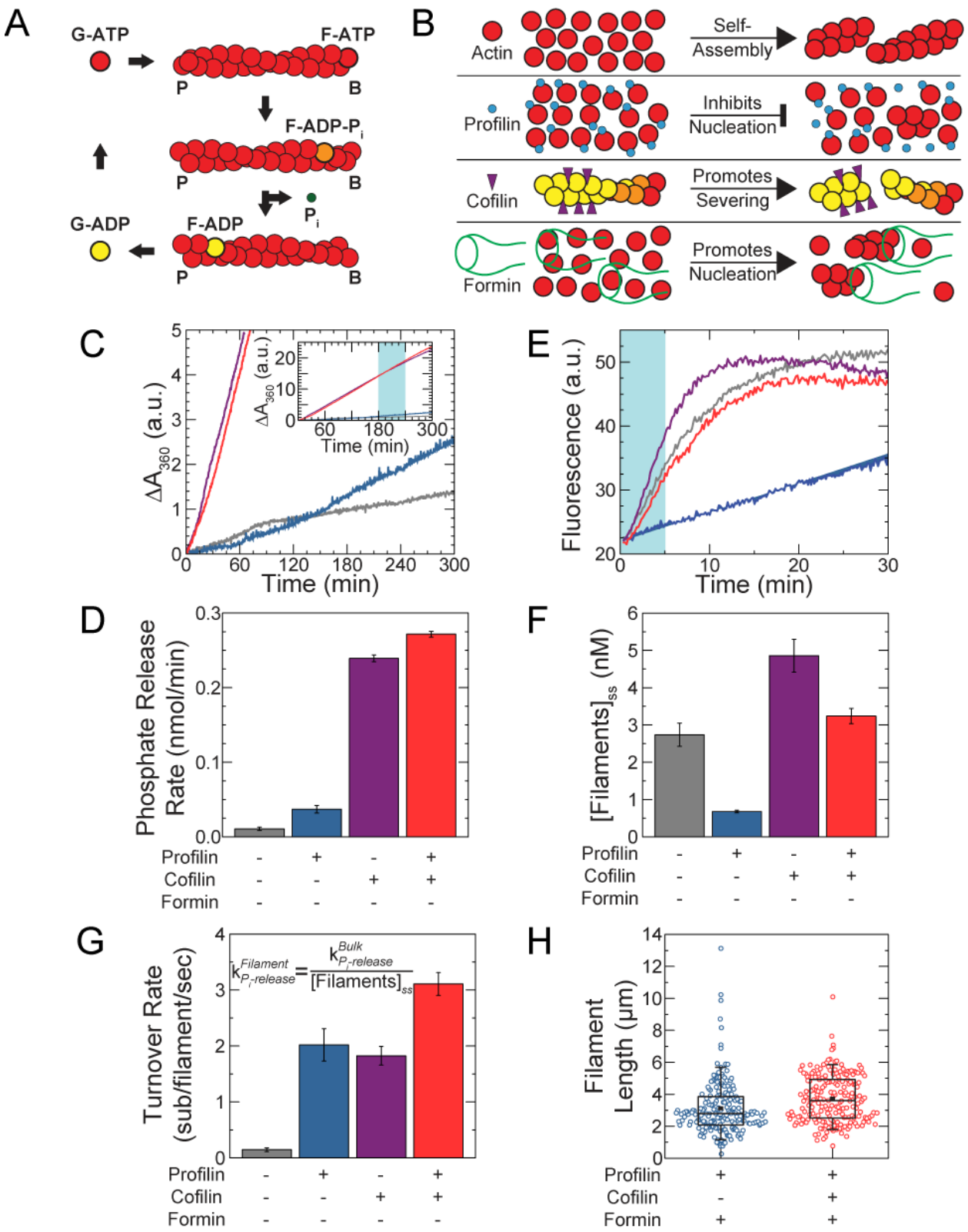

Figure 3.1. Independent control of actin length and turnover at steady-state *in vitro*.

(A) Schematic of actin turnover cycle. B and P denote filament barbed and pointed ends, respectively. (B) Schematic of important biochemical activities of actin, profilin, cofilin, and formin. (C) Timecourse of inorganic phosphate (Pi) production for 1.5 µM Mg-ATP-actin alone (gray), with 4.5 µM profilin (R_p = 3, blue), with 0.75 µM cofilin (R_c = 0.5, purple), or with 4.5 µM profilin and 0.75 µM cofilin (red), all in the presence of 0.2 mM MESG and 1 U/ml PNP. (Inset) Extended vertical axis showing the linear increase in all samples at long times. (D) Bulk phosphate release rate from linear fits to the Pi-release time courses during the time-window shaded in light blue (C, inset). Error bars indicate SEM, N = 4 for the profilin + cofilin condition, and N = 2 for each of the others. (E) Typical time courses of seeded assembly reactions in which 0.25 µM Mg-ATP-actin monomers (10 % pyrene-labeled) are added to 0.5 µM unlabeled actin seeds formed in the absence of additional proteins (gray), with 1.5 µM profilin (R_p = 3, blue), with 0.25 µM cofilin (R_c = 0.5, purple), or with 1.5 µM profilin and 0.25 µM cofilin (red). (F) Steady-state filament concentrations calculated using linear fits to the seeded assembly time courses during the time-window shaded in light blue in (E). Error bars indicate SEM, N = 3 for each condition. (G) Single filament turnover rates calculated from the data in (D,F) and rescaled by actin concentration for actin alone, with R_p = 3, with R_c = 0.5, or with R_p = 3 and R_c = 0.5. (H) Distribution of Alexa488-phalloidin-labeled filaments from source solutions containing 11.9 µM actin, R_p = 3, R_f = 0.01, and either no cofilin (R_c = 0, blue), or 6.95 µM cofilin (R_c = 0.5, red). Each length distribution is composed of 100 filaments from each of two independent samples, for a total of 200 filaments/condition.

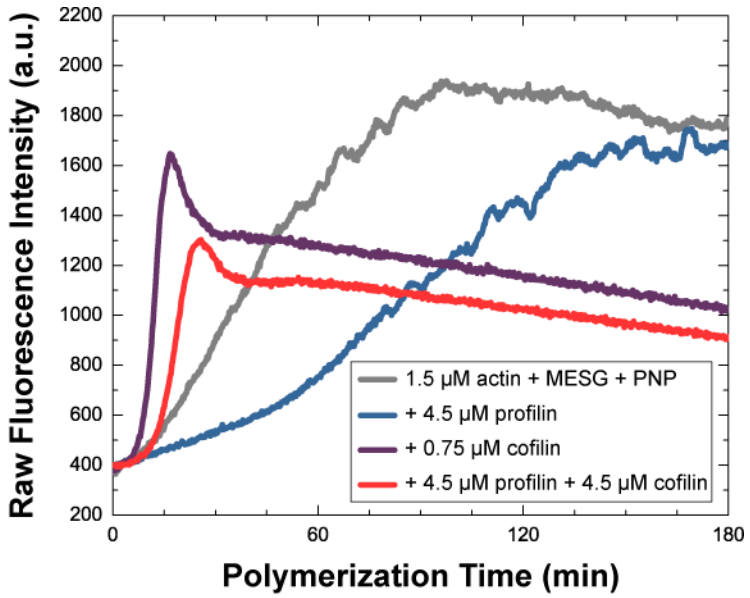

Figure 3.2. Spontaneous assembly of actin monitored by pyrene fluorescence. Timecourse of pyrene fluorescence for 1.5 µM Mg-ATP-actin (10 % pyrene-labeled) alone (gray), with 4.5 µM profilin (R_p = 3, blue), with 0.75 µM cofilin (R_c = 0.5, purple), or with 4.5 µM profilin and 0.75 µM cofilin (red), all in the presence of 0.2 mM MESG and 1 U/ml PNP. Pyrene fluorescence was monitored simultaneously MESG absorbance (reporting on release of inorganic phosphate). These curves are of the same samples plotted in Fig. 3.1C.

We find that profilin and cofilin are each sufficient to increase the turnover rate of actin ~15-fold, from 0.14 to ~2.0 subunits/filament/sec. In the presence of both profilin and cofilin, turnover increases further to ~3.1 subunits/filament/sec, qualitatively consistent with previous results (Didry et al., 1998). Taken together, these data demonstrate that profilin and cofilin can combine to increase the turnover rate of individual actin filaments ~22-fold.

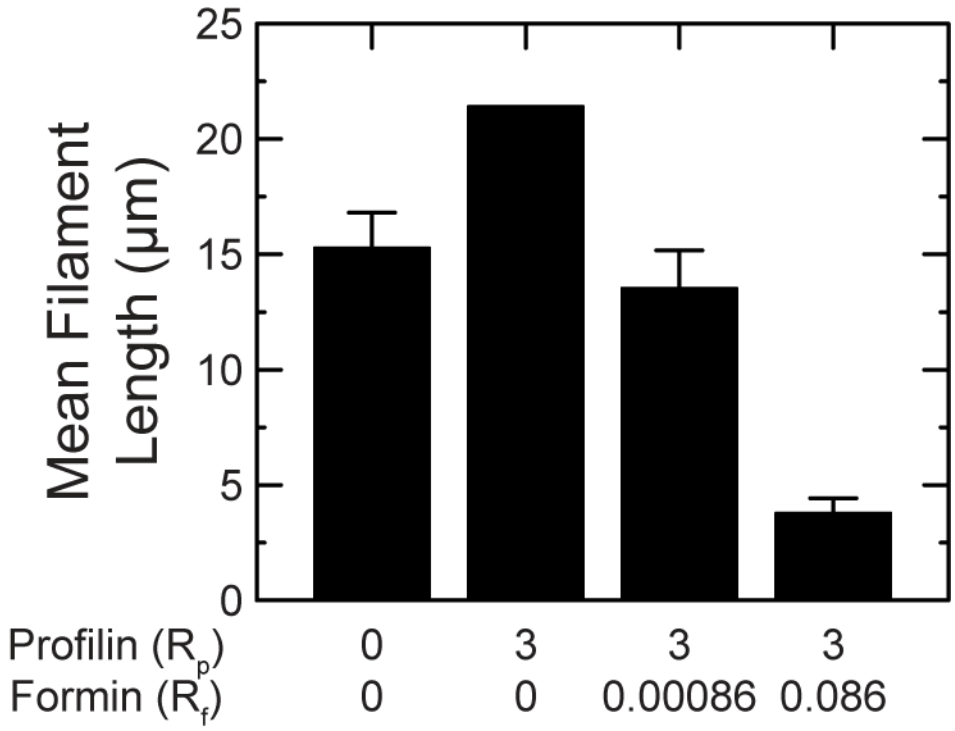

Figure 3.3. Steady-state actin filament lengths are controlled by nucleation. Mean length of actin filaments at steady-state. Filaments were obtained from solutions of 11.9 μM Mg-ATP-actin following 95 minutes of polymerization in the presence of the indicated concentrations of profilin and formin. Filament dynamics were arrested by 10-fold dilution into buffer containing fluorescent phalloidin, incubated for 5 minutes, and imaged. Error bars indicate standard error of the mean.

We control filament length by varying the filament nucleation rate through changes in the concentration of the formin mDia1, which nucleates (Li and Higgs, 2003) and processively

elongates (Kovar et al., 2006) actin filaments (Fig. 1B). Using fluorescence imaging, we find that, for fixed concentrations of actin and profilin, the mean filament length at steady-state can be varied from 21 µm to 3 µm by increasing the formin concentration from 0 to ~1 µM (Fig. S2). Remarkably, the presence of the severing protein cofilin has little effect on the steady-state length distribution in the presence of profilin and formin (Fig. 1H). Indeed, 11.9 µM Mg-ATP-actin polymerized in the presence of profilin (R_p = 3, 35.7 µM) and formin (R_f = 0.01, 119 nM) without (R_c = 0, blue) or with cofilin (R_c = 0.5, 5.95 µM, red) have very similar length distributions with mean lengths of 3.1 µm without cofilin and 3.7 µm in the presence of cofilin. Together these data demonstrate that nucleation during assembly sets the steady-state F-actin length distribution nearly independent of cofilin-mediated severing and increased filament turnover dynamics.

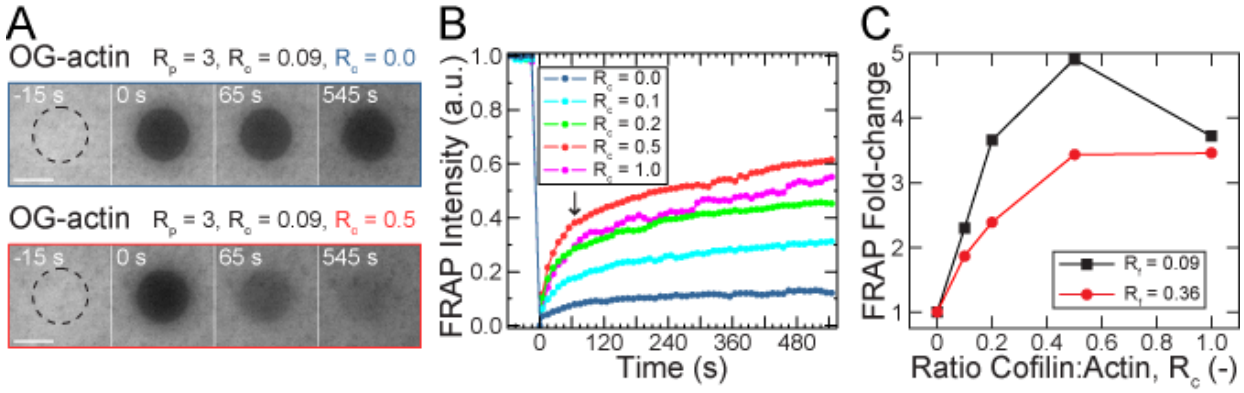

Figure 3.4. Cofilin enhances reorganization in entangled actin solutions. (A-C) All samples are polymerized from 11.9 µM Mg-ATP-actin (5 % Oregon Green-labeled) with R_p = 3 (35.7 µM), R_f = 0.09 (1.07 µM), and R_c as indicated (0-11.9 µM), except for the red circles in (C), for which R_f = 0.36 (4.28 µM). (A) Confocal fluorescence time-lapse micrographs with R_c = 0 (B, blue) or R_c = 0.5 (C, red) at steady-state. A dashed black circle denotes the region exposed to the bleaching laser. Time is relative to the end of the 5-s bleach. Scale bar is 50 µm. (B) Time course of the normalized fluorescence intensity averaged across the bleached region for entangled solutions with R_c as indicated in the legend. (C) Ratio of the normalized fluorescence intensity measured 65 s post-bleach (dashed gray line in (B)) in the presence of cofilin to that in the absence of cofilin. Each point represents a single experiment.

Cofilin enhances reorganization dynamics in entangled actin solutions

To explore the consequences of severing and turnover on the dynamic redistribution of actin, we performed steady-state Fluorescence Recovery After Photobleaching (FRAP) measurements on entangled solutions of fluorescently-labeled actin (11.9 μM = 0.5 mg/ml) assembled with a constant molar excess of profilin (Rp = 3) and a range of cofilin and formin concentrations. At this actin concentration, the expected distance between actin filaments is ~ 420 nm, yielding spatially uniform actin fluorescence prior to bleaching (Fig. 2A).

Two distinct processes contribute to the post-bleach recovery of actin fluorescence: diffusion and turnover. Since the average filament length is larger than this mesh size, the thermally-driven translational, rotational and bending motions of filaments are constrained (Morse, 1998a; Schmidt et al., 1989), giving rise to very slow diffusion of filaments (Schmidt et al., 1989). In contrast, monomers are much smaller than the mesh size, and diffuse rapidly (Fritzsche et al., 2013; Schmidt et al., 1989), displaying exponential recovery with a time constant of ~14 s over the 63-um diameter spot used here (Fig.S3). Actin turnover contributes to recovery on the 1-60 s timescale in the cortex of cells (Fritzsche et al., 2013), and negligibly in reconstituted *Listeria* comet tails (Kueh et al., 2010) and motility assays (Reymann et al., 2011), where local turnover via incorporation of unbleached monomer is inhibited by filament capping, despite rapid global turnover of the network. We thus anticipate monomer diffusion and actin turnover to contribute to FRAP recovery predominantly on timescales less than ~1 min, and for slow filament diffusion to dominate on longer timescales.

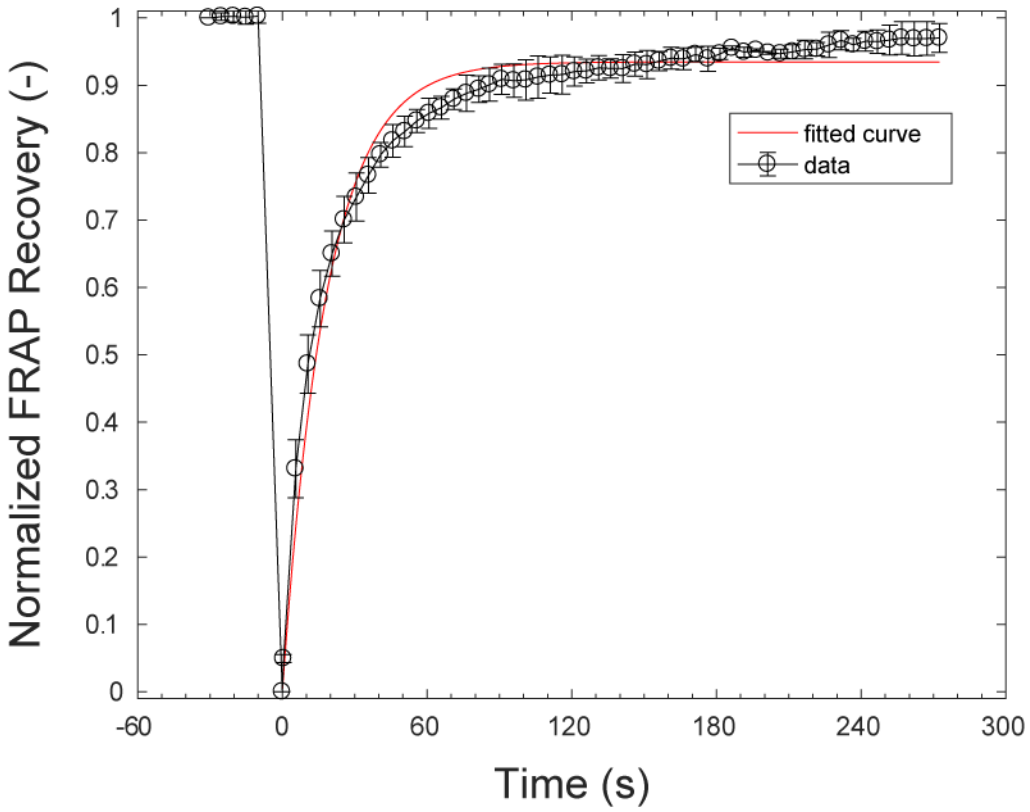

Figure 3.5. Fluorescence recovery of G-actin. Normalized fluorescence recovery timecourse for 1.07 µM Mg-ATP-actin (5 % Oregon Green-labeled). Error bars indicate standard error of the mean from N = 3 measurements in different locations of a single sample. Red curve indicates an exponential fit to the post-bleach timecourse, yielding a time constant of 18.37 s.

Consistent with this, the post-bleach recovery of actin fluorescence we observe is qualitatively described by two phases: a relatively rapid recovery in the first ~60 s, and a much slower recovery thereafter (Fig. 2B). In the absence of cofilin, the average fluorescence intensity of the bleached region recovers to approximately 8 % of the pre-bleach value within 65 seconds, and then only to 12 % after 545 seconds (blue). By contrast, the recovery is much more rapid in the presence of cofilin (Fig. 2A-B, red), reaching approximately 40 % in 65 seconds and more than 60 % by 545 seconds for $R_c = 0.5$. Changes in the diffusivity of monomers or filaments are insufficient to fully account for this recovery profile, since the presence of cofilin increases the size of the monomer pool from ~1 % to only ~4 % total actin, and cofilin doesn't reduce the

mean filament length (Fig. 1H). Instead, we interpret the pronounced recovery enhancement at early times as resulting primarily from accelerated actin turnover (Fig. 1G), where the rates at which unbleached subunits are incorporated and bleached subunits are removed from existing filaments are elevated through the action of cofilin.

We quantify the degree of cofilin-mediated FRAP recovery enhancement by calculating the fold-change in actin fluorescence intensity at 65 s post-bleach at varying cofilin concentrations relative to the cofilin-free sample. On this timescale, we find that recovery is tuned by cofilin concentration, with up to a five-fold enhancement (Fig. 2C, black squares). At higher formin concentrations, filaments are shorter and the cofilin-dependent recovery enhancement is somewhat attenuated, reaching only 3.5-fold (Fig. 2C, red circles). This difference stems from greater recovery at 65 s for $R_f = 0.36$ relative to $R_f = 0.09$, presumably owing to the faster diffusion of shorter filaments at the higher formin concentration. At $R_c = 0.5$, the absolute recovery at 65 s is actually comparable for both formin concentrations (SI), suggesting that filament length plays a minimal role in the recovery on this timescale. The slow diffusion of long filaments is likely responsible for the incomplete recovery after 545 s observed in all cases, however. Taken together, these data demonstrate that *in vitro* actin turnover, catalyzed by cofilin and relying on monomer diffusion, is the dominant process controlling the steady-state reorganization of actin on the timescale of 10s of seconds.

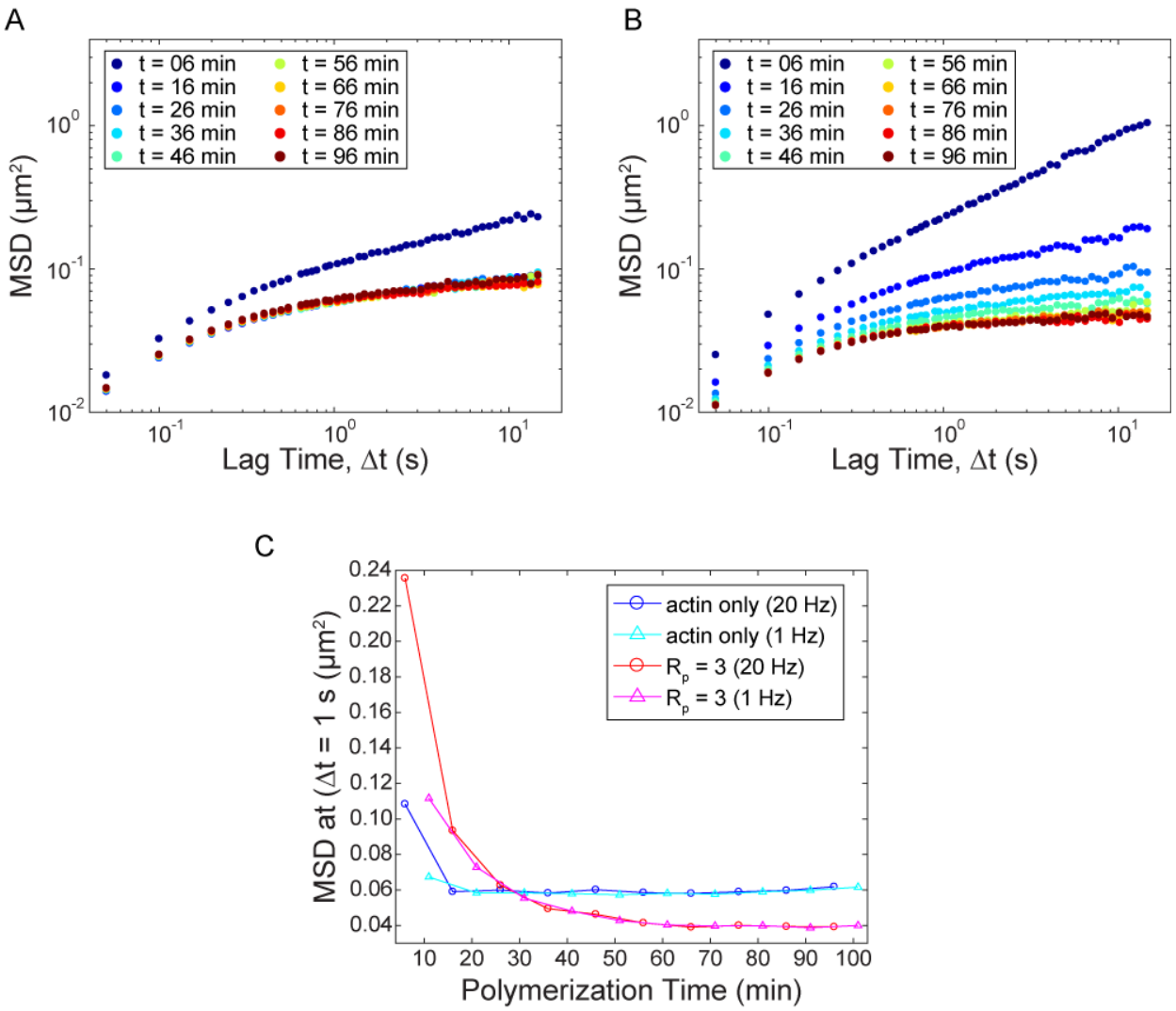

Figure 3.6. Attainment of steady-state by 95-minutes post-polymerization. Mean squared displacement (MSD) for 1-um diameter polystyrene beads during polymerization of 11.9 μM Mg-ATP-actin alone (A) or in the presence of profilin (R_p = 3, B). The time of measurement during polymerization is denoted by color, and the center of the two-minute measurement window is indicated for each trace in the legend. (C) MSD measured at a lag time of 1 s as function of polymerization time. Blue and cyan correspond to actin alone (R_p = 0, A), while red and magenta correspond to R_p = 3 (B). Blue and red are MSDs measured during 2-minute windows, imaging at 20 Hz. Cyan and magenta are MSDs measured at 1 Hz during 8-minute windows immediately following the 2-minute windows. The measurements over the 2-minute and 8-minute windows superimpose to give smooth curves for both samples. While the MSD has stabilized by 16 minutes (at 1 s lag time) for actin alone, suppression of nucleation delays attainment of steady-state until ~70-90 minutes in the presence of profilin. All other microrheology measurements presented in this work were obtained at least 95 minutes after initiation of polymerization.

Cofilin fluidizes entangled F-actin solutions

We employ microrheology to measure the frequency-dependent viscoelasticity of entangled F-actin solutions with varying concentrations of cofilin at steady-state. Mg-ATP-Actin (11.9 μM = 0.5 mg/ml) is copolymerized with the desired concentrations of profilin, formin, cofilin, and 1-μm diameter fluorescent polystyrene beads for 95 minutes to reach steady-state (Fig. S4). From fluorescent images, the bead centroids are tracked over time and the ensemble-averaged mean-squared-displacements (MSDs) as a function of lag time (Δt) are calculated. In the presence of saturating profilin ($R_p = 3$) and moderate formin ($R_f = 0.1$) but the absence of cofilin, bead MSDs are characteristic of that observed in semi-dilute, entangled F-actin solutions (Fig. 4A, blue). For times less than 0.3 sec, the time-dependence of the MSD arises from bending fluctuations of individual F-actin (Amblard et al., 1996; Broedersz and MacKintosh, 2014). At longer times, the MSD approaches a plateau value that reflects the local elastic modulus (Gardel et al., 2003). The local viscoelasticity can be measured by using the Generalized Stokes-Einstein Relationship, to obtain the frequency-dependent elastic, G', and viscous, G", moduli (Gardel et al., 2003; Squires and Mason, 2010). The elastic modulus is nearly constant and much larger than the viscous modulus at frequencies between ~1 Hz and 0.01 Hz. This is indicative of a material that is predominantly elastic over this frequency regime, consistent with previous measurements on entangled F-actin solutions (Gardel et al., 2003; Liu et al., 2006).

The presence of cofilin at increasing concentrations raises the magnitude and modifies the time-dependence of the MSD. The plateau in the MSD is truncated by the emergence of a gradual upturn at lag times greater than 10 s for $R_c = 0.1$ (Fig.3A, cyan). The location of the upturn shifts toward shorter lag times as R_c increases, with the MSD approaching diffusive scaling ($\sim t^{1.0}$) at the longest lag times for $R_c = 0.5$. This increased bead mobility reflects

dramatic changes in the local viscoelasticity (Fig. 3B). At moderate cofilin concentration (cyan), the elastic modulus systematically decays from 1 to 0.01 Hz, resulting in a low frequency crossover where, presumably, the viscous modulus becomes dominant at frequencies below 0.1 Hz. At higher cofilin concentrations, the elastic and viscous modulus are similar in magnitude and decay with time. A parameterization of the frequency-dependent viscoelasticity is the phase angle Φ, or arc tangent of the ratio G"/G', and would be 0º and 90º for purely elastic and viscous materials, respectively, at a given frequency. Calculating Φ at 0.1 Hz, we find that it increases from 10º to 60º as the cofilin concentration is increased from $R_c = 0$ to $R_c = 1$ (Fig. 3C). Thus, increased cofilin concentration results in a transition between a viscoelastic solid to a viscoelastic fluid. Since cofilin is not reducing the mean filament length (Fig.1H), the fluidization likely results from elevated actin filament turnover.

To explore how the fluidity of actin solutions can be regulated by changes to filament length and turnover dynamics, we measure how Φ at 0.1 Hz changes over a range of cofilin and formin concentrations (Fig. 3D). For all filament lengths (formin concentrations) examined, the addition of sufficient cofilin increases the phase angle. The most fluid-like samples are those with short filaments (highest formin concentration) undergoing rapid turnover (high cofilin concentration). Interestingly, for the longest filaments, we see a hint that the phase angle a biphasic function of cofilin concentration, peaking near $R_c = 0.5\text{-}1$, and decreasing above $R_c \sim 1$, implicating the severing activity of cofilin (De La Cruz, 2009b; McCullough et al., 2011; Suarez et al., 2011) in driving the fluidization. While fluidization of entangled F-actin solutions by shortening the steady-state filament length has been previously appreciated (Gardel et al., 2003), we demonstrate here that by accelerating steady-state turnover, fluidization can also be achieved without reducing the average length of filaments.

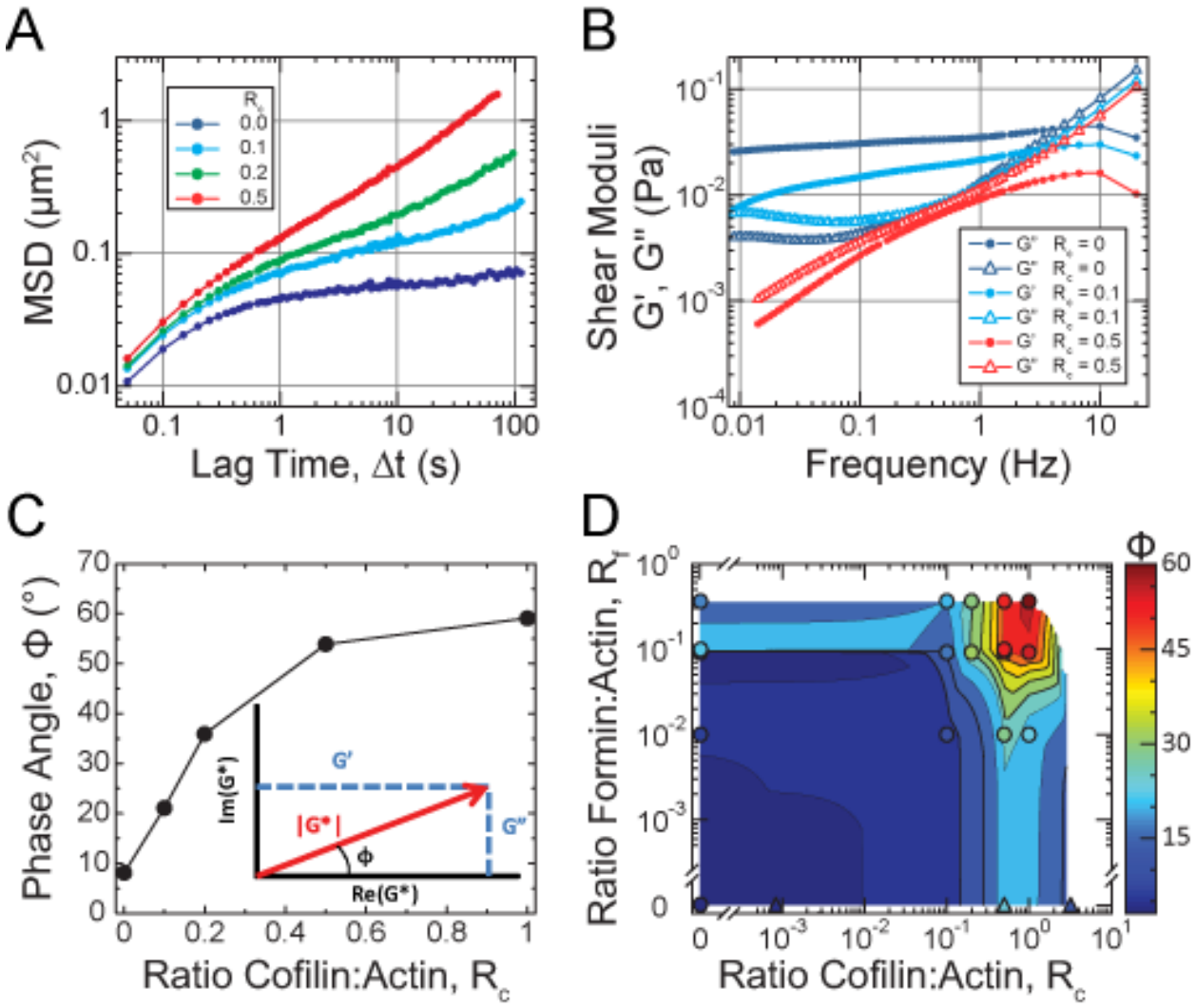

Figure 3.7. Cofilin-mediated turnover tunes the steady-state fluidity of entangled F-actin solutions. (A-D) All microrheology measurements are of steady-state entangled actin solutions polymerized from 11.9 μM Mg-ATP-actin (0 % or 5 % Oregon-Green labeled) with R_p = 3 (35.7 μM), R_f = 0.09 (1.07 μM), and R_c as indicated, except for (D), where R_f is as indicated, and R_p = 0 for samples denoted by triangles. (A) Ensemble-averaged mean-squared-displacement (MSD) of 1-um diameter beads with R_c as indicated in the legend. Each point is calculated from at least 1000 displacements from a single sample. (B) Real and imaginary components of the complex shear modulus (G' and G'', respectively) for the R_c = 0, 0.1, and 0.5 samples from (A), denoted by closed circles (G') and open triangle (G''), respectively. (C) Phase angle (Φ) evaluated at 0.1 Hz for conditions with R_c as indicated. (Inset) Geometric relationship between the magnitude of the complex shear modulus (|G*|, red), its real and imaginary components (G', G'', blue) and the phase angle (Φ), shown in the complex plane. (D) State diagram displaying the phase angle (Φ, color) evaluated at 0.1 Hz for entangled solutions with R_f and R_c as indicated. In most cases, each point represents a single sample, though some are the average of multiple samples. The heatmap represents a 2D interpolation of the discrete data points.

Rapid cofilin-mediated turnover is a single-timescale mode of stress relaxation

To compare the mechanism of enhanced fluidity that arises from accelerated filament turnover to shortened filament length, we compare the MSD of two microscopically distinct F-actin solutions that have identical values of Φ at 0.1 Hz. Interestingly, these samples are rheologically indistinguishable at all timescales probed (Fig.4A). Thus, an entangled solution of relatively long filaments undergoing rapid turnover (cyan) is mechanically equivalent to a solution of relatively short, stable filaments (black).

Notably, such global equivalence in the mechanical response requires equivalence in the long-timescale relaxation dynamics, despite the differences in underlying microscopic processes. Since the stress relaxation of entangled solutions is dominated by a single timescale (Morse, 1998b), we infer that the enhanced relaxation resulting from cofilin-mediated actin turnover is also a single-timescale process. In a manner analogous to time-temperature superposition (Ferry, 1980; Tobolsky, 1956), we estimate the relaxation timescale for individual F-actin solutions by rescaling the measured MSDs by a shift-factor *b*, and the separation time Δt by a shift-factor *a*, such that the long-time behavior superposes with that of a single reference sample composed of relatively short filaments in the absence of cofilin (black, Fig. 4A-B), for which the relaxation time, τ_{ref}, could be directly inferred from the low-frequency crossover of G' and G" (Fig. S5). The estimated relaxation timescale for the ith entangled solution is then given by $\tau_i = \tau_{ref}/a_i$. The successful superposition of the long-timescale MSDs for entangled solutions with a wide variety of filament lengths and cofilin concentrations (Fig. 4B) validates the use of this approach.

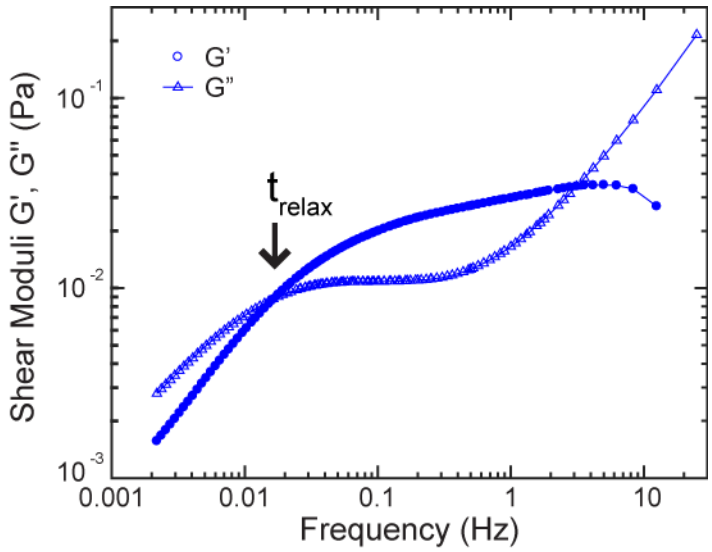

Figure 3.8. Measurement of viscoelastic cross-over time in reference sample of short, stable filaments. Elastic and viscous shear moduli (G', open triangles; G" closed circles) for entangled solutions polymerized from 11.9 μM Mg-ATP-actin with profilin (R_p = 3) and formin (R_f = 0.1) in the presence (red) and absence (blue) of cofilin (R_c = 0.5). The viscoelastic relaxation time is indicated by the frequency at which the elastic and viscous moduli cross, and is observable for entangled solutions of relatively short, stable filaments (blue) in the absence of cofilin. For this sample, $t_{relax} = 1/f_{cross\text{-}over}$ = 58.6 s. This is the value used to set a time-scale from measurements of the shift-factor *a* in Figure 4B.

We examine the dependence of the relaxation time on filament length. In the absence of cofilin, the increase in relaxation time as a function of L is consistent with L^3 (Fig. 4C, blue). This scaling is that predicted for stress relaxation via reptation (Doi and Edwards, 1986), roughly the time it takes a filament to diffuse its own length, which is the expected mechanism of stress-relaxation in entangled actin solutions (Isambert and Maggs, 1996; Morse, 1998a, 1998b). By contrast, at optimal cofilin concentrations, the relaxation time is reduced at all values of filament lengths examined, and exhibits much weaker scaling, consistent with linear, or even sub-linear, dependence on filament length (Fig. 4C, red). This indicates that cofilin-mediated turnover accelerates stress relaxation in entangled solutions by a mechanism distinct from reptation.

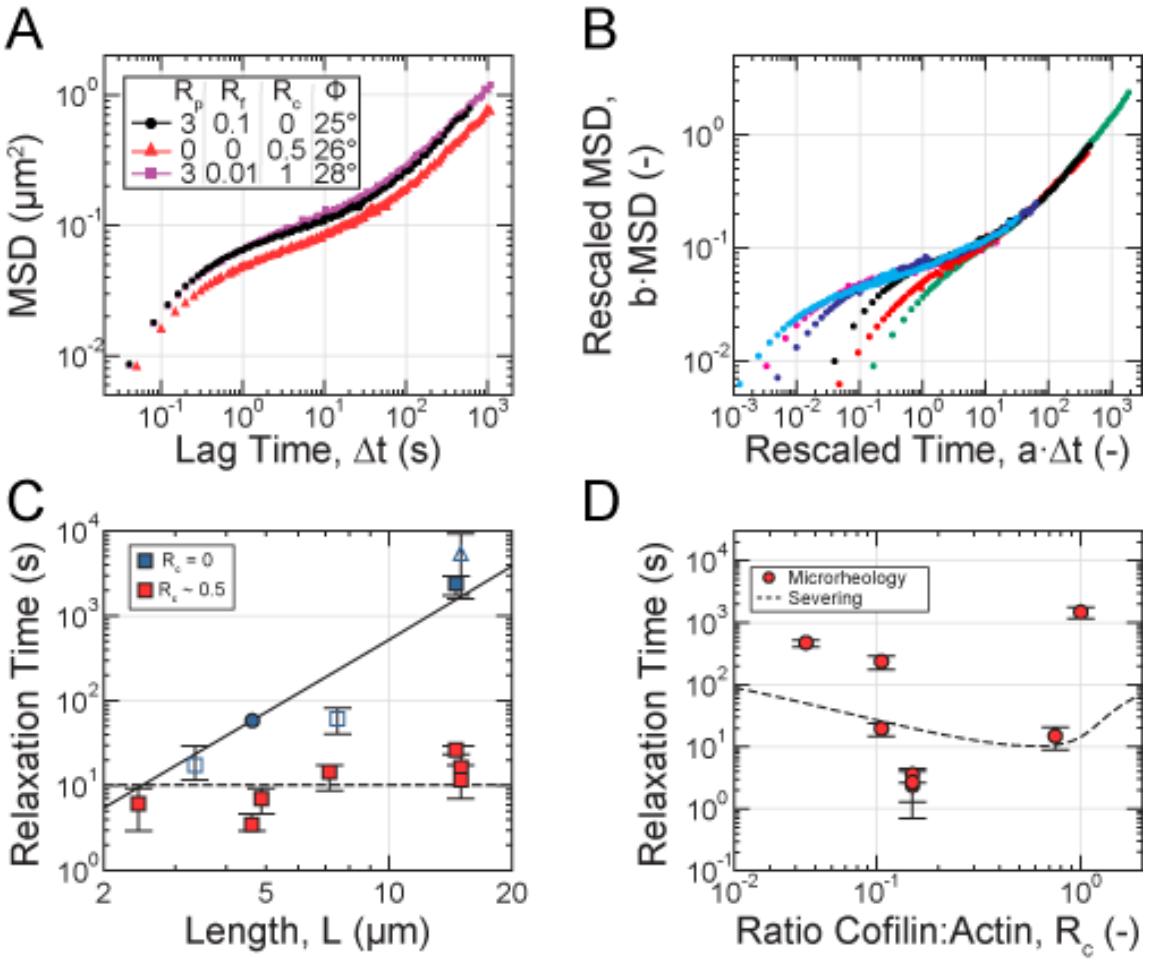

Figure 3.9. Rapid cofilin-mediated turnover is a single-timescale mode of stress relaxation and dominates reptation. (A-D) All microrheology measurements are of steady-state entangled actin solutions polymerized from 11.9 μM Mg-ATP-actin (0 % or 5 % Oregon-Green labeled) with R_p = 3 (35.7 μM), R_f and R_c as indicated, except for the sample denoted by triangles in (A,C), where R_p = 0. (A) Ensemble-averaged MSD for samples with similar values of the phase angle (Φ) evaluated at 0.1 Hz. (B) Collapse of MSD curves at long times to a reference sample of short stable filaments (A-B, black; C, circle) after rescaling lag time and MSD by shift factors *a* and *b*, respectively. (C) Dependence of relaxation time, estimated from the shift factor *a*, on filament length with (red) and without (blue) cofilin. Closed and open symbols represent measurements from a single sample and from two or more samples, respectively. Solid curve is the relaxation time predicted for reptation alone. Dashed line is a fit of the length-independent severing-based model to the cofilin-containing data. (D) Dependence of relaxation time on R_c. Dashed line is the relaxation time dependence on cofilin concentration predicted by the severing-based model, using the severing rate inferred from the fit in (C), association constant for cofilin:F-actin binding of K_a = 1/10 μM, and a cofilin-binding cooperativity parameter of ω = 7.5 (De La Cruz, 2005).

Taken together, these data demonstrate that cofilin-meditated turnover results in a single-timescale mode of stress relaxation that can dominate over filament reptation.

We explore how changing the severing rate can modulate the stress relaxation time. As the cofilin molar ratio is increased from 0.05 to 0.15 (towards the optimal concentration), we see that the relaxation time decreases nearly ~200-fold from 600 s to ~3 s (Fig.4D). As the cofilin ratio is increased further to 1, the relaxation time increases back to ~1000 s. This biphasic dependence of stress relaxation time on cofilin concentration is qualitatively consistent with the biphasic dependence of severing rate on cofilin binding density (De La Cruz, 2005, 2009b; Suarez et al., 2011) (Fig.4D, dashed line). Importantly, this data underscores how non-equilibrium severing activity can decouple mechanical stress relaxation from material structure, as all of these samples contain actin filaments at the same density and nearly the same length.

To understand the mechanism of cofilin-mediated stress relaxation observed in Fig. 4C and D, we explore a simple physical model which explicitly incorporates filament severing, and which captures the weak dependence of the relaxation time on filament length. Assuming a steady-state length distribution P_L^{SS}, we approximate the residual stress at time *t* following application of a step strain as the fraction of polymer present at *t = 0* which remains at time *t* and which is longer than the entanglement length L_e, $\sigma(t) \sim \sum_{L=L_e}^{\infty} L P_L(t)$. If we additionally assume that depolymerization is slow relative to severing, then $P_L(t)$ evolves according to $\dot{P}_L = k_s \left[-(L-1) P_L + 2 \sum_{M=1}^{\infty} P_{L+M} \right]$ due to severing alone at a rate k_s. This time evolution is analogous to that used previously to describe the rheology of worm-like micelles (Cates, 1987), but neglecting filament annealing reactions, which should be suppressed here by depolymerization and formins (Skau et al., 2009). We emphasize that $P_L(t)$ represents the

distribution of "stressed" filaments, and not the instantaneous filament length distribution P_L^{SS}, which differs due to both depolymerization and stress-free elongation and is stationary. This model is exactly solvable for exponential P_L^{SS} (Supplemental Information), and interestingly yields a stress that decays with a characteristic timescale $\tau_{relax} \sim \left(k_s L_e\right)^{-1}$ which depends on polymer density (through the entanglement length) but not filament length.

A fit of this length-independent model to the relaxation times measured with cofilin (Fig. 4C, dashed line) predicts a severing rate of ~3.3 events/sub/s at optimal concentrations. Although ~12-fold higher than rates measured for isolated, unconstrained filaments (McCullough et al., 2011), constraints like those introduced by entanglements are known to enhance severing by cofilin (De La Cruz et al., 2015; Pavlov et al., 2007). Including depolymerization in the evolution of P_L could further reduce this discrepancy, and likely contributes to the differences in Fig. 4D. Taken together, however, these modeling results support severing as a crucial ingredient for the weak length dependence of mechanical relaxation on filament length.

Section 3.6 DISCUSSION

Here we show that cofilin-mediated turnover tunes the steady-state fluidity of entangled solutions of F-actin. In the presence of formin and profilin, cofilin-mediated severing does not reduce the mean filament length or number density at steady-state, factors known to control mechanics and filament mobility. Instead, the enhanced fluidity arises from non-equilibrium actin turnover catalyzed by cofilin severing.

Our work provides a new microscopic model of how a steady-state length is achieved in the presence of cofilin activity (Fig. 5). The textbook view of actin turnover is treadmilling,

wherein barbed-end elongation proceeds at the turnover rate, and is exactly balanced at steady-state by pointed-end disassembly (Phillips et al., 2008). A treadmilling-based mechanism predicts that the relaxation time would be linear in L, which is the strongest dependence with which our data is reasonably consistent (Fig. 4D). However, the 8 nm/s treadmilling velocity we obtain from turnover measurements is too slow by more than 100-fold to account for the relaxation times we estimate (Fig. 4D).

Instead, non-equilibrium ATP hydrolysis directs cofilin severing and asymmetric (dis)assembly (Fig. 5C). Cofilin binds with an ~40-fold higher affinity to ADP-F-actin than either ADP-Pi- or ATP-actin (Blanchoin and Pollard, 1998; Carlier et al., 1997), preferentially localizing both binding and severing away from the filament barbed (McCullough et al., 2011; Suarez et al., 2011). Importantly, the two fragments formed upon filament severing differ in their nucleotide composition. The fragment with the newly-created barbed end is ADP-rich throughout, resulting in its rapid disassembly from both pointed and barbed ends, at a combined rate on the order of ~0.1 μm/s. In contrast, the fragment with the pre-existing barbed end retains an ATP gradient along its length, and is thus stable, independent of the presence of the formin (SI). This stable fragment continues to elongate, and by consuming monomer released through the rapid disassembly of unstable severed fragments, it quickly regenerates length lost through severing (Fig. 5C). Thus, severing couples to asymmetric (dis)assembly dynamics generated by non-equilibrium ATP-hydrolysis to preserve steady-state filament length while catalyzing turnover.

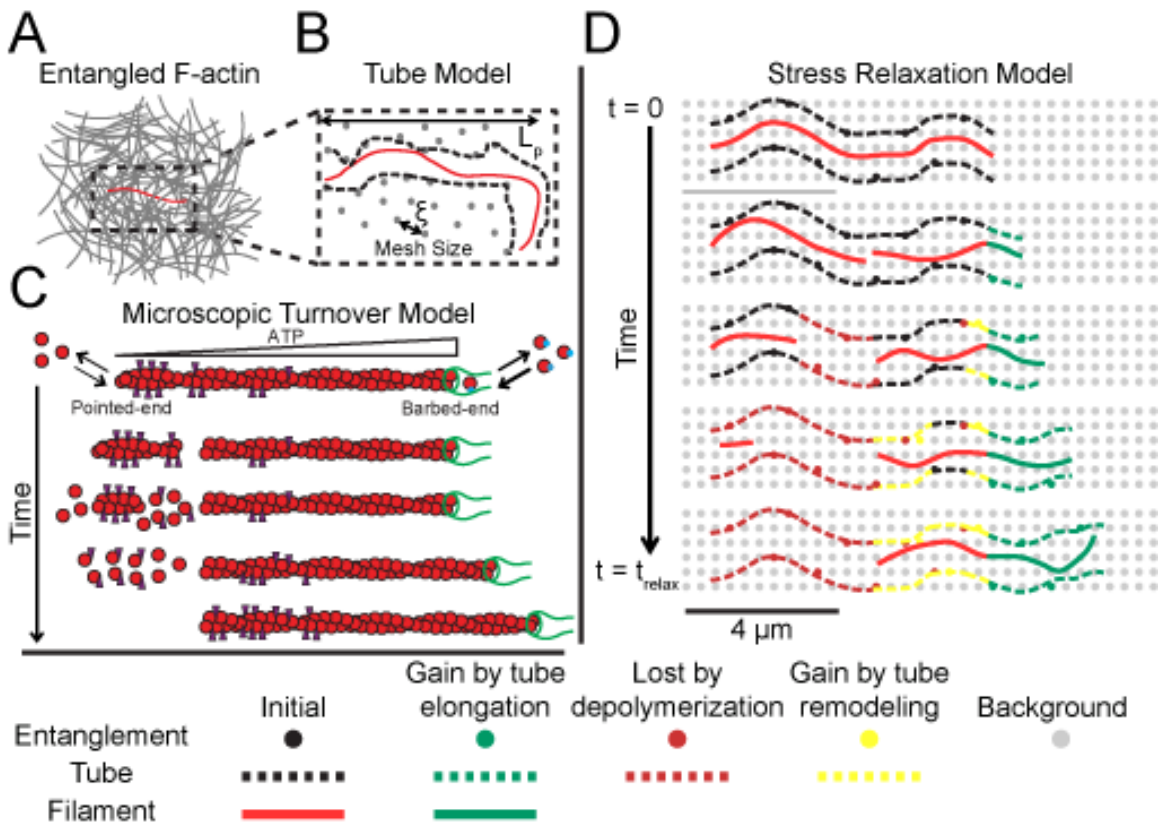

Figure 3.10. Microscopic model of cofilin-mediated actin turnover and stress relaxation. (A) Cartoon of a test filament (red) entangled with other filaments (gray) in a semi-dilute actin solution. (B) Representation of tube model. Entanglements (black) between the test chain and background filaments constrain test chain fluctuations to a tube (black dashed line) and thereby store stress. The entanglement length is set by solution mesh size (gray dots) and filament persistence length. (C) Microscopic dynamics of the test filament regulated by cofilin, profilin, and formin. Cofilin binds and severs ADP-rich filament regions, creating unstable ADP-rich filaments which depolymerize from both ends. The additional G-actin is incorporated onto the stable ATP-barbed end, restoring the length lost from severing. (D) Tube memory, and thus stress, decays by depolymerization (maroon) and tube remodeling (yellow) after severing of the test filament and background filaments, respectively. Polymerization (green) is stress-free, so newly created tube does not contribute.

The possibility for non-equilibrium effects to fluidize materials is of great interest in understanding active biological materials. The mechanical response of entangled F-actin solutions is typically dominated by filament length and density, and understood in terms of a tube model (Fig.5A-B), wherein stress relaxes by filament reptation. Our results demonstrate that

rapid turnover catalyzed by cofilin can fluidize these solutions without major changes to global architecture. The enhanced stress relaxation arises from rapid disassembly of large filament portions, while filament assembly and tube remodeling occur stress-free (Fig. 5D). In contrast to other active processes (e.g. myosin motors), here the non-equilibrium activity primarily effects the dynamical properties of the filament steady-state, enabling rapid (dis)assembly with no nucleation and ultimately enhancing stress relaxation, rather than altering local mechanics via generating local forces per say. This suggests that the bead motions are likely still thermally driven, implying that the fluctuation-dissipation theorem (Squires and Mason, 2010) is only weakly broken by the non-equilibrium turnover, and validating our use of the Generalized Stokes-Einstein Relation (Fig. 3).

It will be interesting to explore the effects of severing-mediated stress relaxation in more physiological cross-linked networks of F-actin. While saturation of actin networks with cross-linkers (Schmoller et al., 2011) or the side-binding protein tropomyosin (Christensen et al., 2017) inhibits disassembly in vitro, consistent with suppression of cofilin binding (De La Cruz, 2009b), more sparsely distributed attachment points give both sufficient space to allow cofilin binding, and actually accelerate severing (Pavlov et al., 2007), suggesting an important role for crosslink density in tuning severing and thereby fluidity.

Finally, in cells, actin turnover has been considered an important mechanism to support the fluidization of the actin cortex (Salbreux et al., 2012), but is mechanistically best understood in the context of protrusive structures like lamellipodia, which facilitate cell motility (Blanchoin et al., 2014). Turnover of polarized lamellipodial networks and listeria comet tails (Loisel et al., 1999; Theriot and Mitchison, 1991) is thought to proceed via a treadmilling array model (Pollard and Borisy, 2003) in which new filaments are continually nucleated near the leading edge, and

elongate only briefly before being capped. Following transport away from the membrane by retrograde flow, capped filaments are then disassembled by cofilin and recycled by profilin, giving rise to spatially separated zones of assembly and disassembly. In contrast, a direct consequence of the dynamical regime of actin turnover we describe in the present work, which does not require steady-state filament nucleation, is that assembly and disassembly are spatially uniform. This mechanism may therefore be better-suited for isotropic networks like the cortex compared to polarized ones like the lamellipodia. Future work exploring potential coupling between cofilin-mediated non-equilibrium turnover and network architecture, both in cells and reconstituted systems, will help elucidate how cells differentially tune the dynamics and mechanics of actin networks to facilitate distinct functions.

Section 3.7 ACKNOWLEDGEMENTS

We are grateful to members of the M.L.G. and D.R.K. Laboratories, especially C. Suarez, D. Zimmermann, J. Winkelman, and P. Oakes, as well as W. McFadden, E. Munro, and E. De La Cruz for helpful discussions and suggestions. This work was supported by University of Chicago Materials Research Science and Engineering Center (NSF DMR-1420709).

Section 3.8 SUPPLEMENTARY MATERIALS AND METHODS

Protein Purification and Storage

Actin was purified from rabbit skeletal muscle acetone powder (Pel-Freez) as previously described (Spudich and Watt, 1971). A subset of gel-filtered actin was labeled on Cys-347 with either Oregon green 488 iodoacetamide (OG) or pyrenyl iodoacetamide (Invitrogen) (Kovar et al., 2003; Kuhn and Pollard, 2005). All actins were stored in Calcium Buffer-G (CaBG:

2 mM Tris-HCl, pH 8.0 at 22 °C, 0.2 mM ATP (adenosine triphosphate), 0.5 mM DTT (1,4-Dithiothreitol), 0.1 mM $CaCl_2$, 1 mM NaN_3). Unlabeled, OG- and pyrene-labeled actins were stored at 4 °C. Prior to use, non-frozen actins were dialyzed against 0.2 L fresh CaBG for 18-24 h, and clarified via ultracentrifugation at 177,000 x g (average relative centrifugal force) for 30 minutes at 4 °C. The top 90% of the supernatant was retained, stored on ice, and used within 6 days.

Recombinant human profilin 1 was expressed in *E. coli* and purified by affinity chromatography with poly-L-proline resin as described previously (Kovar et al., 2003). Recombinant human non-muscle cofilin was expressed in *E. coli* and purified by precipitation in ammonium sulfate, followed by size exclusion (S200) and ion-exchange (DEAE) chromatography, as described previously (Andrianantoandro and Pollard, 2006; Blanchoin and Pollard, 1999).

Two constitutively active formin constructs derived from the mouse formin mDia1 with comparable actin assembly characteristics were used interchangeably in this study. Both constructs contain the FH1 and FH2, and C-terminal domains of mDia1, with a C-terminal tag composed of 6 histidine residues (mDia1(552-1255(FH1-C))-6xHis). The constructs differ only in the presence of either a Maltose Binding Protein (MBP)-tag and TEV cleavage site or SNAP-tag on the N-terminus. The full constructs are thus MBP(TEV)-mDia1(552-1255(FH1-C))-6xHis and SNAP-mDia1(552-1255(FH1-C))-6xHis. Both recombinant constructs were expressed in *E. coli* and purified by affinity chromatography with Ni-containing resin (Talon, GE Healthcare) followed by either a second affinity chromatography step with amylose resin (MBP-construct) or ion-exchange chromatography using a Q-column (GE Healthcare) (SNAP-construct) as described previously (Kovar et al., 2003).

Protein Concentration Determination

Protein concentrations were determined spectrophotometrically. Absorbance measurements were made using an Ultrospec 2100 pro (Amersham Biosciences) or a NanoDrop ND-1000 (Thermo Scientific) UV/VIS Spectrophotometer with optical path lengths b = 1 cm and b = 0.1 cm, respectively. Sample absorbance was converted to protein concentration (and corrected for label absorbance, as appropriate) using the following expressions:

For unlabeled (black) actin (Hansen et al., 2013):

$$[\text{Unlabeled-actin}] = \langle A_{290} \rangle * (38.5\ \mu M\ cm) / b$$

For OG-labeled actin (Kuhn and Pollard, 2005):

$$[\text{Total actin}] = (\langle A_{290} \rangle - (0.17 * \langle A_{491} \rangle)) * (38.5\ \mu M\ cm) / b$$

$$[\text{OG-actin}] = \langle A_{491} \rangle / ((0.0778\ \mu M^{-1}\ cm^{-1}) * b)$$

For Pyrene-labeled actin (Hansen et al., 2013):

$$[\text{Total actin}] = (\langle A_{290} \rangle - (0.127 * \langle A_{344} \rangle)) * (38.5\ \mu M\ cm) / b$$

$$[\text{Pyrene-actin}] = \langle A_{344} \rangle * (45.0\ \mu M\ cm) / b$$

For profilin, cofilin, and formin constructs, the molar extinction coefficients were estimated using the online tool (ProtParam) (http://web.expasy.org/protparam/), the amino acid sequence associated with the UniProt IDs corresponding to the proteins and tags, and assuming reduced Cys residues.

For Human profilin 1:

$$[\text{Total profilin}] = \langle A_{280} \rangle / ((18450\ M^{-1}\ cm^{-1}) * b)$$

For Human non-muscle cofilin:

$$[\text{Total cofilin}] = \langle A_{280} \rangle / ((14440\ M^{-1}\ cm^{-1}) * b)$$

For MBP-tagged mouse formin MBP-mDia1(FH1-C):

[Total formin] = $\langle A_{280} \rangle$ / ((89458 M^{-1} cm^{-1})*b)

For SNAP-tagged mouse formin SNAP-mDia1(FH1-C):

[Total formin] = $\langle A_{280} \rangle$ / ((42400 M^{-1} cm^{-1})*b)

Entangled Solution Preparation

Entangled solutions of F-actin at a concentration of 11.9 μM total actin (0.5 mg/ml) and final volume of 50 μL are prepared by combining the contents of two microcentrifuge tubes. Tube A is prepared from 10x KMEI buffer (1x KMEI: 50 mM KCl, 1 mM $MgCl_2$, 1 mM EGTA (ethylene glycol-bis(beta-aminoethyl ether)-N,N,N',N'-tetraacetic acid), 10 mM Imidazole, pH 7.0, stored at room temperature (RT)), Magnesium Buffer-G (MgBG: 2 mM Tris-HCl, pH 8.0, 22 °C, 0.2 mM ATP, 0.5 mM DTT, 0.1 mM $MgCl_2$, 1 mM NaN_3, stored on ice), 50x GOC (Glucose oxidase and catalase), 50x GLU (glucose and β-mercaptoethanol), 50x pC (phospho-creatine), 50x pCP (purine creatine phosphokinase), profilin (or profilin storage buffer), cofilin (or cofilin storage buffer), and formin (or formin storage buffer) in the order listed at RT. To reduce pipette error, Tube B is prepared at 1.2x the volume required for the final reaction. Mg-ATP-actin is then prepared in Tube B (also at 1.2x the needed volume) from Ca-ATP-actin by 2-minute incubation at RT with 1/10th volume 10x Magnesium Exchange buffer (1x ME buffer: 50 μM $MgCl_2$, 200 μM EGTA in MilliQ-purified water, stored at RT). During the Mg exchange, 1 μL of 1-μm diameter fluorescent carboxylate-functionalized polystyrene bead slurry is pipetted into to a clean 1.5 mL microcentrifuge tube (Tube C). Following the Mg exchange, 1.0x volume of Mg-ATP-actin is pipetted into Tube C and mixed thoroughly with the beads. Finally, a 1.0x

volume of Tube A is pipetted into Tube C, bringing the reaction volume up to 50 µL and initiating polymerization.

Microscopy

Samples (25-45 µL) were loaded into custom-built glass chambers built from 20-mm square coverglass (1.5, Corning) and a 3"-x-1" microscope slide, using segments of microscope slide glass cut with a diamond knife as a spacer. The chamber is bonded with UV-cure epoxy and incubated under a UV lamp for 5 min prior to loading the sample. The sample is sealed in the chamber with high vacuum grease.

Samples were imaged at room temperature (~24 °C) on an inverted microscope (Ti-Eclipse; Nikon, Melville, NY) equipped with a confocal scan head (CSU-X, Yokogawa Electric, Musashino, Tokyo, Japan), a laser merge module (LMM5, Spectral Applied Research, Richmond Hill, Ontario, Canada) containing 488-nm, 560-nm, and 635-nm laser lines for fluorescence imaging. A 405-nm laser line was used as an excitation source for photobleaching experiments. The location of the bleached region was controlled with a micromirror array (MOSAIC, Photonics Instruments).

For microrheology and FRAP measurements, images were formed using a 20x, multi-immersion objective (Nikon, Melville, NY) in mineral oil with a numerical aperature (NA) of 0.75, and corrections for fluorite and flat field aberrations (Plan Fluor) with and without an additional 1.5x optivar in the light path, respectively. For filament length measurements, images were formed using a 60x, DIC-compatible, water-immersion objective (Nikon, Melville, NY) with a numerical aperture (NA) of 1.2, and corrections for apochromatic and flat field aberrations (Plan Apo) with no optivar in the light path. Images were acquired on either a CCD camera

(CoolSnap HQ2; Photometrics, Tucson, AZ) or a scientific complementary metal-oxide-semiconductor (sCMOS) camera (Zyla 4.2; Andor Technologies, Belfast, Northern Ireland), with physical pixel sizes of 6.45 and 6.5 microns per side. All imaging hardware was controlled using METAMORPH acquisition software (Molecular Devices, Eugene, OR).

Filament Length Measurements

The F-actin length distribution at steady-state in 0.5 mg/ml entangled solutions was measured by simultaneously arresting (dis)assembly dynamics, fluorescently labeling filaments, and diluting the solution sufficiently for individual filaments to be observable. At least 95 min after the initiation of polymerization, entangled solutions of un-labeled actin was gently diluted 50-fold by pipetting into an open chamber (well formed by high vacuum grease on a coverslip) mounted on a the confocal microscope and containing Imaging Buffer (1x KMEI, 1x MgBG, 0.25 % methylcellulose (15 cP at 2 % (w/v)), 1x GOC, 1x GLU) supplemented with Alexa488-phalloidin, such that the ratio of the final actin and phalloidin concentrations was 1:1. The entangled solutions gradually dispersed, and phalloidin-stabilized filaments crowded to the surface. Filaments were imaged 10 minutes after dilution. Images of filaments were analyzed in ImageJ (NIH, imagej.nih.gov/ij/) and MetaMorph, and lengths were determined by tracing filament contours by hand.

Fluorescence Recovery After Photobleaching (FRAP)

Following acquisition of 5 pre-bleach images, photobleaching was performed by illuminating a circular region of interest (ROI) 63-µm in diameter and located near the center of the field of view with the 405-nm laser for 4 seconds using the MOSAIC micromirror array. Photobleaching

was done after 95 min to ensure that samples were at steady-state (Fig. S4), and at a focal plane 150 μm above the coverslip (~ 850 μm below the microscope slide) to avoid edge effects.

All quantitative image analysis of FRAP data was performed with custom code written in MATLAB (MathWorks, Natick, MA). Camera dark noise (100 counts) was subtracted from all fluorescence images prior to analysis. Following camera noise subtraction, fluorescence images were corrected for uneven illumination (Jönsson et al., 2008) using the average of the pre-bleach images as a reference fluorescence image. The average fluorescence within the bleached region is calculated for each illumination-corrected image using a mask created in ImageJ from the bleaching ROI. The average fluorescence intensity of the bleached region is then normalized according to:

$$\tilde{I}_{\text{spot}}(t) = \frac{I_{\text{spot}}(t) - I_{\text{spot}}(t_{bleach})}{I_{\text{spot}}(t_0) - I_{\text{spot}}(t_{bleach})} \tag{1}$$

where t_{bleach} is the first post-bleach frame, t_0 is the first frame acquired, and $I(t)$ is the average fluorescence intensity of the bleached region following subtraction of camera noise and correction for un-even illumination.

Additional, unwanted photobleaching inevitably occurs during fluorescence imaging. The timecourse of this bleaching is approximated by the decay of the fractional average fluorescence remaining outside the bleaching ROI (i.e. in the "not spot") at time t:

$$f_{Photobleaching} = \frac{I_{\neg\text{spot}}(t)}{I_{\neg\text{spot}}(t_0)} \tag{2}$$

Note that $f_{Photobleaching}$ is unity at t_0, and decays monotonically to between 0.8 and 0.95 over 10 minutes. To account for this imaging-derived photobleaching, the normalized intensity (1) is divided by the fractional average fluorescence remaining:

$$\tilde{I}_{\text{spot,PBC}}(t) = \frac{\tilde{I}_{\text{spot}}(t)}{f_{Photobleaching}} \ . \quad (3)$$

It is this photobleach-corrected, normalized spot intensity, $\tilde{I}_{\text{spot,PBC}}(t)$, that is plotted as the FRAP recovery in Figure 2B.

Microrheology

Confocal fluorescence images of 1-μm beads were acquired at 20 Hz for 2 minutes, followed immediately by acquisition at 1 Hz for 18 minutes to 2 h, typically with between 100 and 500 beads per field of view (depending on camera). Imaging began at least 95 min after the initiation of polymerization to ensure that samples were at steady-state (Fig. S4), and occured at a focal plane 150 μm above the coverslip (~ 850 μm below the microscope slide) to avoid edge effects.

All quantitative image analysis of microrheology data was performed in MATLAB. Images were processed by band-pass filtering prior to bead identification, sub-pixel centroid localization, and tracking using bpass.m, pkfnd.m, cntrd.m, and track.m, respectively. These functions, distributed by Daniel Blair and Eric Dufresne (Blair and Dufresne), represent the core components of the MATLAB implementation of the Crocker-Grier particle tracking algorithm (Crocker and Grier, 1996) from IDL.

Particle mean-squared-displacements (MSDs) were calculated with non-overlapping windows from individual trajectories, and then ensemble-averaged over all particles for log-spaced lag times (i.e. frame separations) using custom-written code. It is these ensemble-averaged MSDs that are plotted in Fig. 3A and Fig. 4A,B), and filtered to include only lag times calculated from at least 1000 displacements. MSDs were then converted to shear moduli by application of the Generalized Stokes-Einstein and Kramers-Kronig Relationships, using MATLAB code distributed by Maria Kilfoil (Pelletier et al., 2009). The phase angle at 0.1 Hz

(Fig. 3C,D, Fig. 4A) is directly computed from the values of G' and G" according to $\phi = \arctan(G''/G')$.

Microrheology Shift Analysis. The values of the temporal and mobility shift-factors *a* and *b* were estimated for each sample by manually superposing the MSD vs Δt curves and seeking to maximize the domain of overlap at long times. Error bars report the largest and smallest values of *a* and *b* for which the domain of overlap is at least roughly 50 % of that obtained at the values for maximal overlap.

Fluorescence Spectroscopy

Spontaneous Assembly Assay. A stock solution of 15 µM Ca-ATP-actin (typically 10-20 % pyrene-labeled) is prepared from solutions of unlabeled and highly-labeled (typically > 90 %) actin in a 1.5-mL microcentrifuge tube, and then converted from Ca-ATP-actin by 2-minute incubation with 1/10th volume 10x ME buffer and 1/10th volume of 100x anti-foam (Antifoam 204, Sigma) at RT. Mg-ATP-actin is then loaded in up to 12 rows of a 96-well plate (Assay Plate 3686, Corning). A multichannel pipette is then used to simultaneously deliver solution assembled from 10x KMEI buffer, MgBG, and regulatory proteins (or equivalent volumes of protein storage buffers) from an adjacent row of wells to the wells containing actin, thereby initiating assembly (through the addition of $MgCl_2$ and KCl). The final reaction volume is 150 µL. Actin assembly is monitored at RT by pyrene fluorescence (Excitation: 365 nm, Emission: 407 nm) in a fluorescence plate reader (Saphire2, Tecan). Spontaneous assembly assays were used to assess activity of purified profilin, cofilin, and formin, and to confirm attainment of steady-state during phosphate release assays (Fig. 1C and Fig.S1).

Seeded Assembly Assay. Unlabeled Mg-ATP actin is assembled as above at a concentration of 5 µM in the presence of desired regulatory proteins (or equal volumes of protein storage buffers) for 3 h at RT. Reaction volume is 15 µL during assembly, and occurs in wells of a 96-well plate sealed with parafilm to prevent evaporation. After 3 h, the unlabeled actin filament solutions are diluted 10-fold by gentle addition and mixing with a multi-channel pipette of Mg-ATP-G-actin (10 % pyrene labeled). Upon mixing, the final concentration of unlabeled F-actin is 0.5 µM, and the finale concentration pyrene-labeled G-actin is 0.5 µM. Assembly is then monitored in a plate reader by pyrene fluorescence as above. The concentration of filament barbed ends is calculated from the slope of the pyrene fluorescence timecourse during the first 5 minutes (Fig. 1E, shaded blue region) according to (Higgs et al., 1999)

$$\left[N_{\text{filaments}}\right] = \frac{\text{slope}}{k_{+}\left[\text{G-actin}\right]} \tag{4}$$

where k_{+} = 11.6 $\mu M^{-1}s^{-1}$.

Phosphate Release Assay. The rate of phosphate release is monitored in solution using an EnzChek kit (Molecular Probes), commercialized from the work of (Webb, 1992). The principle is that purine nucleoside phosphotransferase (PNP) catalyzes a reaction between inorganic phosphate and the substrate MESG, which results in a characteristic increase in absorbance of phosphorylated substrate at 360 nm relative to un-phosphorylated substrate.

1.5 µM Mg-ATP-actin (10 % pyrene-labeled) is assembled with desired regulatory proteins in wells of a 96-well plate as in spontaneous assembly assays above, but supplemented with 1 mM MESG and 1 U/mL PNP (all concentrations final). An additional "background" reaction is performed in parallel in which actin and all regulatory proteins are replaced by equivalent volumes of CaBG and protein storage buffers, but MESG and PNP are included. All reactions

are then followed by measuring both pyrene fluorescence (as above) and absorbance at 360 nm on a fluorescence plate reader (Saphire2, Tecan) to monitor polymerization and phosphate release (Webb, 1992), respectively. The timecourse of the background reaction is subtracted from all other reactions to yield the traces shown in Fig. 1C. Slopes of absorbance change over time are converted to nmol inorganic phosphate released per second using a standard curve according to the manufacturers protocol.

Section 3.9 REFERENCES

Alberts, B., Johnson, A., Lewis, J., Raff, M., Roberts, K., and Walter, P. (2007). Molecular Biology of the Cell (New York, NY: Garland Science).

Amblard, F., Maggs, A.C., Yurke, B., Pargellis, A.N., and Leibler, S. (1996). Subdiffusion and Anomalous Local Viscoelasticity in Actin Networks. Phys. Rev. Lett. *77*, 4470–4473.

Andelman, D., and Joanny, J.-F. (2000). Polyelectrolyte adsorption. Comptes Rendus Académie Sci. - Ser. IV - Phys. *1*, 1153–1162.

Andrianantoandro, E., and Pollard, T.D. (2006). Mechanism of actin filament turnover by severing and nucleation at different concentrations of ADF/cofilin. Mol. Cell *24*, 13–23.

Asakura, S., and Oosawa, F. (1954). On Interaction between Two Bodies Immersed in a Solution of Macromolecules. J. Chem. Phys. *22*, 1255–1256.

Aumiller Jr, W.M., and Keating, C.D. (2016). Phosphorylation-mediated RNA/peptide complex coacervation as a model for intracellular liquid organelles. Nat. Chem. *8*, 129–137.

Banani, S.F., Rice, A.M., Peeples, W.B., Lin, Y., Jain, S., Parker, R., and Rosen, M.K. (2016). Compositional Control of Phase-Separated Cellular Bodies. Cell *166*, 651–663.

Berro, J., Sirotkin, V., and Pollard, T.D. (2010). Mathematical Modeling of Endocytic Actin Patch Kinetics in Fission Yeast: Disassembly Requires Release of Actin Filament Fragments. Mol. Biol. Cell *21*, 2905–2915.

Black, K.A., Priftis, D., Perry, S.L., Yip, J., Byun, W.Y., and Tirrell, M. (2014). Protein Encapsulation via Polypeptide Complex Coacervation. ACS Macro Lett. *3*, 1088–1091.

Blair, D., and Dufresne, E. Matlab Particle Tracking.

Blanchoin, L., and Pollard, T.D. (1998). Interaction of Actin Monomers with AcanthamoebaActophorin (ADF/Cofilin) and Profilin. J. Biol. Chem. *273*, 25106–25111.

Blanchoin, L., and Pollard, T.D. (1999). Mechanism of Interaction of Acanthamoeba Actophorin (ADF/Cofilin) with Actin Filaments. J. Biol. Chem. *274*, 15538–15546.

Blanchoin, L., Boujemaa-Paterski, R., Sykes, C., and Plastino, J. (2014). Actin Dynamics, Architecture, and Mechanics in Cell Motility. Physiol. Rev. *94*, 235–263.

Bon, S.A.F. (2014). CHAPTER 1:The Phenomenon of Pickering Stabilization: A Basic Introduction. In Particle-Stabilized Emulsions and Colloids, pp. 1–7.

Brangwynne, C.P., Eckmann, C.R., Courson, D.S., Rybarska, A., Hoege, C., Gharakhani, J., Jülicher, F., and Hyman, A.A. (2009). Germline P Granules Are Liquid Droplets That Localize by Controlled Dissolution/Condensation. Science *324*, 1729–1732.

Brangwynne, C.P., Mitchison, T.J., and Hyman, A.A. (2011). Active liquid-like behavior of nucleoli determines their size and shape in Xenopus laevis oocytes. Proc. Natl. Acad. Sci. *108*, 4334–4339.

Bray, D., and White, J.G. (1988). Cortical flow in animal cells. Science *239*, 883–888.

Breitsprecher, D., Jaiswal, R., Bombardier, J.P., Gould, C.J., Gelles, J., and Goode, B.L. (2012). Rocket Launcher Mechanism of Collaborative Actin Assembly Defined by Single-Molecule Imaging. Science *336*, 1164–1168.

Brieher, W. (2013). Mechanisms of actin disassembly. Mol. Biol. Cell *24*, 2299–2302.

Broedersz, C.P., and MacKintosh, F.C. (2014). Modeling semiflexible polymer networks. Rev. Mod. Phys. *86*, 995–1036.

Broedersz, C.P., Depken, M., Yao, N.Y., Pollak, M.R., Weitz, D.A., and MacKintosh, F.C. (2010). Cross-Link-Governed Dynamics of Biopolymer Networks. Phys. Rev. Lett. *105*, 238101.

Brown, S.S., and Spudich, J.A. (1979). Nucleation of polar actin filament assembly by a positively charged surface. J. Cell Biol. *80*, 499–504.

Bubb, M.R., Govindasamy, L., Yarmola, E.G., Vorobiev, S.M., Almo, S.C., Somasundaram, T., Chapman, M.S., Agbandje-McKenna, M., and McKenna, R. (2002). Polylysine Induces an Antiparallel Actin Dimer That Nucleates Filament Assembly CRYSTAL STRUCTURE AT 3.5-Å RESOLUTION. J. Biol. Chem. *277*, 20999–21006.

Bugyi, B., and Carlier, M.-F. (2010). Control of Actin Filament Treadmilling in Cell Motility. Annu. Rev. Biophys. *39*, 449–470.

Burtnick, L.D., Koepf, E.K., Grimes, J., Jones, E.Y., Stuart, D.I., McLaughlin, P.J., and Robinson, R.C. (1997). The Crystal Structure of Plasma Gelsolin: Implications for Actin Severing, Capping, and Nucleation. Cell *90*, 661–670.

Carlier, M.-F., Laurent, V., Santolini, J., Melki, R., Didry, D., Xia, G.-X., Hong, Y., Chua, N.-H., and Pantaloni, D. (1997). Actin Depolymerizing Factor (ADF/Cofilin) Enhances the Rate of Filament Turnover: Implication in Actin-based Motility. J. Cell Biol. *136*, 1307–1322.

Cates, M.E. (1987). Reptation of living polymers: dynamics of entangled polymers in the presence of reversible chain-scission reactions. Macromolecules *20*, 2289–2296.

Chaudhry, F., Breitsprecher, D., Little, K., Sharov, G., Sokolova, O., and Goode, B.L. (2012). Srv2/CAP (cyclase-associated protein) forms hexameric shurikens that directly catalyze actin filament severing by cofilin. Mol. Biol. Cell mbc.E12-08-0589.

Chen, D.T.N., Wen, Q., Janmey, P.A., Crocker, J.C., and Yodh, A.G. (2010). Rheology of Soft Materials. Annu. Rev. Condens. Matter Phys. *1*, 301–322.

Christensen, J.R., Hocky, G.M., Homa, K.E., Morganthaler, A.N., Hitchcock-DeGregori, S.E., Voth, G.A., and Kovar, D.R. (2017). Competition between Tropomyosin, Fimbrin, and ADF/Cofilin drives their sorting to distinct actin filament networks. eLife *6*, e23152.

Cooper, J.A., Walker, S.B., and Pollard, T.D. (1983). Pyrene actin: documentation of the validity of a sensitive assay for actin polymerization. J. Muscle Res. Cell Motil. *4*, 253–262.

Courson, D.S., and Rock, R.S. (2010). Actin Cross-link Assembly and Disassembly Mechanics for α-Actinin and Fascin. J. Biol. Chem. *285*, 26350–26357.

Courtemanche, N., and Pollard, T.D. (2013). Interaction of Profilin with the Barbed End of Actin Filaments. Biochemistry (Mosc.) *52*, 6456–6466.

Crocker, J.C., and Grier, D.G. (1996). Methods of Digital Video Microscopy for Colloidal Studies. J. Colloid Interface Sci. *179*, 298–310.

Crocker, J.C., Valentine, M.T., Weeks, E.R., Gisler, T., Kaplan, P.D., Yodh, A.G., and Weitz, D.A. (2000). Two-Point Microrheology of Inhomogeneous Soft Materials. Phys. Rev. Lett. *85*, 888–891.

De La Cruz, E.M. (2005). Cofilin Binding to Muscle and Non-muscle Actin Filaments: Isoform-dependent Cooperative Interactions. J. Mol. Biol. *346*, 557–564.

De La Cruz, E.M. (2009a). How cofilin severs an actin filament. Biophys. Rev. *1*, 51–59.

De La Cruz, E.M. (2009b). How cofilin severs an actin filament. Biophys. Rev. *1*, 51–59.

De La Cruz, E.M., and Pollard, T.D. (1995). Nucleotide-Free Actin: Stabilization by Sucrose and Nucleotide Binding Kinetics. Biochemistry (Mosc.) *34*, 5452–5461.

De La Cruz, E.M., Martiel, J.-L., and Blanchoin, L. (2015). Mechanical Heterogeneity Favors Fragmentation of Strained Actin Filaments. Biophys. J. *108*, 2270–2281.

Didry, D., Carlier, M.-F., and Pantaloni, D. (1998). Synergy between Actin Depolymerizing Factor/Cofilin and Profilin in Increasing Actin Filament Turnover. J. Biol. Chem. *273*, 25602–25611.

Doi, M., and Edwards, S.F. (1986). The Theory of Polymer Dynamics (New York, NY: Oxford University Press).

Drenckhahn, D., and Pollard, T.D. (1986). Elongation of actin filaments is a diffusion-limited reaction at the barbed end and is accelerated by inert macromolecules. J. Biol. Chem. *261*, 12754–12758.

Feric, M., Vaidya, N., Harmon, T.S., Mitrea, D.M., Zhu, L., Richardson, T.M., Kriwacki, R.W., Pappu, R.V., and Brangwynne, C.P. (2016). Coexisting Liquid Phases Underlie Nucleolar Subcompartments. Cell *165*, 1686–1697.

Ferry, D.J. (1980). Viscoelastic Properties of Polymers (New York, NY: Wiley).

Foth, B.J., Goedecke, M.C., and Soldati, D. (2006). New insights into myosin evolution and classification. Proc. Natl. Acad. Sci. U. S. A. *103*, 3681–3686.

Frederick, K.B., Sept, D., and De La Cruz, E.M. (2008). Effects of Solution Crowding on Actin Polymerization Reveal the Energetic Basis for Nucleotide-Dependent Filament Stability. J. Mol. Biol. *378*, 540–550.

Fritzsche, M., Lewalle, A., Duke, T., Kruse, K., and Charras, G. (2013). Analysis of turnover dynamics of the submembranous actin cortex. Mol. Biol. Cell *24*, 757–767.

Fritzsche, M., Erlenkämper, C., Moeendarbary, E., Charras, G., and Kruse, K. (2016). Actin kinetics shapes cortical network structure and mechanics. Sci. Adv. *2*, e1501337.

Fujiwara, I., Vavylonis, D., and Pollard, T.D. (2007). Polymerization kinetics of ADP- and ADP-Pi-actin determined by fluorescence microscopy. Proc. Natl. Acad. Sci. *104*, 8827–8832.

Gardel, M.L., Valentine, M.T., Crocker, J.C., Bausch, A.R., and Weitz, D.A. (2003). Microrheology of Entangled F-Actin Solutions. Phys. Rev. Lett. *91*, 158302.

Gardel, M.L., Shin, J.H., MacKintosh, F.C., Mahadevan, L., Matsudaira, P., and Weitz, D.A. (2004b). Elastic Behavior of Cross-Linked and Bundled Actin Networks. Science *304*, 1301–1305.

Gardel, M.L., Shin, J.H., MacKintosh, F.C., Mahadevan, L., Matsudaira, P.A., and Weitz, D.A. (2004a). Scaling of F-Actin Network Rheology to Probe Single Filament Elasticity and Dynamics. Phys. Rev. Lett. *93*, 188102.

Gardel, M.L., Nakamura, F., Hartwig, J.H., Crocker, J.C., Stossel, T.P., and Weitz, D.A. (2006). Prestressed F-actin networks cross-linked by hinged filamins replicate mechanical properties of cells. Proc. Natl. Acad. Sci. U. S. A. *103*, 1762–1767.

de Gennes, P.-G. (1979). Scaling Concepts in Polymer Physics (Ithaca, NY: Cornell University Press).

Goode, B.L., and Eck, M.J. (2007). Mechanism and Function of Formins in the Control of Actin Assembly. Annu. Rev. Biochem. *76*, 593–627.

Gucht, J. van der, Spruijt, E., Lemmers, M., and Cohen Stuart, M.A. (2011). Polyelectrolyte complexes: Bulk phases and colloidal systems. J. Colloid Interface Sci. *361*, 407–422.

Gunning, P., O'Neill, G., and Hardeman, E. (2008). Tropomyosin-Based Regulation of the Actin Cytoskeleton in Time and Space. Physiol. Rev. *88*, 1–35.

Hanke, F., Serr, A., Kreuzer, H.J., and Netz, R.R. (2010). Stretching single polypeptides: The effect of rotational constraints in the backbone. EPL Europhys. Lett. *92*, 53001.

Hansen, S., Zuchero, J.B., and Mullins, R.D. (2013). Cytoplasmic Actin: Purification and Single Molecule Assembly Assays. In Adhesion Protein Protocols, A.S. Coutts, ed. (Humana Press), pp. 145–170.

Higgs, H.N., Blanchoin, L., and Pollard, T.D. (1999). Influence of the C Terminus of Wiskott-Aldrich Syndrome Protein (WASp) and the Arp2/3 Complex on Actin Polymerization. Biochemistry (Mosc.) *38*, 15212–15222.

Isambert, H., and Maggs, A.C. (1996). Dynamics and Rheology of Actin Solutions. Macromolecules *29*, 1036–1040.

Israelachvili, J.N. (2011). Intermolecular and Surface Forces (Amsterdam: Elsevier).

Jansen, S., Collins, A., Chin, S.M., Ydenberg, C.A., Gelles, J., and Goode, B.L. (2015). Single-molecule imaging of a three-component ordered actin disassembly mechanism. Nat. Commun. *6*, 7202.

Jégou, A., Niedermayer, T., Orbán, J., Didry, D., Lipowsky, R., Carlier, M.-F., and Romet-Lemonne, G. (2011). Individual Actin Filaments in a Microfluidic Flow Reveal the Mechanism of ATP Hydrolysis and Give Insight Into the Properties of Profilin. PLOS Biol. *9*, e1001161.

Jégou, A., Carlier, M.-F., and Romet-Lemonne, G. (2013). Formin mDia1 senses and generates mechanical forces on actin filaments. Nat. Commun. *4*, 1883.

Johnston, A.B., Collins, A., and Goode, B.L. (2015). High-speed depolymerization at actin filament ends jointly catalysed by Twinfilin and Srv2/CAP. Nat. Cell Biol. *17*, 1504–1511.

Jönsson, P., Jonsson, M.P., Tegenfeldt, J.O., and Höök, F. (2008). A Method Improving the Accuracy of Fluorescence Recovery after Photobleaching Analysis. Biophys. J. *95*, 5334–5348.

Kakran, M., and Antipina, M.N. (2014). Emulsion-based techniques for encapsulation in biomedicine, food and personal care. Curr. Opin. Pharmacol. *18*, 47–55.

Kang, H., Bradley, M.J., McCullough, B.R., Pierre, A., Grintsevich, E.E., Reisler, E., and Cruz, E.M.D.L. (2012). Identification of cation-binding sites on actin that drive polymerization and modulate bending stiffness. Proc. Natl. Acad. Sci. *109*, 16923–16927.

Kinosian, H.J., Selden, L.A., Estes, J.E., and Gershman, L.C. (1993). Nucleotide binding to actin. Cation dependence of nucleotide dissociation and exchange rates. J. Biol. Chem. *268*, 8683–8691.

Koestler, S.A., Rottner, K., Lai, F., Block, J., Vinzenz, M., and Small, J.V. (2009). F- and G-Actin Concentrations in Lamellipodia of Moving Cells. PLOS ONE *4*, e4810.

Koga, S., Williams, D.S., Perriman, A.W., and Mann, S. (2011). Peptide–nucleotide microdroplets as a step towards a membrane-free protocell model. Nat. Chem. *3*, 720–724.

Kovar, D.R., Kuhn, J.R., Tichy, A.L., and Pollard, T.D. (2003). The fission yeast cytokinesis formin Cdc12p is a barbed end actin filament capping protein gated by profilin. J. Cell Biol. *161*, 875–887.

Kovar, D.R., Harris, E.S., Mahaffy, R., Higgs, H.N., and Pollard, T.D. (2006). Control of the Assembly of ATP- and ADP-Actin by Formins and Profilin. Cell *124*, 423–435.

Kramer, J.R., and Deming, T.J. (2010). General Method for Purification of α-Amino acid-N-carboxyanhydrides Using Flash Chromatography. Biomacromolecules *11*, 3668–3672.

de Kruif, C.G., Weinbreck, F., and de Vries, R. (2004). Complex coacervation of proteins and anionic polysaccharides. Curr. Opin. Colloid Interface Sci. *9*, 340–349.

Kudryashov, D.S., and Reisler, E. (2003). Solution Properties of Tetramethylrhodamine-Modified G-Actin. Biophys. J. *85*, 2466–2475.

Kueh, H.Y., Brieher, W.M., and Mitchison, T.J. (2010). Quantitative Analysis of Actin Turnover in Listeria Comet Tails: Evidence for Catastrophic Filament Turnover. Biophys. J. *99*, 2153–2162.

Kuhn, J.R., and Pollard, T.D. (2005). Real-Time Measurements of Actin Filament Polymerization by Total Internal Reflection Fluorescence Microscopy. Biophys. J. *88*, 1387–1402.

Lecuit, T., Lenne, P.-F., and Munro, E. (2011). Force Generation, Transmission, and Integration during Cell and Tissue Morphogenesis. Annu. Rev. Cell Dev. Biol. *27*, 157–184.

Lenz, M., Thoresen, T., Gardel, M.L., and Dinner, A.R. (2012). Contractile Units in Disordered Actomyosin Bundles Arise from F-Actin Buckling. Phys. Rev. Lett. *108*, 238107.

Li, F., and Higgs, H.N. (2003). The Mouse Formin mDia1 Is a Potent Actin Nucleation Factor Regulated by Autoinhibition. Curr. Biol. *13*, 1335–1340.

Li, P., Banjade, S., Cheng, H.-C., Kim, S., Chen, B., Guo, L., Llaguno, M., Hollingsworth, J.V., King, D.S., Banani, S.F., et al. (2012). Phase transitions in the assembly of multivalent signalling proteins. Nature *483*, 336–340.

Lindhoud, S., and Claessens, M.M.A.E. (2015). Accumulation of small protein molecules in a macroscopic complex coacervate. Soft Matter *12*, 408–413.

Liu, J., Gardel, M.L., Kroy, K., Frey, E., Hoffman, B.D., Crocker, J.C., Bausch, A.R., and Weitz, D.A. (2006). Microrheology Probes Length Scale Dependent Rheology. Phys. Rev. Lett. *96*, 118104.

Liu, Y., Winter, H.H., and Perry, S.L. (2017). Linear viscoelasticity of complex coacervates. Adv. Colloid Interface Sci. *239*, 46–60.

Loisel, T.P., Boujemaa, R., Pantaloni, D., and Carlier, M.-F. (1999). Reconstitution of actin-based motility of Listeria and Shigella using pure proteins. Nature *401*, 613–616.

Maciver, S.K., Zot, H.G., and Pollard, T.D. (1991). Characterization of actin filament severing by actophorin from Acanthamoeba castellanii. J. Cell Biol. *115*, 1611–1620.

Matsudaira, P., Bordas, J., and Koch, M.H. (1987). Synchrotron x-ray diffraction studies of actin structure during polymerization. Proc. Natl. Acad. Sci. *84*, 3151–3155.

McCullough, B.R., Grintsevich, E.E., Chen, C.K., Kang, H., Hutchison, A.L., Henn, A., Cao, W., Suarez, C., Martiel, J.-L., Blanchoin, L., et al. (2011). Cofilin-Linked Changes in Actin Filament Flexibility Promote Severing. Biophys. J. *101*, 151–159.

Melki, R., Fievez, S., and Carlier, M.-F. (1996). Continuous Monitoring of Pi Release Following Nucleotide Hydrolysis in Actin or Tubulin Assembly Using 2-Amino-6-mercapto-7-methylpurine Ribonucleoside and Purine-Nucleoside Phosphorylase as an Enzyme-Linked Assay. Biochemistry (Mosc.) *35*, 12038–12045.

Michelot, A., Berro, J., Guérin, C., Boujemaa-Paterski, R., Staiger, C.J., Martiel, J.-L., and Blanchoin, L. (2007). Actin-Filament Stochastic Dynamics Mediated by ADF/Cofilin. Curr. Biol. *17*, 825–833.

Mitrea, D.M., and Kriwacki, R.W. (2016). Phase separation in biology; functional organization of a higher order. Cell Commun. Signal. *14*, 1.

Mizuno, D., Tardin, C., Schmidt, C.F., and MacKintosh, F.C. (2007). Nonequilibrium Mechanics of Active Cytoskeletal Networks. Science *315*, 370–373.

Molecular Probes The Molecular Probes Handbook.

Morse, D.C. (1998a). Viscoelasticity of Concentrated Isotropic Solutions of Semiflexible Polymers. 1. Model and Stress Tensor. Macromolecules *31*, 7030–7043.

Morse, D.C. (1998b). Viscoelasticity of Concentrated Isotropic Solutions of Semiflexible Polymers. 2. Linear Response. Macromolecules *31*, 7044–7067.

Mullins, R.D., Heuser, J.A., and Pollard, T.D. (1998). The interaction of Arp2/3 complex with actin: Nucleation, high affinity pointed end capping, and formation of branching networks of filaments. Proc. Natl. Acad. Sci. *95*, 6181–6186.

Murrell, M.P., and Gardel, M.L. (2012). F-actin buckling coordinates contractility and severing in a biomimetic actomyosin cortex. Proc. Natl. Acad. Sci. *109*, 20820–20825.

Nadkarni, A.V., and Brieher, W.M. (2014). Aip1 Destabilizes Cofilin-Saturated Actin Filaments by Severing and Accelerating Monomer Dissociation from Ends. Curr. Biol. *24*, 2749–2757.

Nolles, A., Westphal, A.H., de Hoop, J.A., Fokkink, R.G., Kleijn, J.M., van Berkel, W.J.H., and Borst, J.W. (2015). Encapsulation of GFP in Complex Coacervate Core Micelles. Biomacromolecules *16*, 1542–1549.

Normoyle, K.P.M., and Brieher, W.M. (2012). Cyclase-associated Protein (CAP) Acts Directly on F-actin to Accelerate Cofilin-mediated Actin Severing across the Range of Physiological pH. J. Biol. Chem. *287*, 35722–35732.

Obermeyer, A.C., Mills, C.E., Dong, X.-H., Flores, R.J., and Olsen, B.D. (2016). Complex coacervation of supercharged proteins with polyelectrolytes. Soft Matter *12*, 3570–3581.

Oriol-Audit, C. (1978). Polyamine-Induced Actin Polymerization. Eur. J. Biochem. *87*, 371–376.

Ou, Z., and Muthukumar, M. (2006). Entropy and enthalpy of polyelectrolyte complexation: Langevin dynamics simulations. J. Chem. Phys. *124*, 154902.

P G de Gennes, and Leger, and L. (1982). Dynamics of Entangled Polymer Chains. Annu. Rev. Phys. Chem. *33*, 49–61.

Pacalin, N.M., Leon, L., and Tirrell, M. (2016). Directing the phase behavior of polyelectrolyte complexes using chiral patterned peptides. Eur. Phys. J. Spec. Top. *225*, 1805–1815.

Pak, C.W., Kosno, M., Holehouse, A.S., Padrick, S.B., Mittal, A., Ali, R., Yunus, A.A., Liu, D.R., Pappu, R.V., and Rosen, M.K. (2016). Sequence Determinants of Intracellular Phase Separation by Complex Coacervation of a Disordered Protein. Mol. Cell *63*, 72–85.

Pavlov, D., Muhlrad, A., Cooper, J., Wear, M., and Reisler, E. (2007). ACTIN FILAMENT SEVERING BY COFILIN. J. Mol. Biol. *365*, 1350–1358.

Pelletier, V., Gal, N., Fournier, P., and Kilfoil, M.L. (2009). Microrheology of Microtubule Solutions and Actin-Microtubule Composite Networks. Phys. Rev. Lett. *102*, 188303.

Perry, S.L., Leon, L., Hoffmann, K.Q., Kade, M.J., Priftis, D., Black, K.A., Wong, D., Klein, R.A., Iii, C.F.P., Margossian, K.O., et al. (2015). Chirality-selected phase behaviour in ionic polypeptide complexes. Nat. Commun. *6*, 6052.

Phillips, R., Kondev, J., and Theriot, J. (2008). Physical Biology of the Cell (New York, NY: Garland Science).

Pollard, T.D. (1986). Rate constants for the reactions of ATP- and ADP-actin with the ends of actin filaments. J. Cell Biol. *103*, 2747–2754.

Pollard, T.D. (2007). Regulation of Actin Filament Assembly by Arp2/3 Complex and Formins. Annu. Rev. Biophys. Biomol. Struct. *36*, 451–477.

Pollard, T.D. (2010). Mechanics of cytokinesis in eukaryotes. Curr. Opin. Cell Biol. *22*, 50–56.

Pollard, T.D. (2016). Actin and Actin-Binding Proteins. Cold Spring Harb. Perspect. Biol. a018226.

Pollard, T.D., and Borisy, G.G. (2003). Cellular Motility Driven by Assembly and Disassembly of Actin Filaments. Cell *112*, 453–465.

Pollard, T.D., Goldberg, I., and Schwarz, W.H. (1992). Nucleotide exchange, structure, and mechanical properties of filaments assembled from ATP-actin and ADP-actin. J. Biol. Chem. *267*, 20339–20345.

Pollard, T.D., Blanchoin, L., and Mullins, R.D. (2000). Molecular Mechanisms Controlling Actin Filament Dynamics in Nonmuscle Cells. Annu. Rev. Biophys. Biomol. Struct. *29*, 545–576.

Ponti, A., Matov, A., Adams, M., Gupton, S., Waterman-Storer, C.M., and Danuser, G. (2005). Periodic Patterns of Actin Turnover in Lamellipodia and Lamellae of Migrating Epithelial Cells Analyzed by Quantitative Fluorescent Speckle Microscopy. Biophys. J. *89*, 3456–3469.

Priftis, D., Farina, R., and Tirrell, M. (2012). Interfacial Energy of Polypeptide Complex Coacervates Measured via Capillary Adhesion. Langmuir *28*, 8721–8729.

ProtParam, E. ExPASy - ProtParam tool.

Pubchem L-glutamic acid | C5H9NO4 - PubChem.

Rao, J.N., Madasu, Y., and Dominguez, R. (2014). Mechanism of actin filament pointed-end capping by tropomodulin. Science *345*, 463–467.

Reymann, A.-C., Suarez, C., Guérin, C., Martiel, J.-L., Staiger, C.J., Blanchoin, L., and Boujemaa-Paterski, R. (2011). Turnover of branched actin filament networks by stochastic fragmentation with ADF/cofilin. Mol. Biol. Cell *22*, 2541–2550.

Robin, F.B., McFadden, W.M., Yao, B., and Munro, E.M. (2014). Single-molecule analysis of cell surface dynamics in Caenorhabditis elegans embryos. Nat. Methods *11*, 677–682.

Rould, M.A., Wan, Q., Joel, P.B., Lowey, S., and Trybus, K.M. (2006). Crystal Structures of Expressed Non-polymerizable Monomeric Actin in the ADP and ATP States. J. Biol. Chem. *281*, 31909–31919.

Salbreux, G., Charras, G., and Paluch, E. (2012). Actin cortex mechanics and cellular morphogenesis. Trends Cell Biol. *22*, 536–545.

Schaus, T.E., Taylor, E.W., and Borisy, G.G. (2007). Self-organization of actin filament orientation in the dendritic-nucleation/array-treadmilling model. Proc. Natl. Acad. Sci. *104*, 7086–7091.

Schmidt, C.F., Baermann, M., Isenberg, G., and Sackmann, E. (1989). Chain dynamics, mesh size, and diffusive transport in networks of polymerized actin: a quasielastic light scattering and microfluorescence study. Macromolecules *22*, 3638–3649.

Schmoller, K.M., Semmrich, C., and Bausch, A.R. (2011). Slow down of actin depolymerization by cross-linking molecules. J. Struct. Biol. *173*, 350–357.

Sekerková, G., Richter, C.-P., and Bartles, J.R. (2011). Roles of the Espin Actin-Bundling Proteins in the Morphogenesis and Stabilization of Hair Cell Stereocilia Revealed in CBA/CaJ Congenic Jerker Mice. PLOS Genet. *7*, e1002032.

Sept, D., and McCammon, J.A. (2001). Thermodynamics and Kinetics of Actin Filament Nucleation. Biophys. J. *81*, 667–674.

Shimozawa, T., Yamagata, K., Kondo, T., Hayashi, S., Shitamukai, A., Konno, D., Matsuzaki, F., Takayama, J., Onami, S., Nakayama, H., et al. (2013). Improving spinning disk confocal microscopy by preventing pinhole cross-talk for intravital imaging. Proc. Natl. Acad. Sci. *110*, 3399–3404.

Sirotkin, V., Berro, J., Macmillan, K., Zhao, L., and Pollard, T.D. (2010). Quantitative Analysis of the Mechanism of Endocytic Actin Patch Assembly and Disassembly in Fission Yeast. Mol. Biol. Cell *21*, 2894–2904.

Skau, C.T., Neidt, E.M., and Kovar, D.R. (2009). Role of Tropomyosin in Formin-mediated Contractile Ring Assembly in Fission Yeast. Mol. Biol. Cell *20*, 2160–2173.

Sokolova, E., Spruijt, E., Hansen, M.M.K., Dubuc, E., Groen, J., Chokkalingam, V., Piruska, A., Heus, H.A., and Huck, W.T.S. (2013). Enhanced transcription rates in membrane-free protocells formed by coacervation of cell lysate. Proc. Natl. Acad. Sci. *110*, 11692–11697.

Spruijt, E., Westphal, A.H., Borst, J.W., Cohen Stuart, M.A., and van der Gucht, J. (2010). Binodal Compositions of Polyelectrolyte Complexes. Macromolecules *43*, 6476–6484.

Spudich, J.A., and Watt, S. (1971). The Regulation of Rabbit Skeletal Muscle Contraction I. BIOCHEMICAL STUDIES OF THE INTERACTION OF THE TROPOMYOSIN-TROPONIN COMPLEX WITH ACTIN AND THE PROTEOLYTIC FRAGMENTS OF MYOSIN. J. Biol. Chem. *246*, 4866–4871.

Squires, T.M., and Mason, T.G. (2010). Fluid Mechanics of Microrheology. Annu. Rev. Fluid Mech. *42*, 413–438.

Srivastava, S., and Tirrell, M.V. (2016). Polyelectrolyte Complexation. In Advances in Chemical Physics, S.A. Rice, and A.R. Dinner, eds. (Hoboken, NJ: John Wiley & Sons, Inc.), pp. 499–544.

Stuhrmann, B., Soares e Silva, M., Depken, M., MacKintosh, F.C., and Koenderink, G.H. (2012). Nonequilibrium fluctuations of a remodeling in vitro cytoskeleton. Phys. Rev. E *86*, 020901.

Su, X., Ditlev, J.A., Hui, E., Xing, W., Banjade, S., Okrut, J., King, D.S., Taunton, J., Rosen, M.K., and Vale, R.D. (2016). Phase separation of signaling molecules promotes T cell receptor signal transduction. Science *352*, 595–599.

Suarez, C., Roland, J., Boujemaa-Paterski, R., Kang, H., McCullough, B.R., Reymann, A.-C., Guérin, C., Martiel, J.-L., De La Cruz, E.M., and Blanchoin, L. (2011). Cofilin Tunes the Nucleotide State of Actin Filaments and Severs at Bare and Decorated Segment Boundaries. Curr. Biol. *21*, 862–868.

Svitkina, T.M., and Borisy, G.G. (1999). Arp2/3 Complex and Actin Depolymerizing Factor/Cofilin in Dendritic Organization and Treadmilling of Actin Filament Array in Lamellipodia. J. Cell Biol. *145*, 1009–1026.

Svitkina, T.M., Bulanova, E.A., Chaga, O.Y., Vignjevic, D.M., Kojima, S., Vasiliev, J.M., and Borisy, G.G. (2003). Mechanism of filopodia initiation by reorganization of a dendritic network. J Cell Biol *160*, 409–421.

Tang, J.X., and Janmey, P.A. (1996). The Polyelectrolyte Nature of F-actin and the Mechanism of Actin Bundle Formation. J. Biol. Chem. *271*, 8556–8563.

Theriot, J.A., and Mitchison, T.J. (1991). Actin microfilament dynamics in locomoting cells. Nature *352*, 126–131.

Theriot, J.A., and Mitchison, T.J. (1992). Comparison of actin and cell surface dynamics in motile fibroblasts. J. Cell Biol. *119*, 367–377.

Thoresen, T., Lenz, M., and Gardel, M.L. (2011). Reconstitution of Contractile Actomyosin Bundles. Biophys. J. *100*, 2698–2705.

Tinevez, J.-Y., Schulze, U., Salbreux, G., Roensch, J., Joanny, J.-F., and Paluch, E. (2009). Role of cortical tension in bleb growth. Proc. Natl. Acad. Sci. *106*, 18581–18586.

Tobolsky, A.V. (1956). Stress Relaxation Studies of the Viscoelastic Properties of Polymers. J. Appl. Phys. *27*, 673–685.

Tojkander, S., Gateva, G., and Lappalainen, P. (2012). Actin stress fibers – assembly, dynamics and biological roles. J Cell Sci *125*, 1855–1864.

Vandekerckhove, J., Deboben, A., Nassal, M., and Wieland, T. (1985). The phalloidin binding site of F-actin. EMBO J. *4*, 2815–2818.

Vieregg, J.R., and Tang, T.-Y.D. (2016). Polynucleotides in cellular mimics: Coacervates and lipid vesicles. Curr. Opin. Colloid Interface Sci. *26*, 50–57.

Vinson, V.K., De La Cruz, E.M., Higgs, H.N., and Pollard, T.D. (1998). Interactions of Acanthamoeba profilin with actin and nucleotides bound to actin. Biochemistry (Mosc.) *37*, 10871–10880.

Webb, M.R. (1992). A continuous spectrophotometric assay for inorganic phosphate and for measuring phosphate release kinetics in biological systems. Proc. Natl. Acad. Sci. *89*, 4884–4887.

Wegner, A. (1976). Head to tail polymerization of actin. J. Mol. Biol. *108*, 139–150.

Winkelman, J.D., Bilancia, C.G., Peifer, M., and Kovar, D.R. (2014). Ena/VASP Enabled is a highly processive actin polymerase tailored to self-assemble parallel-bundled F-actin networks with Fascin. Proc. Natl. Acad. Sci. *111*, 4121–4126.

Winkelman, J.D., Suarez, C., Hocky, G.M., Harker, A.J., Morganthaler, A.N., Christensen, J.R., Voth, G.A., Bartles, J.R., and Kovar, D.R. (2016). Fascin- and α-Actinin-Bundled Networks Contain Intrinsic Structural Features that Drive Protein Sorting. Curr. Biol. *26*, 2697–2706.

Wong, I.Y., Gardel, M.L., Reichman, D.R., Weeks, E.R., Valentine, M.T., Bausch, A.R., and Weitz, D.A. (2004). Anomalous Diffusion Probes Microstructure Dynamics of Entangled F-Actin Networks. Phys. Rev. Lett. *92*, 178101.

Xue, B., Leyrat, C., Grimes, J.M., and Robinson, R.C. (2014). Structural basis of thymosin-β4/profilin exchange leading to actin filament polymerization. Proc. Natl. Acad. Sci. *111*, E4596–E4605.

Yamashita, A., Maeda, K., and Maéda, Y. (2003). Crystal structure of CapZ: structural basis for actin filament barbed end capping. EMBO J. *22*, 1529–1538.

CHAPTER 4: FILAMENT RECYCLING IS NECESSARY FOR SUSTAINED CONTRACTILE FLOWS IN A MODEL ACTOMYOSIN CORTEX

Section 4.1 PREFACE

The contents of this chapter are reproduced from a revised version of McFadden, W.M., McCall, P.M., and Munro, E.M. (2016). Filament turnover is essential for continuous long range contractile flow in a model actomyosin cortex. ArXiv 1612.07430. (McFadden et al., 2016) is a computational study of the mechanical consequences of actin turnover in 2D contractile actomyosin networks. This topic is very closely related to that of the preceding chapter, albeit in crosslinked networks with active stresses generated by motors as opposed to an entangled F-actin solution. The manuscript is first and foremost the work my fellow graduate student Mr. William McFadden in the laboratory of Prof. Ed Munro at the University of Chicago. Mr. McFadden wrote all of the code and performed all of the simulations reported. Mr. McFadden and Prof. Munro wrote the manuscript, with feedback and input from me.

My contributions to the work include 1) in vivo experiments performed as part of my Phys 335 project (supervised by Prof. Munro) which were at one time considered for inclusion in the manuscript but eventually withheld; 2) frequent discussion and brainstorming with Mr. McFadden about actin dynamics, polymer physics, mechanics, interpretation of simulation results and analysis, and the appropriate direction for the project; 3) careful vetting of both a) derivations of analytic results and b) scaling relations derived from the simulations, which uncovered some inconsistencies that we were eventually able to resolve. Specific contributions from me which appear in the final manuscript include the second half of the derivation in Section 4.9.3 (equations 21-24 and the solution for the steady-state density), preparation of Fig.

4.16, and help with analysis presented in Fig. 4.4 and the scaling relationships described in Fig. 4.8. Additionally, the idea for organizing the predicted flow rates in terms of the state diagram shown in Fig. 4.13C came from a productive discussion between Mr. McFadden and I.

Section 4.2 ABSTRACT

Actomyosin-based cortical flow is a fundamental engine for cellular morphogenesis. Cortical flows are generated by cross-linked networks of actin filaments and myosin motors, in which active stress produced by motor activity is opposed by passive resistance to network deformation. Continuous flow requires local remodeling through crosslink unbinding and and/or filament disassembly. But how local remodeling tunes stress production and dissipation, and how this in turn shapes long range flow, remains poorly understood. Here, we introduce a computational model for a cross-linked networks with active motors based on minimal requirements for production and dissipation of contractile stress, namely asymmetric filament compliance, spatial heterogeneity of motor activity, reversible cross-links and filament turnover. We characterize how the production and dissipation of network stress depend, individually, on cross-link dynamics and filament turnover, and how these dependencies combine to determine overall rates of cortical flow. Our analysis predicts that filament turnover is required to maintain active stress against external resistance and steady state flow in response to external stress. Steady state stress increases with filament lifetime up to a characteristic time τ_m, then decreases with lifetime above τ_m. Effective viscosity increases with filament lifetime up to a characteristic time τ_c, and then becomes independent of filament lifetime and sharply dependent on crosslink dynamics. These individual dependencies of active stress and effective viscosity define multiple regimes of steady state flow. In particular our model predicts the existence of a regime, when

filament lifetimes are shorter than both τ_c and τ_m, in which dependencies of effective viscosity and steady state stress cancel one another, such that flow speed is insensitive to filament turnover, and shows simple dependence on motor activity and crosslink dynamics. These results provide a framework for understanding how animal cells tune cortical flow through local control of network remodeling.

Section 4.3 AUTHOR SUMMARY

In this paper, we develop and analyze a minimal model for a 2D network of cross-linked actin filaments and myosin motors, representing the cortical cytoskeleton of eukaryotic cells. We implement coarse-grained representations of force production by myosin motors and stress dissipation through an effective cross-link friction and filament turnover. We use this model to characterize how the sustained production of active stress, and the steady dissipation of elastic stress, depend individually on motor activity, effective cross-link friction and filament turnover. Then we combine these results to gain insights into how microscopic network parameters control steady state flow produced by asymmetric distributions of motor activity. Our results provide a framework for understanding how local modulation of microscopic interactions within contractile networks control macroscopic quantities like active stress and effective viscosity to control cortical deformation and flow at cellular scales.

Section 4.4 INTRODUCTION

Cortical flow is a fundamental and ubiquitous form of cellular deformation that underlies cell polarization, cell division, cell crawling and multi-cellular tissue morphogenesis (Bray and White, 1988; Hird and White, 1993; Benink et al., 2000; Wilson et al., 2010; Rauzi et al., 2010;

Munro et al., 2004). These flows originate within a thin layer of cross-linked actin filaments and myosin motors, called the actomyosin cortex, which lies just beneath the plasma membrane (Salbreux et al., 2012). Local forces produced by bipolar myosin filaments are integrated within cross-linked networks to build macroscopic contractile stress (Murrell et al., 2015; Bendix et al., 2008; Janson et al., 1991). At the same time, cross-linked networks resist deformation and this resistance must be dissipated by network remodeling to allow macroscopic deformation and flow. How force production and dissipation depend on motor activity and network remodeling remains poorly understood.

One successful approach to modeling cortical flow has relied on coarse-grained phenomenological descriptions of actomyosin networks as active fluids, whose motions are driven by gradients of active contractile stress and opposed by an effectively viscous resistance (Mayer et al., 2010). In these models, spatial variation in active stress is typically assumed to reflect spatial variation in motor activity and force transmission (Bois et al., 2011), while viscous resistance is assumed to reflect the internal dissipation of elastic resistance due to local remodeling of filaments and/or cross-links (Salbreux et al., 2012; De La Cruz and Gardel, 2015). Models combining an active fluid description with simple kinetics for network assembly and disassembly, can successfully reproduce the spatiotemporal dynamics of cortical flow observed during polarization (Mayer et al., 2010), cell division (Turlier et al., 2014; Salbreux et al., 2009), cell motility (Keren et al., 2009; Marchetti et al., 2013) and tissue morphogenesis (Behrndt et al., 2012). However, it remains a challenge to connect this coarse-grained description of cortical flow to the microscopic origins of force generation and dissipation within cross-linked actomyosin networks.

Studies in living cells reveal fluid-like stress relaxation on timescales of 10-100s (Bray and White, 1988; Hird and White, 1993; Mayer et al., 2010; Hochmuth, 2000; Evans and Yeung, 1989; Bausch et al., 1998), which is thought to arise through a combination of cross-link unbinding and actin filament turnover (Salbreux et al., 2012; De La Cruz and Gardel, 2015; De La Cruz, 2009). Theoretical (Broedersz et al., 2010; Müller et al., 2014) and computational (Kim et al., 2011; Lieleg et al., 2009; Lieleg and Bausch, 2007) studies reveal that cross-link unbinding can endow actin networks with complex time-dependent viscoelasticity. However, while cross-link unbinding is sufficient for viscous relaxation (creep) on very long timescales in vitro, it is unlikely to account for the rapid cortical deformation and flow observed in living cells (Lieleg et al., 2009; Wachsstock et al., 1994; Lieleg et al., 2008; Yao et al., 2011; Liu et al., 2007). Experimental studies in living cells reveal rapid turnover of cortical actin filaments on timescales comparable to stress relaxation (10-100s) (Robin et al., 2014; Fritzsche et al., 2013, 2016; Carlsson, 2010; Lai et al., 2008). Perturbing turnover can lead to changes in cortical mechanics and in the rates and patterns of cortical flow (Fritzsche et al., 2016; Goor et al., 2012). However, the specific contributions of actin turnover to stress relaxation and how these depend on network architecture remain unclear.

Recent work has also begun to reveal mechanisms for active stress generation in disordered actomyosin networks. Theoretical studies suggest that spatial heterogeneity in motor activity along individual filaments, and asymmetrical filament compliance (stiffer in extension than in compression), are sufficient for macroscopic contraction (Lenz et al., 2012; Lenz, 2014), although other routes to contractility may also exist (Lenz, 2014). Local interactions among actin filaments and myosin motors are sufficient to drive macroscopic contraction of disordered networks in vitro (Murrell and Gardel, 2012), and the kinematics of contraction observed in these

studies support a mechanism based on asymmetrical filament compliance and filament buckling. However, in these studies, the filaments were preassembled and network contraction was transient, because of irreversible network collapse (Alvarado et al., 2013), or buildup of elastic resistance (Murrell and Gardel, 2014), or because network rearrangements (polarity sorting) dissipate the potential to generate contractile force (Ennomani et al., 2016; Reymann et al., 2012; Nedelec et al., 1997; Surrey et al., 2001). This suggests that network turnover may play essential role(s) in allowing sustained production of contractile force. Recent theoretical and modeling studies have begun to explore how this might work (Hiraiwa and Salbreux, 2016; Mak et al., 2016; Zumdieck et al., 2007), and to explore dynamic behaviors that can emerge when contractile material undergoes turnover (Salbreux et al., 2009; Dierkes et al., 2014). However, it remains a challenge to understand how force production and dissipation depend individually on the local interplay of network architecture, motor activity and filament turnover, and how these dependencies combine to mediate tunable control of long range cortical flow.

Here, we construct and analyze a simple computational model that bridges between the microscopic description of cross-linked actomyosin networks and the coarse grained description of an active fluid. We represent actin filaments as simple springs with asymmetric compliance; we represent dynamic binding/unbinding of elastic cross-links as molecular friction (Vanossi et al., 2013; Spruijt et al., 2010; Filippov et al., 2004) at filament crossover points; we represent motor activity as force coupling on a subset of filament cross-over points with a simple linear force/velocity relationship (Banerjee et al., 2011). Finally, we model filament turnover by allowing entire filaments to appear with a fixed probability per unit area and disappear with fixed probabilities per unit time. We use this model first to characterize the passive response of a cross-linked network to externally applied stress, then the buildup and maintenance of active

stress against an external resistance, and finally the steady state flows produced by an asymmetric distribution of active motors in which active stress and passive resistance are dynamically balanced across the network. Our results reveal how network remodeling can tune cortical flow through simultaneous effects on active force generation and passive resistance to network deformation.

Section 4.5 MODELS

Our goal was to construct a minimal model that is detailed enough to capture essential microscopic features of cross-linked actomyosin networks (actin filaments with asymmetric compliance, dynamic cross-links, active motors and and continuous filament turnover), but simple enough to explore, systematically, how these microscopic features control macroscopic deformation and flow. We focus on 2D networks because they capture a reasonable approximation of the quasi-2D cortical actomyosin networks that govern flow and deformation in many eukaryotic cells (Mayer et al., 2010; Chugh et al., 2016), or the quasi-2D networks studied recently in vitro (Murrell and Gardel, 2012; Sanchez et al., 2012).

Fig. 4.1 provides a schematic overview of our model's assumptions. We model each filament as an oriented elastic spring with relaxed length L. If the index i enumerates over all filaments, then the state of a filament is defined by the positions of its endpoints $\mathbf{b}_i$ and $\mathbf{p}_i$, marking its barbed (+) and pointed (-) ends, respectively. We define $\hat{\mathbf{u}}_i$ to be the unit vector oriented along filament i towards its barbed end.

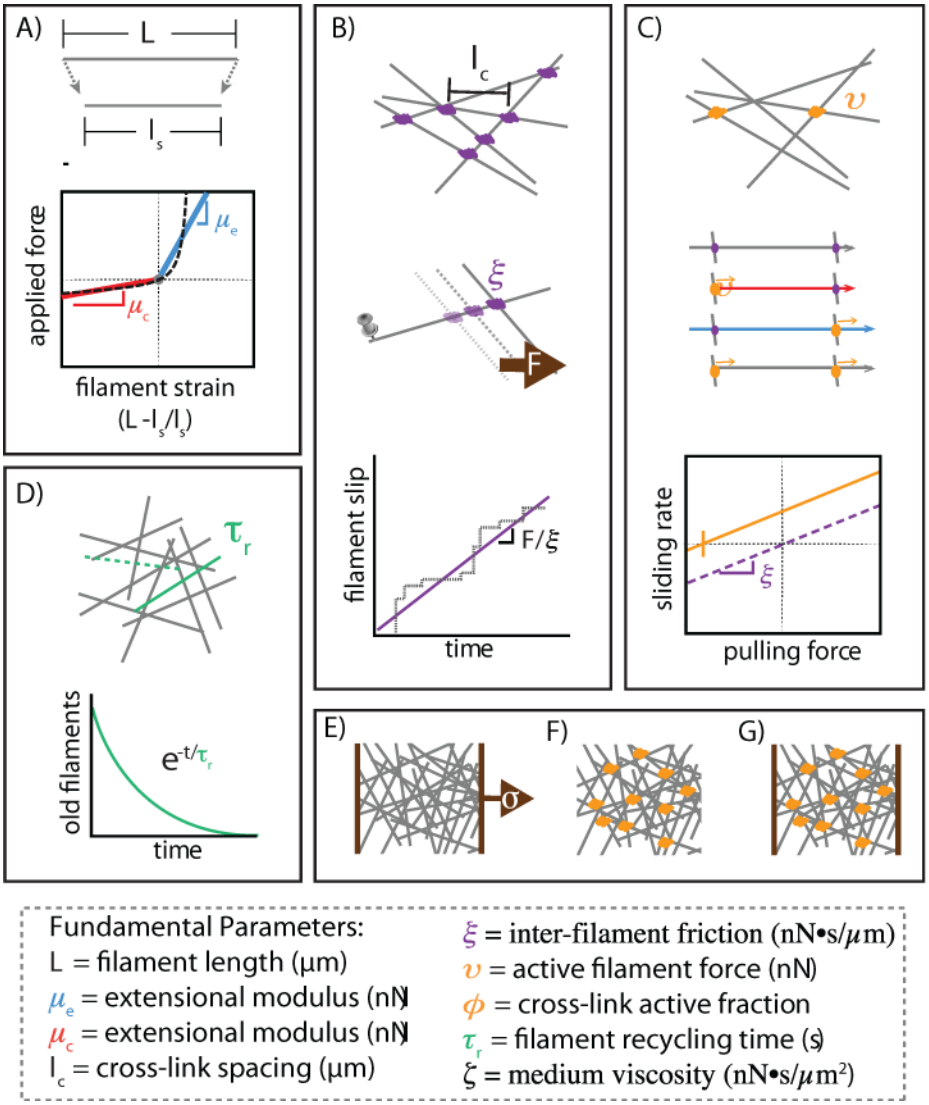

Figure 4.1. Schematic overview of modeling framework and assumptions. A) Filaments are oriented linear springs that are stiffer in extension than in compression. B) Cross-linking occurs at all filament crossings; we represent cross link resistance as an effective drag, proportional to the relative velocity of the overlapping filaments. C) We represent motor activity as a linear force-velocity relationship with a fixed force at zero velocity directed towards a filament's (-) end. We implement spatial heterogeneity by imposing motor activity at a fixed fraction of filament crossover points, resulting in variation in the magnitudes of compressive versus extensile versus translational forces along individual filament segments. D) Whole filaments disappear at a constant rate; new filaments appear with random positions and orientations at the constant rate per unit area, such that entire network refreshes on a characteristic timescale τ_r. E-G) Three different simulation scenarios: E) Passive response to uniaxial stress, F) Free contraction of an active network and G) Isometric contraction against a fixed boundary.

Asymmetric filament compliance

We assume (Fig. 4.1A) that local deformation of filament i gives rise to an elastic force:

$$\mathbf{F}_{\mathrm{p,i}}^{\mathrm{elas}} = \mu\gamma_{\mathrm{i}}\hat{\mathbf{u}}_{\mathrm{i}}, \qquad \mathbf{F}_{\mathrm{b,i}}^{\mathrm{elas}} = -\mathbf{F}_{\mathrm{p,i}}^{\mathrm{elas}} \tag{1}$$

where $\gamma_{\mathrm{i}} = \left(\left|\mathbf{b}_{\mathrm{i}} - \mathbf{p}_{\mathrm{i}}\right| - L\right)/L$ is the strain on filament i, and the normalized spring constant μ is a composite quantity that represents both filament and cross-linker compliance as in the effective medium theory of Broedersz and colleagues (Broedersz et al., 2009). To model asymmetric filament compliance, we set $\mu = \mu_e$ if the strain is positive (extension), and $\mu = \mu_c$ if the strain is negative (compression).

Drag-like coupling between overlapping filaments

Previous models represent cross-linkers as elastic connections between pairs of points on neighboring filaments that appear and disappear with either fixed or force-dependent probabilities (Kim et al., 2011; Broedersz et al., 2009). Here, we introduce a coarse-grained representation of crosslink dynamics by introducing an effective drag force that couples every pair of overlapping filaments, and which represents a molecular friction arising from the time-averaged contributions of many individual transient crosslinks (Fig. 4.1B). This is a reasonable approximation if all pairs of overlapping filaments have equal access to a non-limiting pool of cross-links, and if the rate at which filaments move past one another is slow relative to the unbinding rate of individual cross-links (Howard, 2001). This coarse-grained approach has been used to model frictional forces arising from ionic cross-linking of actin filaments *in vitro* (Ward et al., 2015; Chandran and Mofrad, 2010), and simple force-velocity relationships for systems of

cytoskeletal filaments and cross-linking motors (Banerjee et al., 2011; Schoenberg, 1985; Tawada and Sekimoto, 1991; Leibler and Huse, 1993).

To implement coupling through effective drag, for any pair of overlapping filaments i and j, we write the drag force on filament i as:

$$\mathbf{F}_{i,j}^{\xi} = -\xi\left(\mathrm{v}_i - \mathrm{v}_j\right) \tag{2}$$

where ξ is the drag coefficient and v_i, v_j are the average centroid velocities of filaments i and j. We apportion this drag force to the two endpoints p_i and b_i of filament i as follows: If $x_{i,j}$ is the position of the filament overlap, then we define $\lambda_{i,j} = \left|x_{i,j} - p_i\right| / \left|b_i - p_i\right|$ to be the fractional position of the overlap point along filament i, and we assign $\left(1-\lambda_{i,j}\right)\mathbf{F}_{i,j}^{\xi}$ to endpoint p_i and $\lambda_{i,j}\mathbf{F}_{i,j}^{\xi}$ to endpoint b_i.

The total cross-link coupling force on endpoints p_i and b_i, due to overlaps along filament i, can then be written:

$$\begin{aligned}\mathbf{F}_{p,i}^{xl} &= \sum_j \left(1-\lambda_{i,j}\right)\mathbf{F}_{i,j}^{\xi} \\ \mathbf{F}_{b,i}^{xl} &= \sum_j \lambda_{i,j}\mathbf{F}_{i,j}^{\xi}\end{aligned} \tag{3}$$

where the sums are taken over all filaments j that overlap with filament i.

This model assumes a linear relation between the drag force and the velocity difference between attached filaments. Although non-linearities can arise through force dependent detachment kinetics and/or non-linear force extension of cross-links, we assume here that these non-linear effects are of second or higher order.

Active coupling for motor driven filament interactions

To add motor activity at the point of overlap between two filaments i and j as follows: for each filament in the pair, we impose an additional force of magnitude ν, directed towards its pointed (-) end (Fig. 4.1C):

$$\mathbf{F}_{\mathrm{i}}^{\nu} = -\nu \hat{\mathbf{u}}_{\mathrm{i}} \tag{4}$$

We impose an equal and opposite force on its overlapping partner. We distribute these forces to filament endpoints as described above for crosslink coupling forces. Thus, the total force on endpoints p_{i} and b_{i} due to motor activity on overlap points between filaments i and j can be written as:

$$\begin{aligned} \mathbf{F}_{\mathrm{p,i}}^{\mathrm{motor}} &= \sum_{\mathrm{j}} \left(1-\lambda_{\mathrm{i,j}}\right)\left(\mathbf{F}_{\mathrm{i}}^{\nu} - \mathbf{F}_{\mathrm{j}}^{\nu}\right) q_{\mathrm{i,j}} = \nu \sum_{\mathrm{j}} \left(1-\lambda_{\mathrm{i,j}}\right)\left(\hat{\mathbf{u}}_{\mathrm{j}} - \hat{\mathbf{u}}_{\mathrm{i}}\right) q_{\mathrm{i,j}} \\ \mathbf{F}_{\mathrm{b,i}}^{\mathrm{motor}} &= \nu \sum_{\mathrm{j}} \left(\lambda_{\mathrm{i,j}}\right)\left(\hat{\mathbf{u}}_{\mathrm{j}} - \hat{\mathbf{u}}_{\mathrm{i}}\right) q_{\mathrm{i,j}} \end{aligned} \tag{5}$$

where j enumerates over all filaments that overlap with filament i, and $q_{\mathrm{i,j}}$ equals 0 or 1 depending on whether there is an "active" motor at this location. To model dispersion of motor activity, we set $q_{\mathrm{i,j}}$ = 1 on a randomly selected subset of filament overlaps, such that $\bar{q} = \phi$, where $\bar{q}$ indicates the mean of q (Fig. 4.1C).

Equations of motion

To write the full equation of motion for a network of actively and passively coupled elastic filaments, we assume the low Reynold's number limit in which inertial forces can be neglected, and we equate the sum of all forces acting on each filament endpoint to zero to obtain:

$$\begin{aligned} 0 &= -\zeta \mathrm{v}_{\mathrm{i}}^{\mathrm{p}}\, L/2 - \mathbf{F}_{\mathrm{p,i}}^{\mathrm{xl}} + \mathbf{F}_{\mathrm{p,i}}^{\mathrm{elas}} + \mathbf{F}_{\mathrm{p,i}}^{\mathrm{motor}} \\ 0 &= -\zeta \mathrm{v}_{\mathrm{i}}^{\mathrm{b}}\, L/2 - \mathbf{F}_{\mathrm{b,i}}^{\mathrm{xl}} + \mathbf{F}_{\mathrm{b,i}}^{\mathrm{elas}} + \mathbf{F}_{\mathrm{b,i}}^{\mathrm{motor}} \end{aligned} \tag{6}$$

where the first term in each equation represents the hydrodynamic drag on the half-filament adjoining endpoints p_i or b_i with respect to motion at velocities v_i^p or v_i^b against the surrounding fluid, and ζ is the drag coefficient.

2D network formation

We used a Mikado model approach (Unterberger and Holzapfel, 2014) to initialize a minimal network of overlapping unstressed linear filaments in a rectangular 2D domain. We generate individual filaments by laying down straight lines, of length *L*, with random position and orientation. We define the density using the average distance between cross-links along a filament, l_c. A simple geometrical argument can then be used to derive the number of filaments filling a domain as a function of *L* and l_c (Head et al., 2003). Here, we use the approximation that the number of filaments needed to tile a rectangular domain of size $D_x \times D_y$ is $2D_xD_y / Ll_c$, and that the length density is therefore simply $2 / l_c$.

Modeling filament turnover

In living cells, actin filament assembly is governed by multiple factors that control filament nucleation, branching and elongation. Likewise filament disassembly is governed by multiple factors that promote filament severing and monomer dissociation at filament ends. Here, we implement a very simple model for filament turnover in which entire filaments appear with a fixed rate per unit area, k_{app}, and disappear at a rate $k_{diss}\rho$, where ρ is a filament density (Fig. 4.1D). With this assumption, in the absence of network deformation, the density of filaments will equilibrate to a steady state density, k_{app}/k_{diss}, with time constant $\tau_r = 1/k_{diss}$. In

deforming networks, filament density will also decrease under extensional strain and increase under compressional strain. Thus, filament density will be set by a dynamic interplay of deformation and density equilibration via turnover (see below and Section 4.9.3). To implement this model, at fixed time intervals $\tau_s < 0.01 \cdot \tau_r$ (i.e. 1% of the equilibration time), we selected a fraction, τ_s / τ_r , of existing filaments (i.e. less than 1% of the total filaments) for degradation. We then generated a fixed number of new unstrained filaments $k_{app} \tau_s D_x D_y$ at random positions and orientations within the original domain. We refer to $k_{diss} = 1/\tau_r$ as the turnover rate, and to τ_r as the turnover time.

Simulation methods

Further details regarding our simulation approach and references to our code can be found in Section 4.9.1. Briefly, equations 1-6 define a coupled system of ordinary differential equations that can be written in the form:

$$\mathbf{A} \cdot \dot{\mathrm{x}} = \mathrm{f}\left(\mathrm{x}\right) \tag{7}$$

where x is a vector of filament endpoint positions, $\dot{\mathrm{x}}$ the endpoint velocities, **A** is a matrix with constant coefficients that represents crosslink coupling forces between overlapping filaments, and f (x) represents the active (motor) and elastic forces on filament endpoints. We smoothed all filament interactions, force fields, and constraints linearly over small regions such that the equations contained no sharp discontinuities. We used a fourth-order Runga-Kutta method to numerically integrate this system of equations to find the time evolution of the positions of all filament endpoints. We generate a network of filaments with random positions and orientations as described above within a domain of size D_x by D_y . For all simulations, we imposed periodic

boundaries in the y-dimension. To impose an extensional force per unit length (2D stress) on the network, we constrained all filament endpoints within a fixed distance $0.05 \cdot D_x$ from the left edge of the domain to be non-moving, then we imposed a rightwards force on all endpoints within a distance $0.05 \cdot D_x$ from the right edge of the domain, such that the force per unit length of the boundary equals the desired stress value. To simulate free contraction, we removed all constraints at domain boundaries; to assess buildup and maintenance of contractile stress under isometric conditions, we used periodic boundary conditions in both x and y dimensions.

Measuring stress, strain, and strain rate

In our 2D model, we measure stress as a force per unit length. We measured the internal network stress at each axial position by summing the axial (x) component of the tensions on all filaments intersecting that position, and dividing by the network height D_y. We measured the strain on an individual filament as the change in filament length, divided by its equilibrium length. Then we averaged this measurement over all filaments in a network to obtain an average filament strain. To measure the average network strain rate, we first measured the mean velocity v(X) at position X (relative to the network boundary at x = 0) to be the average velocity of all filaments intersecting that position. In the case where we measure network strain or strain rates, we observed an approximately linear dependence of v(X) on X; hence the strain rate is approximately uniform across the network (Fig. 4.2B and Fig 4.15). Accordingly, for each filament, we took $\frac{1}{X}\frac{dX}{dt}$ to be an estimate of the strain rate on the network between x = 0 and x = X. We averaged this estimate over all filaments in a domain to get an average strain rate. Finally,

to estimate the cumulative network strain at a given time T in the simulation, we integrated the strain rate with respect to time for t = 0 to T.

We assigned biological plausible reference values for all parameters (Table 4.1). For individual analyses, we sampled the ranges of parameter values around these reference values shown in Table 4.2.

Table 4.1. Simulation parameters with reference values

Parameter	Symbol	Reference Value
extensional spring constant	μ_e	$100pN$
compressional spring constant	μ_c	$1pN$
cross-link drag coefficient	ξ	$100\frac{pNs}{\mu m}$
solvent drag coefficient	ζ	$0.05\frac{pNs}{\mu m^2}$
filament length	L	$5\mu m$
cross-link spacing	l_c	$0.5\mu m$
active filament force	υ	$10pN$
active cross-link fraction	ϕ	$0.1 - 0.9$
domain size	$D_x \times D_y$	$50 \times 20\mu m$

Table 4.2. List of parameter values used for simulations presented in specific figures.

Parameter	Units	Figure 4.4	Figure 4.5	Figure 4.8A,B	Figure 4.8C,D	Figure 4.10	Figure 4.14
L	μm	$1, 3, 5, 7, 10$	3	$3, 5$	$3, 5$	5	$3, 5, 8$
l_c	μm	$0.2, 0.3, 0.5, 0.8$	$0.3, 0.5$	0.3	$0.15, 0.2, 0.3, 0.4$	$0.2, 0.3$	$0.15, 0.2, 0.3, 0.4$
μ_e/μ_c		100	100	$3 - 300$	100	100	100
μ_e	pN	100	100	100	$10 - 300$	100	100
μ_c	pN	1	1	$1 - 30$	1	1	1
ξ	$\frac{pNs}{\mu m}$	$10 - 100$	$5, 10, 100$	$1, 10, 100$	$10, 100$	$10, 100, 330$	$10 - 100$
υ	pN			$10, 30, 100$	$10, 100$	$10, 100, 300$	10
ϕ				0.25	0.5	$0.25, 0.75$	0.25
τ_r	s		$0.1 - 10^4$			$0.01 - 10^3$	$0.01 - 10^3$
σ	$\frac{pNs}{\mu m^2}$	$0.02 - 1$	$0.003 - 0.5$				

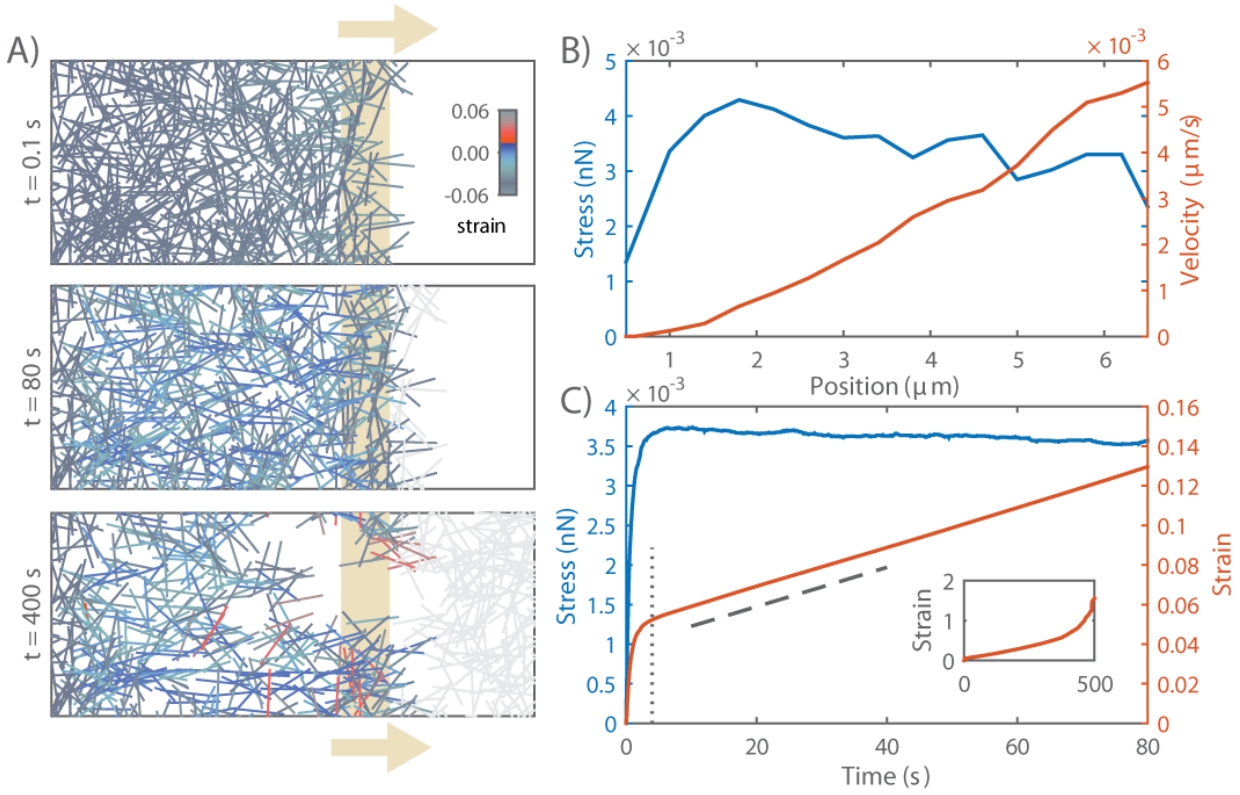

Figure 4.2. Networks with passive cross-links and no filament turnover undergo three stages of deformation in response to an extensional stress. A) Three successive time points from a simulation of a 4 x 6.6 µm network deforming under an applied stress of 0.005 nN/µm. Stress (tan arrows) is applied to filaments in the region indicated by the tan bar. In this and all subsequent figures, filaments are color-coded with respect to state of strain (blue = tension, red = compression). Network parameters: L = 1 µm, l_c = 0.3 µm, ξ = 100 nN s/µm. B) Mean filament stress and velocity profiles for the network in (A) at t = 88 s. Note that the stress is nearly constant and the velocity is nearly linear as predicted for a viscous fluid under extension. C) Plots of the mean stress and strain versus time for the simulation in (A), illustrating the three stages of deformation: (i) A fast initial deformation accompanies rapid buildup of internal network stress; (ii) after a characteristic time τ_c (indicated by vertical dotted line) the network deforms at a constant rate, i.e. with a constant effective viscosity, η_c, given by the slope of the dashed line; (iii) at long times, the network undergoes strain thinning and tearing (see inset).

Section 4.6 RESULTS

The goal of this study is to understand how cortical flow is shaped by the simultaneous dependencies of active stress and effective viscosity on filament turnover, crosslink drag and on "network parameters" that control filament density, elasticity and motor activity. We approach

this in three steps: First, we analyze the passive deformation of a cross-linked network in response to an externally applied stress; we identify regimes in which the network response is effectively viscous and characterize the dependence of effective viscosity on network parameters and filament turnover. Second, we analyze the buildup and dissipation of active stress in cross-linked networks with active motors, as they contract against an external resistance; we identify conditions under which the network can produce sustained stress at steady state, and characterize how steady state stress depends on network parameters and filament turnover. Finally, we confirm that the dependencies of active stress and effective viscosity on network parameters and filament turnover are sufficient to predict the dynamics of networks undergoing steady state flow in response to spatial gradients of motor activity.

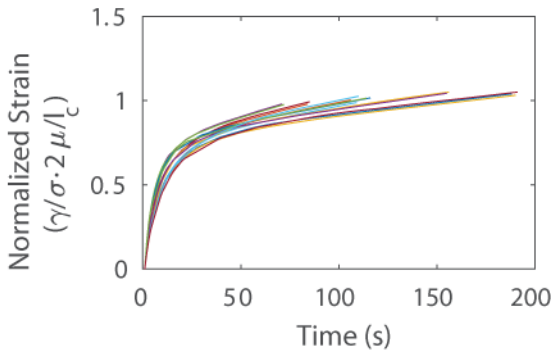

Figure 4.3. Fast viscoelastic response to extensional stress. Plots of normalized strain versus time during the elastic phase of deformation in passive networks under extensional stress. Measured strain is normalized by the equilibrium strain predicted for a network of elastic filaments without crosslink slip $\gamma_{eq} = \sigma / G_0 = \sigma / \left(2\mu / l_c \right)$.

Filament turnover allows and tunes effectively viscous steady state flow.

Networks with passive cross-links and no filament turnover undergo three stages of deformation in response to an extensional force. To characterize the passive response of a cross-linked filament network without filament recycling, we simulated a simple uniaxial strain experiment in

which we pinned the network at one end, imposed an external stress at the opposite end, and then quantified network strain and internal stress as a function of time (Fig. 4.1E). The typical response occurred in three qualitatively distinct phases (Fig. 4.2A,C). At short times the response was viscoelastic, with a rapid buildup of internal stress and a rapid approximately exponential approach to a fixed strain (Fig. 4.3A), which represents the elastic limit in the absence of cross-link slip predicted by (Head et al., 2003). At intermediate times, the local stress and strain rate were approximately constant across the network (Fig. 4.2B), and the response was effectively viscous; internal stress remained constant while the network continued to deform slowly and continuously with nearly constant strain rate (shown as dashed line in Fig. 4.2C) as filaments slip past one another against the effective cross-link drag. In this regime, we can quantify effective viscosity, η_c, as the ratio of applied stress to the measured strain rate. Finally, as the network strain approached a critical value (~30% for the simulation in Fig. 4.2), strain thinning lead to decreased network connectivity, local tearing, and rapid acceleration of the network deformation (see inset in Fig. 4.2C).

Network architecture sets the rate and timescales of deformation. To characterize how effective viscosity and the timescale for transition to effectively viscous behavior depend on network architecture and cross-link dynamics, we simulated a uniaxial stress test, holding the applied stress constant, while varying filament length *L*, density l_c, elastic modulus μ_e and cross link drag ξ (see Table 4.2). We measured the elastic modulus, G_0, the effective viscosity, η_c, and the timescale τ_c for transition from viscoelastic to effectively viscous behavior, and compared these to theoretical predictions (Fig. 4.4). We observed a transition from viscoelastic to effectively viscous deformation for the entire range of parameter values that we sampled. Our

estimate of G_0 from simulation agreed well with the closed form solution $G_0 \sim \mu / l_c$ predicted by a previous theoretical model (Head et al., 2003) for networks of semi-flexible filaments with irreversible cross-links (Fig. 4.4A).

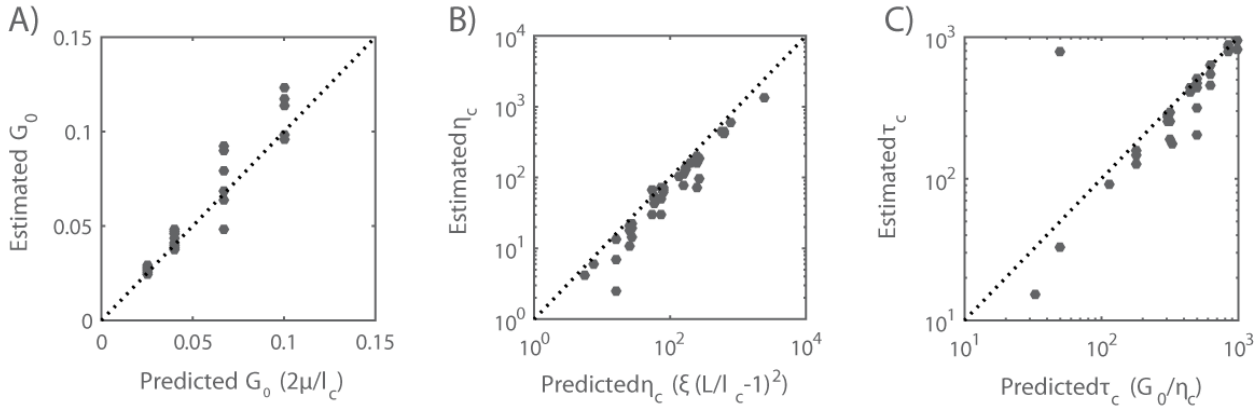

Figure 4.4. Network architecture sets the rate and timescales of deformation. (A-C) Comparison of predicted and simulated values for: A) the bulk elastic modulus G_0, B) the effective viscosity η_c and C) the timescale for transition from viscoelastic to viscous behavior τ_c, given by the ratio of the bulk elastic modulus G_0 to effective viscosity, η_c. Dotted lines indicates the relationships predicted by theory.

A simple theoretical analysis of filament networks with frictional cross link slip, operating in the intermediate viscous regime (see Section 4.9.2), predicts that the effective viscosity η_c should be proportional to the cross-link drag coefficient and to the square of the number of cross-links per filament:

$$\eta_c = 4\pi\xi\left(\frac{L}{l_c} - 1\right)^2 \quad . \tag{8}$$

As shown in Fig. 4.4B, our simulations agree well with this prediction for a large range of sampled network parameters. Finally, for many linear viscoelastic materials, the ratio of effective viscosity to the elastic modulus η_c / G_0 sets the timescale for transition from elastic to

viscous behavior (McCrum et al., 1997). Combining our approximations for G_0 and η_c, we predict a transition time, $\tau_c \approx L^2\xi/l_c\mu$. Measuring the time at which the strain rate became nearly constant (i.e. $\gamma \sim t^n$ with n > 0.8) yields an estimate of τ_c that agrees well with this prediction over the entire range of sampled parameters (Fig. 4.4C). Thus the passive response of filament networks with frictional cross link drag is well-described on short (viscoelastic) to intermediate (viscous) timescales by an elastic modulus G_0, an effective viscosity η_c, and a transition timescale τ_c, with well-defined dependencies on network parameters. However, without filament turnover, strain thinning and network tearing limits the extent of viscous deformation to small strains.

Filament turnover allows sustained large-scale viscous flow and defines two distinct flow regimes. To characterize how filament turnover shapes the passive network response to an applied force, we introduced a simple form of turnover in which entire filaments disappear at a rate $k_{\text{diss}}\rho$, where ρ is the filament density, and new unstrained filaments appear with a fixed rate per unit area, k_{app}. In a non-deforming network, filament density will equilibrate to a steady state value, $\rho_0 = k_{\text{ass}}/k_{\text{diss}}$, with time constant $\tau_{\text{r}} = 1/k_{\text{diss}}$. However, in networks deforming under extensional stress, the density will be set by a competition between strain thinning and density equilibration via turnover.

We simulated a uniaxial stress test for different values of τ_{r}, while holding all other parameters fixed (Fig. 4.5A-C). For large τ_{r}, as described above, the network undergoes strain thinning and ultimately tears. Decreasing τ_{r} increases the rate at which the network equilibrates towards a steady state density ρ_0. However, it also increases the rate of deformation and thus the

rate of strain thinning (Fig. 4.5B). We found that the former effect dominates, such that below a critical value $\tau_r = \tau_{crit}$, the network can achieve a steady state characterized by a fixed density and a constant strain rate (Fig. 4.6 and Section 4.9.3).

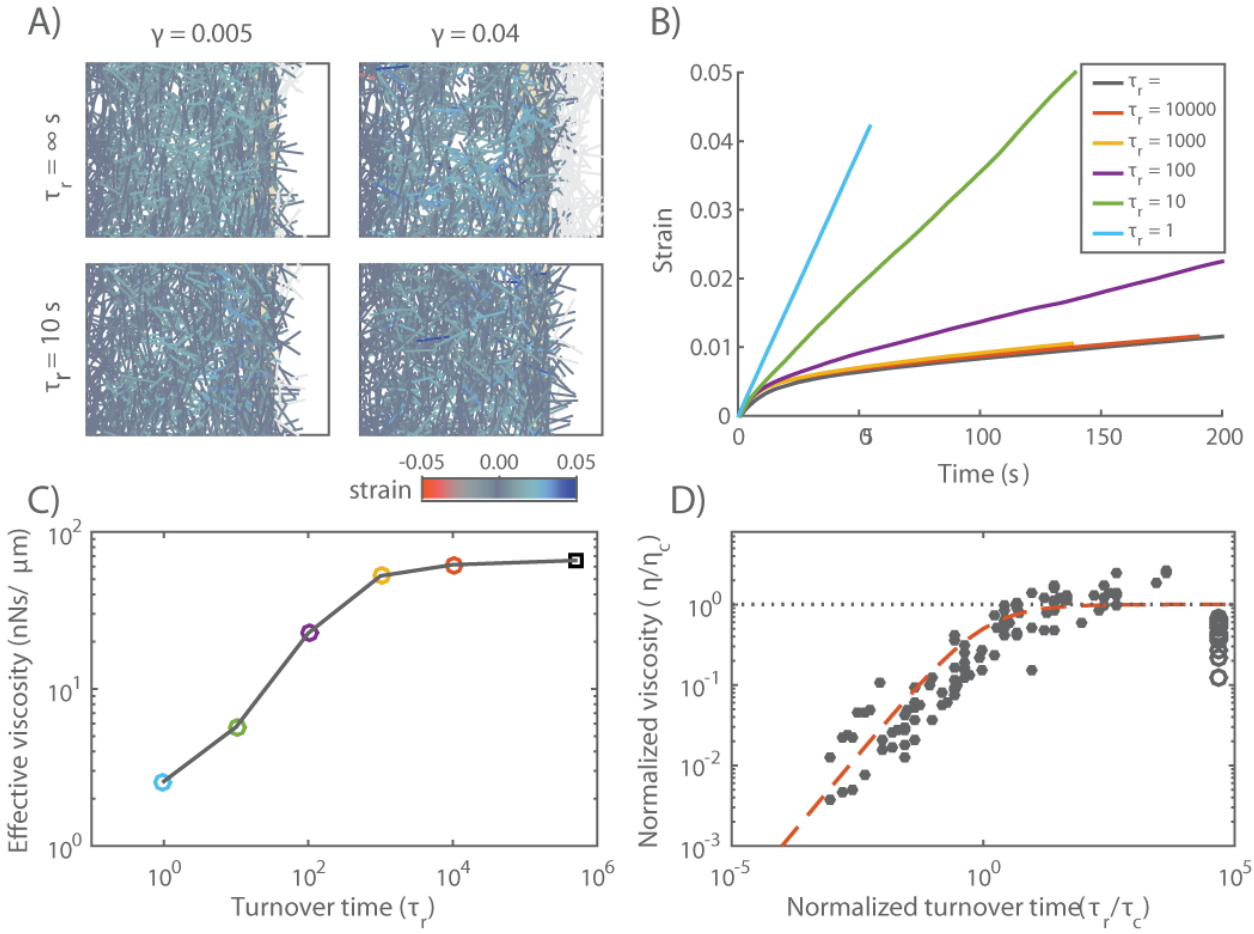

Figure 4.5. Filament turnover defines two regimes of effectively viscous flow. A) Comparison of 20 x 12 µm networks under 0.001 nN/µm extensional stress without (top) and with (bottom) filament turnover. Both images are taken when the networks had reached a net strain of 0.04. For clarity, filaments that leave the domain of applied stress are grayed out. B) Plots of strain vs time for identical networks with different rates of filament turnover. Network parameters: L = 5 µm, l_c = 0.5 µm, ξ = 10 nN s/µm. C) Plot of effective viscosity versus turnover time derived from the simulations shown in (B). Square dot is the $\tau_r = \infty$ condition. D) Plot of normalized effective viscosity (η/η_c) versus normalized turnover time (τ_r/τ_c) for a large range of network parameters and turnover times. For $\tau_r \ll \tau_c$, the viscosity of the network becomes dependent on recycling time. Red dashed line indicates the approximation given in equation 9 for m = 3/4.

For $\tau_r < \tau_{crit}$, we observed two distinct steady state flow regimes (Fig. 4.5B,C). For intermediate values of τ_r, effective viscosity remains constant with decreasing τ_r. However, below a certain value of τ_r ($\approx 10^3$ for the parameters used in Fig. 4.5C), effective viscosity decreased monotonically with further decreases in τ_r. To understand what sets the timescale for transition between these two regimes, we measured effective viscosity at steady steady for a wide range of network parameters (L, μ, l_c), crosslink drags (ξ) and filament turnover times (Fig. 4.5D). Strikingly, when we plotted the normalized effective viscosity η_r/η_c versus a normalized turnover rate τ_r/τ_c for all parameter values, the data collapsed onto a single curve, with a transition at $\tau_r \approx \tau_c$ between an intermediate turnover regime in which effective viscosity is independent of τ_r and an high turnover regime in which effective viscosity falls monotonically with decreasing τ_r/τ_c (Fig. 4.5D).

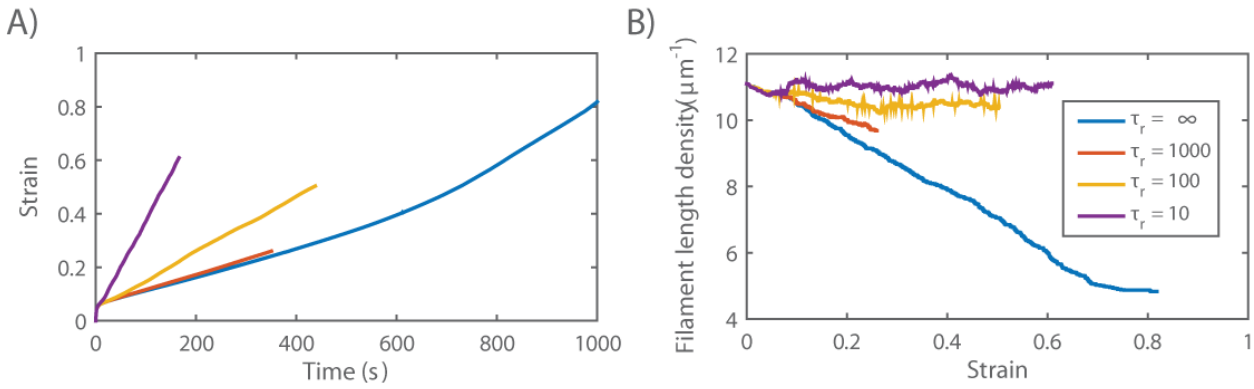

Figure 4.6. Filament turnover limits density decrease under extensional strain and allows continuous flow without material failure. A) Plots of strain versus time for different turnover times (see inset in (B)). Note the increase in strain rates with decreasing turnover time. B) Plots of filament density versus strain for different turnover times τ_r. For intermediate τ_r, simulations predict progressive strain thinning, but at a lower rate than in the complete absence of recycling. For higher τ_r, densities approach steady state values at longer times as connectivity is lost as a result of the flow-induced density loss, and the network is no longer under load.

This biphasic dependence of effective viscosity on filament turnover can be understood intuitively as follows: As new filaments are born, they become progressively stressed as they stretch and reorient under local influence of surrounding filaments, eventually reaching an elastic limit where their contribution to resisting network deformation is determined by effective crosslink drag. The time to reach this limit is about the same as the time, τ_c, for an entire network of initially unstrained filaments to reach an elastic limit during the initial viscoelastic response to uniaxial stress, as shown in Fig. 4.2B. For $\tau_r < \tau_c$, individual filaments do not have time, on average, to reach the elastic limit before turning over; thus the deformation rate is determined by the elastic resistance of partially strained filaments, which increases with lifetime up to $\tau_r = \tau_c$. For $\tau_r > \tau_c$, the deformation rate is largely determined by cross-link resistance to sliding of maximally strained filaments, and the effective viscosity is insensitive to further increase in τ_r.

These results complement and extend a previous computational study of irreversibly cross-linked networks of treadmilling filaments deforming under extensional stress (Kim et al., 2014). Kim et al. identified two regimes of effectively viscous deformation: a "stress-dependent" regime in which filaments turnover before they become strained to an elastic limit and deformation rate is proportional to both applied stress and turnover rate; and a "stress-independent" regime in which filaments reach an elastic limit before turning over and deformation rate depends only on the turnover rate. The fast and intermediate turnover regimes that we observe here correspond to the stress-dependent and independent regimes described by Kim et al., but with a key difference. Without filament turnover, the model of Kim et al. predicts that a network cannot deform beyond its elastic limit. In contrast, our model predicts viscous

flow at low turnover, governed by an effective viscosity that is set by cross-link density and effective drag. Thus our model provides a self-consistent framework for understanding how crosslink unbinding and filament turnover contribute separately to viscous flow and connects these contributions directly to previous theoretical descriptions of cross-linked networks of semi-flexible filaments.

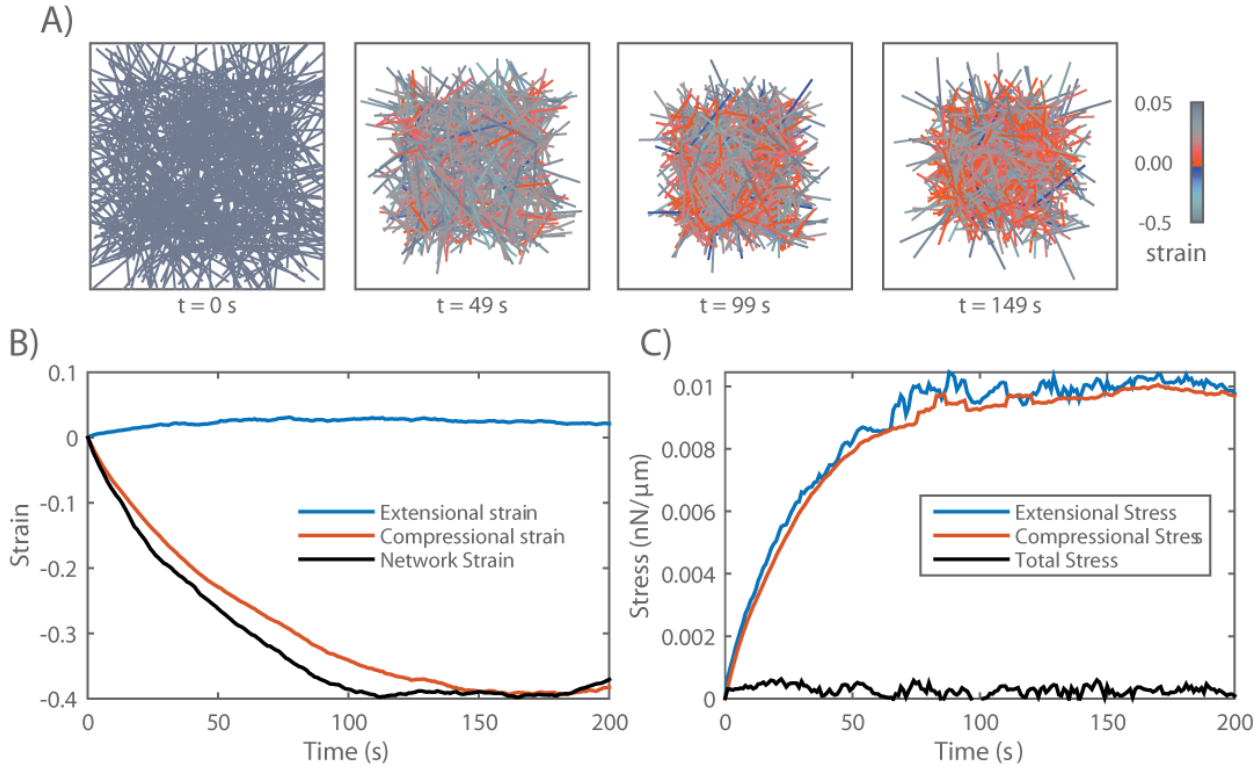

Figure 4.7. In the absence of filament turnover, active networks with free boundaries contract and then stall against passive resistance to network compression. A) Simulation of an active network with free boundaries. Colors represent strain on individual filaments as in previous figures. Note the buildup of compressive strain as contraction approaches stall between 100 s and 150 s. Network parameters: L = 5 μm, l_c = 0.3 μm, ξ = 1 nN s/μm, ν = 0.1 nN. B) Plots showing time evolution of total network strain (black) and the average extensional (blue) or compressive (red) strain on individual filaments. C) Plots showing time evolution of total (black) extensional (blue) or compressive (red) stress. Note that extensional and compressive stress remain balanced as compressive resistance builds during network contraction.

In summary, our simulations predict that filament turnover allows networks to undergo viscous deformation indefinitely, without tearing, over a wide range of different effective viscosities and deformation rates. For $\tau_r < \tau_{crit}$, this behavior can be summarized by an equation of the form:

$$\eta = \frac{\eta_c}{1+\left(\tau_c/\tau_r\right)^m} \tag{9}$$

For $\tau_r \gg \tau_c$, $\eta \approx \eta_c$: effective viscosity depends on crosslink density and effective crosslink drag, independent of changes in recycling rate. For $\tau_r \ll \tau_c$, effective viscosity is governed by the level of elastic stress on network filaments, and becomes strongly dependent on filament lifetime: $\eta \sim \eta_c \left(\tau_r/\tau_c\right)^m$. The origins of the *m* = 3/4 scaling remains unclear (see Discussion).

Filament turnover allows persistent stress buildup in active networks

In the absence of filament turnover, active networks with free boundaries contract and then stall against passive resistance to network compression. Previous work (Lenz et al., 2012; Murrell and Gardel, 2012; Koenderink et al., 2009) identifies asymmetric filament compliance and spatial heterogeneity in motor activity as minimal requirements for macroscopic contraction of disordered networks. To confirm that our simple implementation of these two requirements (see Models section) is sufficient for macroscopic contraction, we simulated active networks that are unconstrained by external attachments, varying filament length, density, crosslink drag and motor activity. We observed qualitatively similar results for all choices of parameter values: Turning on motor activity in an initially unstrained network induced rapid initial contraction, followed by a slower buildup of compressive stress (and strain) on individual filaments, and an

exponential approach to stall (Fig. 4.7). The time to stall, τ_s, scaled as $L\xi/\nu$ (Fig. 4.8). On even longer timescales, polarity sorting of individual filaments, as previously described (Murrell and Gardel, 2014; Reymann et al., 2012; Nedelec et al., 1997; Surrey et al., 2001) lead to network expansion.

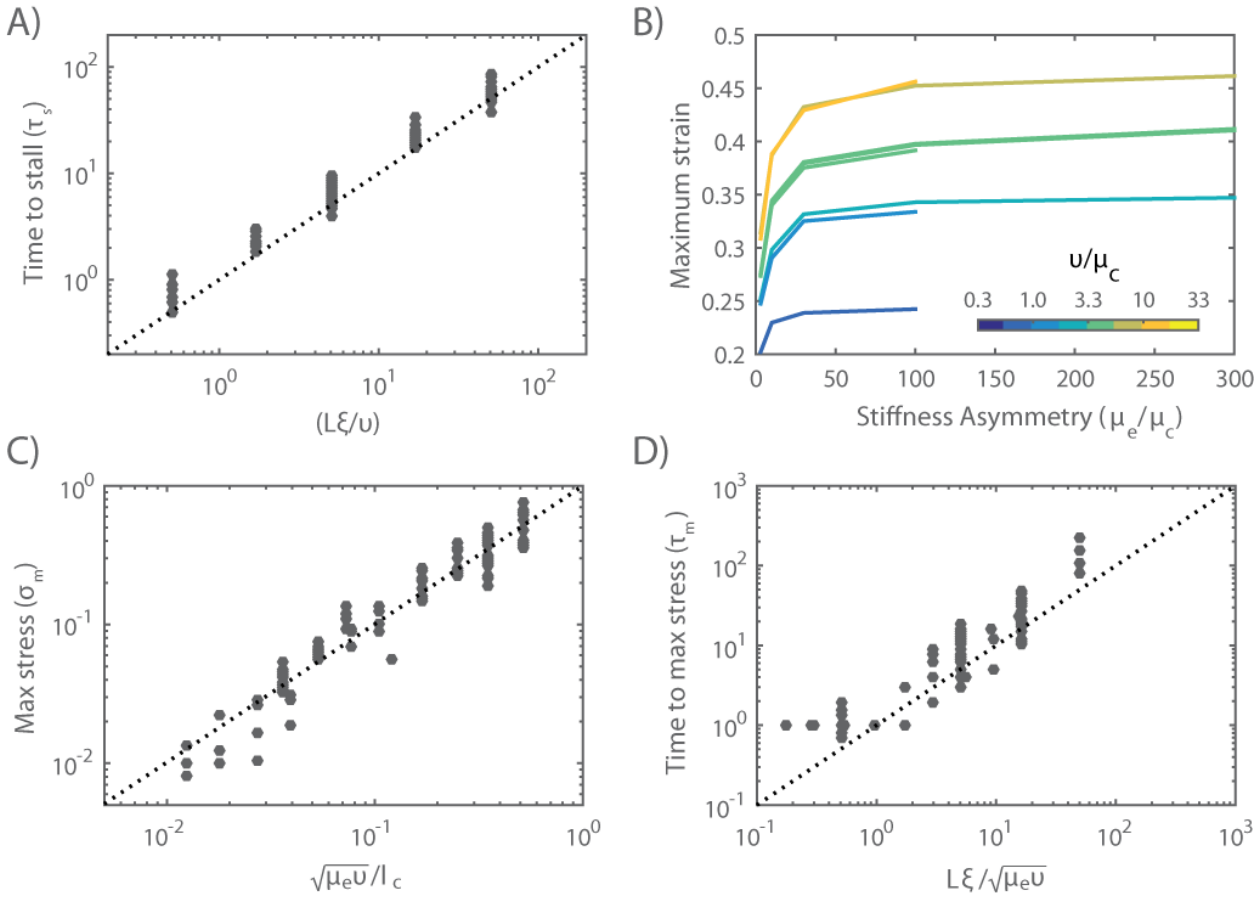

Figure 4.8. Mechanical properties of active networks. A) Time for freely contracting networks to reach maximum strain, τ_s, scales with $L\xi/\nu$. B) Free contraction requires asymmetric filament compliance, and total network strain increases with the applied myosin force ν. Note that the maximum contraction approaches an asymptotic limit as the stiffness asymmetry approaches a ratio of ~100. C) Maximum stress achieved during isometric contraction, σ_m, scales approximately with $\sqrt{\mu_e \nu}/l_c$. D) Time to reach max stress during isometric contraction scales approximately with $L\xi/\sqrt{\mu_e \nu}$. Scaling relations for τ_s, σ_m and τ_m were determined empirically by trial and error, guided by dimensional analysis.

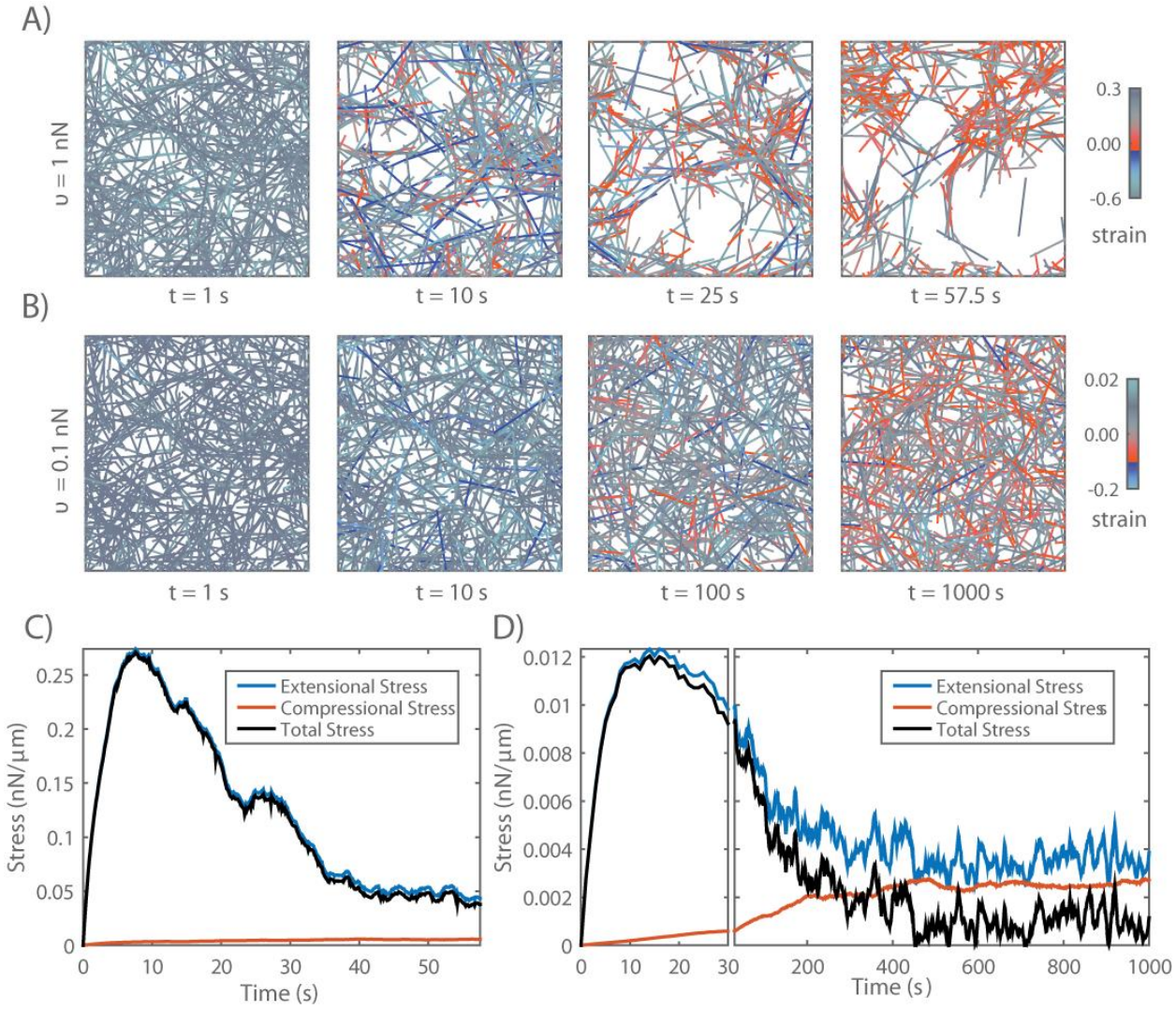

Figure 4.9. In the absence of filament turnover, active networks cannot sustain continuous stress against a fixed boundary. A) Simulation of an active network with fixed boundaries. Rearrangement of network filaments by motor activity leads to rapid loss of network connectivity. Network parameters: L = 5 μm, l_c = 0.3 μm, ξ = 1 nN s/μm, ν = 1 nN. B) Simulation of the same network, with the same parameter values, except with ten-fold lower motor activity ν = 0:1 nN. In this case, connectivity is preserved, but there is a progressive buildup of compressive strain on individual filaments. C) Plots of total network stress and the average extensional (blue) and compressive (red) stress on individual filaments for the simulation shown in (A). Rapid buildup of extensional stress allows the network transiently to exert force on its boundary, but this force is rapidly dissipated as network connectivity breaks down. D) Plots of total network stress and the average extensional (blue) and compressive (red) stress on individual filaments for the simulation shown in (B). Rapid buildup of extensional

stress allows the network transiently to exert force on its boundary, but is dissipated at longer times as decreasing extensional stress and increasing compressive stress approach balance.
Figure 4.9 Continued. Note the different time scales used for plots and subplots in C) and D) to emphasize the similar timescales for force buildup, but very different timescales for force dissipation.

During the rapid initial contraction, the increase in network strain closely matched the increase in mean compressive strain on individual filaments Fig. 4.7B, as predicted theoretically (Lenz et al., 2012; Lenz, 2014) and observed experimentally (Murrell and Gardel, 2012). Contraction required asymmetric filament compliance and spatial heterogeneity of motor activity($\mu_e/\mu_c > 1$, $\phi < 1$, Fig. 4.8). Thus our model captures a minimal mechanism for bulk contractility in disordered networks through asymmetric filament compliance and dispersion of motor activity. However, in the absence of turnover, contraction is limited by internal buildup of compressive resistance and the dissipative effects of polarity sorting.

Active networks cannot sustain stress against a fixed boundary in the absence of filament turnover. During cortical flow, regions with high motor activity contract against a passive resistance from neighboring regions with lower motor activity. To understand how the active stresses that drive cortical flow are shaped by motor activity and network remodeling, we analyzed the buildup and maintenance of contractile stress in active networks contracting against a rigid boundary. We simulated active networks contracting from an initially unstressed state against a fixed boundary (Fig. 4.9A,B), and monitored the time evolution of mean extensional (blue), compressional (red) and total (black) stress on network filaments (Fig. 4.9C,D). We focused initially on the scenario in which there is no, or very slow, filament turnover, sampling a range of parameter values controlling filament length and density, motor activity, and crosslink drag.

We observed a similar behavior in all cases: total stress built rapidly to a peak value σ_m, and then decayed towards zero (Fig. 4.9C,D). The rapid initial increase in total stress was determined largely by the rapid buildup of extensional stress (Fig. 4.9C,D) on a subset of network filaments (Fig. 4.9A,B t = 10 s). The subsequent decay involved two different forms of local remodeling: under some conditions, e.g. for higher motor activity (e.g. Fig. 4.9A,C), the decay was associated with rapid local tearing and fragmentation, leading to global loss of network connectivity as described previously both in simulations (Mak et al., 2016) and in vitro experiments (Alvarado et al., 2013). However, for many parameters, (e.g. for higher motor activity as in Fig. 4.9B,D), the decay in stress occurred with little or no loss of global connectivity. Instead, local filament rearrangements changed the balance of extensile versus compressive forces along individual filaments, leading to a slow decrease in the average extensional stress, and a correspondingly slow increase in the compressional stress, on individual filaments (see Fig. 4.9D).

Combining dimensional analysis with trial and error, we were able to find empirical scaling relationships describing the dependence of maximum stress σ_m and the time to reach maximum stress, τ_m, on network parameters and effective crosslink drag ($\sigma_m \sim \sqrt{\mu_e \nu}/l_c$, $\tau_m \sim L\xi/\sqrt{\mu_e \nu}$, Fig. 4.8C,D). Although these relationships should be taken with a grain of salt, they are reasonably consistent with our simple intuition that the peak stress should increase with motor force (ν), extensional modulus (μ_e) and filament density ($1/l_c$), and that the time to reach peak stress should increase with crosslink drag (ξ) and decrease with motor force (ν) and extensional modulus (μ_e).

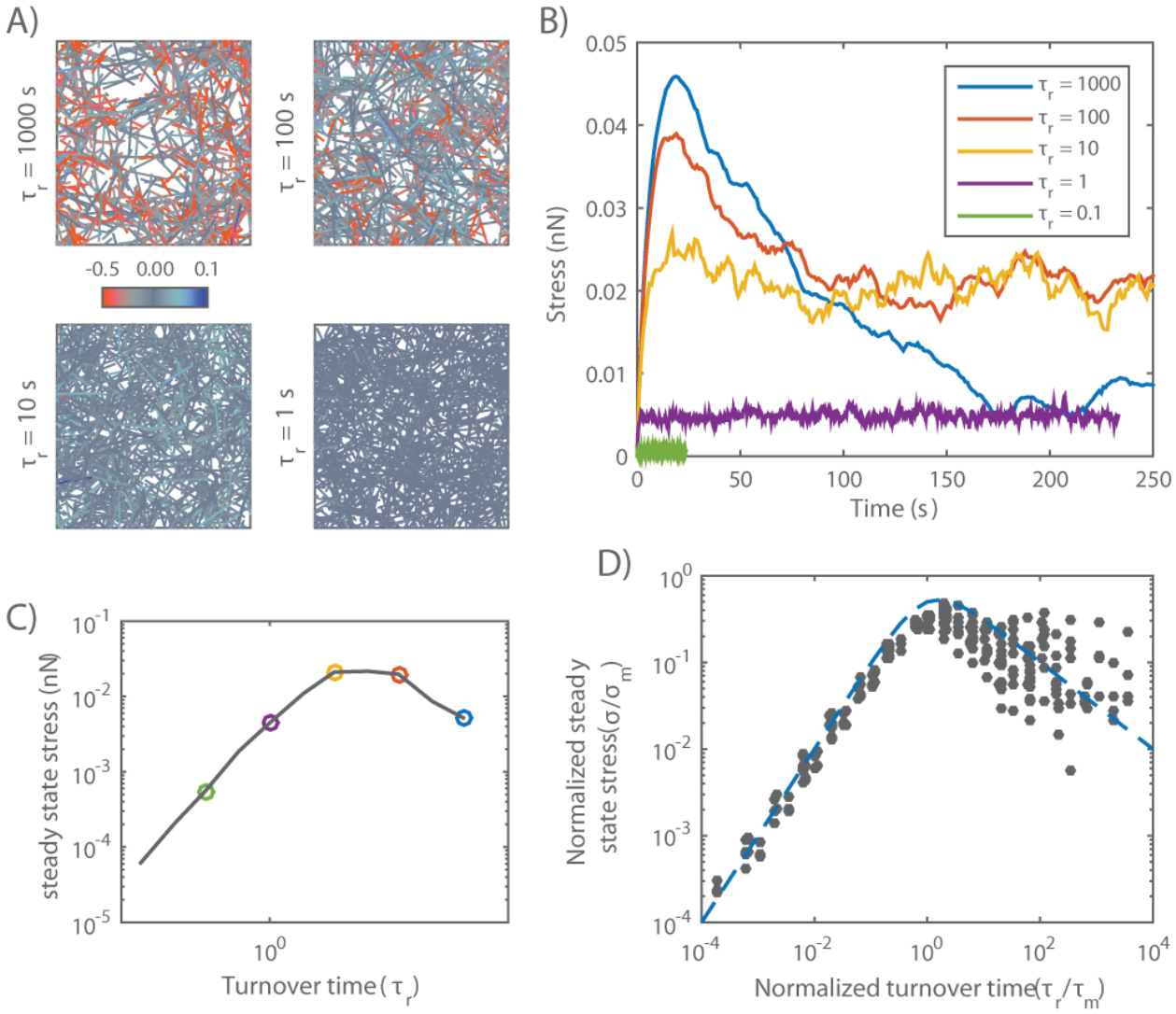

Figure 4.10. Filament turnover allows active networks to exert sustained stress on a fixed boundary. A) Snapshots from simulations of active networks with fixed boundaries and different rates of filament turnover. All other parameter values are the same as in Fig. 4.9A. Note the significant buildup of compressive strain and significant remodeling for longer, but not shorter, turnover times. B) Plots of net stress exerted by the network on its boundaries for different recycling times; for long-lived filaments, stress is built rapidly, but then dissipates. Decreasing filament lifetimes reduces stress dissipation by replacing compressed with uncompressed filaments, allowing higher levels of steady state stress; for very short lifetimes, stress is reduced, because individual filaments do not have time to build stress before turning over. C) Plot of steady state stress estimated from the simulations in (B) versus turnover time. D) Plot of normalized steady state stress versus normalized recycling time for a wide range of network parameters and turnover times. Steady state stress is normalized by the predicted maximum stress σ_m achieved in the absence of filament turnover. Turnover time is normalized by the predicted time to achieve maximum stress τ_m, in the absence of filament turnover.

Figure 4.10 Continued. Predictions for σ_m and τ_m were obtained from the phenomenological scaling relations shown in (Fig. 4.8C,D). Dashed blue line indicates the approximation given in equation 10 for $n = 1$.

Filament turnover allows active networks to exert sustained stress on a fixed boundary.

Regardless of the exact scaling dependencies of σ_m and τ_m on network parameters, these results reveal a fundamental limit on the ability of active networks to sustain force against an external resistance in the absence of filament turnover. To understand how this limit can be overcome by filament turnover, we simulated networks contracting against a fixed boundary from an initially unstressed state, for increasing rates of filament turnover (decreasing τ_r), while holding all other parameter values fixed (Fig. 4.10A-C). While the peak stress decreased monotonically with decreasing τ_r, the steady state stress showed a biphasic response, increasing initially with decreasing τ_r, and then falling off as $\tau_r \to 0$. We observed a biphasic response regardless of how stress decays in the absence of turnover, i.e. whether decay involves loss of network connectivity, or local remodeling without loss of connectivity, or both (Fig. 4.11 and data not shown). Significantly, when we plot normalized steady state stress (σ/σ_m) versus normalized turnover time (τ_r/τ_m) for a wide range of network parameters, the data collapse onto a single biphasic response curve, with a peak near $\tau_r/\tau_m = 1$ (Fig. 4.10D). In particular, for $\tau_r < \tau_m$, the scaled data collapsed tightly onto a single curve representing a linear increase in steady state stress with increasing τ_r. For $\tau_r > \tau_m$, the scaling was less consistent, although the trend towards a monotonic decrease with increasing τ_r was clear. These results reveal that filament turnover can "rescue" the dissipation of active stress during isometric contraction due to network

remodeling, and they show that, for a given choice of network parameters, there is an optimal choice of filament lifetime that maximizes steady state stress.

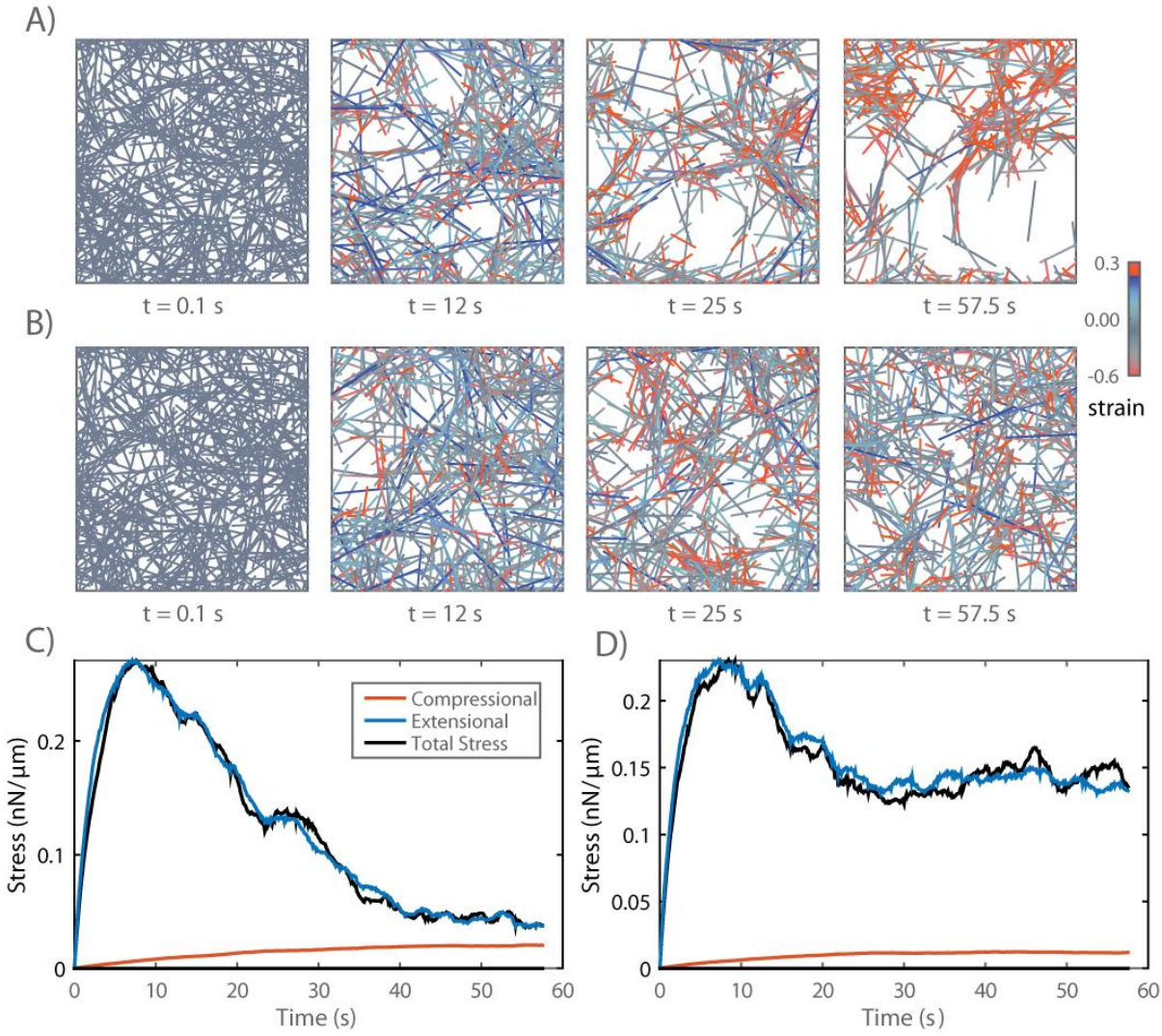

Figure 4.11. Filament turnover prevents tearing of active networks. A) An active network undergoing large scale deformations due to active filament rearrangements. B) The same network as in (A) but with a shorter filament turnover time. C) Plots of internal stress versus time for the network in (A). D) Plots of internal stress versus time for the network in (B).

We can understand the biphasic dependence of steady state stress on filament lifetime using the same reasoning applied to the case of passive flow: during steady state contraction, the

average filament should build and dissipate active stress on approximately the same schedule as an entire network contracting from an initially unstressed state (Fig. 4.10B). Therefore for $\tau_r < \tau_m$, increasing lifetime should increase the mean stress contributed by each filament. For $\tau_r > \tau_m$, further increases in lifetime should begin to reduce the mean stress contribution. Directly comparing the time-dependent buildup and dissipation of stress in the absence of turnover, with the dependence of steady state stress on τ_r, supports this interpretation (Fig. 4.12).

As for the passive response (i.e. Equation 10), we can describe this biphasic dependence phenomenologically with an equation of the form:

$$\sigma_{ss} = \frac{\sigma_m}{\left(\tau_r/\tau_m\right)^n + \tau_m/\tau_r} \tag{10}$$

where the origins of the exponent *n* remain unclear.

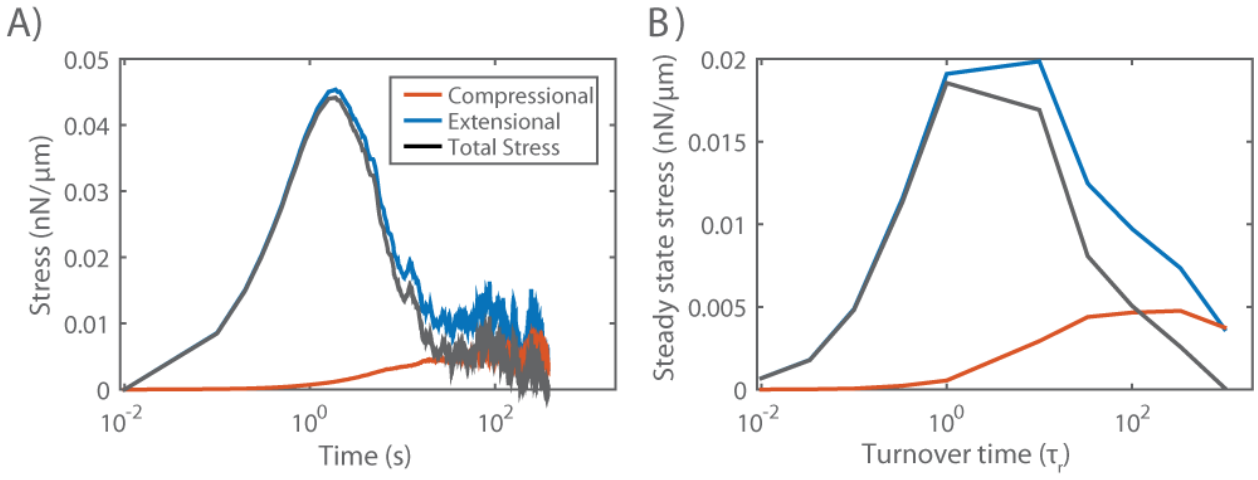

Figure 4.12. Bimodal dependence on turnover time matches bimodal buildup and dissipation of stress in the absence of turnover. A) Bimodal buildup of stress in a network with very slow turnover (τ_r = 1000 s). B) Steady state stress for networks with same parameters as in (A), but for a range of filament turnover times.

Filament turnover tunes the balance between active stress buildup and viscous stress relaxation to generate flows.

Thus far, we have considered independently how network remodeling controls the passive response to an external stress, or the steady state stress produced by active contraction against an external resistance. We now consider how these two forms of dependence will combine to shape steady state flow produced by spatial gradients of motor activity. We consider a simple scenario in which a network is pinned on either side and motor activity is continuously patterned such that the right half network has uniformly high levels of motor activity (controlled by ν, with $\phi = 0.5$), while the left half network has none. Under these conditions, the right half network will contract continuously against a passive resistance from the left half network. Because of asymmetric filament compliance, the internal resistance of the right half network to active compression should be negligible compared to the external resistance of the left half network.

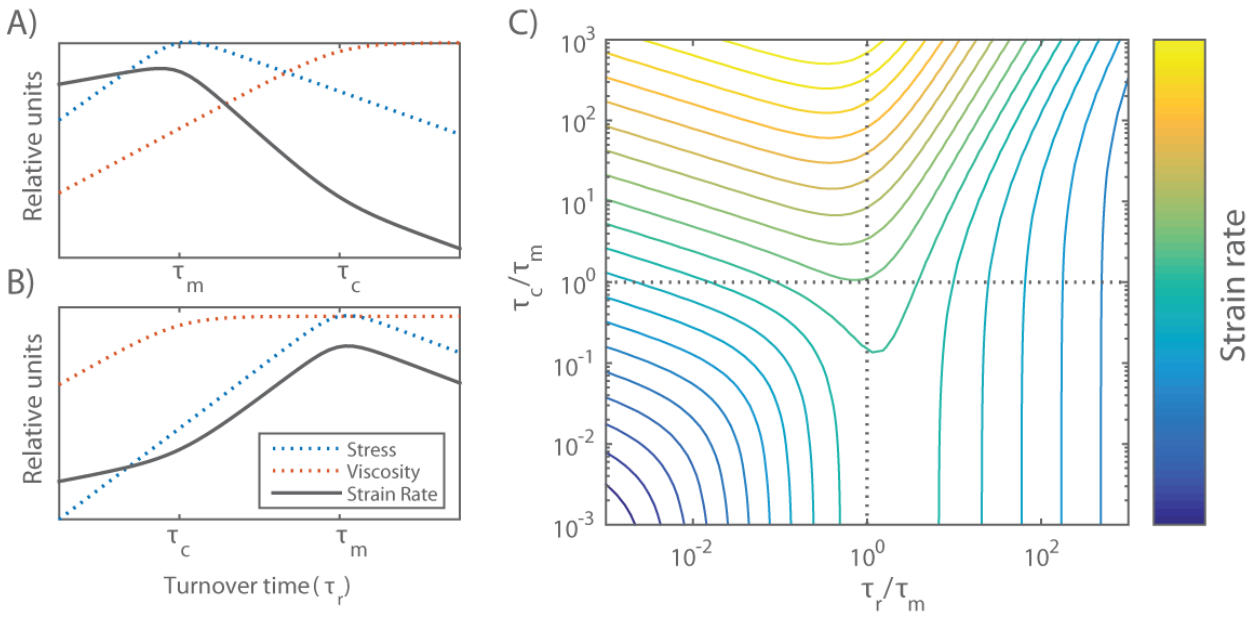

Figure 4.13. Filament turnover tunes the magnitudes of both effective viscosity and steady state stress.

Figure 4.13 Continued. A) Dependence of steady state stress, effective viscosity, and resulting strain rate on recycling time τ_r under the condition $\tau_m < \tau_c$. B) Same as (A) but for $\tau_c < \tau_m$. C) State space of flow rate dependence relative to the two relaxation timescales, τ_r and τ_c normalized by the stress buildup timescale, τ_m.

Thus the steady state flow will be described by:

$$\dot{\gamma} = \frac{\sigma_{ss}}{\eta} \tag{11}$$

where σ_{ss} is the active stress generated by the right half-network (less the internal resistance to filament compression), η is the effective viscosity of the left half network and the strain rate γ is measured in the left half-network.

Note that strain rate can be related to the steady state flow velocity v at the boundary between right and left halves through $v = \dot{\gamma} D_x$. Therefore, we can understand the dependence of flow speed on filament turnover and other parameters using the approximate relationships summarized by equations 9 and 10 for η and σ_{ss}. As shown in Fig. 4.13, there are two qualitatively distinct possibilities for the dependence of strain rate on τ_r, depending on the relative magnitudes of τ_m and τ_c. In both cases, for fast enough turnover ($\tau_r < \min(\tau_m, \tau_c)$), we expect weak dependence of strain rate on τ_r ($\dot{\gamma} \sim \tau_r^{1/4}$). For all parameter values that we sampled in this study (which were chosen to lie in a physiological range), $\tau_m > \tau_c$. Therefore we predict the dependence of steady state strain rate on τ_r shown in Fig. 4.13A.

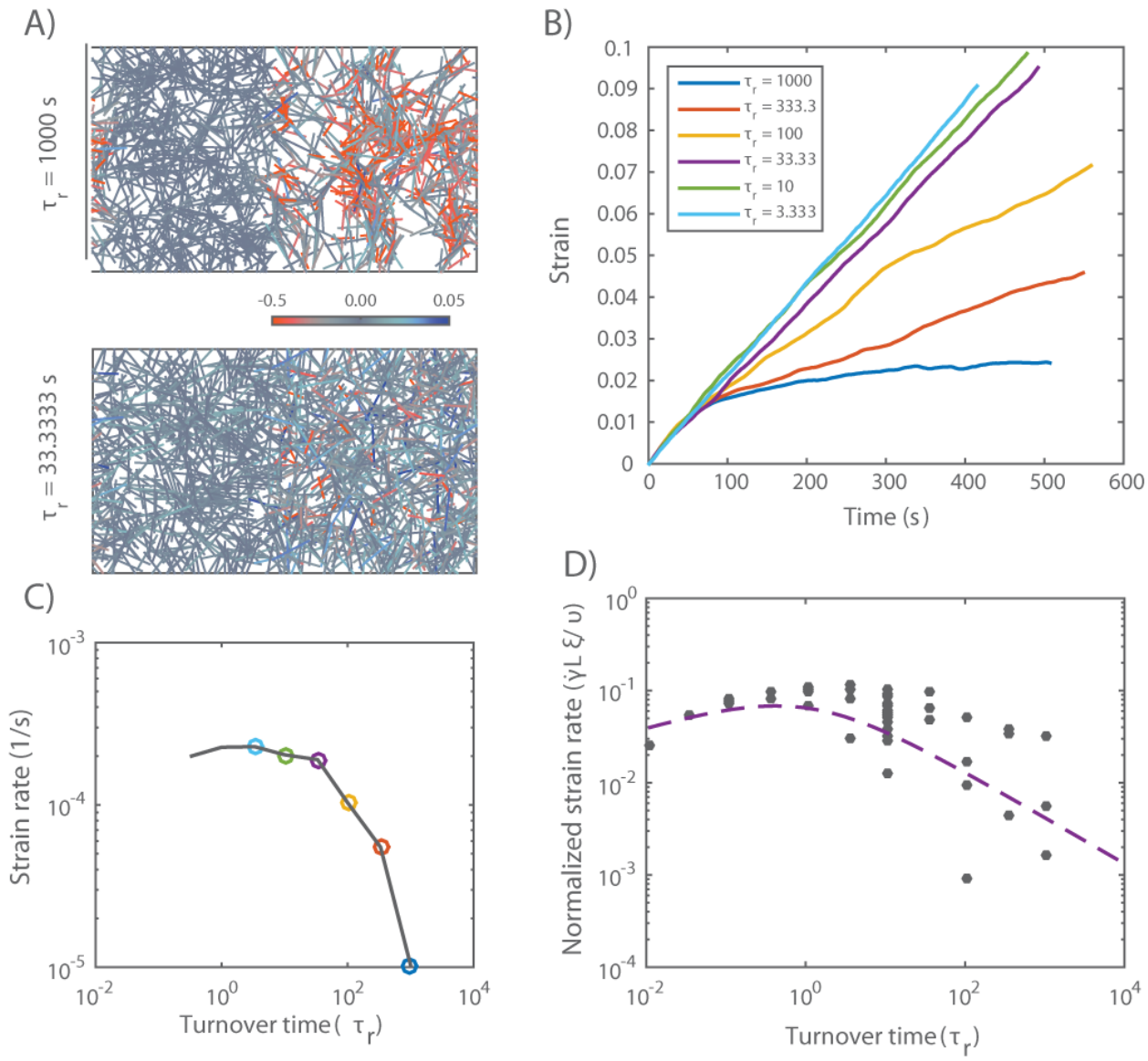

Figure 4.14. Filament recycling allows sustained flows in networks with non-uniform activity. A) Example simulations of non-uniform networks with long (τ_r = 1000) and short (τ_r = 33) turnover timescales. In these networks the left half of the network is passive while the right half is active. Network parameters are same as in Figs. 4.9 and 4.10. Importantly, in all simulations $\tau_m < \tau_c$. B) Graph of strain for identical networks with varying recycling timescales. With long recycling times, the network stalls; reducing the recycling timescale allows the network to persist in its deformation. However, for the shortest recycling timescales, the steady state strain begins to slowly return to zero net motion. Measurements are based on the passive side of the network. C) Steady state strain rates for the networks in (B). D) Graph of network's long-term strain rate as a function of recycling timescale. Dashed line is form of dependence predicted by the theoretical arguments shown in Fig. 4.13.

To confirm this prediction, we simulated the simple scenario described above for a range of values of τ_r, with all other parameter values initially fixed. As expected, we observed a sharp dependence of steady state flow speeds on filament recycling rate (Fig. 4.14B,C). For very long recycling times, (τ_r = 1000 s, dark blue line), there was a rapid initial deformation (contraction of the active domain and dilation of the passive domain), followed by a slow approach to a steady state flow characterized by slow contraction of the right half-domain and a matching dilation of the left half-domain (see Fig. 4.15). However, with decreasing values of τ_r, steady state flow speeds increased steadily, before reaching an approximate plateau on which flow speeds varied by less than 15 % over more than two decades of variation in τ_r (Fig. 4.14C).

We repeated these simulations for a wider range of parameter values, and saw similar dependence of $\dot{\gamma}$ on τ_r in all cases. Using equation 9 with $\tau_r < \tau_c$ and equation 10 with $\tau_r < \tau_m$, and the theoretical or empirical scaling relationships found above for η_c, τ_c, σ_m, and τ_m, we predict from equation 11 a simple scaling relationship for $\dot{\gamma}$ (for small τ_r):

$$\dot{\gamma} = \frac{\nu}{\xi L}\left(\tau_r\right)^{1/4} \tag{12}$$

Indeed, when we plot the steady state measurements of $\dot{\gamma}$, normalized by $\nu/\xi L$, for all parameter values, the data collapse onto a single curve for small τ_r. Thus. our simulations identify a flow regime, characterized by sufficiently fast filament turnover, in which the steady state flow speed is buffered against variation in turnover, and has a relatively simple dependence on other network parameters.

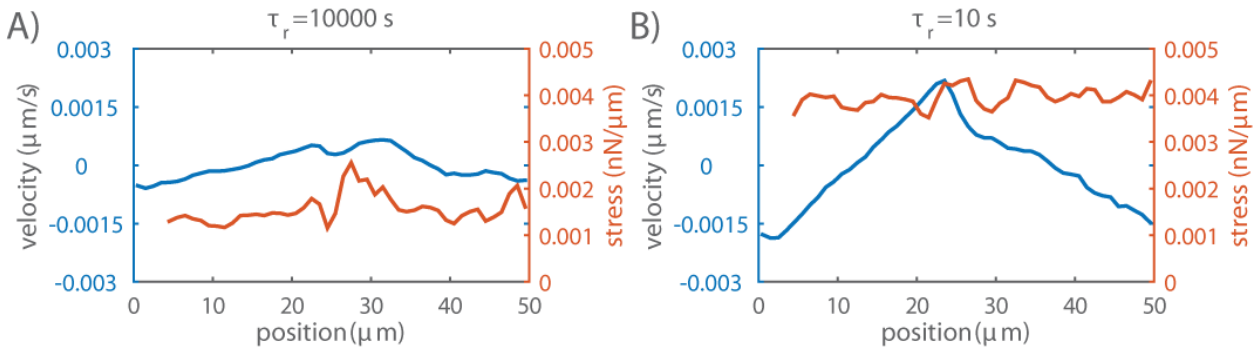

Figure 4.15. Dynamics of steady state flow. Plots of stress and strain versus position for networks in which motor activity is limited to the right-half domain and filament turnover time is either A) τ_r = 10000 s or B) τ_r = 10 s. Blue indicates velocity while orange represents total stress, measured as described in the main text.

Section 4.7 DISCUSSION

Cortical flows are shaped by the dynamic interplay of force production and dissipation within cross-linked actomyosin networks. Here we combined computational models with simple theoretical analyses to explore how this interplay depends on filament turnover, crosslink dynamics and network architecture. Our results reveal an essential requirement for filament turnover during cortical flow, both to sustain active stress and to continuously relax elastic resistance without catastrophic loss of network connectivity. Moreover, we find that biphasic dependencies of active stress and passive relaxation on filament lifetime define multiple regimes for steady state flow with distinct dependencies on network parameters and filament turnover.

We identify two regimes of passive response to external stress: a low turnover regime in which filaments strain to an elastic limit before turning over, and effective viscosity depends on cross-link density and effective crosslink friction, and a high turnover regime in which filaments turn over before reaching an elastic limit and effective viscosity is proportional to elastic resistance and roughly proportional to filament lifetime. Thus our model captures the qualitatively distinct contributions of transient cross-links and filament turnover within a single

self-consistent framework. We note that the weakly sub-linear dependence of effective viscosity on filament lifetime that we observe here may simply reflect a failure to capture very local modes of filament deformation, since a previous study (Kim et al., 2014) in which filaments were represented as connected chains of smaller segments predicted linear dependence of effective viscosity on filament lifetime.

Our simulations of active networks confirm the theoretical prediction (Lenz et al., 2012) that spatial heterogeneity of motor activity and asymmetric filament compliance are sufficient to support macroscopic contraction of unconstrained networks. However, under isometric conditions, and without filament turnover, our simulations predict that active stress cannot be sustained. On short timescales, motor forces drive local buildup of extensional stress, but on longer timescales, local motor-driven filament rearrangements and thus local changes in connectivity, invariably lead to a decay in active stress. Under some conditions, contractile forces drive networks towards a critically connected state, leading to tearing and fragmentation, as previously described (Alvarado et al., 2013; Mak et al., 2016). However, we find that stress decay can also occur without any global loss of connectivity, through a gradual decrease in extensile force and a gradual increase in compressive force along individual filaments. When filaments can slide relative to one another, the motor forces that produce active stress will inevitably lead to local changes in connectivity that decrease active stress. These results suggest that for contractile networks to maintain isometric tension on long timescales, they must either form stable cross-links to prevent filament rearrangements, or they must continuously recycle network filaments (or active motors) to renew the local potential for production of active stress.

Indeed, our simulations predict that filament turnover is sufficient for maintenance of active stress and they predict a biphasic dependence of steady state stress on filament turnover:

For short-lived filaments ($\tau_r < \tau_m$), steady state stress increases linearly with filament lifetime because filaments have more time to build towards peak extensional stress before turning over. For longer loved filaments ($\tau_r > \tau_m$), steady state stress decreases monotonically with filament lifetime because local rearrangements decrease the mean contributions of longer lived filaments. These findings imply that for cortical networks that sustain contractile stress under approximately isometric conditions, tuning filament turnover can control the level of active stress, and there will be an optimal turnover rate that maximizes the stress, all other things equal. This may be important, for example in early development, where contractile forces produced by cortical actomyosin networks play key roles in maintaining, or controlling slow changes in cell shape and tissue geometry (Salbreux et al., 2012; Turlier et al., 2014; Gorfinkiel and Blanchard, 2011).

For cortical networks that undergo steady state flows driven by spatial gradients of motor activity, our simulations predict that the biphasic dependencies of steady state stress and effective viscosity on filament lifetime define multiple regimes of steady state flow, characterized by different dependencies on filament turnover (and other network parameters). In particular, the _linear dependencies of steady state stress and effective viscosity on filament lifetime for short-lived filaments define a fast turnover regime in which steady state flow speeds are buffered against variations in filament lifetime, and are predicted to depend in a simple way on motor activity and crosslink resistance. Measurements of F-actin turnover times in cells that undergo cortical flow (Fritzsche et al., 2013, 2016; Theriot and Mitchison, 1991; Murthy and Wadsworth, 2005; Watanabe and Mitchison, 2002; Guha et al., 2005) suggests that they may indeed operate in this fast turnover regime, and recent studies in *C. elegans* embryos suggests that cortical flow speeds are surprisingly insensitive to depletion of factors (ADF/Cofilin) that

govern filament turnover (Mayer et al., 2010), consistent with our model's predictions. Stronger tests of our model's predictions will require more systematic analyses of how flow speeds vary with filament and crosslink densities, motor activities, and filament lifetimes.

Section 4.8 ACKNOWLEDGEMENTS

We would like to thank Shiladitya Banerjee for stimulating discussions. This research was supported by the University of Chicago Materials Research Science and Engineering Center (National Science Foundation Division of Materials Research Grant 1420709).

Section 4.9 APPENDIX

4.9.1 Simulation and Analysis Code Available Online

All of the simulation and analysis code for generating the figures in this paper is available online. To find the source code please visit our Github repository at

https://github.com/wmcfadden/activnet

4.9.2 Steady-state Approximation of Effective Viscosity

We begin with a calculation of a strain rate estimate of the effective viscosity for a network described by our model in the limit of highly rigid filaments. We carry this out by assuming we have applied a constant stress along a transect of the network. With moderate stresses, we assume the network reaches a steady state affine creep. In this situation, we would find that the stress in the network exactly balances the sum of the drag-like forces from cross-link slip. So for any transect of length D, we have a force balance equation:

$$\sigma = \frac{1}{D} \sum_{\text{filaments}} \sum_{\text{crosslinks}} \xi \left(\mathrm{v_i(x)} - \mathrm{v_j(x)} \right) \tag{13}$$

where $\mathrm{v_i(x)} - \mathrm{v_j(x)}$ is the difference between the velocities of filaments i and j, which are connected by a cross-link at position x. We can convert the sum over cross-links to an integral over the length using the average density of cross-links, $1/l_c$, and invoking the assumption of (linear order) affine strain rate, $\mathrm{v_i(x)} - \mathrm{v_j(x)} \approx \dot{\gamma} x$. This results in

$$\begin{aligned} \sigma &= \frac{1}{D} \sum_{\text{filaments}} \int_0^L \xi \left(\mathrm{v_i(s)} - \mathrm{v_j(s)} \right) \frac{ds \cos\theta}{l_c} \\ &= \frac{1}{D} \sum_{\text{filaments}} \frac{\xi \dot{\gamma} L}{l_c} \cos\theta \cdot \left(x_l + \frac{L}{2} \cos\theta \right) \end{aligned} \tag{14}$$

Here we have introduced the variables x_l and θ to describe the leftmost endpoint and the angular orientation of a given filament respectively. Next, to perform the sum over all filaments, we convert this to an integral over all orientations and endpoints that intersect our line of stress. We assume for simplicity that filament stretch and filament alignment are negligible in this low strain approximation. Therefore, the max distance for the leftmost endpoint is the length of a filament, L, and the maximum angle as a function of endpoint is $\arccos\left(x_l / L\right)$. The linear density of endpoints is the constant D/Ll_c, so our integrals can be rewritten as this density over x_l and θ between our maximum and minimum allowed bounds:

$$\sigma = \frac{1}{D} \int_0^L dx_l \int_{-\arccos(x_l/L)}^{\arccos(x_l/L)} \pi d\theta \frac{\xi \dot{\gamma} L}{l_c} \cdot \frac{D}{L l_c} \left(x_l \cos\theta + \frac{L}{2} \cos^2\theta \right) \tag{15}$$

Carrying out the integrals and correcting for dangling filament ends leaves us with a relation between stress and strain rate:

$$\sigma = 4\pi\left(\frac{L}{l_c} - 1\right)^2 \xi\dot{\gamma} \tag{16}$$

We recognize the constant of proportionality between stress and strain rate as a viscosity (in 2 dimensions). Therefore, our approximation for the effective viscosity, η_c, at steady state creep in this low strain limit is

$$\eta_c = 4\pi\left(\frac{L}{l_c} - 1\right)^2 \xi \tag{17}$$

4.9.3 Critical filament lifetime for steady state filament extension

We seek to demonstrate the existence of a critical filament lifetime, τ_{crit}, below which the density of filaments approaches a stable steady state under constant extensional strain. To this end, let ρ be the filament density (i.e. number of filaments per unit area). We consider a simple coarse-grained model for how ρ changes as a function of filament assembly at rate k_{ass}, filament disassembly at rate $k_{\text{diss}}\rho$, and flow $\dot{\gamma}\rho$, namely

$$\frac{d\rho}{dt} = k_{\text{ass}} - k_{\text{diss}}\rho - \dot{\gamma}\rho \ . \tag{18}$$

Using $\rho_0 = k_{\text{ass}}/k_{\text{diss}}$, $\tau_{\text{r}} = 1/k_{\text{diss}}$, and $\dot{\gamma} = \sigma/\eta_c$, equation (18) can be re-written as

$$\frac{d\rho}{dt} = \frac{1}{\tau_{\text{r}}}\left(\rho_0 - \rho - \frac{\sigma\tau_{\text{r}}}{\eta_c(\rho)}\rho\right) \tag{19}$$

where $\eta_c = \eta_c(\rho)$ on the right hand side reflects the dependence of effective viscosity on network density. The strength of this dependence determines whether there exists a stable steady

state, representing continuous flow. Using $\eta_c(\rho) \sim \xi\left(L/l_c(\rho)-1\right)^2$ from above (ignoring the numerical prefactor) $\rho \sim 2/Ll_c$, we obtain:

$$\frac{d\rho}{dt} = \frac{1}{\tau_r}\left(\rho_0 - \rho - \frac{\sigma\tau_r}{\xi\left(\rho L^2/2-1\right)^2}\rho\right). \tag{20}$$

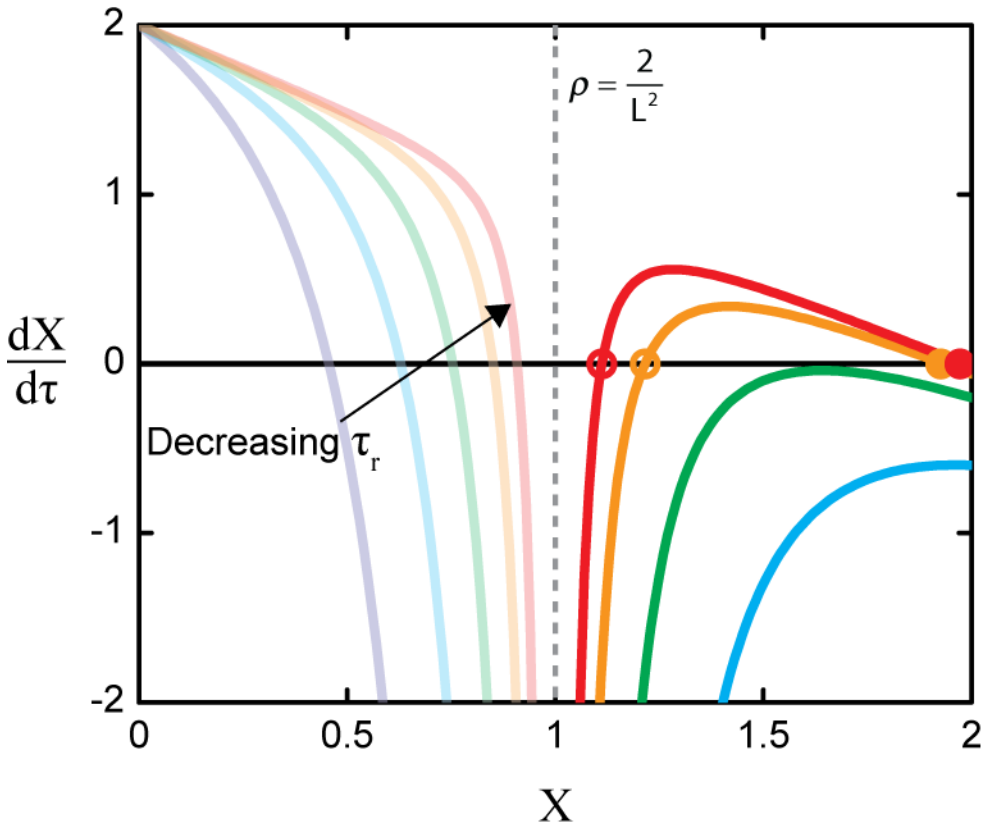

Figure 4.16. Flux balance analysis of network density. Phase portraits of the first order ODE describing the time evolution of the normalized density, $dX/d\tau = X_0 - X - AX/\left(X-1\right)^2$, where $X \equiv \rho L^2/2$, $\tau \equiv t/\tau_r$, $X_0 \equiv \rho_0 L^2/2$, and $A \equiv \sigma\tau_r/\xi$ for different values of τ_r. Cool colors correspond to large τ_r, while warm colors correspond to small τ_r. Fixed points corresponding to steady-state densities are represented by zero crossings ($dX/d\tau = 0$). Open and closed circles represent unstable and stable fixed points, respectively. The dashed line at $X = 1$ corresponds to the filament overlap concentration. Since densities below this are not fully connected, and therefore cannot transmit stress, we ignore fixed points in this region.

Figure 4.16 Continued. For sufficiently large τ_r, there are no crossings (cyan, green). For $\tau_r < \tau_{crit}$, there are two crossings (orange, red): the rightmost crossing represents a stable steady state.

Defining the a normalized density $X \equiv \rho L^2 / 2$, normalized time $\tau \equiv t / \tau_r$, normalized filament lifetime $A \equiv \sigma \tau_r / \xi$, and parameter $X_0 \equiv \rho_0 L^2 / 2$, equation (20) can be rewritten

$$\frac{dX}{d\tau} = X_0 - X - \frac{AX}{(X-1)^2} \quad . \tag{21}$$

Fig. 4.16 plots phase portraits of equation 21 (the right-hand-side versus *X*) for several values of the normalized filament lifetime, *A*. For sufficiently large *A*, there is no stable state, i.e. flow will reduce density until connectivity is lost. However, as *A* decreases below a critical value, A_{crit}, a stable steady state appears. Note that when $A = A_{crit}$, the $dX/d\tau$ curve is tangent to the *X*-axis at *X**. Accordingly, to determine *X**, we solve

$$0 = \frac{d}{dX}\left(X_0 - X - \frac{AX}{(X-1)^2} \right) = -1 - \frac{A}{(X-1)^2} + \frac{2AX}{(X-1)^3} \quad . \tag{22}$$

After a little algebra, this can be recast as the following cubic polynomial

$$0 = X^3 - 3X^2 + (3-A)X - (A+1) \tag{23}$$

which has a single real positive root

$$X^* = 1 + A^{1/3}\left[\left(1 + \sqrt{1 - A/27}\right)^{1/3} + \left(1 - \sqrt{1 - A/27}\right)^{1/3} \right] . \tag{24}$$

Note that a purely real *X** exists for all *A* > 0, even for *A* > 27, because the imaginary components from the two radicals cancel exactly.

In principle, A_{crit} is determined by setting equation 22 equal to zero, $X = X^*$, and solving for *A*. Unfortunately, the complicated form of *X** makes this extremely challenging to do

analytically. However, it is straight-forward to determine A_{crit} to high precision computationally from equations 21 and 24, for any $X_0 > 1$, for instance by plotting the right-hand-side of equation 21 as a function of *A*, with *X* determined by equation 24, and looking for the x-intercept of the resulting plot (there is only one).

Section 4.10 REFERENCES

Alvarado, J., Sheinman, M., Sharma, A., MacKintosh, F.C., and Koenderink, G.H. (2013). Molecular motors robustly drive active gels to a critically connected state. Nat. Phys. *9*, 591–597.

Banerjee, S., Marchetti, M.C., and Müller-Nedebock, K. (2011). Motor-driven dynamics of cytoskeletal filaments in motility assays. Phys. Rev. E *84*, 011914.

Bausch, A.R., Ziemann, F., Boulbitch, A.A., Jacobson, K., and Sackmann, E. (1998). Local Measurements of Viscoelastic Parameters of Adherent Cell Surfaces by Magnetic Bead Microrheometry. Biophys. J. *75*, 2038–2049.

Behrndt, M., Salbreux, G., Campinho, P., Hauschild, R., Oswald, F., Roensch, J., Grill, S.W., and Heisenberg, C.-P. (2012). Forces Driving Epithelial Spreading in Zebrafish Gastrulation. Science *338*, 257–260.

Bendix, P.M., Koenderink, G.H., Cuvelier, D., Dogic, Z., Koeleman, B.N., Brieher, W.M., Field, C.M., Mahadevan, L., and Weitz, D.A. (2008). A Quantitative Analysis of Contractility in Active Cytoskeletal Protein Networks. Biophys. J. *94*, 3126–3136.

Benink, H.A., Mandato, C.A., and Bement, W.M. (2000). Analysis of Cortical Flow Models In Vivo. Mol. Biol. Cell *11*, 2553–2563.

Bois, J.S., Jülicher, F., and Grill, S.W. (2011). Pattern Formation in Active Fluids. Phys. Rev. Lett. *106*, 028103.

Bray, D., and White, J.G. (1988). Cortical flow in animal cells. Science *239*, 883–888.

Broedersz, C.P., Storm, C., and MacKintosh, F.C. (2009). Effective-medium approach for stiff polymer networks with flexible cross-links. Phys. Rev. E *79*, 061914.

Broedersz, C.P., Depken, M., Yao, N.Y., Pollak, M.R., Weitz, D.A., and MacKintosh, F.C. (2010). Cross-Link-Governed Dynamics of Biopolymer Networks. Phys. Rev. Lett. *105*, 238101.

Carlsson, A.E. (2010). Actin Dynamics: From Nanoscale to Microscale. Annu. Rev. Biophys. *39*, 91–110.

Chandran, P.L., and Mofrad, M.R.K. (2010). Averaged implicit hydrodynamic model of semiflexible filaments. Phys. Rev. E *81*, 031920.

Chugh, P., Clark, A.G., Smith, M.B., Cassani, D.A.D., Charras, G., Salbreux, G., and Paluch, E.K. (2016). Nanoscale Organization of the Actomyosin Cortex during the Cell Cycle. Biophys. J. *110*, 198a.

De La Cruz, E.M. (2009). How cofilin severs an actin filament. Biophys. Rev. *1*, 51–59.

De La Cruz, E.M., and Gardel, M.L. (2015). Actin mechanics and fragmentation. J. Biol. Chem. jbc.R115.636472.

Dierkes, K., Sumi, A., Solon, J., and Salbreux, G. (2014). Spontaneous Oscillations of Elastic Contractile Materials with Turnover. Phys. Rev. Lett. *113*, 148102.

Ennomani, H., Letort, G., Guérin, C., Martiel, J.-L., Cao, W., Nédélec, F., De La Cruz, E.M., Théry, M., and Blanchoin, L. (2016). Architecture and Connectivity Govern Actin Network Contractility. Curr. Biol. *26*, 616–626.

Evans, E., and Yeung, A. (1989). Apparent viscosity and cortical tension of blood granulocytes determined by micropipet aspiration. Biophys. J. *56*, 151–160.

Filippov, A.E., Klafter, J., and Urbakh, M. (2004). Friction through Dynamical Formation and Rupture of Molecular Bonds. Phys. Rev. Lett. *92*, 135503.

Fritzsche, M., Lewalle, A., Duke, T., Kruse, K., and Charras, G. (2013). Analysis of turnover dynamics of the submembranous actin cortex. Mol. Biol. Cell *24*, 757–767.

Fritzsche, M., Erlenkämper, C., Moeendarbary, E., Charras, G., and Kruse, K. (2016). Actin kinetics shapes cortical network structure and mechanics. Sci. Adv. *2*, e1501337.

Goor, D.V., Hyland, C., Schaefer, A.W., and Forscher, P. (2012). The Role of Actin Turnover in Retrograde Actin Network Flow in Neuronal Growth Cones. PLOS ONE *7*, e30959.

Gorfinkiel, N., and Blanchard, G.B. (2011). Dynamics of actomyosin contractile activity during epithelial morphogenesis. Curr. Opin. Cell Biol. *23*, 531–539.

Guha, M., Zhou, M., and Wang, Y. (2005). Cortical Actin Turnover during Cytokinesis Requires Myosin II. Curr. Biol. *15*, 732–736.

Head, D.A., Levine, A.J., and MacKintosh, F.C. (2003). Deformation of Cross-Linked Semiflexible Polymer Networks. Phys. Rev. Lett. *91*, 108102.

Hiraiwa, T., and Salbreux, G. (2016). Role of Turnover in Active Stress Generation in a Filament Network. Phys. Rev. Lett. *116*, 188101.

Hird, S.N., and White, J.G. (1993). Cortical and cytoplasmic flow polarity in early embryonic cells of Caenorhabditis elegans. J. Cell Biol. *121*, 1343–1355.

Hochmuth, R.M. (2000). Micropipette aspiration of living cells. J. Biomech. *33*, 15–22.

Howard, J. (2001). Mechanics of Motor Proteins and the Cytoskeleton (Sunderland, MA: Sinauer Associates).

Janson, L.W., Kolega, J., and Taylor, D.L. (1991). Modulation of contraction by gelation/solation in a reconstituted motile model. J. Cell Biol. *114*, 1005–1015.

Keren, K., Yam, P.T., Kinkhabwala, A., Mogilner, A., and Theriot, J.A. (2009). Intracellular fluid flow in rapidly moving cells. Nat. Cell Biol. *11*, 1219–1224.

Kim, T., Hwang, W., and Kamm, R.D. (2011). Dynamic Role of Cross-Linking Proteins in Actin Rheology. Biophys. J. *101*, 1597–1603.

Kim, T., Gardel, M.L., and Munro, E. (2014). Determinants of Fluidlike Behavior and Effective Viscosity in Cross-Linked Actin Networks. Biophys. J. *106*, 526–534.

Koenderink, G.H., Dogic, Z., Nakamura, F., Bendix, P.M., MacKintosh, F.C., Hartwig, J.H., Stossel, T.P., and Weitz, D.A. (2009). An active biopolymer network controlled by molecular motors. Proc. Natl. Acad. Sci. *106*, 15192–15197.

Lai, F.P., Szczodrak, M., Block, J., Faix, J., Breitsprecher, D., Mannherz, H.G., Stradal, T.E., Dunn, G.A., Small, J.V., and Rottner, K. (2008). Arp2/3 complex interactions and actin network turnover in lamellipodia. EMBO J. *27*, 982–992.

Leibler, S., and Huse, D.A. (1993). Porters versus rowers: a unified stochastic model of motor proteins. J. Cell Biol. *121*, 1357–1368.

Lenz, M. (2014). Geometrical Origins of Contractility in Disordered Actomyosin Networks. Phys. Rev. X *4*, 041002.

Lenz, M., Gardel, M.L., and Dinner, A.R. (2012). Requirements for contractility in disordered cytoskeletal bundles. New J. Phys. *14*, 033037.

Lieleg, O., and Bausch, A.R. (2007). Cross-Linker Unbinding and Self-Similarity in Bundled Cytoskeletal Networks. Phys. Rev. Lett. *99*, 158105.

Lieleg, O., Claessens, M.M.A.E., Luan, Y., and Bausch, A.R. (2008). Transient Binding and Dissipation in Cross-Linked Actin Networks. Phys. Rev. Lett. *101*, 108101.

Lieleg, O., Schmoller, K.M., Claessens, M.M.A.E., and Bausch, A.R. (2009). Cytoskeletal Polymer Networks: Viscoelastic Properties are Determined by the Microscopic Interaction Potential of Cross-links. Biophys. J. *96*, 4725–4732.

Liu, J., Koenderink, G.H., Kasza, K.E., MacKintosh, F.C., and Weitz, D.A. (2007). Visualizing the Strain Field in Semiflexible Polymer Networks: Strain Fluctuations and Nonlinear Rheology of F-Actin Gels. Phys. Rev. Lett. *98*, 198304.

Mak, M., Zaman, M.H., Kamm, R.D., and Kim, T. (2016). Interplay of active processes modulates tension and drives phase transition in self-renewing, motor-driven cytoskeletal networks. Nat. Commun. *7*, 10323.

Marchetti, M.C., Joanny, J.F., Ramaswamy, S., Liverpool, T.B., Prost, J., Rao, M., and Simha, R.A. (2013). Hydrodynamics of soft active matter. Rev. Mod. Phys. *85*, 1143–1189.

Mayer, M., Depken, M., Bois, J.S., Jülicher, F., and Grill, S.W. (2010). Anisotropies in cortical tension reveal the physical basis of polarizing cortical flows. Nature *467*, 617–621.

McCrum, N.G., Buckley, C.P., and Bucknall, C.B. (1997). Principles of Polymer Engineering (New York, NY: Oxford University Press).

McFadden, W.M., McCall, P.M., and Munro, E.M. (2016). Filament turnover is essential for continuous long range contractile flow in a model actomyosin cortex. ArXiv161207430 Cond-Mat Physicsphysics Q-Bio.

Müller, K.W., Bruinsma, R.F., Lieleg, O., Bausch, A.R., Wall, W.A., and Levine, A.J. (2014). Rheology of Semiflexible Bundle Networks with Transient Linkers. Phys. Rev. Lett. *112*, 238102.

Munro, E., Nance, J., and Priess, J.R. (2004). Cortical Flows Powered by Asymmetrical Contraction Transport PAR Proteins to Establish and Maintain Anterior-Posterior Polarity in the Early C. elegans Embryo. Dev. Cell *7*, 413–424.

Murrell, M., and Gardel, M.L. (2014). Actomyosin sliding is attenuated in contractile biomimetic cortices. Mol. Biol. Cell *25*, 1845–1853.

Murrell, M.P., and Gardel, M.L. (2012). F-actin buckling coordinates contractility and severing in a biomimetic actomyosin cortex. Proc. Natl. Acad. Sci. *109*, 20820–20825.

Murrell, M., Oakes, P.W., Lenz, M., and Gardel, M.L. (2015). Forcing cells into shape: the mechanics of actomyosin contractility. Nat. Rev. Mol. Cell Biol. *16*, 486–498.

Murthy, K., and Wadsworth, P. (2005). Myosin-II-Dependent Localization and Dynamics of F-Actin during Cytokinesis. Curr. Biol. *15*, 724–731.

Nedelec, F.J., Surrey, T., Maggs, A.C., and Leibler, S. (1997). Self-organization of microtubules and motors. Nature *389*, 305–308.

Rauzi, M., Lenne, P.-F., and Lecuit, T. (2010). Planar polarized actomyosin contractile flows control epithelial junction remodelling. Nature *468*, 1110–1114.

Reymann, A.-C., Boujemaa-Paterski, R., Martiel, J.-L., Guérin, C., Cao, W., Chin, H.F., Cruz, E.M.D.L., Théry, M., and Blanchoin, L. (2012). Actin Network Architecture Can Determine Myosin Motor Activity. Science *336*, 1310–1314.

Robin, F.B., McFadden, W.M., Yao, B., and Munro, E.M. (2014). Single-molecule analysis of cell surface dynamics in Caenorhabditis elegans embryos. Nat. Methods *11*, 677–682.

Salbreux, G., Prost, J., and Joanny, J.F. (2009). Hydrodynamics of Cellular Cortical Flows and the Formation of Contractile Rings. Phys. Rev. Lett. *103*, 058102.

Salbreux, G., Charras, G., and Paluch, E. (2012). Actin cortex mechanics and cellular morphogenesis. Trends Cell Biol. *22*, 536–545.

Sanchez, T., Chen, D.T.N., DeCamp, S.J., Heymann, M., and Dogic, Z. (2012). Spontaneous motion in hierarchically assembled active matter. Nature *491*, 431–434.

Schoenberg, M. (1985). Equilibrium muscle cross-bridge behavior. Theoretical considerations. Biophys. J. *48*, 467–475.

Spruijt, E., Sprakel, J., Lemmers, M., Stuart, M.A.C., and van der Gucht, J. (2010). Relaxation Dynamics at Different Time Scales in Electrostatic Complexes: Time-Salt Superposition. Phys. Rev. Lett. *105*, 208301.

Surrey, T., Nédélec, F., Leibler, S., and Karsenti, E. (2001). Physical Properties Determining Self-Organization of Motors and Microtubules. Science *292*, 1167–1171.

Tawada, K., and Sekimoto, K. (1991). Protein friction exerted by motor enzymes through a weak-binding interaction. J. Theor. Biol. *150*, 193–200.

Theriot, J.A., and Mitchison, T.J. (1991). Actin microfilament dynamics in locomoting cells. Nature *352*, 126–131.

Turlier, H., Audoly, B., Prost, J., and Joanny, J.-F. (2014). Furrow Constriction in Animal Cell Cytokinesis. Biophys. J. *106*, 114–123.

Unterberger, M.J., and Holzapfel, G.A. (2014). Advances in the mechanical modeling of filamentous actin and its cross-linked networks on multiple scales. Biomech. Model. Mechanobiol. *13*, 1155–1174.

Vanossi, A., Manini, N., Urbakh, M., Zapperi, S., and Tosatti, E. (2013). Colloquium: Modeling friction: From nanoscale to mesoscale. Rev. Mod. Phys. *85*, 529–552.

Wachsstock, D.H., Schwarz, W.H., and Pollard, T.D. (1994). Cross-linker dynamics determine the mechanical properties of actin gels. Biophys. J. *66*, 801–809.

Ward, A., Hilitski, F., Schwenger, W., Welch, D., Lau, A.W.C., Vitelli, V., Mahadevan, L., and Dogic, Z. (2015). Solid friction between soft filaments. Nat. Mater. *14*, 583–588.

Watanabe, N., and Mitchison, T.J. (2002). Single-Molecule Speckle Analysis of Actin Filament Turnover in Lamellipodia. Science *295*, 1083–1086.

Wilson, C.A., Tsuchida, M.A., Allen, G.M., Barnhart, E.L., Applegate, K.T., Yam, P.T., Ji, L., Keren, K., Danuser, G., and Theriot, J.A. (2010). Myosin II contributes to cell-scale actin network treadmilling through network disassembly. Nature *465*, 373–377.

Yao, N.Y., Becker, D.J., Broedersz, C.P., Depken, M., MacKintosh, F.C., Pollak, M.R., and Weitz, D.A. (2011). Nonlinear Viscoelasticity of Actin Transiently Cross-linked with Mutant α-Actinin-4. J. Mol. Biol. *411*, 1062–1071.

Zumdieck, A., Kruse, K., Bringmann, H., Hyman, A.A., and Jülicher, F. (2007). Stress Generation and Filament Turnover during Actin Ring Constriction. PLOS ONE *2*, e696.

CHAPTER 5: PARTITIONING AND ENHANCED SELF-ASSEMBLY OF ACTIN IN POLYPEPTIDE COACERVATES

Section 5.1 PREFACE

The content of Chapter 5 is from a draft of the manuscript McCall, P.M.*, Srivastava, S.*, Perry, S.L., Kovar, D.R., Gardel, M.L., and Tirrell, M.V. (2017). Partitioning and Enhanced Self-Assembly of Actin in Polypeptide Coacervates. bioRxiv 152025. This material is the result of a collaboration between the laboratories of Prof. Matthew Tirrell, Prof. Margaret Gardel, and Prof. David Kovar at the University of Chicago, and which now receives support from the University of Chicago Materials Research Science and Engineering Center (MRSEC). The collaboration was founded by Dr. Sarah Perry (then a postdoctoral researcher in the Tirrell laboratory) and Prof. Gardel, aiming to examine actin assembly reactions in the crowded biomimetic interior of liquid coacervate droplets. Dr. Perry and I designed and performed preliminary microscopy and kinetic studies together; she contributed the polypeptide reagents used to form the coacervates (with support from the Tirrell lab) and coacervate expertise, while I provided experimental expertise in microscopy, kinetics, and actin biochemistry. Profs. Gardel and Kovar provided equipment, suggestions, and support. Actins used in the studies were purified variously by the Kovar laboratory and by Dr. Kimberley Weirich in the Gardel laboratory. Glass coverslips treated with polyethylene-glycol-silane (PEG-silane), which were a crucial reagent for the microscopy experiments, were provided by the Kovar laboratory. The idea to add BSA and actin simultaneously, as well as the idea to image actin below the critical concentration for actin assembly (which is now a central point in Fig. 5.8), came from discussions with Dr. Cristian Suarez and other members of the Kovar laboratory.

Dr. Samanvaya Srivastava (a postdoctoral researcher in the Tirrell laboratory) joined the collaboration as Dr. Perry left to start a junior faculty position at the University of Massachusetts Amherst, from where she has continued to contribute in an advisory role. Dr. Srivastava contributed polypeptide reagents (with the support of the Tirrell laboratory) and knowledge of complex coacervation and phase separation phenomena. Dr. Srivastava was present for many experiments and frequent conversations with him helped frame and move the project forward. Additionally, Dr. Srivastava wrote the first draft of the manuscript body, performed the analysis to measure the time to half assembly of actin from pyrene fluroescence timeseries data presented in Fig. 5.7C, and formulated the coacervate mesh-size estimate.

I designed and performed all experiments presented in the manuscript, developing experimental protocols as necessary. I performed all quantitative image analysis, prepared all figures and movies, and wrote the Supplemental Information and Materials and Methods sections. Additionally, with input from Prof. Gardel, I completely re-wrote the manuscript body. The submitted manuscript was revised collectively by all co-authors.

Section 5.2 ABSTRACT

Biomolecules exist and function in cellular micro-environments that control their spatial organization, local concentration and biochemical reactivity. Due to the complexity of native cytoplasm, the development of artificial bioreactors and cellular mimics to compartmentalize, concentrate and control the local physicochemical properties is of great interest. Here, we employ self-assembling polypeptide coacervates to explore the partitioning of the ubiquitous cytoskeletal protein actin into liquid polymer-rich droplets. We find that actin spontaneously partitions into coacervate droplets and is enriched by up to ≈30-fold. Actin polymerizes into

micrometer-long filaments and, in contrast to the globular protein BSA, these filaments localize predominately to the droplet periphery. We observe up to a 50-fold enhancement in the actin filament assembly rate inside coacervate droplets, consistent with the enrichment of actin within the coacervate phase. Together these results suggest that coacervates can serve as a versatile platform in which to localize and enrich biomolecules to study their reactivity in physiological environments.

Section 5.3 SIGNIFICANCE STATEMENT

Living cells harbor many protein-rich membrane-less organelles, the biological functions of which are defined by compartment composition and properties. Significant differences between the physico-chemical properties of these crowded compartments and the dilute solutions in which biochemical reactions are traditionally studied pose a major challenge for understanding regulation of organelle composition and component activity. Here, we report the spontaneous partitioning and accelerated polymerization of the cytoskeletal protein actin inside model polypeptide coacervates as a proof-of-concept demonstration of coacervates as bioreactors for studying biomolecular reactions in cell-like environments. Our work introduces exciting avenues for the use of synthetic polymers to control the physical and biological properties of bioreactors in vitro, enabling studies of biochemical reactions in cell-like micro-environments.

Section 5.4 INTRODUCTION

The biological functions of intracellular organelles are defined by the composition and properties of the compartments, which often differ significantly from that of bulk cytoplasm. Well known examples include the acidic pH of lysosomes and the mitochondrial redox potential (Alberts et

al., 2007). While the compartmentalization of these organelles require a lipid bilayer as a physical barrier, recent work has shown that organelles can also form as phase-separated droplets that do not require such a membrane (Brangwynne et al., 2009; Mitrea and Kriwacki, 2016). The physicochemical properties of membrane-less organelles likely regulate partitioning and reactivity of biomolecules, thereby serving an important role in their physiological function. The compositional complexity of individual cellular bodies, granules, and organelles pose a major challenge in discerning general mechanisms for partitioning and reaction regulation. One useful strategy has been to reduce compositional complexity by *in vitro* reconstitution of cellular bodies (Banani et al., 2016; Feric et al., 2016). However, the sequence and structural complexity of natural biopolymers make systematic variation of micro-environment properties difficult.

A complementary approach is to selectively tune the physical and chemical properties of phase-separated micro-environments through the rational design of synthetic polymers that spontaneously phase separate via known mechanisms, and then use these materials as a platform to study biomolecule partitioning and reactivity. For instance, charged homopolymers (polyelectrolytes) form polymer-dense liquid phases via complex coacervation (Gucht et al., 2011; Srivastava and Tirrell, 2016) and localize charged proteins (Black et al., 2014; de Kruif et al., 2004; Lindhoud and Claessens, 2015). Precise chemical control of polypeptide-based polyelectrolytes allows for fine-tuning of several physio-chemical properties of the coacervate phase (Liu et al., 2017; Srivastava and Tirrell, 2016), including functional groups, water content, viscosity, and surface tension, thereby enabling systematic investigations of protein interactions and activities in controlled micro-environments (Aumiller Jr and Keating, 2016; Koga et al., 2011). Knowledge of the general mechanisms by which micro-environment properties tune

protein partitioning and activity could provide needed insight into the function of membrane-less organelles as well as design principles for synthetic biology and engineering applications.

Here, we report the spontaneous partitioning and polymerization of the cytoskeletal protein actin inside model polypeptide coacervates (Pacalin et al., 2016; Perry et al., 2015) as a proof-of-concept demonstration of coacervates as bioreactors for studying biomolecular reactions in cell-like physical environments. Our results establish polyelectrolyte complex coacervates as a viable platform to study mechanisms of partitioning and biochemical regulation by controlled perturbation of condensed-phase micro-environment.

Section 5.5 RESULTS

We use a model coacervate system (Perry et al., 2015) composed of the polycation poly-L-lysine (pLK) and the polyanion poly-(L,D)-glutamic acid (pRE), typically with ~100 amino acids per polypeptide (Table 5.1). Phase separation at room temperature is rapid; initially clear aqueous solutions become visibly turbid in seconds upon mixing of pLK- and pRE-containing solutions at total polypeptide concentrations of 10 μM or more, and is driven primarily by the release of condensed counterions (Ou and Muthukumar, 2006). The presence of a polydisperse size distribution of polypeptide-rich coacervate droplets in solution, ranging in size from $\sim 0.4 < R < 4$ μm, is confirmed directly by differential interference contrast (DIC) microscopy (Fig. 5.1A-C, Fig. 5.2). The round, droplet-like appearance of the condensed pLK/pRE coacervate phase is suggestive of a fluid phase (Perry et al., 2015). Under similar conditions, the surface tension has been measured to be $\gamma \sim 1$ mN/m (Priftis et al., 2012). Consistent with liquid-like properties on the timescale of seconds and longer, merging pLK/pRE droplets rapidly coalescence into a single, larger droplet (Fig. 5.2). From coalescence observations, we estimate

the inverse capillary velocity $v^{-1} = \eta/\gamma$ = 1.6 ms/μm (Fig. 5.2, (Brangwynne et al., 2011; Feric et al., 2016)). This yields a viscosity of η = 1.6 Pa·s, ~1000-fold higher than water. Thus, this simple model system is sufficient to create viscous phase-separated droplets with picoliter volumes.

Polypeptie	Source	Degree of Polymerization	Molecular Weight (kDa)	Polydispersity	Experiments
pLK100	purchased	100	12.8	1.004	Fig. 5.1, 2, 3D, 4 Fig. 5.2, S2, S3, S4
pLK126	in-house	126	16.2	1.30	Fig. 5.7B-C, S5
pRE100	purchased	100	12.9	1.15	Fig. 5.1, 2, 3D, 4 Fig. 5.2, S2, S3, S4
pRE98	purchased	98	12.7	1.02	Fig. 5.7B-C, S5

Table 5.1. Summary of polypeptides used in this study.

Charged proteins spontaneously partition into coacervate droplets. Using a previously published protocol, proteins are mixed with the cationic pLK prior to initiation of phase separation by the addition of anionic pRE (Black et al., 2014). It was previously found that the negatively-charged protein BSA localizes preferentially to pLK/pRE coacervates, and is uniformly distributed within them (Fig. 5.1A-D, Fig. 5.3). This preference for the coacervate phase is described quantitatively by a partition coefficient, defined as the ratio of fluorescence intensity inside to outside the coacervates (Banani et al., 2016). We find an average partition coefficient of $PC_{avg} \cong 8$, whether BSA is added to solution prior to or following phase separation (Fig. 5.1E, Fig. 5.4), indicative of spontaneous partitioning.

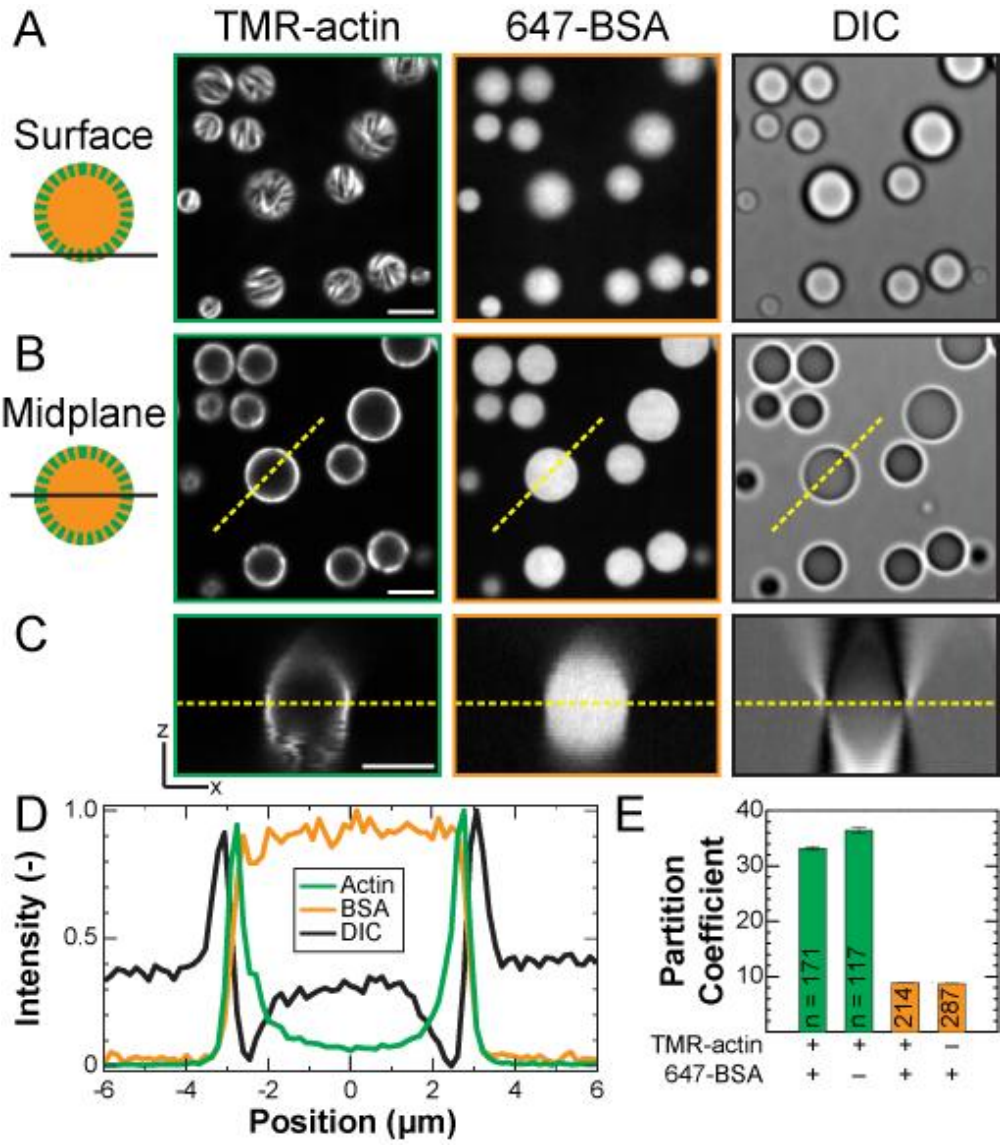

Figure 5.1. F-actin localizes to the periphery of polypeptide coacervates. (A-B) Confocal fluorescence (left and middle) and DIC (right) micrographs of polypeptide coacervates containing both TMR-actin (green) and 647-BSA (orange) on non-adherent substrates. (A) is focused at the interface of the coacervates and the substrate (surface), and (B) is approximately the droplet midplane, indicated by the dashed yellow line in (C). (C) x-z cross-section taken along the dashed yellow line in (B) applied to all planes of a confocal z-stack. Scale bar is 5 μm in (A-C). (D) Normalized intensity linescans along the dashed yellow lines indicated in (B-C). (E) Average partition coefficient for coacervates containing 0.5 μM actin alone, 0.5 μM BSA alone, or 0.25 μM actin and 0.25 μM BSA (A-D). Error bars denote standard error of the mean. The number of droplets included in each condition is listed on the bar. Conditions are 0.5 μM total protein (0.25 μM Mg-ATP-actin (47% TMR-labeled) and 0.25 μM BSA (91% Alexa-647-labeled)) incubated with 5 mM pLK prior to addition of 5 mM pRE in 50 mM KCl, 1 mM $MgCl_2$, 1 mM EGTA, 10 mM imidazole (pH 7.0), and 72 μM ATP (all concentrations final).

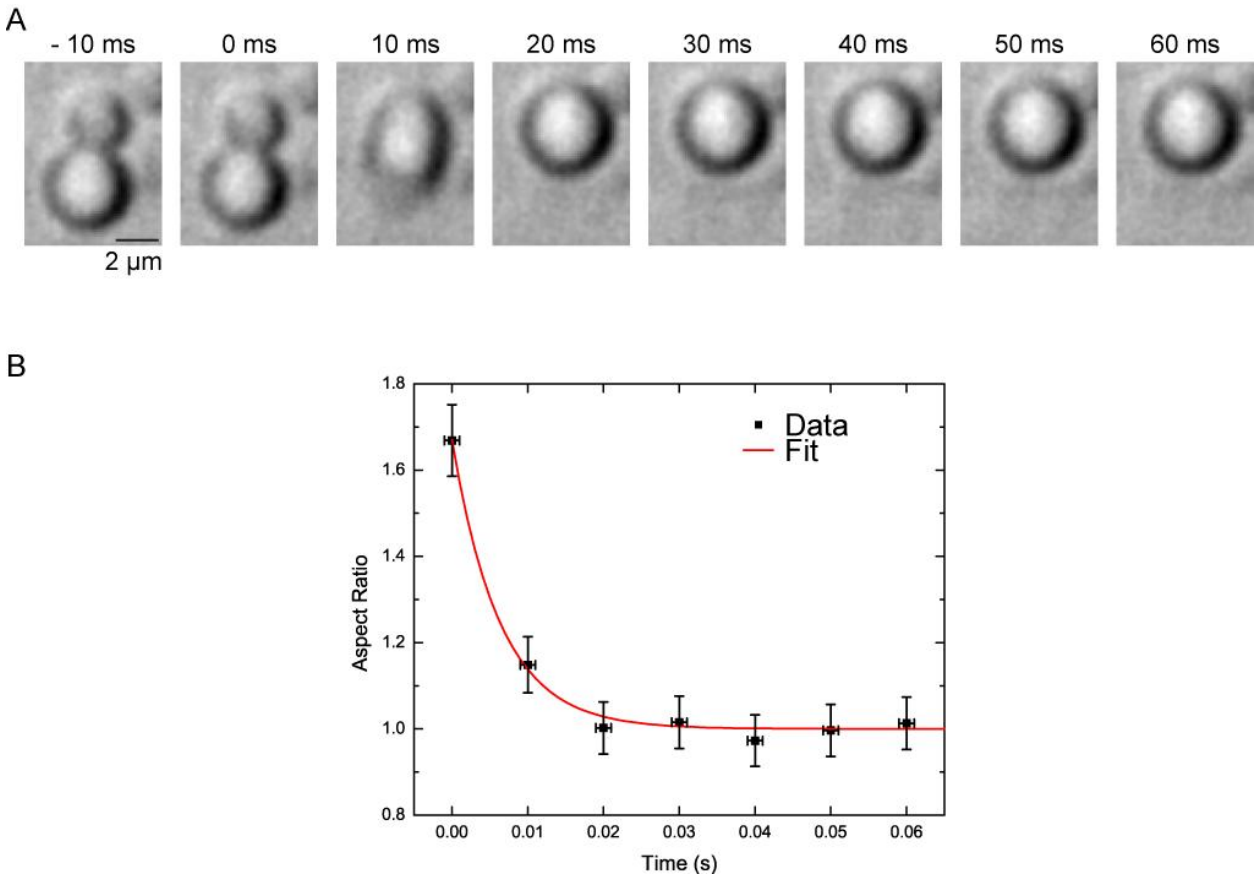

Figure 5.2. Liquid-like properties of pLK/pRE coacervates. (A) DIC microscopy timelapse of two coacervates merging. Both droplets are initially round, suggestive of surface-tension dominated shapes. Upon fusing, the initially dumbbell-shaped interface rapidly relaxes to a round, surface-area-minimizing conformation of diameter d = 4 μm. (B) Aspect ratio of droplets in (A) during coalescence (black). Red line is an exponential fit, with a time constant of τ = 6.33 ms. We estimate the inverse capillary velocity as $v^{-1} = \tau/d$ = 1.6 ms/μm. Error bars represent uncertainty in aspect ratio from a single coalescence event (dy) and acquisition time (dx). Conditions are 5 mM pLK, 5 mM pRE, 50 mM KCl, 1 mM $MgCl_2$, 1 mM EGTA, 10 mM imidazole (pH 7.0), and 80 μM ATP (all concentrations final).

Here, we study the partitioning of actin, a cytoskeletal protein that self-assembles to form linear filaments (F-actin). Actin monomers and the chemically inert BSA are globular proteins of similar size (42 and 66 kDa, respectively) and carry comparable negative charge (isoelectric points of 5.23 and 5.60) (ProtParam). We find that actin partitions to pLK/pRE coacervates and immediately observe linear structures localized preferentially to the coacervate periphery

(Fig. 5.1A-D). Integrating the total actin intensity within the droplet, we find an average partition coefficient that is 4-fold higher than that for BSA (Fig. 5.1E). Interestingly, the partition coefficients for BSA and actin are the same whether one or both proteins are present in solution (Fig. 5.1E, Fig. 5.3). This suggests that, under the conditions explored here, BSA and actin do not compete directly for space in the coacervate. Both partitioning and peripheral localization of actin are robust to the order of addition (Fig. 5.5).

Self-assembled F-actin of canonical structure localizes to the coacervate periphery. To test whether the linear actin structures are bona fide F-actin, we stained with fluorescently-labeled phalloidin (647-phalloidin). Phalloidin is a small, uncharged toxin recognized for its ability to specifically bind to F-actin (Vandekerckhove et al., 1985). 647-phalloidin was introduced into the solution after the coacervate formation and actin assembly, and found to localize along the linear actin structures. Confocal fluorescence micrographs at both the coverslip surface (Fig. 5.6A,C) and droplet midplane (Fig. 5.6B,D) reveal strong co-localization of phalloidin fluorescence to the linear actin structures with a Pearson's correlation coefficient of 0.86 (Fig 2E, Section 5.8). This provides strong evidence that these linear actin-rich structures are composed of F-actin of canonical structure. Given the brightness of the F-actin structures, and previous work demonstrating that concentrations of polycations (and pLK in particular) lower than those in the coacervate phase are sufficient to bundle F-actin (Tang and Janmey, 1996), we presume that the structures visible in Figs. 5.1 and 5.6 are F-actin bundles, rather than individual filaments.

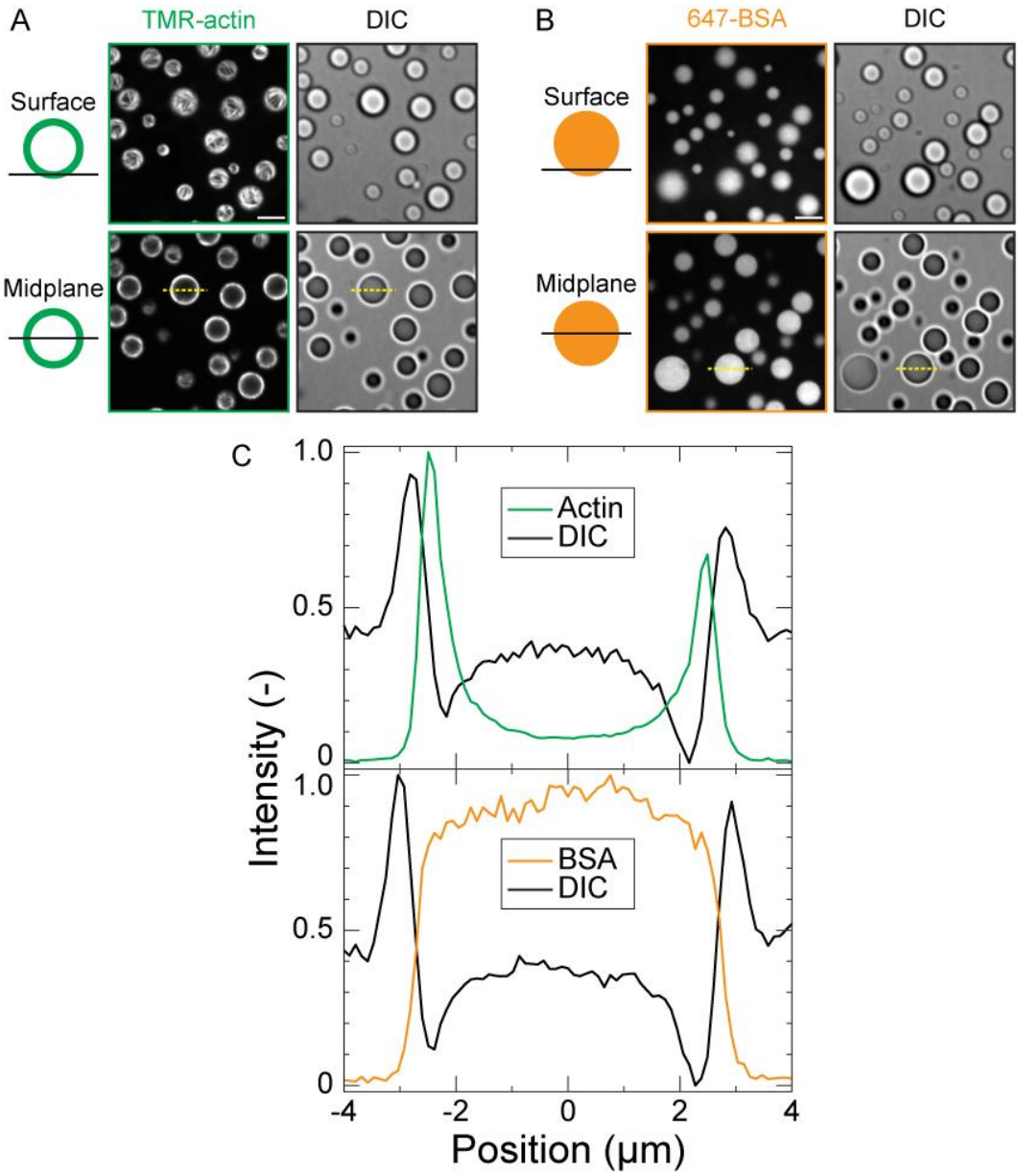

Figure 5.3. Peripheral localization of F-actin in polypeptide coacervates is BSA-independent. (A-B) Confocal fluorescence (left) and DIC (right) micrographs of polypeptide coacervates containing either TMR-actin (A, red) or 647-BSA (B, cyan) on non-adherent substrates. Top row is focused at the interface of the coacervates and the substrate (surface), and bottom row is approximately the droplet midplane. Scale bar is 5 μm. (C) Normalized fluorescence intensity linescans along the dashed yellow lines indicated in (A) (top) and in (B) (bottom). Conditions are 0.5 μM protein (either Mg-ATP-actin (47% TMR-labeled) or BSA (91% Alexa-647-labeled)) incubated with 5 mM pLK prior to addition of 5 mM pRE in 50 mM KCl, 1 mM $MgCl_2$, 1 mM EGTA, 10 mM imidazole (pH 7.0), and 72 μM ATP (all concentrations final). Note that the average partition coefficients for (A) and (B) are reported in Fig. 5.1.

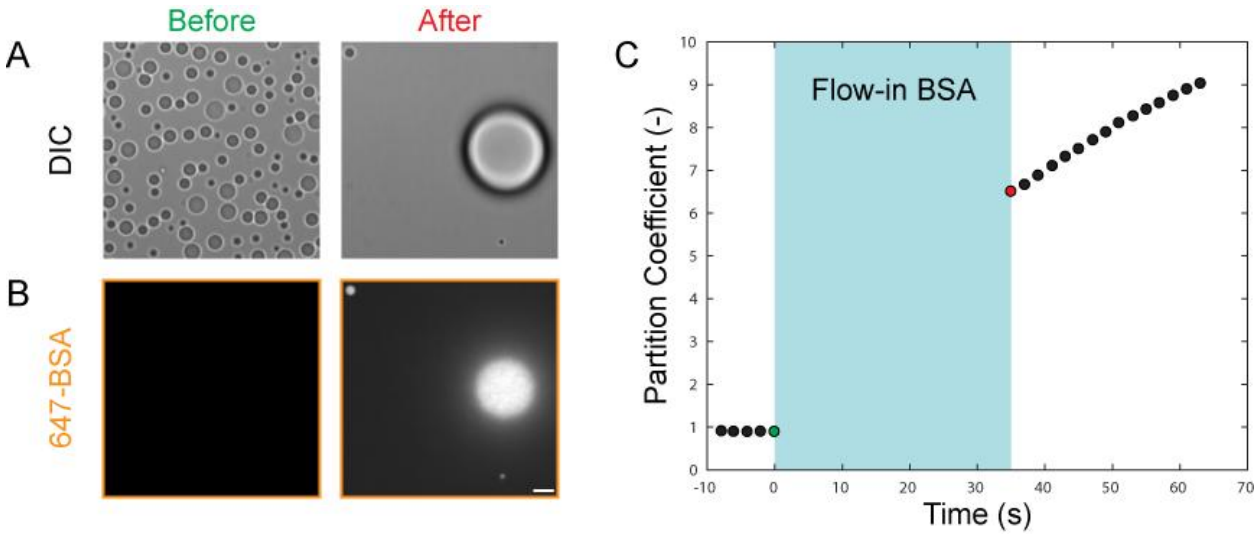

Figure 5.4. Flow-in of BSA to pre-formed pLK/pRE coacervates. (A-B) Time-lapse confocal DIC (A) and fluorescence (B) micrographs of pLK/pRE coacervates before (left, green) and immediately after (right, red) the addition of 1.5 μM 647-BSA to the flow-cell chamber. Flow causes many of the sedimented droplets to fuse into larger droplets (A). While only background fluorescence is detectable prior to addition of BSA (B, left), BSA is partitioned to and uniformly localized within the few coacervate droplets remaining in the field of view within 35 s. Scale bar is 5 μm. (C) The partition coefficient of the large droplet visible after BSA flow-in increases with time, but is already above 6 in the first image acquired. Conditions are 5 mM pLK, 5 mM pRE, 50 mM KCl, 1 mM $MgCl_2$, 1 mM EGTA, 10 mM imidazole (pH 7.0), and 72 μM ATP (all concentrations final). 1.5 μM 647-BSA is perfused into the chamber in buffer containing 50 mM KCl, 1 mM $MgCl_2$, 1 mM EGTA, 10 mM imidazole (pH 7.0), and 72 μM ATP (all concentrations final).

Actin assembly is enhanced in coacervates. Having demonstrated that the actin polymerization proceeds in pLK/pRE coacervates, we next ask to what extent the coacervate micro-environment impacts the reaction rate. Actin is a convenient model protein for this purpose owing to the existence of established spectroscopic tools for quantitatively monitoring assembly kinetics (Cooper et al., 1983). In particular, the fluorescence intensity of the pyrene fluorophore increases ~20-fold when pyrene-labeled monomers are incorporated into filaments and is a well-established method to track actin assembly (Cooper et al., 1983), as depicted in the schematic in Fig. 5.7A. In solution, the polymerization time course of 1.5 μM actin shows a characteristic lag

phase, indicative of the kinetically slow filament nucleation step (Sept and McCammon, 2001), followed by a phase of rapid growth and then saturation once a steady-state is reached (Fig. 5.7A) (Cooper et al., 1983). At this actin concentration, the initial lag phase is typically ~10 min and steady-state is reached in ~120 min (Fig. 5.7B, black). The presence of pLK/pRE coacervates eliminates the lag phase and steady-state is achieved within 10 minutes (Fig. 5.7B, red). Thus, actin filament assembly is stimulated significantly by pLK/pRE coacervates.

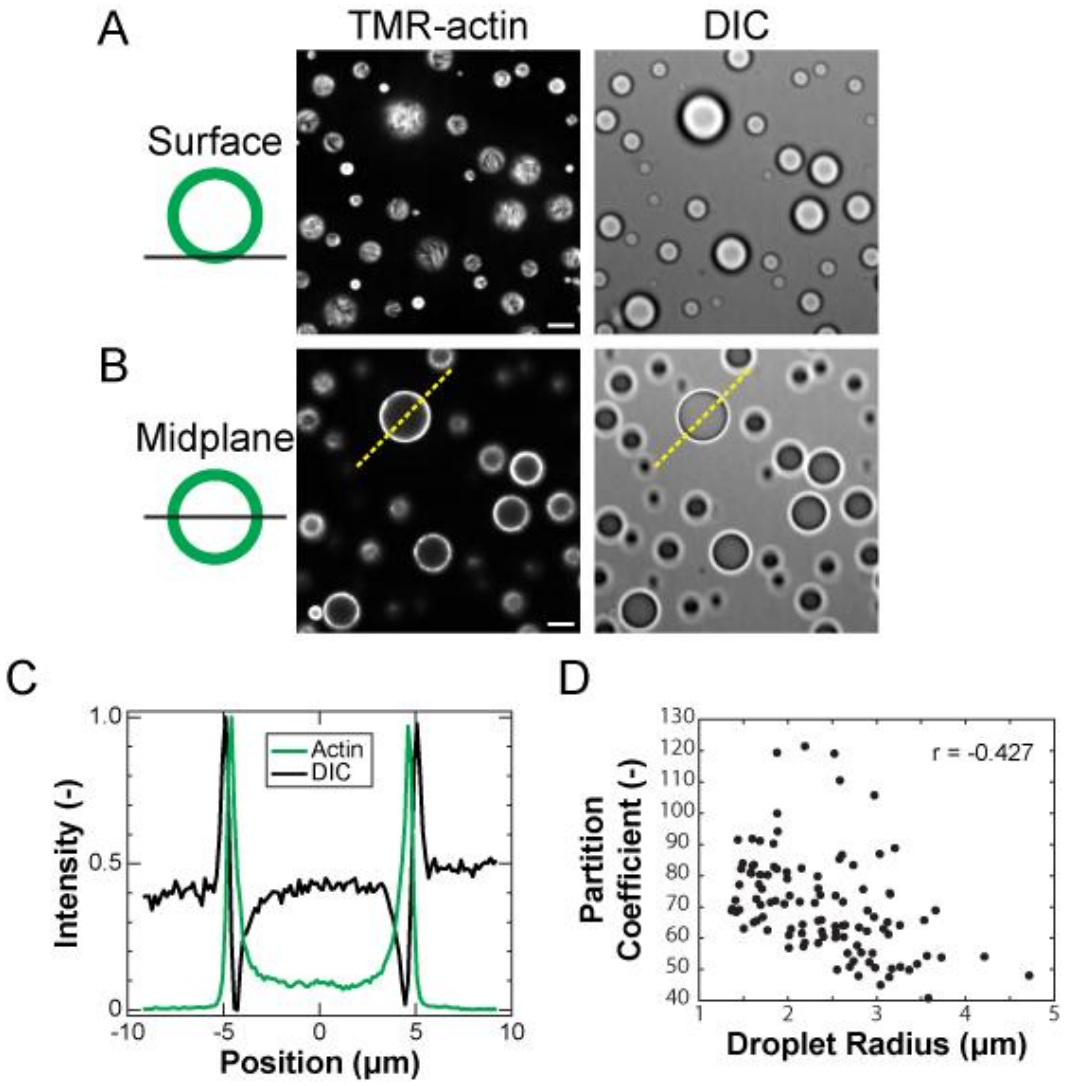

Figure 5.5. Partitioning and localization patterns are robust to order of addition.

Figure 5.5 Continued. (A-B) Confocal fluorescence (left) and DIC (right) micrographs of polypeptide coacervates containing TMR-actin (green) on non-adherent substrates. (A) is focused at the interface of the coacervates and the substrate (surface), and (B) is approximately the droplet midplane. Scale bar is 5 μm. (C) Normalized fluorescence intensity linescans along the dashed yellow lines indicated in (B). (D) Partition coefficients as a function of droplet radius, calculated for a total of N = 117 individual pLK/pRE coacervates with TMR-actin added immediately following phase separation. The average partitioning coefficient is 70.3 +/- 15.9. Error bars denote the standard error of the mean. The Pearson's correlation coefficient for the data in (D) is r = -0.427, indicating a lower average partition coefficient for larger droplets. Conditions are 5 mM pLK, 5 mM pRE, 50 mM KCl, 1 mM $MgCl_2$, 1 mM EGTA, 10 mM imidazole (pH 7.0), and 72 μM ATP (all concentrations final). Following mixing and subsequent phase separation, this solution is added to a small volume of Mg-ATP-actin (47% TMR-labeled), and imaged. The final (global) concentration of actin is 0.5 μM.

To assess reaction kinetics quantitatively, we estimate the assembly rate $1/t_{1/2}$, defined as the inverse of the time at which the pyrene fluorescence intensity reaches half of its relative change during the course of actin polymerization (Fig. 5.7A, Section 5.8). The actin assembly rate $1/t_{1/2}$ increases from 0.03 to >1 min^{-1} as the total pLK concentration increases from 0.3 to 30 μM, while maintaining a pLK:pRE ratio of 1 (Fig. 5.7C). Above 30 μM, the assembly rate saturates. Thus, the actin assembly rate is enhanced by nearly two orders of magnitude in the presence of coacervates (Figs. 5.1, 5.6, 5.8).

Polylysine and coacervates stimulate actin assembly via distinct mechanisms. One possible explanation for the enhanced assembly rate is polycation-mediated F-actin nucleation. Polylysine has been shown to promote formation of antiparallel actin dimers (Bubb et al., 2002) that nucleate F-actin (Brown and Spudich, 1979; Oriol-Audit, 1978). Spontaneous assembly of pyrene-labeled actin in the presence of pLK shows a concentration-dependent increase in the rate of actin assembly (Fig. 5.7B,C, blue data). It is tempting to compare the filament formation rate in solution directly to the rates observed within coacervates. However, the local pLK

concentration within the coacervate phase is actually much higher, on the order of 1-3 M, such that the pLK concentrations reported in Fig. 5.7C should not be directly compared. Furthermore, pLK/pRE interactions within the coacervate could limit pLK-mediated antiparallel dimer formation.

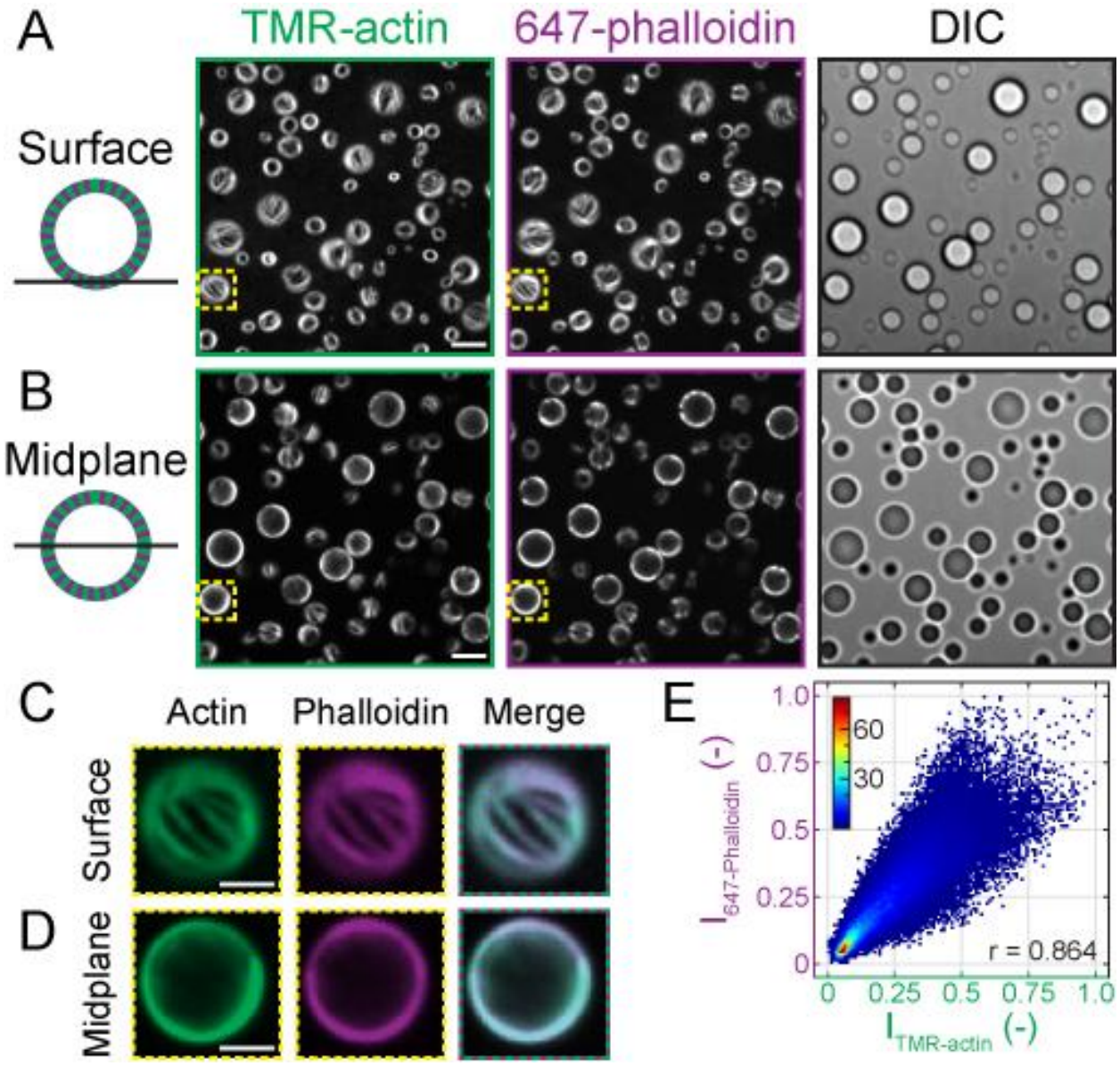

Figure 5.6. Linear actin fibers maintain canonical F-actin structure. (A-B) Confocal fluorescence (left and middle) and DIC (right) micrographs of polypeptide coacervates containing TMR-actin (green) after the addition of Alexa-647-Phalloidin (purple) on non-adherent substrates.

Figure 5.6 Continued. (A) is focused at the interface of the coacervates and the substrate (surface), and (B) is approximately the droplet midplane. Scale bar is 5 µm. Conditions are 0.5 µM Mg-ATP-actin (47% TMR-labeled) incubated with 5 mM pLK prior to addition of 5 mM pRE in 50 mM KCl, 1 mM $MgCl_2$, 1 mM EGTA, 10 mM imidazole (pH 7.0), and 72 µM ATP (all concentrations final). 0.25 µM Alexa-647-Phalloidin was flown into the chamber in the same buffer after droplets had sedimented. (C-D) False-colored fluorescence images of the regions outlined in yellow boxes in (A-B) from the surface (C) and midplane (D). Right column shows a merge. Scale bar is 2 µm. (D) Correlation between TMR-actin and 647-phalloidin fluorescence intensity values for all pixels in (A). Colors represent count density. Pearson's correlation coefficient is r = 0.864.

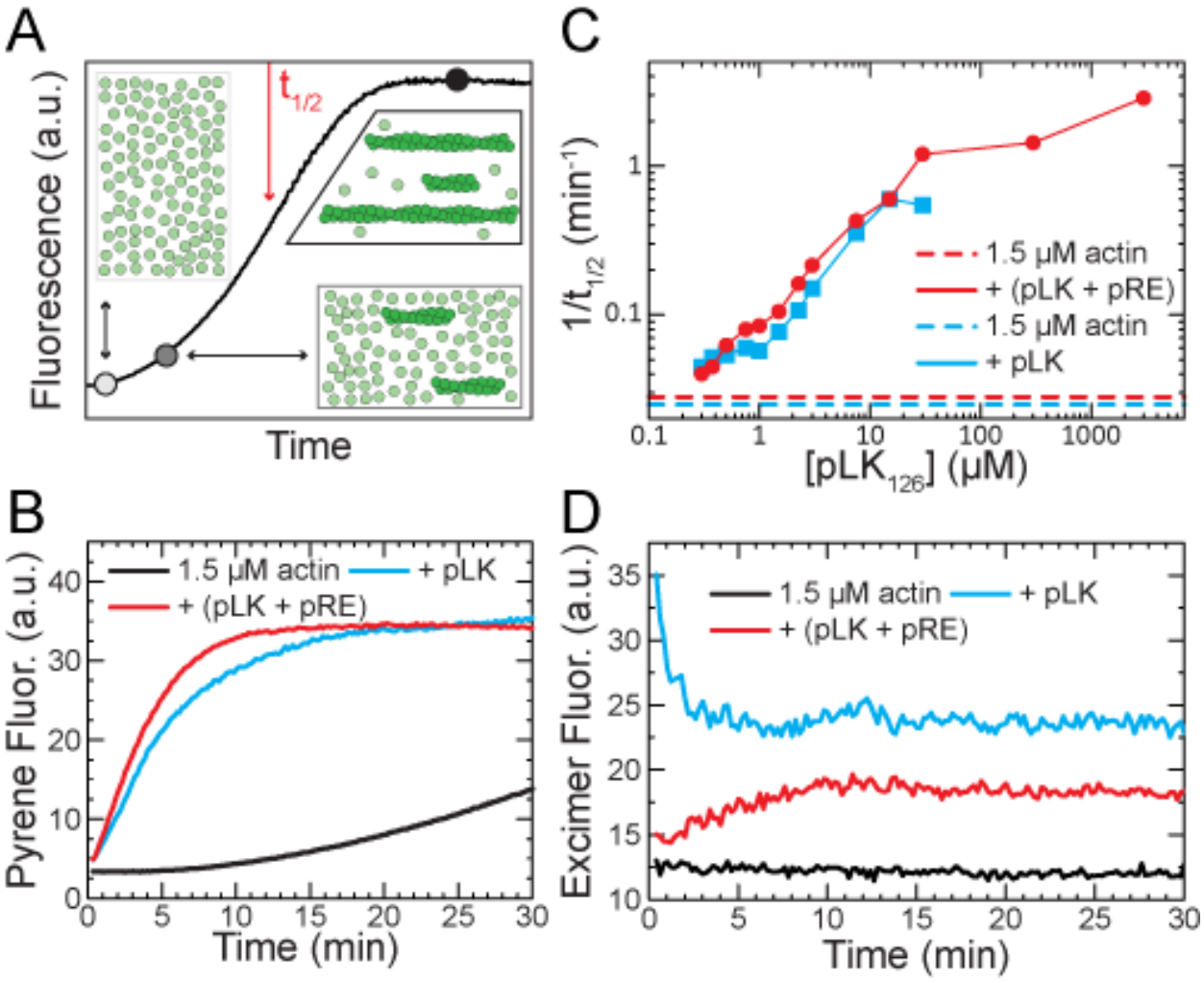

Figure 5.7 Coacervates and poly-L-lysine enhance actin assembly via different mechanisms. (A) Cartoon depicting the timecourse for spontaneous actin assembly monitored by changes in pyrene-actin fluorescence. (B) Spontaneous assembly of 1.5 µM Mg-ATP-actin (12% Pyrene-labeled) alone (black), with 3 µM pLK (cyan), or with 3 µM pLK and 3 µM pRE (red).

Figure 5.7 Continued. (C) The assembly rate ($1/t_{1/2}$) for 1.5 μM actin for samples with pLK alone (cyan) or equal concentrations of pLK and pRE (red) as a function of the concentration of pLK. Dashed lines denote the assembly rate of 1.5 μM actin alone measured in parallel with pLK-containing (cyan dashed) or pLK- and pRE-containing (red dashed) samples. (D) Timecourse of pyrene excimer fluorescence during spontaneous assembly of 1.5 μM Mg-ATP-actin (12% Pyrene-labeled) alone (black), with 3 μM pLK (cyan), or with 3 μM pLK and 3 μM pRE (red). In all experiments with polypeptides, Mg-ATP-actin is incubated with variable pLK in low salt prior to addition of pRE (red) or a buffer blank (cyan) in 50 mM KCl, 1 mM $MgCl_2$, 1 mM EGTA, 10 mM imidazole (pH 7.0), and 72-150 μM ATP (all concentrations final).

To test whether pLK-stabilized antiparallel actin dimers contribute to the assembly of F-actin in pLK/pRE coacervates, we monitored pyrene excimer fluorescence (Bubb et al., 2002). In the absence of pLK, 1.5 μM actin displays no change in pyrene excimer fluorescence during the nucleation-dominated early phase of assembly (Fig. 5.7D, black). In the presence of pLK, excimer fluorescence is highest during the initial nucleation phase, and decays rapidly as assembly proceeds (Fig. 5.7D, blue). This excimer fluorescence time course is the hallmark of actin assembly mediated by pLK-stabilized antiparallel actin dimers (Bubb et al., 2002). Importantly, in the presence of pLK/pRE coacervates, excimer fluorescence does not have these features characteristic of anti-parallel dimer-mediated nucleation events (Fig. 5.7D, red). These data strongly suggest that pLK-mediated nucleation is not the dominant mechanism by which actin assembly is enhanced in pLK/pRE coacervates.

Partitioning increases the local protein concentration in coacervates. A direct consequence of partitioning is that the local actin concentration in the coacervate phase is higher than that in the polymer-dilute phase. Thus, an alternate mechanism underlying enhanced assembly rates is an increased local actin concentration, c_{local}, within coacervates.

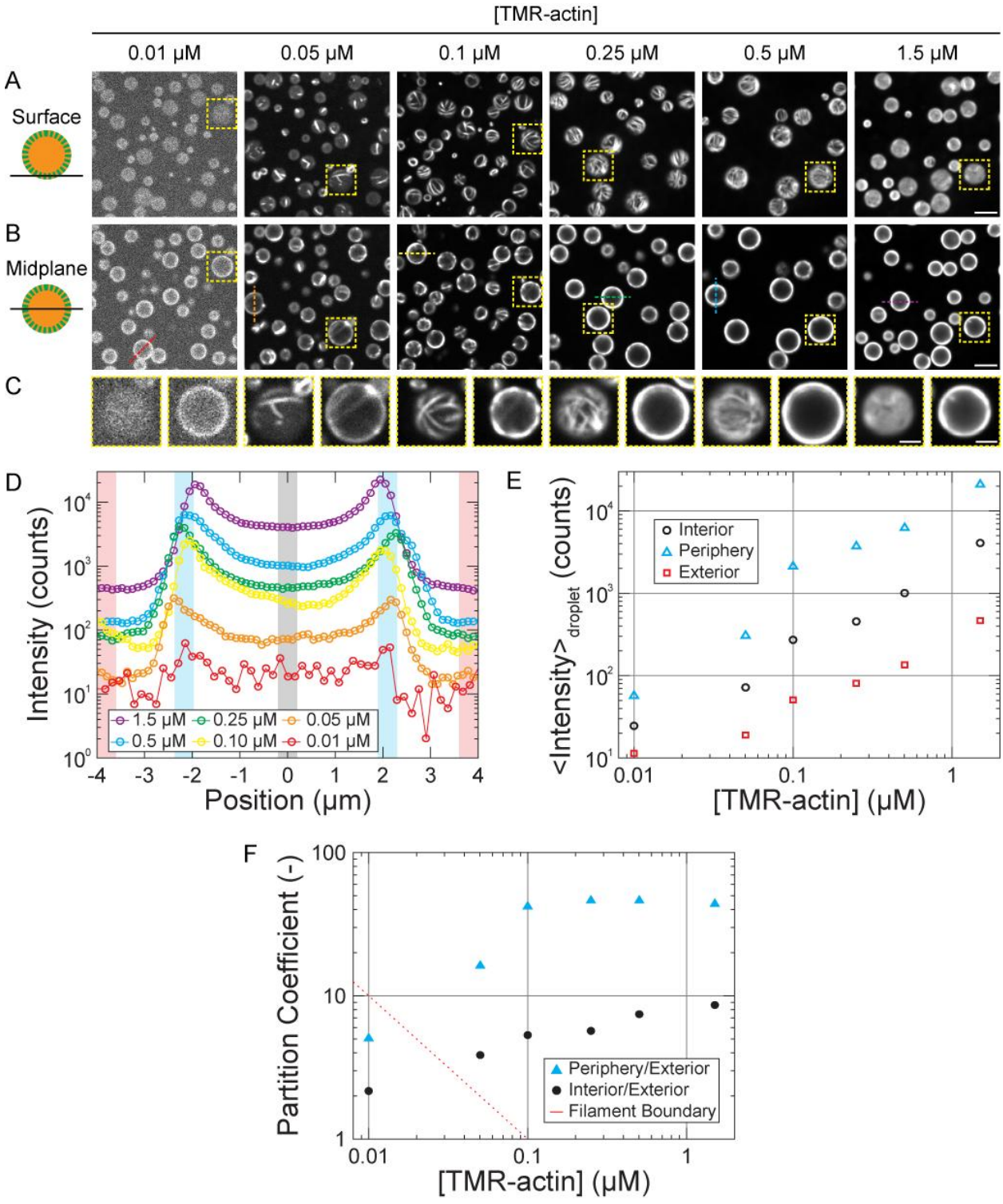

Figure 5.8. Partitioning increases the local protein concentration in coacervates. (A-B) Confocal fluorescence micrographs of polypeptide coacervates containing variable concentrations of TMR-actin on non-adherent substrates, focused at the interface of the coacervates and the substrate (surface, A), or approximately the droplet midplane (B).

Figure 5.8 Continued. Contrast is adjusted individually for each concentration of TMR-actin, but is consistent between confocal slices for each condition. (C) Magnified images of the yellow boxed regions outlined in (A-B). Scale bars are 5 μm (A-B) and 2 μm (C). (D) Fluorescence intensity along the colored dashed lines in (B). (E) Mean fluorescence intensity of interior (circle, black), periphery (triangle, cyan), and exterior (square, red) of coacervates droplets, obtained from the black-, cyan-, and red-shaded regions in (D). (F) Partition coefficients (ratio of peripheral to exterior (triangles, cyan) and interior to exterior (circles, black) fluorescence) for the data in (D-E). Red line indicates where product of the partitioning coefficient and the total actin concentration equals the critical concentration for actin assembly of ~0.1 μM. Filaments are expected to the right of the red line, but not to the left. Conditions are a range of Mg-ATP-actin (47% TMR-labeled) concentrations incubated with 5 mM pLK (either alone (1.5- and 0.5-μM actin) or with 0.25 μM or BSA (91% Alexa-647-labeled) (0.25-, 0.1-, 0.05-, 0.01-μM actin)) prior to addition of 5 mM pRE in 50 mM KCl, 1 mM $MgCl_2$, 1 mM EGTA, 10 mM imidazole (pH 7.0), and 72 μM ATP (all concentrations final).

We tested this possibility by varying the global actin concentration, $c_{global,}$ from 0.01 μM to 1.5 μM. The threshold monomer concentration, or critical concentration c*, required for polymerization of Mg-ATP-actin is ≈0.1 μM (Fujiwara et al., 2007; Pollard, 1986). If actin is concentrated in coacervate droplets ≈30-fold via partitioning, we would expect actin assembly within coacervates at global actin concentrations of ≈0.003 μM. Importantly, we observe coacervate-associated F-actin at global actin concentrations as low as 0.05 μM (Fig. 5.8A-C). Interestingly, we observe peripherally-biased partitioning of actin to pLK/pRE coacervates at all actin concentrations examined, even at the lowest concentration (0.01 μM) for which no filaments are clearly discernible. We note that the density of peripherally localized F-actin changes as a function of the global actin concentration. Whereas isolated filaments or bundles are visible at 0.05 μM, an F-actin shell too dense to resolve individual structures forms at 1.5 μM (Fig. 5.8A-C).

To systematically characterize the localization of actin fluorescence, we examined fluorescence intensity line scans through the midplane, depicted in Fig. 5.8B and shown in Fig. 5.8D. These curves may be divided into three regions: the droplet exterior (red), periphery

(blue) and interior (black). Under each experimental condition, fluorescence is highest at the droplet periphery, followed by the droplet interior. The lowest fluorescence intensities are consistently observed exterior to droplets (Fig. 5.8E). The fluorescence increases nearly linearly with actin concentration both inside and outside the coacervate droplets (Fig. 5.8E).

In addition to the average partition coefficient (Fig. 5.1E), we report two additional partition coefficients derived from these intensity profiles; one for the ratio of droplet periphery (maximum observed intensity) to average intensity in the exterior of the droplet (PC_{Periph}) (Fig. 5.8F, blue/red), and a second for the ratio of droplet interior intensity (near the center of the droplet) to the average intensity in the exterior (PC_{Int}) (Fig. 5.8F, black/red). Both partition coefficients are greater than unity, indicative of partitioning of actin to the polymer-dense coacervate phase from the polymer-dilute phase. PC_{Periph} and PC_{Int} both tend to reach plateaus for actin concentrations above 0.1 μM; PC_{Periph} values grow almost 10-fold before stabilizing at ≈45 once the global actin concentration reached 0.1 μM, while PC_{Int} values increase over the range of actin concentrations investigated in the current study, and appear to approach a plateau value of ≈10. The saturation of the PC_{Periph} with global actin concentration suggests that exchange of protein between the polymer-dense and dilute phases occurs readily, as has been reported in other liquid phase-separated systems (Banani et al., 2016).

Section 5.6 DISCUSSION

We present proof-of-concept experiments demonstrating that a polypeptide-based complex coacervate can be used as a model bioreactor to control the localization and activity of the self-assembling cytoskeletal protein actin. We find that actin partitions spontaneously to the coacervate phase, and that its partitioning is not influenced by BSA. Strong partitioning of actin

to pLK/pRE coacervates increases the local actin concentration, contributing substantially to a >50-fold increase in the actin assembly rate at the highest concentrations of actin and coacervate. Actin filaments of canonical structure localize to the coacervate periphery, effectively forming core-shell particles, with the actin shell density controlled by the actin concentration.

Partitioning vs. encapsulation of client proteins. Previous work interpreted the preferential localization of the client protein BSA to the pLK/pRE coacervate phase as "encapsulation" (Black et al., 2014; Nolles et al., 2015; Obermeyer et al., 2016). The implication of this language is that exchange of client molecules between the coacervate and dilute phases is either non-existent or so small as to be negligible, as with encapsulation within lipid vesicles or emulsion droplets (Kakran and Antipina, 2014; Vieregg and Tang, 2016). Indeed, Black et al. argued that entry of the large (66 kDa) client into the coacervate phase requires the formation of an intermediate electrostatic complex between the client and an oppositely-charged polyelectrolyte in solution prior to phase separation, and that client release is triggered by pH-induced dissolution of the coacervate phase (Black et al., 2014).

Our present results are more consistent with a molecular view termed partitioning (Banani et al., 2016), where the partition coefficient reflects the equilibration of steady fluxes of client molecules into and out of the coacervate phase. For instance, we observe partitioning of BSA within ≈30 s upon addition to pre-formed pLK/pRE coacervates (Fig. 5.4). Given the very low polypeptide concentration in the dilute phase (< 30 nM pLK), this suggests that recruitment of the client to the coacervate does not require the formation of an intermediate complex with a polyelectrolyte. Additionally, the saturation of the partition coefficient for actin concentrations

above 0.1 μM (Fig. 5.8F) is indicative of an equilibration between the client concentrations in the dilute and coacervate phases, which necessarily requires exchange.

Equilibrium partitioning in synthetic polypeptide coacervates is reminiscent of other recent *in vitro* work wherein client proteins of low-valency spontaneously partition into liquid phase-separated structures composed of high-valency scaffold proteins (Banani et al., 2016), as well as in coacervates formed from natural biopolymers (Pak et al., 2016). This is particularly interesting in that binding is mediated by specific low-affinity protein-protein interactions in the former case, in contrast to the non-specific electrostatic interactions presumed in the case of coacervates. This suggests that the capacity to selectively partition client molecules may be a general property of condensed liquid-like phases, independent of the interactions driving partitioning.

Origin of peripheral F-actin localization. Below, we examine three non-mutually exclusive physical mechanisms for the peripheral localization of F-actin in coacervates droplets: filament buckling, macromolecular depletion, and interfacial adsorption.

F-actin does not appear to protrude from micron-sized coacervate droplets, suggesting that coacervate surface tension may play a role in confining F-actin. One mechanism for peripheral filament localization is that surface tension causes filaments to buckle once the contour length exceeds the droplet diameter. A comparison of the energy required to increase the coacervate surface area to accommodate a protruding filament of length L and diameter d with a cylindrical cap, $E_{Area} = \pi d(L - 2R)\gamma$, with the energy required to bend the filament into a circular arc with radius R equal to that of the droplet, $E_{Bend} = (\frac{k_B T l_p}{2}) \int_0^L |1/R|^2 ds = \frac{k_B T l_p L}{2R^2}$, yields the shortest length greater than 2R for which bending is energetically favorable:

$$L^* = \frac{2R}{1 - \frac{k_B T l_p}{2\pi d \gamma R^2}}$$

where k_B is the Boltzmann constant, T is temperature, and l_p = 10 μm is the persistence length of F-actin (McCullough et al., 2011). In a 1-μm diameter coacervate droplet with the surface tension γ = 1 mN/m (Priftis et al., 2012) at room temperature, bending is preferable for filaments longer than ≈1 μm. Coacervate surface tension is thus sufficient to bend F-actin with contour lengths larger than the droplet diameter. However, the observation that filaments and bundles even shorter than the droplet diameter are peripherally localized (Fig. 5.8A-C, 0.05 μM panels) indicates that surface tension-induced buckling cannot be the sole cause.

The peripheral localization of F-actin is reminiscent of the well-known crowding of F-actin to interfaces observed in the presence of macromolecular crowding agents (Kuhn and Pollard, 2005; Murrell and Gardel, 2012), which arises from depletion interactions (Asakura and Oosawa, 1954). To assess this, we estimate the osmotic pressure needed to crowd F-actin to an interface to be $\Pi^* \cong 450$ Pa (see Section 5.8). We estimate the osmotic pressure of the coacervate interior as that arising from a solution of flexible polymers characterized by a mesh size (de Gennes, 1979), ξ, as $\Pi = k_B T/\xi^3$. This suggests that a coacervate with mesh size $\xi \leq 20$ nm would generate sufficient osmotic pressure to drive peripheral localization of F-actin. We estimate the mesh size of our pLK/pRE coacervates to be 2-3 nm (see Section 5.8), which supports the plausibility of a depletion-based mechanism. Noting the empirical observation that long filaments crowd more readily than short ones, macromolecular depletion could preferentially crowd long, high aspect ratio filaments and bundles, leaving short filaments, actin monomer, and BSA uniformly distributed.

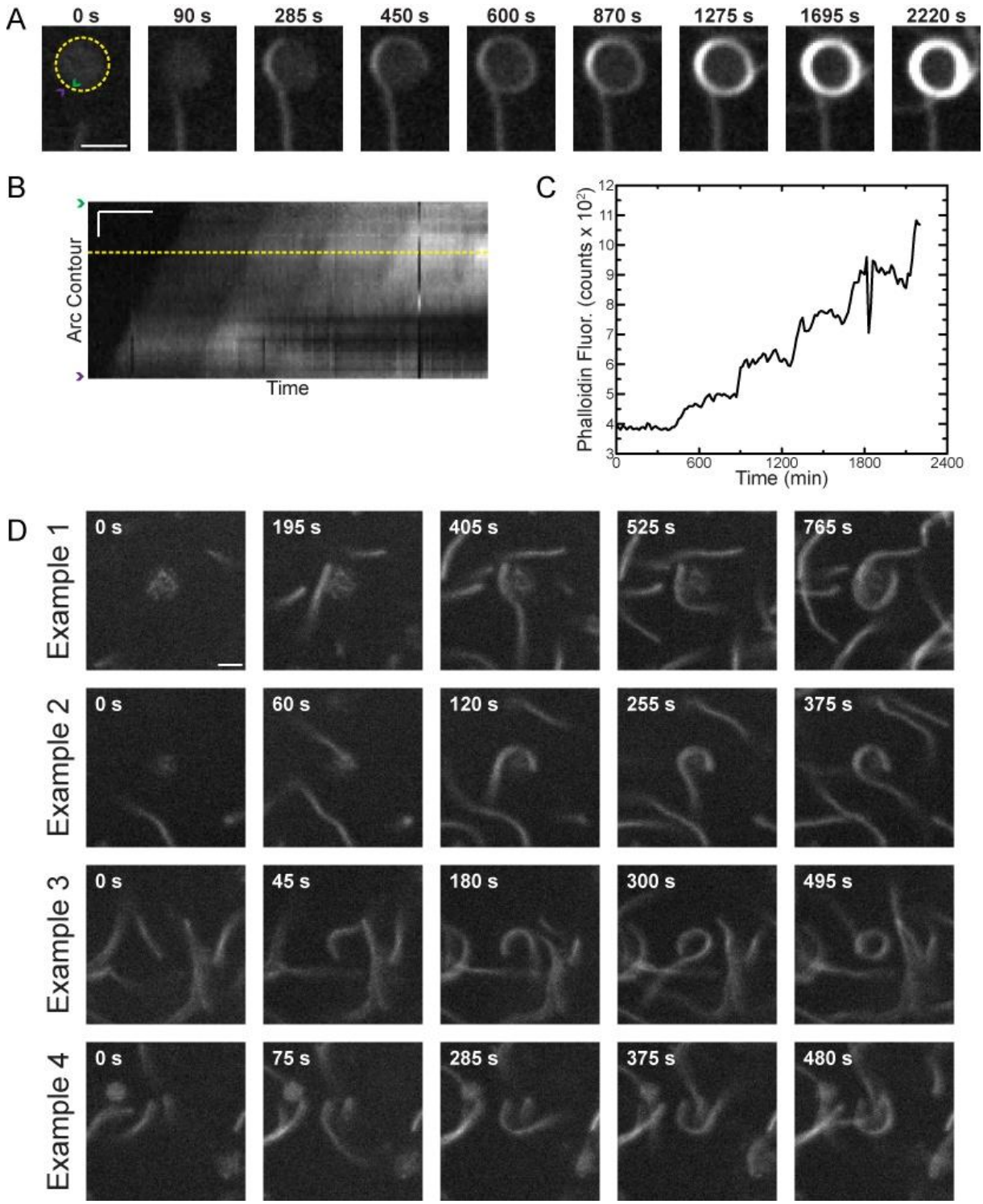

Figure 5.9. Adhesion of soluble F-actin to the coacervate interface. (A-D) 0.3 μM Mg-ATP-actin (unlabeled) added to a solution of 6 mM pLK/pRE coacervates in 50 mM KCl, 1 mM $MgCl_2$, 1 mM EGTA, 10 mM imidazole (pH 7.0), and 72 μM ATP (all concentrations final).

Figure 5.9 Continued. (A-C) Also contain 0.5 % (w/v) 14 kDa methylcellulose (MC) and oxygen scavenging system. (A) Fluorescence time-lapse of a growing actin filament approaching a presumed coacervate droplet in presence of MC. Filament contacts coacervate, and winds around the coacervate 4 times upon further elongation. (B) Kymograph along circular yellow path in (A). (C) Intensity along yellow linescan in (B). Step-like increases indicate successive windings. (D) Examples of winding in the absence of MC. Scale bars: 2 μm (A); 1 μm and 300 s (B), 2 μm (D).

A third, non-mutually exclusive mechanism for peripheral localization of F-actin is filament adsorption to the coacervate/bulk interface. For example, electrostatic interactions between F-actin and the coacervate could drive adsorption in a process akin to that of polyelectrolyte-mediated emulsion stabilization (Andelman and Joanny, 2000). Alternately, a difference in the interfacial tensions between F-actin and the solution and the coacervate, respectively, could drive localization of filaments to the coacervate/solution interface, such as seen in Pickering emulsions (Bon, 2014). In support of an adhesion-based mechanism, we note that filaments occasionally wrap around coacervate droplets when assembling in solution (Fig. 5.9), indicative of an attractive interaction between F-actin and the coacervate/solution interface.

Importantly, not all actin fluorescence is peripherally localized. Actin fluorescence intensity in the center of pLK/pRE coacervates is diffuse and enriched by as much as 10-fold compared to the surrounding solution (Fig. 5.8F). Interior fluorescence increases with global actin concentration, which is inconsistent with the peripheral localization of all filaments. In that case, the interior fluorescence would correspond to solely actin monomers, which we would predict to have a constant local concentration of $c_{local} = c^* = 0.1$ μM at steady-state. This suggests that the coacervate interior contains a mixture of monomers and filaments. Given that a 250-nm filament (~90 actin subunits) cannot be resolved with conventional light microscopy, an interior

including both monomers and short filaments is consistent with the diffuse fluorescence signal we observe. The aforementioned mechanisms of peripheral localization all depend on F-actin length. As such, the presence of short filaments in the interior does not qualitatively distinguish between them. Understanding how peripheral localization is regulated will be an exciting avenue for future studies.

Mechanism of actin assembly enhancement. The assembly of actin within coacervates for global actin concentrations below the critical concentration is largely predicted by the 30-fold increase in the local actin concentration via partitioning into the coacervate phase. Using measured partition coefficients, we calculate the concentrations at which filament assembly within coacervates is expected and find that partitioning is sufficient to explain filament assembly down to 0.05 μM (red dashed line, Fig. 5.8F). However, our measured partitioning is not quite sufficient to polymerize actin within coacervates at the lowest concentration (0.01 μM), yet we observe strong peripheral intensity (and interpret this to be polymerized actin). It is possible that the coacervate environment may alter the reaction rate kinetics of actin assembly (Drenckhahn and Pollard, 1986; Frederick et al., 2008), as has been seen for transcription in cell-lysate coacervates (Sokolova et al., 2013). Indeed, since the coacervate-phase volume fraction (40%) and viscosity (2 Pa-s) are similar to those of the cytoplasm, this system may serve as a useful platform to study biochemical reactions in a more physiological environment.

Implications for biochemical reaction regulation. The high local concentrations generated by partitioning provide for an elegant means to both spatially localize and enhance the rates of biochemical reactions. Spontaneous partitioning to a condensed liquid-like phase substantially

reduces the quantities of protein needed to study reactions under more physiological conditions. Of particular interest is the possibility of having direct control over partition coefficients and other local physicochemical properties of the coacervate phase as a means to control biochemical reactivity.

In summary, we have illustrated spontaneous partitioning of proteins inside coacervate droplets, leading to markedly increased actin assembly rates and spatial confinement of filaments. Assembly rate enhancements reported here are qualitatively consistent with a model in which these enhancements were contributed by an increase in the local effective concentration of actin monomers in the coacervate phase. Our work introduces exciting avenues for the use of synthetic polymers to control physical and biological properties of bioreactors, and address questions in biology about the biochemistry of molecules in cell-like micro-environments.

Section 5.7 ACKNOWLEDGEMENTS

The authors thank C. Suarez, K. Weirich, T. Witten, and J. Vieregg, as well as the Gardel, Kovar, and Tirrell labs, for helpful discussion and suggestions. We thank L. Li for assistance with gel permeation chromatography measurements. DRK, MLG, and MVT acknowledge support from the University of Chicago MRSEC (NSF DMR-1420709). PMM thanks the University of Chicago MRSEC for a graduate fellowship.

Section 5.8 SUPPLEMENTAL MATERIALS AND METHODS

Polypeptide Synthesis and Storage

The racemic polyanion poly(L,D)-glutamate sodium salt (pRE) was purchased from Alamanda Polymers Inc. This is a 50/50 random copolymer of L- and D-glatamate stereoisomers. Poly(L-

lysine hydrochloride) (pLK) was purchased from Alamanda Polymers Inc. or prepared in-house via N-carboxyanhydride (NCA) polymerization and characterized using gel permeation chromatography (GPC) and ^{1}H NMR (Kramer and Deming, 2010). See Table 5.11 for the source, mean degree of polymerization, molecular weight, polydispersity, for the polypeptides used in each figure.

Stock solutions were prepared gravimetrically using MilliQ water (resistivity of 18.2 MΩ-cm, Millipore) at concentrations of either 10 or 20 mM with respect to the number of monomers (that is, the number of acid or base groups) present in solution and then adjusted to pH 7.0 using concentrated solutions of HCl and NaOH, as needed. These solutions were stored at 4 °C, and wrapped in parafilm to minimize evaporation. Unless otherwise noted, peptide concentrations are reported in terms of charge equivalents. For instance, a concentration of 5 mM pLK indicates a 5 mM concentration of lysine residues, each with an average charge equivalent of +1 at pH 7. Correspondingly, the concentration of pLK molecules is 50 μM, with each pLK molecule composed of, on average, 100 +1-charged lysine residues.

Protein Purification, Labeling, and Storage

Actin was purified from rabbit skeletal muscle acetone powder (Pel-Freez) as previously described (Spudich and Watt, 1971). A subset of gel-filtered actin was labeled on Cys-347 with either Oregon green 488 iodoacetamide (OG), Tetramethylrhodamine-5-maleimide (TMR), or pyrenyl iodoacetamide (Invitrogen) (Kovar et al., 2003; Kudryashov and Reisler, 2003; Kuhn and Pollard, 2005). All actins were stored in Calcium Buffer-G (CaBG: 2 mM Tris-HCl, pH 8.0 at 22 °C, 0.2 mM ATP (adenosine triphosphate), 0.5 mM DTT (1,4-Dithiothreitol), 0.1 mM $CaCl_2$, 1 mM NaN_3). Unlabeled, OG- and pyrene-labeled actins were stored at 4 °C,

while TMR-labeled actin was flash-frozen with liquid nitrogen and stored at -80 °C. Prior to use, non-frozen actins were dialyzed against 0.2 L fresh CaBG for 18-24 h, and clarified via ultracentrifugation at 177,000 x g (average relative centrifugal force) for 30 minutes at 4 °C. The top 90% of the supernatant was retained, stored on ice, and used within 6 days. TMR-actin was rapidly thawed by hand, and similarly clarified via ultracentrifugation at 177,000 x g for 30 minutes at 4 °C. The top 75% of the supernatant was retained, stored on ice, and used within 2 days.

Bovine Serum Albumin (BSA) (Fraction V, Fisher Scientific) was labeled on exposed cysteines with Alexa Fluor 647 Maleimide (Invitrogen) according to the manufacturer's protocol, and stored in 1x Phosphate-Buffered Saline (PBS, pH 7.5 at room temperature) at -80 °C. Prior to use, labeled BSA was thawed rapidly by hand, and clarified by centrifugation at 21,000 x g for 20 minutes at 4 °C. The entire supernatant was retained, stored at 4 °C, and used within one month.

Protein Concentration Determination

Protein concentrations were determined spectrophotometrically. Absorbance measurements were made using an Ultrospec 2100 pro (Amersham Biosciences) or a NanoDrop ND-1000 (Thermo Scientific) UV/VIS Spectrophotometer with optical path lengths b = 1 cm and b = 0.1 cm, respectively. Sample absorbance was converted to protein concentration (and corrected for label absorbance, as appropriate) using the following expressions:

[Unlabeled-actin] = $\langle A_{290} \rangle$ *(38.5 µM cm) / b (Hansen et al., 2013)

For OG-labeled actin (Kuhn and Pollard, 2005):

[Total actin] = ($\langle A_{290} \rangle$ - (0.17*$\langle A_{491} \rangle$))*(38.5 µM cm) / b

[OG-actin] = $\langle A_{491} \rangle$ / ((0.0778 μM^{-1} cm^{-1})*b)

For TMR-labeled actin:

[Total actin] = ($\langle A_{290} \rangle$ - (0.1185* $\langle A_{557} \rangle$))*(38.5 µM cm) / b

[TMR-actin] = $\langle A_{557} \rangle$ / ((0.1009 μM^{-1} cm^{-1})*b)

For Pyrene-labeled actin (Hansen et al., 2013):

[Total actin] = ($\langle A_{290} \rangle$ - (0.127*$\langle A_{344} \rangle$))*(38.5 µM cm) / b

[Pyrene-actin] = $\langle A_{344} \rangle$*(45.0 µM cm) / b

For BSA, the molar extinction coefficient was estimated to be E_{280} = 40,800 M^{-1} cm^{-1} using the online tool ProtParam (http://web.expasy.org/protparam/), the amino acid sequence associated with the UniProt ID P02769 for *Bos taurus* serum albumin, and assuming reduced Cys residues. The approximate extinction coefficient for Alexa Fluor 647 C_2 maleimide is E_{650} = 265,000 M^{-1} cm^{-1} (Molecular Probes). The concentration of BSA and Alexa Fluor 647 were thus calculated according to:

[Total BSA] = ($\langle A_{280} \rangle$ -(0.03*$\langle A_{651} \rangle$)) / ((0.0408 μM^{-1} cm^{-1})*b)

[Alexa 647] = $\langle A_{651} \rangle$ / ((0.265 μM^{-1} cm^{-1})*b)

Sample Preparation

Mg-ATP-actin is prepared in Tube A from Ca-ATP-actin by 2-minute incubation at room temperature (RT) with 1/10th volume 10x Magnesium Exchange buffer (1x ME buffer: 50 µM $MgCl_2$, 200 µM EGTA (ethylene glycol-bis(beta-aminoethyl ether)-N,N,N',N'-tetraacetic acid) in MilliQ-purified water, stored at RT). Mg-ATP-actin is then incubated at RT with either Latrunculin A dissolved in DMSO (dimethyl sulfoxide) for 5 min or an equivalent volume of DMSO, as a blank, for minimal time (< 30 s), followed by addition of pLK (or a blank of

MilliQ-purified water) and incubation for 2-3 min at RT. Tube B is assembled from 10x KMEI buffer (1x KMEI: 50 mM KCl, 1 mM $MgCl_2$, 1 mM EGTA, 10 mM Imidazole, pH 7.0, stored at RT), Magnesium Buffer-G (MgBG: 2 mM Tris-HCl, pH 8.0, 22 °C, 0.2 mM ATP, 0.5 mM DTT, 0.1 mM $MgCl_2$, 1 mM NaN_3, stored on ice), and pRE (or a blank of MilliQ-purified water). Polyelectrolyte phase separation and actin polymerization is then initiated simultaneously through the addition of Tube B to Tube A and rapid mixing by pipette. Samples with ~ 1 mM or more total polypeptide are visibly turbid < 2 s after addition of Tube B to Tube A.

Microscopy

Samples were loaded into flow cells constructed from mPEG-Silane-treated glass and double-sided tape, as described previously (Winkelman et al., 2014). Samples were imaged at room temperature (~24 °C) on an inverted microscope (Ti-Eclipse; Nikon, Melville, NY) equipped with a confocal scan head (CSU-X, Yokogawa Electric, Musashino, Tokyo, Japan), a laser merge module (LMM5, Spectral Applied Research, Richmond Hill, Ontario, Canada) containing 488-nm, 560-nm, and 635-nm laser lines for fluorescence imaging, as well as polarizers, Nemarski prisms, and a white transmitted-light source for differential interference contrast (DIC) imaging. Images were formed using a 60x, DIC-compatible, water-immersion objective (Nikon, Melville, NY) with a numerical aperature (NA) of 1.2, and corrections for apochromatic and flat field aberrations (Plan Apo). Images were acquired on a scientific complementary metal-oxide-semiconductor (sCMOS) camera (Zyla 4.2; Andor Technologies, Belfast, Northern Ireland), with a physical pixel size of 6.5 microns per side. All imaging hardware was controlled using METAMORPH acquisition software (Molecular Devices, Eugene, OR).

Image Analysis

All quantitative image analysis was performed using imageJ (NIH, imagej.nih.gov/ij/) and custom code written in MATLAB (MathWorks, Natick, MA). Camera dark noise (100 counts) was subtracted from all fluorescence images prior to analysis.

Measurement of average partition coefficient. Following camera noise subtraction, fluorescence images were corrected for uneven illumination (Jönsson et al., 2008) using a reference fluorescence image of a plastic slide. Two masks were created for each corrected fluorescence image by thresholding. The first is called the background mask, and the second is called the droplet mask. Note that in order to reduce the impact of imaging artifacts which result from spinning-disk confocal imaging, such as pin-hole crosstalk, the background mask is not simply the inverse of the droplet mask (Banani et al., 2016; Shimozawa et al., 2013). We used the modal pixel intensity from the illumination-corrected fluorescence image as the threshold for the background mask. After application of the threshold, the close, invert, close, and fill holes operations were applied in ImageJ. This procedure yields a mask which excludes droplets, as well as regions outside of droplets where systematic pin-hole cross-talk effects are visible.

To create the droplet mask, the illumination-corrected image was thresholded again, this time using the average full-width-at-half-max intensity obtained from linescans across 5-10 coacervate droplets in the field of view. After application of the threshold, the invert, close, fill holes, and invert operations were applied in ImageJ.

Individual candidate droplets were then automatically identified from the droplet mask using custom code written in MATLAB. Candidate droplets were filtered by size and eccentricity. As a result of the strong peripheral localization of actin fluorescence, candidate droplets occasionally had a crescent-like morphology, similar to an unclosed circle. This occurred if the fluorescence

at some position along the droplet boundary was below the masking threshold. To remove droplets for which the mask gave unclosed circles, candidate droplets in actin fluorescence images were further filtered by removing candidates for which the center of mass fell outside the candidate droplet region. The size and average intensity of each filtered droplet was then computed using the droplet mask and the illumination-corrected fluorescence image. The average background intensity was computed using the background mask and the illumination-corrected image. Finally, the average partition coefficient for each droplet was calculated as the ratio of the average intensity within the droplet mask to the average background intensity.

Measurement of peripheral and interior partition coefficients. Fluorescence intensity linescans are calculated using a transverse width of 5 pixels along paths indicated in the accompanying image, and normalized according to

$$I_{\text{norm}}(x) = \left(I(x) - I_{\text{min}}\right) / \left(I_{\text{max}} - I_{\text{min}}\right) \quad (1)$$

where *I(x)* is the intensity at position *x* along the path, and I_{min} and I_{max} are the minimum and maximum values of the intensity along the path, respectively. Interior, Periphery, and Exterior fluorescence values (e.g. Fig. 5.8F) are obtained from individual linescans. Interior is the average of a 5-pixel segment along the linescan, co-centered with the droplet. Periphery is the average of the maximum intensity along the linescan from either side of the droplet center. Exterior signal is calculated on each side of the droplet as the average intensity along the 6-pixel segment of the linescan extending from 10 pixels beyond the periphery peak to 15 pixels beyond the peak. The reported Exterior value is the average of the Exterior signals from each side of the linescan. One-sided Exterior values (as opposed to the average of both sides) are reported when the relevant segment on one side of the linescan impinges upon an adjacent droplet. Linescan orientation is

chosen to minimize the frequency of this. Partitioning coefficients (Banani et al., 2016) are calculated as the ratio of either Periphery or Interior fluorescence to Exterior fluorescence.

Measurement of fluorescence intensity correlation coefficients. Calculation of fluorescence intensity correlation coefficients is restricted to include only pixels within droplets using a mask for each field of view. Masks were generated in ImageJ from DIC images taken at the approximate midplane of the droplet of interest by application of a Gaussian blur (radius 1.00), threshold-based conversion to a binary image, and the sequential application of the binary operations close, fill holes, and dilate, where dilate is applied twice. The intensities in the fluorescence cross-correlation histogram (e.g. Fig. 5.6C) are normalized independently in each channel according to equation (1) above, where the domain of x is all pixels identified from the mask as within droplets.

Fluorescence Spectroscopy

A stock solution of 15 µM Ca-ATP-actin (typically 10-20 % pyrene-labeled) is prepared from solutions of unlabeled and highly-labeled (typically > 90 %) actin in a 1.5-mL microcentrifuge tube, and then converted from Ca-ATP-actin by 2-minute incubation with 1/10th volume 10x ME buffer and 1/10th volume of 100x anti-foam (Antifoam 204, Sigma) at RT. Mg-ATP-actin is then incubated with the desired concentration of pLK (or a blank of MilliQ-purified water) for 2-3 min at RT in up to 12 rows of a 96-well plate (Assay Plate 3686, Corning). A multichannel pipette is then used to simultaneously deliver solution assembled from 10x KMEI buffer MgBG, and pRE (or a blank of MilliQ-purified water) to the wells containing actin, thereby initiating assembly (through the addition of $MgCl_2$ and KCl) and phase separation (through the addition of the polyanion) simultaneously. The final reaction volume is 150 µL. Actin assembly is

monitored at RT by pyrene fluorescence (Excitation: 365 nm, Emission: 407 nm) in a fluorescence plate reader (Saphire2, Tecan). The timecourse of pyrene excimer fluorescence (Excitation: 343 nm, Emission: 478 nm (Bubb et al., 2002) was monitored concomitantly with assembly by sequentially alternating the excitation/emission wavelength pairs on a fluorescence plate reader (Infiniti m200, Tecan). We report the reciprocal of the time to 50 %-assembly ($1/t_{1/2}$) as a measure of the mean assembly rate. $t_{1/2}$ is determined for each 407-nm fluorescence timecourse as the time-point at which the fluorescence intensity is closest to $I_{1/2}$, which is defined as

$$I_{1/2} = \left(I_{\max} + I_0\right)/2 \tag{2}$$

where $I_{\max}$ is the maximum intensity of the timecourse, and I_0 is the initial fluorescence value of the actin-only control sample, which is an estimate of the sum of background contributions from the detector, buffers, and pyrene-actin monomers for all conditions.

Physical Estimates

Estimation of osmotic pressure required to crowd F-actin to an interface. We estimate the minimum osmotic pressure needed to crowd F-actin to an interface as that of a 0.25 % (w/v) methylcellulose solution, which is known to be sufficient (Murrell and Gardel, 2012). Using the van 't Hoff formula $\Pi = cN_A k_B T$ for the osmotic pressure of a dilute polymer at molar concentration c, where N_A is Avagadro's number, we find that a concentration of $c = 0.25\% \cong 180\ \mu M$ of 14-kDa methylcellulose gives a pressure of $\Pi^* \cong 450$ Pa at room temperature.

Estimation of polypeptide species concentration in dilute phase. The dilute phase concentration of a polypeptide is the critical concentration for phase separation at that temperature and salt concentration. Thus, observation of droplet formation upon mixing of pLK

with pRE, each at a final global concentration X, indicates that X is greater than the critical concentration, and thereby greater than the dilute phase concentration. pLK/pRE coacervate droplets are visible by DIC at concentrations of 30 μM per polypeptide and above. However, punctate BSA fluorescence is observed at 3 μM per polypeptide, even though droplets are not readily discernible by DIC. This suggests that phase separation does still occur at this concentration. We thus use 3000 nM / 100 residues per polypeptide = 30 nM as a conservative upper bound on the dilute phase concentration for each polypeptide chain species.

Estimation of polypeptide concentration in coacervate phase. From dimensional analysis, we estimate the polypeptide concentration in the coacervate phase from the mass fraction according to $c = \rho_{pp} f_{pp} / M_W$, where ρ_{pp} is the mass density of a solid polypeptide substance, f_{pp} is the polypeptide mass fraction in the coacervate phase, and M_W is the polypeptide molecular weight. We estimate the polypeptide mass density ρ_{pp} as the density of solid glutamic acid, ρ_E = 1538 mg/mL (Pubchem). Unpublished measurements of f_{pp} for pLK/pRE coacervates under similar conditions find a total polypeptide mass fraction of 0.38, or 0.19 per polypeptide species. This is comparable to previously published reports on other coacervate systems, where the water content was reported to saturate at ~ 60 % (Spruijt et al., 2010). Using these values, and approximating the molecular weight as 12.9 kDa (Table 5.1), yields a polypeptide chain concentration of ~2 mM per species, corresponding to a peptide concentration of ~ 2 M per species. In the main text, we thus report the pLK concentration estimate as being on the order of 1-3 M in the coacervate phase.

Estimation of coacervate mesh size. We estimate the mesh size as (de Gennes, 1979) $\xi = R_F \left(\Phi^*_{pp} / \Phi_{pp} \right)^{3/4}$, where R_F is the root-mean-square end-to-end distance of the polypeptide,

Φ^*_{pp} is the polypeptide volume fraction at which spheres of radius R_F containing one polymer each begin to overlap, and Φ_{pp} is the polypeptide volume fraction of the coacervate phase. Treating the polypeptides as self-avoiding flexible chains in good solvent, we have that (de Gennes, 1979) $R_F = aN^{\nu} = aN^{3/5}$, where a is the effective monomer size of the self-avoiding chain, N is the number of such monomers per chain, and ν is the Flory exponent. We also have that $\Phi^*_{pp} \cong c^* a^3 = \frac{N}{R_F{}^3} a^3 = N^{-4/5}$, where c^* is the overlap polymer concentration. Combining these expressions gives (de Gennes, 1979) $\xi = a\Phi_{pp}{}^{-3/4}$.

We take the effective monomer size of a polypeptide in the coacervate phase to be the Kuhn length, which we estimate as (Hanke et al., 2010) 0.8 +/- 0.1 nm. We estimate the volume fraction as

$$\Phi_{pp} = \frac{f_{pp}}{f_{pp} + \left(1 - f_{pp}\right)\frac{\rho_{pp}}{\rho_{\text{solvent}}}}. \quad (3)$$

Taking the total polypeptide mass fraction to be f_{pp} = 0.38 as above, and approximating ρ_{solvent} as 1000 mg/mL, we estimate the volume fraction as Φ_{pp} = 0.28. Combined with the Kuhn length estimate, this gives a mesh size estimate of ~2.1 nm. In the main text, we estimate the mesh-size as 2-3 nm in the coacervate phase.

Section 5.9 REFERENCES

Alberts, B., Johnson, A., Lewis, J., Raff, M., Roberts, K., and Walter, P. (2007). Molecular Biology of the Cell (New York, NY: Garland Science).

Amblard, F., Maggs, A.C., Yurke, B., Pargellis, A.N., and Leibler, S. (1996). Subdiffusion and Anomalous Local Viscoelasticity in Actin Networks. Phys. Rev. Lett. *77*, 4470–4473.

Andelman, D., and Joanny, J.-F. (2000). Polyelectrolyte adsorption. Comptes Rendus Académie Sci. - Ser. IV - Phys. *1*, 1153–1162.

Andrianantoandro, E., and Pollard, T.D. (2006). Mechanism of actin filament turnover by severing and nucleation at different concentrations of ADF/cofilin. Mol. Cell *24*, 13–23.

Asakura, S., and Oosawa, F. (1954). On Interaction between Two Bodies Immersed in a Solution of Macromolecules. J. Chem. Phys. *22*, 1255–1256.

Aumiller Jr, W.M., and Keating, C.D. (2016). Phosphorylation-mediated RNA/peptide complex coacervation as a model for intracellular liquid organelles. Nat. Chem. *8*, 129–137.

Banani, S.F., Rice, A.M., Peeples, W.B., Lin, Y., Jain, S., Parker, R., and Rosen, M.K. (2016). Compositional Control of Phase-Separated Cellular Bodies. Cell *166*, 651–663.

Berro, J., Sirotkin, V., and Pollard, T.D. (2010). Mathematical Modeling of Endocytic Actin Patch Kinetics in Fission Yeast: Disassembly Requires Release of Actin Filament Fragments. Mol. Biol. Cell *21*, 2905–2915.

Black, K.A., Priftis, D., Perry, S.L., Yip, J., Byun, W.Y., and Tirrell, M. (2014). Protein Encapsulation via Polypeptide Complex Coacervation. ACS Macro Lett. *3*, 1088–1091.

Blair, D., and Dufresne, E. Matlab Particle Tracking.

Blanchoin, L., and Pollard, T.D. (1998). Interaction of Actin Monomers with AcanthamoebaActophorin (ADF/Cofilin) and Profilin. J. Biol. Chem. *273*, 25106–25111.

Blanchoin, L., and Pollard, T.D. (1999). Mechanism of Interaction of Acanthamoeba Actophorin (ADF/Cofilin) with Actin Filaments. J. Biol. Chem. *274*, 15538–15546.

Blanchoin, L., Boujemaa-Paterski, R., Sykes, C., and Plastino, J. (2014). Actin Dynamics, Architecture, and Mechanics in Cell Motility. Physiol. Rev. *94*, 235–263.

Bon, S.A.F. (2014). CHAPTER 1:The Phenomenon of Pickering Stabilization: A Basic Introduction. In Particle-Stabilized Emulsions and Colloids, pp. 1–7.

Brangwynne, C.P., Eckmann, C.R., Courson, D.S., Rybarska, A., Hoege, C., Gharakhani, J., Jülicher, F., and Hyman, A.A. (2009). Germline P Granules Are Liquid Droplets That Localize by Controlled Dissolution/Condensation. Science *324*, 1729–1732.

Brangwynne, C.P., Mitchison, T.J., and Hyman, A.A. (2011). Active liquid-like behavior of nucleoli determines their size and shape in Xenopus laevis oocytes. Proc. Natl. Acad. Sci. *108*, 4334–4339.

Bray, D., and White, J.G. (1988). Cortical flow in animal cells. Science *239*, 883–888.

Breitsprecher, D., Jaiswal, R., Bombardier, J.P., Gould, C.J., Gelles, J., and Goode, B.L. (2012). Rocket Launcher Mechanism of Collaborative Actin Assembly Defined by Single-Molecule Imaging. Science *336*, 1164–1168.

Brieher, W. (2013). Mechanisms of actin disassembly. Mol. Biol. Cell *24*, 2299–2302.

Broedersz, C.P., and MacKintosh, F.C. (2014). Modeling semiflexible polymer networks. Rev. Mod. Phys. *86*, 995–1036.

Broedersz, C.P., Depken, M., Yao, N.Y., Pollak, M.R., Weitz, D.A., and MacKintosh, F.C. (2010). Cross-Link-Governed Dynamics of Biopolymer Networks. Phys. Rev. Lett. *105*, 238101.

Brown, S.S., and Spudich, J.A. (1979). Nucleation of polar actin filament assembly by a positively charged surface. J. Cell Biol. *80*, 499–504.

Bubb, M.R., Govindasamy, L., Yarmola, E.G., Vorobiev, S.M., Almo, S.C., Somasundaram, T., Chapman, M.S., Agbandje-McKenna, M., and McKenna, R. (2002). Polylysine Induces an Antiparallel Actin Dimer That Nucleates Filament Assembly CRYSTAL STRUCTURE AT 3.5-Å RESOLUTION. J. Biol. Chem. *277*, 20999–21006.

Bugyi, B., and Carlier, M.-F. (2010). Control of Actin Filament Treadmilling in Cell Motility. Annu. Rev. Biophys. *39*, 449–470.

Burtnick, L.D., Koepf, E.K., Grimes, J., Jones, E.Y., Stuart, D.I., McLaughlin, P.J., and Robinson, R.C. (1997). The Crystal Structure of Plasma Gelsolin: Implications for Actin Severing, Capping, and Nucleation. Cell *90*, 661–670.

Carlier, M.-F., Laurent, V., Santolini, J., Melki, R., Didry, D., Xia, G.-X., Hong, Y., Chua, N.-H., and Pantaloni, D. (1997). Actin Depolymerizing Factor (ADF/Cofilin) Enhances the Rate of Filament Turnover: Implication in Actin-based Motility. J. Cell Biol. *136*, 1307–1322.

Cates, M.E. (1987). Reptation of living polymers: dynamics of entangled polymers in the presence of reversible chain-scission reactions. Macromolecules *20*, 2289–2296.

Chaudhry, F., Breitsprecher, D., Little, K., Sharov, G., Sokolova, O., and Goode, B.L. (2012). Srv2/CAP (cyclase-associated protein) forms hexameric shurikens that directly catalyze actin filament severing by cofilin. Mol. Biol. Cell mbc.E12-08-0589.

Chen, D.T.N., Wen, Q., Janmey, P.A., Crocker, J.C., and Yodh, A.G. (2010). Rheology of Soft Materials. Annu. Rev. Condens. Matter Phys. *1*, 301–322.

Christensen, J.R., Hocky, G.M., Homa, K.E., Morganthaler, A.N., Hitchcock-DeGregori, S.E., Voth, G.A., and Kovar, D.R. (2017). Competition between Tropomyosin, Fimbrin, and ADF/Cofilin drives their sorting to distinct actin filament networks. eLife *6*, e23152.

Cooper, J.A., Walker, S.B., and Pollard, T.D. (1983). Pyrene actin: documentation of the validity of a sensitive assay for actin polymerization. J. Muscle Res. Cell Motil. *4*, 253–262.

Courson, D.S., and Rock, R.S. (2010). Actin Cross-link Assembly and Disassembly Mechanics for α-Actinin and Fascin. J. Biol. Chem. *285*, 26350–26357.

Courtemanche, N., and Pollard, T.D. (2013). Interaction of Profilin with the Barbed End of Actin Filaments. Biochemistry (Mosc.) *52*, 6456–6466.

Crocker, J.C., and Grier, D.G. (1996). Methods of Digital Video Microscopy for Colloidal Studies. J. Colloid Interface Sci. *179*, 298–310.

Crocker, J.C., Valentine, M.T., Weeks, E.R., Gisler, T., Kaplan, P.D., Yodh, A.G., and Weitz, D.A. (2000). Two-Point Microrheology of Inhomogeneous Soft Materials. Phys. Rev. Lett. *85*, 888–891.

De La Cruz, E.M. (2005). Cofilin Binding to Muscle and Non-muscle Actin Filaments: Isoform-dependent Cooperative Interactions. J. Mol. Biol. *346*, 557–564.

De La Cruz, E.M. (2009a). How cofilin severs an actin filament. Biophys. Rev. *1*, 51–59.

De La Cruz, E.M. (2009b). How cofilin severs an actin filament. Biophys. Rev. *1*, 51–59.

De La Cruz, E.M., and Pollard, T.D. (1995). Nucleotide-Free Actin: Stabilization by Sucrose and Nucleotide Binding Kinetics. Biochemistry (Mosc.) *34*, 5452–5461.

De La Cruz, E.M., Martiel, J.-L., and Blanchoin, L. (2015). Mechanical Heterogeneity Favors Fragmentation of Strained Actin Filaments. Biophys. J. *108*, 2270–2281.

Didry, D., Carlier, M.-F., and Pantaloni, D. (1998). Synergy between Actin Depolymerizing Factor/Cofilin and Profilin in Increasing Actin Filament Turnover. J. Biol. Chem. *273*, 25602–25611.

Doi, M., and Edwards, S.F. (1986). The Theory of Polymer Dynamics (New York, NY: Oxford University Press).

Drenckhahn, D., and Pollard, T.D. (1986). Elongation of actin filaments is a diffusion-limited reaction at the barbed end and is accelerated by inert macromolecules. J. Biol. Chem. *261*, 12754–12758.

Feric, M., Vaidya, N., Harmon, T.S., Mitrea, D.M., Zhu, L., Richardson, T.M., Kriwacki, R.W., Pappu, R.V., and Brangwynne, C.P. (2016). Coexisting Liquid Phases Underlie Nucleolar Subcompartments. Cell *165*, 1686–1697.

Ferry, D.J. (1980). Viscoelastic Properties of Polymers (New York, NY: Wiley).

Foth, B.J., Goedecke, M.C., and Soldati, D. (2006). New insights into myosin evolution and classification. Proc. Natl. Acad. Sci. U. S. A. *103*, 3681–3686.

Frederick, K.B., Sept, D., and De La Cruz, E.M. (2008). Effects of Solution Crowding on Actin Polymerization Reveal the Energetic Basis for Nucleotide-Dependent Filament Stability. J. Mol. Biol. *378*, 540–550.

Fritzsche, M., Lewalle, A., Duke, T., Kruse, K., and Charras, G. (2013). Analysis of turnover dynamics of the submembranous actin cortex. Mol. Biol. Cell *24*, 757–767.

Fritzsche, M., Erlenkämper, C., Moeendarbary, E., Charras, G., and Kruse, K. (2016). Actin kinetics shapes cortical network structure and mechanics. Sci. Adv. *2*, e1501337.

Fujiwara, I., Vavylonis, D., and Pollard, T.D. (2007). Polymerization kinetics of ADP- and ADP-Pi-actin determined by fluorescence microscopy. Proc. Natl. Acad. Sci. *104*, 8827–8832.

Gardel, M.L., Valentine, M.T., Crocker, J.C., Bausch, A.R., and Weitz, D.A. (2003). Microrheology of Entangled F-Actin Solutions. Phys. Rev. Lett. *91*, 158302.

Gardel, M.L., Shin, J.H., MacKintosh, F.C., Mahadevan, L., Matsudaira, P., and Weitz, D.A. (2004b). Elastic Behavior of Cross-Linked and Bundled Actin Networks. Science *304*, 1301–1305.

Gardel, M.L., Shin, J.H., MacKintosh, F.C., Mahadevan, L., Matsudaira, P.A., and Weitz, D.A. (2004a). Scaling of F-Actin Network Rheology to Probe Single Filament Elasticity and Dynamics. Phys. Rev. Lett. *93*, 188102.

Gardel, M.L., Nakamura, F., Hartwig, J.H., Crocker, J.C., Stossel, T.P., and Weitz, D.A. (2006). Prestressed F-actin networks cross-linked by hinged filamins replicate mechanical properties of cells. Proc. Natl. Acad. Sci. U. S. A. *103*, 1762–1767.

de Gennes, P.-G. (1979). Scaling Concepts in Polymer Physics (Ithaca, NY: Cornell University Press).

Goode, B.L., and Eck, M.J. (2007). Mechanism and Function of Formins in the Control of Actin Assembly. Annu. Rev. Biochem. *76*, 593–627.

Gucht, J. van der, Spruijt, E., Lemmers, M., and Cohen Stuart, M.A. (2011). Polyelectrolyte complexes: Bulk phases and colloidal systems. J. Colloid Interface Sci. *361*, 407–422.

Gunning, P., O'Neill, G., and Hardeman, E. (2008). Tropomyosin-Based Regulation of the Actin Cytoskeleton in Time and Space. Physiol. Rev. *88*, 1–35.

Hanke, F., Serr, A., Kreuzer, H.J., and Netz, R.R. (2010). Stretching single polypeptides: The effect of rotational constraints in the backbone. EPL Europhys. Lett. *92*, 53001.

Hansen, S., Zuchero, J.B., and Mullins, R.D. (2013). Cytoplasmic Actin: Purification and Single Molecule Assembly Assays. In Adhesion Protein Protocols, A.S. Coutts, ed. (Humana Press), pp. 145–170.

Higgs, H.N., Blanchoin, L., and Pollard, T.D. (1999). Influence of the C Terminus of Wiskott-Aldrich Syndrome Protein (WASp) and the Arp2/3 Complex on Actin Polymerization. Biochemistry (Mosc.) *38*, 15212–15222.

Isambert, H., and Maggs, A.C. (1996). Dynamics and Rheology of Actin Solutions. Macromolecules *29*, 1036–1040.

Israelachvili, J.N. (2011). Intermolecular and Surface Forces (Amsterdam: Elsevier).

Jansen, S., Collins, A., Chin, S.M., Ydenberg, C.A., Gelles, J., and Goode, B.L. (2015). Single-molecule imaging of a three-component ordered actin disassembly mechanism. Nat. Commun. *6*, 7202.

Jégou, A., Niedermayer, T., Orbán, J., Didry, D., Lipowsky, R., Carlier, M.-F., and Romet-Lemonne, G. (2011). Individual Actin Filaments in a Microfluidic Flow Reveal the Mechanism of ATP Hydrolysis and Give Insight Into the Properties of Profilin. PLOS Biol. *9*, e1001161.

Jégou, A., Carlier, M.-F., and Romet-Lemonne, G. (2013). Formin mDia1 senses and generates mechanical forces on actin filaments. Nat. Commun. *4*, 1883.

Johnston, A.B., Collins, A., and Goode, B.L. (2015). High-speed depolymerization at actin filament ends jointly catalysed by Twinfilin and Srv2/CAP. Nat. Cell Biol. *17*, 1504–1511.

Jönsson, P., Jonsson, M.P., Tegenfeldt, J.O., and Höök, F. (2008). A Method Improving the Accuracy of Fluorescence Recovery after Photobleaching Analysis. Biophys. J. *95*, 5334–5348.

Kakran, M., and Antipina, M.N. (2014). Emulsion-based techniques for encapsulation in biomedicine, food and personal care. Curr. Opin. Pharmacol. *18*, 47–55.

Kang, H., Bradley, M.J., McCullough, B.R., Pierre, A., Grintsevich, E.E., Reisler, E., and Cruz, E.M.D.L. (2012). Identification of cation-binding sites on actin that drive polymerization and modulate bending stiffness. Proc. Natl. Acad. Sci. *109*, 16923–16927.

Kinosian, H.J., Selden, L.A., Estes, J.E., and Gershman, L.C. (1993). Nucleotide binding to actin. Cation dependence of nucleotide dissociation and exchange rates. J. Biol. Chem. *268*, 8683–8691.

Koestler, S.A., Rottner, K., Lai, F., Block, J., Vinzenz, M., and Small, J.V. (2009). F- and G-Actin Concentrations in Lamellipodia of Moving Cells. PLOS ONE *4*, e4810.

Koga, S., Williams, D.S., Perriman, A.W., and Mann, S. (2011). Peptide–nucleotide microdroplets as a step towards a membrane-free protocell model. Nat. Chem. *3*, 720–724.

Kovar, D.R., Kuhn, J.R., Tichy, A.L., and Pollard, T.D. (2003). The fission yeast cytokinesis formin Cdc12p is a barbed end actin filament capping protein gated by profilin. J. Cell Biol. *161*, 875–887.

Kovar, D.R., Harris, E.S., Mahaffy, R., Higgs, H.N., and Pollard, T.D. (2006). Control of the Assembly of ATP- and ADP-Actin by Formins and Profilin. Cell *124*, 423–435.

Kramer, J.R., and Deming, T.J. (2010). General Method for Purification of α-Amino acid-N-carboxyanhydrides Using Flash Chromatography. Biomacromolecules *11*, 3668–3672.

de Kruif, C.G., Weinbreck, F., and de Vries, R. (2004). Complex coacervation of proteins and anionic polysaccharides. Curr. Opin. Colloid Interface Sci. *9*, 340–349.

Kudryashov, D.S., and Reisler, E. (2003). Solution Properties of Tetramethylrhodamine-Modified G-Actin. Biophys. J. *85*, 2466–2475.

Kueh, H.Y., Brieher, W.M., and Mitchison, T.J. (2010). Quantitative Analysis of Actin Turnover in Listeria Comet Tails: Evidence for Catastrophic Filament Turnover. Biophys. J. *99*, 2153–2162.

Kuhn, J.R., and Pollard, T.D. (2005). Real-Time Measurements of Actin Filament Polymerization by Total Internal Reflection Fluorescence Microscopy. Biophys. J. *88*, 1387–1402.

Lecuit, T., Lenne, P.-F., and Munro, E. (2011). Force Generation, Transmission, and Integration during Cell and Tissue Morphogenesis. Annu. Rev. Cell Dev. Biol. *27*, 157–184.

Lenz, M., Thoresen, T., Gardel, M.L., and Dinner, A.R. (2012). Contractile Units in Disordered Actomyosin Bundles Arise from F-Actin Buckling. Phys. Rev. Lett. *108*, 238107.

Li, F., and Higgs, H.N. (2003). The Mouse Formin mDia1 Is a Potent Actin Nucleation Factor Regulated by Autoinhibition. Curr. Biol. *13*, 1335–1340.

Li, P., Banjade, S., Cheng, H.-C., Kim, S., Chen, B., Guo, L., Llaguno, M., Hollingsworth, J.V., King, D.S., Banani, S.F., et al. (2012). Phase transitions in the assembly of multivalent signalling proteins. Nature *483*, 336–340.

Lindhoud, S., and Claessens, M.M.A.E. (2015). Accumulation of small protein molecules in a macroscopic complex coacervate. Soft Matter *12*, 408–413.

Liu, J., Gardel, M.L., Kroy, K., Frey, E., Hoffman, B.D., Crocker, J.C., Bausch, A.R., and Weitz, D.A. (2006). Microrheology Probes Length Scale Dependent Rheology. Phys. Rev. Lett. *96*, 118104.

Liu, Y., Winter, H.H., and Perry, S.L. (2017). Linear viscoelasticity of complex coacervates. Adv. Colloid Interface Sci. *239*, 46–60.

Loisel, T.P., Boujemaa, R., Pantaloni, D., and Carlier, M.-F. (1999). Reconstitution of actin-based motility of Listeria and Shigella using pure proteins. Nature *401*, 613–616.

Maciver, S.K., Zot, H.G., and Pollard, T.D. (1991). Characterization of actin filament severing by actophorin from Acanthamoeba castellanii. J. Cell Biol. *115*, 1611–1620.

Matsudaira, P., Bordas, J., and Koch, M.H. (1987). Synchrotron x-ray diffraction studies of actin structure during polymerization. Proc. Natl. Acad. Sci. *84*, 3151–3155.

McCullough, B.R., Grintsevich, E.E., Chen, C.K., Kang, H., Hutchison, A.L., Henn, A., Cao, W., Suarez, C., Martiel, J.-L., Blanchoin, L., et al. (2011). Cofilin-Linked Changes in Actin Filament Flexibility Promote Severing. Biophys. J. *101*, 151–159.

Melki, R., Fievez, S., and Carlier, M.-F. (1996). Continuous Monitoring of Pi Release Following Nucleotide Hydrolysis in Actin or Tubulin Assembly Using 2-Amino-6-mercapto-7-methylpurine Ribonucleoside and Purine-Nucleoside Phosphorylase as an Enzyme-Linked Assay. Biochemistry (Mosc.) *35*, 12038–12045.

Michelot, A., Berro, J., Guérin, C., Boujemaa-Paterski, R., Staiger, C.J., Martiel, J.-L., and Blanchoin, L. (2007). Actin-Filament Stochastic Dynamics Mediated by ADF/Cofilin. Curr. Biol. *17*, 825–833.

Mitrea, D.M., and Kriwacki, R.W. (2016). Phase separation in biology; functional organization of a higher order. Cell Commun. Signal. *14*, 1.

Mizuno, D., Tardin, C., Schmidt, C.F., and MacKintosh, F.C. (2007). Nonequilibrium Mechanics of Active Cytoskeletal Networks. Science *315*, 370–373.

Molecular Probes The Molecular Probes Handbook.

Morse, D.C. (1998a). Viscoelasticity of Concentrated Isotropic Solutions of Semiflexible Polymers. 1. Model and Stress Tensor. Macromolecules *31*, 7030–7043.

Morse, D.C. (1998b). Viscoelasticity of Concentrated Isotropic Solutions of Semiflexible Polymers. 2. Linear Response. Macromolecules *31*, 7044–7067.

Mullins, R.D., Heuser, J.A., and Pollard, T.D. (1998). The interaction of Arp2/3 complex with actin: Nucleation, high affinity pointed end capping, and formation of branching networks of filaments. Proc. Natl. Acad. Sci. *95*, 6181–6186.

Murrell, M.P., and Gardel, M.L. (2012). F-actin buckling coordinates contractility and severing in a biomimetic actomyosin cortex. Proc. Natl. Acad. Sci. *109*, 20820–20825.

Nadkarni, A.V., and Brieher, W.M. (2014). Aip1 Destabilizes Cofilin-Saturated Actin Filaments by Severing and Accelerating Monomer Dissociation from Ends. Curr. Biol. *24*, 2749–2757.

Nolles, A., Westphal, A.H., de Hoop, J.A., Fokkink, R.G., Kleijn, J.M., van Berkel, W.J.H., and Borst, J.W. (2015). Encapsulation of GFP in Complex Coacervate Core Micelles. Biomacromolecules *16*, 1542–1549.

Normoyle, K.P.M., and Brieher, W.M. (2012). Cyclase-associated Protein (CAP) Acts Directly on F-actin to Accelerate Cofilin-mediated Actin Severing across the Range of Physiological pH. J. Biol. Chem. *287*, 35722–35732.

Obermeyer, A.C., Mills, C.E., Dong, X.-H., Flores, R.J., and Olsen, B.D. (2016). Complex coacervation of supercharged proteins with polyelectrolytes. Soft Matter *12*, 3570–3581.

Oriol-Audit, C. (1978). Polyamine-Induced Actin Polymerization. Eur. J. Biochem. *87*, 371–376.

Ou, Z., and Muthukumar, M. (2006). Entropy and enthalpy of polyelectrolyte complexation: Langevin dynamics simulations. J. Chem. Phys. *124*, 154902.

P G de Gennes, and Leger, and L. (1982). Dynamics of Entangled Polymer Chains. Annu. Rev. Phys. Chem. *33*, 49–61.

Pacalin, N.M., Leon, L., and Tirrell, M. (2016). Directing the phase behavior of polyelectrolyte complexes using chiral patterned peptides. Eur. Phys. J. Spec. Top. *225*, 1805–1815.

Pak, C.W., Kosno, M., Holehouse, A.S., Padrick, S.B., Mittal, A., Ali, R., Yunus, A.A., Liu, D.R., Pappu, R.V., and Rosen, M.K. (2016). Sequence Determinants of Intracellular Phase Separation by Complex Coacervation of a Disordered Protein. Mol. Cell *63*, 72–85.

Pavlov, D., Muhlrad, A., Cooper, J., Wear, M., and Reisler, E. (2007). ACTIN FILAMENT SEVERING BY COFILIN. J. Mol. Biol. *365*, 1350–1358.

Pelletier, V., Gal, N., Fournier, P., and Kilfoil, M.L. (2009). Microrheology of Microtubule Solutions and Actin-Microtubule Composite Networks. Phys. Rev. Lett. *102*, 188303.

Perry, S.L., Leon, L., Hoffmann, K.Q., Kade, M.J., Priftis, D., Black, K.A., Wong, D., Klein, R.A., Iii, C.F.P., Margossian, K.O., et al. (2015). Chirality-selected phase behaviour in ionic polypeptide complexes. Nat. Commun. *6*, 6052.

Phillips, R., Kondev, J., and Theriot, J. (2008). Physical Biology of the Cell (New York, NY: Garland Science).

Pollard, T.D. (1986). Rate constants for the reactions of ATP- and ADP-actin with the ends of actin filaments. J. Cell Biol. *103*, 2747–2754.

Pollard, T.D. (2007). Regulation of Actin Filament Assembly by Arp2/3 Complex and Formins. Annu. Rev. Biophys. Biomol. Struct. *36*, 451–477.

Pollard, T.D. (2010). Mechanics of cytokinesis in eukaryotes. Curr. Opin. Cell Biol. *22*, 50–56.

Pollard, T.D. (2016). Actin and Actin-Binding Proteins. Cold Spring Harb. Perspect. Biol. a018226.

Pollard, T.D., and Borisy, G.G. (2003). Cellular Motility Driven by Assembly and Disassembly of Actin Filaments. Cell *112*, 453–465.

Pollard, T.D., Goldberg, I., and Schwarz, W.H. (1992). Nucleotide exchange, structure, and mechanical properties of filaments assembled from ATP-actin and ADP-actin. J. Biol. Chem. *267*, 20339–20345.

Pollard, T.D., Blanchoin, L., and Mullins, R.D. (2000). Molecular Mechanisms Controlling Actin Filament Dynamics in Nonmuscle Cells. Annu. Rev. Biophys. Biomol. Struct. *29*, 545–576.

Ponti, A., Matov, A., Adams, M., Gupton, S., Waterman-Storer, C.M., and Danuser, G. (2005). Periodic Patterns of Actin Turnover in Lamellipodia and Lamellae of Migrating Epithelial Cells Analyzed by Quantitative Fluorescent Speckle Microscopy. Biophys. J. *89*, 3456–3469.

Priftis, D., Farina, R., and Tirrell, M. (2012). Interfacial Energy of Polypeptide Complex Coacervates Measured via Capillary Adhesion. Langmuir *28*, 8721–8729.

ProtParam, E. ExPASy - ProtParam tool.

Pubchem L-glutamic acid | C5H9NO4 - PubChem.

Rao, J.N., Madasu, Y., and Dominguez, R. (2014). Mechanism of actin filament pointed-end capping by tropomodulin. Science *345*, 463–467.

Reymann, A.-C., Suarez, C., Guérin, C., Martiel, J.-L., Staiger, C.J., Blanchoin, L., and Boujemaa-Paterski, R. (2011). Turnover of branched actin filament networks by stochastic fragmentation with ADF/cofilin. Mol. Biol. Cell *22*, 2541–2550.

Robin, F.B., McFadden, W.M., Yao, B., and Munro, E.M. (2014). Single-molecule analysis of cell surface dynamics in Caenorhabditis elegans embryos. Nat. Methods *11*, 677–682.

Rould, M.A., Wan, Q., Joel, P.B., Lowey, S., and Trybus, K.M. (2006). Crystal Structures of Expressed Non-polymerizable Monomeric Actin in the ADP and ATP States. J. Biol. Chem. *281*, 31909–31919.

Salbreux, G., Charras, G., and Paluch, E. (2012). Actin cortex mechanics and cellular morphogenesis. Trends Cell Biol. *22*, 536–545.

Schaus, T.E., Taylor, E.W., and Borisy, G.G. (2007). Self-organization of actin filament orientation in the dendritic-nucleation/array-treadmilling model. Proc. Natl. Acad. Sci. *104*, 7086–7091.

Schmidt, C.F., Baermann, M., Isenberg, G., and Sackmann, E. (1989). Chain dynamics, mesh size, and diffusive transport in networks of polymerized actin: a quasielastic light scattering and microfluorescence study. Macromolecules *22*, 3638–3649.

Schmoller, K.M., Semmrich, C., and Bausch, A.R. (2011). Slow down of actin depolymerization by cross-linking molecules. J. Struct. Biol. *173*, 350–357.

Sekerková, G., Richter, C.-P., and Bartles, J.R. (2011). Roles of the Espin Actin-Bundling Proteins in the Morphogenesis and Stabilization of Hair Cell Stereocilia Revealed in CBA/CaJ Congenic Jerker Mice. PLOS Genet. *7*, e1002032.

Sept, D., and McCammon, J.A. (2001). Thermodynamics and Kinetics of Actin Filament Nucleation. Biophys. J. *81*, 667–674.

Shimozawa, T., Yamagata, K., Kondo, T., Hayashi, S., Shitamukai, A., Konno, D., Matsuzaki, F., Takayama, J., Onami, S., Nakayama, H., et al. (2013). Improving spinning disk confocal microscopy by preventing pinhole cross-talk for intravital imaging. Proc. Natl. Acad. Sci. *110*, 3399–3404.

Sirotkin, V., Berro, J., Macmillan, K., Zhao, L., and Pollard, T.D. (2010). Quantitative Analysis of the Mechanism of Endocytic Actin Patch Assembly and Disassembly in Fission Yeast. Mol. Biol. Cell *21*, 2894–2904.

Skau, C.T., Neidt, E.M., and Kovar, D.R. (2009). Role of Tropomyosin in Formin-mediated Contractile Ring Assembly in Fission Yeast. Mol. Biol. Cell *20*, 2160–2173.

Sokolova, E., Spruijt, E., Hansen, M.M.K., Dubuc, E., Groen, J., Chokkalingam, V., Piruska, A., Heus, H.A., and Huck, W.T.S. (2013). Enhanced transcription rates in membrane-free protocells formed by coacervation of cell lysate. Proc. Natl. Acad. Sci. *110*, 11692–11697.

Spruijt, E., Westphal, A.H., Borst, J.W., Cohen Stuart, M.A., and van der Gucht, J. (2010). Binodal Compositions of Polyelectrolyte Complexes. Macromolecules *43*, 6476–6484.

Spudich, J.A., and Watt, S. (1971). The Regulation of Rabbit Skeletal Muscle Contraction I. BIOCHEMICAL STUDIES OF THE INTERACTION OF THE TROPOMYOSIN-TROPONIN COMPLEX WITH ACTIN AND THE PROTEOLYTIC FRAGMENTS OF MYOSIN. J. Biol. Chem. *246*, 4866–4871.

Squires, T.M., and Mason, T.G. (2010). Fluid Mechanics of Microrheology. Annu. Rev. Fluid Mech. *42*, 413–438.

Srivastava, S., and Tirrell, M.V. (2016). Polyelectrolyte Complexation. In Advances in Chemical Physics, S.A. Rice, and A.R. Dinner, eds. (Hoboken, NJ: John Wiley & Sons, Inc.), pp. 499–544.

Stuhrmann, B., Soares e Silva, M., Depken, M., MacKintosh, F.C., and Koenderink, G.H. (2012). Nonequilibrium fluctuations of a remodeling in vitro cytoskeleton. Phys. Rev. E *86*, 020901.

Su, X., Ditlev, J.A., Hui, E., Xing, W., Banjade, S., Okrut, J., King, D.S., Taunton, J., Rosen, M.K., and Vale, R.D. (2016). Phase separation of signaling molecules promotes T cell receptor signal transduction. Science *352*, 595–599.

Suarez, C., Roland, J., Boujemaa-Paterski, R., Kang, H., McCullough, B.R., Reymann, A.-C., Guérin, C., Martiel, J.-L., De La Cruz, E.M., and Blanchoin, L. (2011). Cofilin Tunes the Nucleotide State of Actin Filaments and Severs at Bare and Decorated Segment Boundaries. Curr. Biol. *21*, 862–868.

Svitkina, T.M., and Borisy, G.G. (1999). Arp2/3 Complex and Actin Depolymerizing Factor/Cofilin in Dendritic Organization and Treadmilling of Actin Filament Array in Lamellipodia. J. Cell Biol. *145*, 1009–1026.

Svitkina, T.M., Bulanova, E.A., Chaga, O.Y., Vignjevic, D.M., Kojima, S., Vasiliev, J.M., and Borisy, G.G. (2003). Mechanism of filopodia initiation by reorganization of a dendritic network. J Cell Biol *160*, 409–421.

Tang, J.X., and Janmey, P.A. (1996). The Polyelectrolyte Nature of F-actin and the Mechanism of Actin Bundle Formation. J. Biol. Chem. *271*, 8556–8563.

Theriot, J.A., and Mitchison, T.J. (1991). Actin microfilament dynamics in locomoting cells. Nature *352*, 126–131.

Theriot, J.A., and Mitchison, T.J. (1992). Comparison of actin and cell surface dynamics in motile fibroblasts. J. Cell Biol. *119*, 367–377.

Thoresen, T., Lenz, M., and Gardel, M.L. (2011). Reconstitution of Contractile Actomyosin Bundles. Biophys. J. *100*, 2698–2705.

Tinevez, J.-Y., Schulze, U., Salbreux, G., Roensch, J., Joanny, J.-F., and Paluch, E. (2009). Role of cortical tension in bleb growth. Proc. Natl. Acad. Sci. *106*, 18581–18586.

Tobolsky, A.V. (1956). Stress Relaxation Studies of the Viscoelastic Properties of Polymers. J. Appl. Phys. *27*, 673–685.

Tojkander, S., Gateva, G., and Lappalainen, P. (2012). Actin stress fibers – assembly, dynamics and biological roles. J Cell Sci *125*, 1855–1864.

Vandekerckhove, J., Deboben, A., Nassal, M., and Wieland, T. (1985). The phalloidin binding site of F-actin. EMBO J. *4*, 2815–2818.

Vieregg, J.R., and Tang, T.-Y.D. (2016). Polynucleotides in cellular mimics: Coacervates and lipid vesicles. Curr. Opin. Colloid Interface Sci. *26*, 50–57.

Vinson, V.K., De La Cruz, E.M., Higgs, H.N., and Pollard, T.D. (1998). Interactions of Acanthamoeba profilin with actin and nucleotides bound to actin. Biochemistry (Mosc.) *37*, 10871–10880.

Webb, M.R. (1992). A continuous spectrophotometric assay for inorganic phosphate and for measuring phosphate release kinetics in biological systems. Proc. Natl. Acad. Sci. *89*, 4884–4887.

Wegner, A. (1976). Head to tail polymerization of actin. J. Mol. Biol. *108*, 139–150.

Winkelman, J.D., Bilancia, C.G., Peifer, M., and Kovar, D.R. (2014). Ena/VASP Enabled is a highly processive actin polymerase tailored to self-assemble parallel-bundled F-actin networks with Fascin. Proc. Natl. Acad. Sci. *111*, 4121–4126.

Winkelman, J.D., Suarez, C., Hocky, G.M., Harker, A.J., Morganthaler, A.N., Christensen, J.R., Voth, G.A., Bartles, J.R., and Kovar, D.R. (2016). Fascin- and α-Actinin-Bundled Networks Contain Intrinsic Structural Features that Drive Protein Sorting. Curr. Biol. *26*, 2697–2706.

Wong, I.Y., Gardel, M.L., Reichman, D.R., Weeks, E.R., Valentine, M.T., Bausch, A.R., and Weitz, D.A. (2004). Anomalous Diffusion Probes Microstructure Dynamics of Entangled F-Actin Networks. Phys. Rev. Lett. *92*, 178101.

Xue, B., Leyrat, C., Grimes, J.M., and Robinson, R.C. (2014). Structural basis of thymosin-β4/profilin exchange leading to actin filament polymerization. Proc. Natl. Acad. Sci. *111*, E4596–E4605.

Yamashita, A., Maeda, K., and Maéda, Y. (2003). Crystal structure of CapZ: structural basis for actin filament barbed end capping. EMBO J. *22*, 1529–1538.

CHAPTER 6: CONCLUSIONS, IMPLICATIONS, AND FUTURE DIRECTIONS

Section 6.1 CONSEQUENCES OF NON-EQUILIBRIUM TURNOVER ON THE MECHANICS AND DYNAMICS OF OTHERWISE PASSIVE ACTIN SYSTEMS

Dynamics of individual actin filaments

The textbook picture of actin turnover is the non-equilibrium process of filament treadmilling (Alberts et al., 2007; Phillips et al., 2008). Owing to the lower critical concentration of the barbed end (0.1 μM) relative to the pointed end (0.7 μM) in the presence of ATP and the absence of regulatory proteins, the G-actin concentration at steady state is an intermediate value between the critical concentrations of the two ends. A direct result of this, first appreciated by Wegner more than 40 years ago (Wegner, 1976), is that, at steady-state, individual filaments elongate from their barbed-ends and depolymerize from their pointed ends at equal rates, causing ballistic motion of the filament center-of-mass at a kinetically-defined velocity. The treadmilling velocity of purified actin in solution is very slow in the absence of regulatory proteins, however. From phosphate-release measurements, we calculate the per-filament turnover rate to be 0.14 subunits/s, corresponding to a treadmilling velocity of 0.022 μm/min, and comparable to previous results (Pollard and Borisy, 2003).

In Chapter 3 of this thesis, we examined a related but microscopically distinct form of actin filament turnover which is regulated by cofilin, profilin, and formin. The Blanchoin lab first showed in 2007 that this suite of proteins was sufficient to enhance turnover of individual actin *in vitro* (Michelot et al., 2007). Using formins clustered on microspheres to nucleate filaments, they observed that actin filaments elongating rapidly from the formin-coated beads were stochastically severed by cofilin. Ignoring the filament fragments released to solution, the length

of the formin-associated filament was observed to fluctuate in time around a stable mean value for the duration of the formin's processive run, up to ~10 minutes. The time-averaged mean length of the individual filament thus remained constant, while turnover was enhanced up to 155-fold over actin alone (Michelot et al., 2007). The single-filament dynamics examined by Michelot et al. were not representative of steady-state, however. While the individual filaments were in a quasi-steady-state, in the sense that the elongation rate was ~ constant while the formin remained bound, it was far from steady-state in the sense of the closed system (ATP notwithstanding), because the monomer concentration was still high above steady-state levels and falling as a result of elongation.

We have shown in this thesis that cofilin, profilin, and (soluble) formin are sufficient to enhance *in vitro* actin turnover *at steady-state* in the sense of the closed system, though to a lesser extent (22-fold over actin alone) than the during the quasi-steady-states measured during bulk assembly by Michelot et al. The assessment of filament turnover at steady-state is significant for two reasons. First, it is an essential prerequisite for characterizing the impact of such dynamics on other steady-state system properties, such as mechanical response. Second, the observation of actin turnover sustained at an enhanced rate at steady-state necessitated formulation of a biochemical rationalization which in turn advances our understanding of the underlying microscopic dynamics.

Of particular importance in the case of steady-state turnover is the fate of the severed filament fragment, neglected by Michelot et al., which is not bound to a formin. The strong preference of cofilin to bind and sever in ADP-rich regions of actin filaments gives rise to an asymmetry in the chemical composition of the two filament fragments generated upon severing; whereas the (stable) formin-bound fragment retains an ATP gradient along its length, the other

(unstable) fragment is predominantly ADP along its entire length, and in particular at its ends. The critical concentration for ADP-actin is ~1.8 μM (Fujiwara et al., 2007; Pollard, 1986), and well above the steady-state ~0.5 μM G-actin concentration we infer from the turnover rate. Consequently, the unstable fragment is thermodynamically unstable (as the name implies), and depolymerizes from both ends, with the barbed-end rate incidentally accelerated by the high steady-state concentrations of unbound profilin present in our experiments (Courtemanche and Pollard, 2013; Jégou et al., 2011). The filament number fluctuation incurred by the severing reaction is therefore rectified by the preferential disassembly of exactly one of the fragments. Thus the compositional asymmetry, exposed by cofilin severing, is fundamentally what causes the unstable fragment to disassemble while the stable fragment continues to elongate, thereby enabling a non-equilibrium steady-state characterized by fast turnover, large severing-induced length fluctuations, and rectified filament number fluctuations.

The situation *in vivo* is quite different in at least three respects. First, the cytoplasmic concentrations of G-actin are as much as μM in rapidly migrating cells (Koestler et al., 2009), much higher than those at steady-state in our *in vitro* experiments. Although the majority of that is likely bound by a sequestering factor, such as thymosin-β4, and is therefore assembly incompetent (Pollard and Borisy, 2003), measurements of filament elongation by individual formin dimers *in vivo* (Fritzsche et al., 2016) indicate that the concentration of the polymerizable G-actin pool is still above the ADP-actin critical concentration in HeLa and melanoma M2 cells. This conclusion has also been reached in other cell lines on the basis of protrusion speeds and the rates of intracellular pathogen motility (Pollard and Borisy, 2003). The high concentration of assembly-competent G-actin in cells would indicate that the compositional asymmetry between

severed fragments, which we argue is crucial for fast turnover *in vitro*, should not be relevant *in vivo*.

A second important difference is that a large fraction of the filaments *in vivo* are capped at both ends. In particular, actin networks with some of the fastest turnover rates, including the lamellipodia of migrating cells (Ponti et al., 2005; Theriot and Mitchison, 1991, 1992) and the endocytic patches of fission yeast (Berro et al., 2010; Sirotkin et al., 2010), contain many filaments capped by the Arp2/3 complex at the pointed end and capping protein at the barbed end (Mullins et al., 1998; Svitkina and Borisy, 1999), and are thus unable to turnover via subunit exchange at filament ends. Historically, these *in vivo* observations definitively ruled out canonical filament treadmilling as the mechanism of actin turnover in the relevant for motility, and motivated the dendritic nucleation and treadmilling filament array model (Pollard and Borisy, 2003; Schaus et al., 2007; Svitkina and Borisy, 1999). In this treadmilling filament array model, filaments nucleated at the leading edge elongate, are rapidly capped, recede towards the cell interior via retrograde actin flow, and then are disassembled by cofilin, and recycled for further assembly at the leading edge by profilin. The lamellipodial array is thus said to treadmill, as it maintains a constant width reflecting a balance between leading-edge assembly and interior disassembly. Importantly, although the importance of cofilin and profilin for the treadmilling array model of turnover is codified by their necessity in minimal *in vitro* motility assays (Loisel et al., 1999), filament capping distinguishes this mechanisms fundamentally from the turnover we described in Chapter 3. Whereas the treadmilling array model requires constant nucleation of new filaments at steady-state, nucleation is strongly suppressed in our system, and the stable formin-bound filaments persist indefinitely (formin (un)binding kinetics notwithstanding).

A third major difference between our minimal *in vitro* system and cells is, by definition, the presence of many additional actin regulatory factors *in vivo*. Significant progress towards understanding how multiple actin binding proteins cooperative to facilitate actin disassembly has been made in recently using *in vitro* reconstitutions. Aip1, coronin, Srv2-CAP, and twinfilin (the last of which is contains two tandem cofilin homology domains), have all been shown to catalyze filament disassembly by enhancing cofilin-mediated severing and depolymerization from ends (Brieher, 2013; Chaudhry et al., 2012; Jansen et al., 2015; Johnston et al., 2015; Nadkarni and Brieher, 2014; Normoyle and Brieher, 2012). In particular, Jansen et al. demonstrated that cofilin Aip1 and coronin promoted turnover of formin-bound filaments through severing and preferential disassembly of the unstable, ADP-rich fragments, though with a role played by Aip1 capping and little discussion of profilin. Further, Johnston et al. showed that the increase to pointed-end dissociation kinetics engendered by ADP-biased binding of twinfilin and Srv2-CAP enabled balanced barbed-end elongation and pointed-end disassembly under assembly-promoting conditions. Thus, with the benefit of additional cofactors, the compositional asymmetry in cofilin-severed fragments may still be relevant for understanding the rapid turnover observed in some cellular actin filament networks.

Mechanics of entangled actin filament solutions

While the importance of filament length for the mechanics of entangled actin filament solutions has received both theoretical and experimental attention (Liu et al., 2006; Morse, 1998a, 1998b), previous work on contribution of actin turnover to solution mechanics has, to the best of my knowledge, been limited to passing comments (Carlier et al., 1997; Isambert and Maggs, 1996). We show in this thesis that cofilin-mediated turnover strongly modulates the steady-state

viscoelasticity of entangled actin filament solutions. On timescales longer than the polymer entanglement time of ~ 1 sec, the mobility of 1-μm microspheres embedded in entangled actin solutions is elevated in the presence of cofilin, with a biphasic concentration dependence. The mobility modulation is maximal at a cofilin:actin mole ratio of R_C ~ 0.5, and reduces at higher cofilin concentrations. Assuming the that the fluctuation-dissipation theorem (FDT) is only weakly broken in non-equilibrium conditions present here (discussed more below), and thus that the Generalized Stokes-Einstein Relation holds, we infer that the cofilin-mediated severing and turnover tunes the entangled solution fluidity via a mechanical stress relaxation mechanism characterized by a single timescale. The terminal viscoelastic relaxation time we estimate from rescaled mobility data shows a biphasic cofilin concentration dependence, reminiscent of the biphasic dependence of the cofilin-mediated severing rate (De La Cruz, 2005, 2009b; McCullough et al., 2011; Suarez et al., 2011), strongly implicating severing as a central feature of the relaxation mechanism.

Interestingly, the dependence of the relaxation time of mean filament length which we report in the presence of optimal cofilin concentrations is significantly weaker than the cubic dependence we observe in the absence of cofilin, the latter of which is consistent with expectations for relaxation dominated by filament reptation (Doi and Edwards, 1986; P G de Gennes and Leger, 1982). The strongest length dependence consistent with the data reported in this thesis is linear, consistent with the scaling expectation for a tube model (Doi and Edwards, 1986; de Gennes, 1979) in which the dominant contribution to stress relaxation comes from ballistic filament transport at a constant velocity, as with canonical treadmilling, as opposed to diffusive reptation. However, the magnitude of the treadmilling velocity from steady-state turnover measurements is more than two orders of magnitude too slow to account for the

observed relaxation times. This indicates that canonical filament treadmilling does not readily account for the relaxation.

Scaling predictions for the stress relaxation timescale exist for other polymer systems in which severing plays a key role. Motivated by entangled solutions of worm-like micelles, which break and re-anneal at a constant rate per unit length, Cates (Cates, 1987) showed theoretically that the relaxation of time of such "living polymers" goes as the geometric mean of the severing and reptation times. This gives rise to a quadratic dependence of relaxation time on filament length and linear dependence of relaxation time on the inverse severing rate. Inconsistent with these predictions, the length dependence we observe is weaker than quadratic and the severing rate dependence we estimate from the cofilin concentration dependence is stronger than linear. In addition to severing, the model of Cates includes filament annealing reactions, in accordance with detailed balance in equilibrium. However, annealing is expected to be suppressed in our system by the presence of formins (Skau et al., 2009) on the barbed ends of stable fragments and by profilin on the barbed ends of unstable fragments (Courtemanche and Pollard, 2013). A modification of the Cates model, presented in Chapter 3, which neglects the annealing reaction predicts a relaxation time which is independent of the mean filament length, and is again linear in inverse severing rate. While the prediction of a length-independent stress relaxation timescale is plausibly consistent with our data, the severing timescale constrained by direct visualization of cofilin severing rates in dilute solution by total internal reflection fluorescence (TIRF) microscopy is about ~10-fold too slow. Whether this lingering discrepancy is the result of a small prefactor ommitted from the scaling analysis, enhanced severing in semi-dilute solution (perhaps owing to steric entanglement constraints of filament fluctuations, which have been shown in other contexts to enhance severing (De La Cruz et al., 2015; Pavlov et al., 2007)), or

omission of depolymerization from the severing-based models discussed here is the exciting subject of on-going investigation.

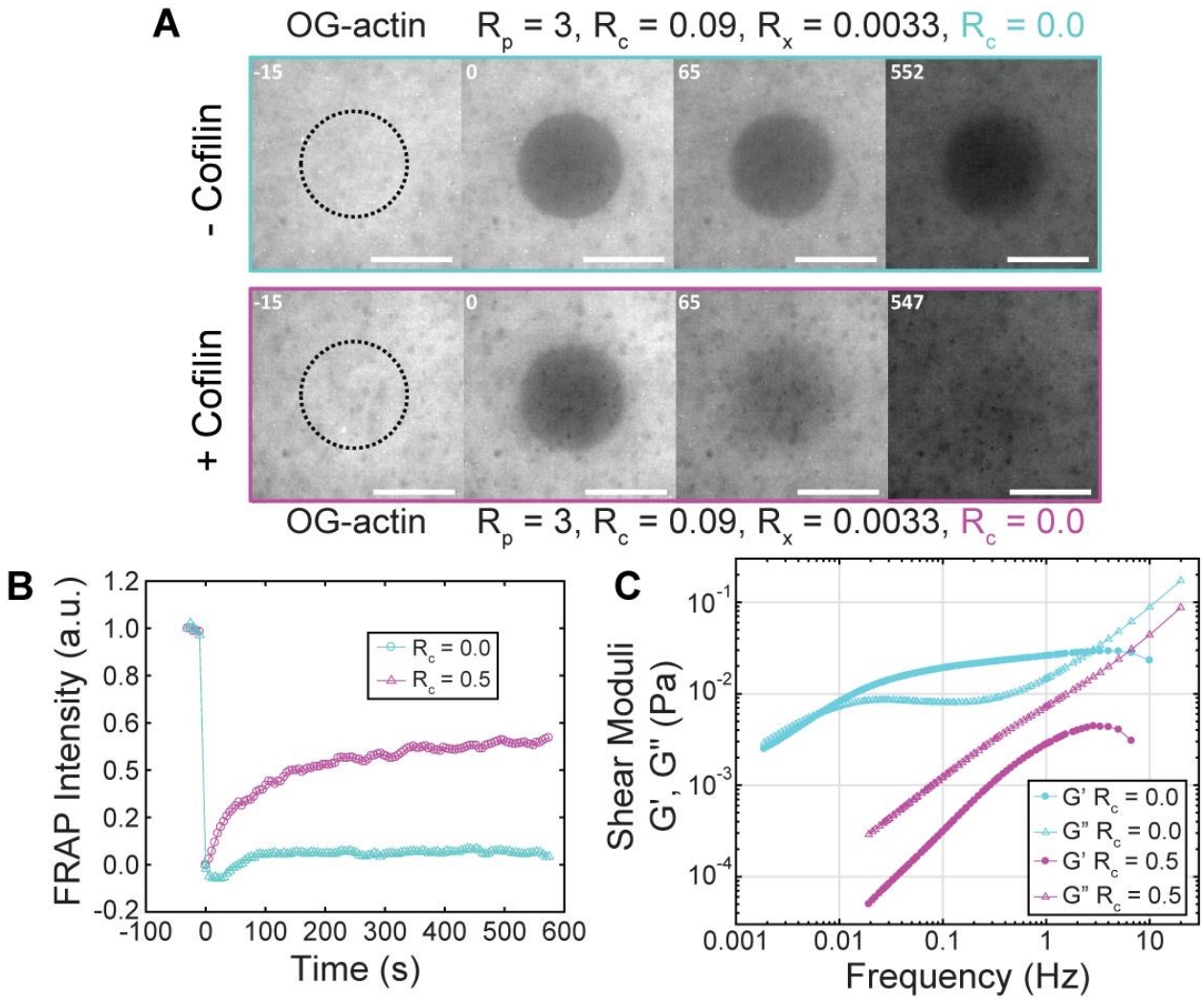

Figure 6.1. Evidence supporting fluidization of cross-linked networks by non-equilibrium cofilin-mediated turnover. (A-C) All samples are polymerized from 11.9 µM Mg-ATP-actin (5 % Oregon Green-labeled) with R_p = 3 (35.7 µM), R_f = 0.09 (1.07 µM), filamin:actin ratio of R_x = 0.0033 (0.04 µM) and R_c as indicated (0-11.9 µM). The filamin cross-linker concentration was chosen to give a mean cross-link spacing equivalent to the entanglement length. (A) Confocal fluorescence time-lapse micrographs with R_c = 0 (top, cyan) or R_c = 0.5 (bottom, purple) at steady-state. A dashed black circle denotes the region exposed to the bleaching laser. Time is relative to the end of the 5-s bleach. Scale bar is 50 µm. (B) Timecourse of the normalized fluorescence intensity averaged across the bleached region for entangled solutions with R_c as indicated in the legend.

Figure 6.1 Continued. (C) Real and imaginary components of the complex shear modulus (G' and G", respectively) of the same samples from (A-B), denoted by closed circles (G') and open triangle (G"), respectively. Notably, the elastic plateau present in the absence of cofilin is absent in the presence of optimal cofilin concentrations.

Structure and mechanics of cross-linked actin filament networks

While entangled actin filament solutions are a useful model system for examining the impact of non-equilibrium turnover on mechanics, actin filaments in cells are cross-linked into networks. Elucidation of possible consequences of non-equilibrium turnover for cell mechanics thus requires examination of cross-linked networks. Preliminary experiments with isotropic actin filament networks lightly cross-linked by filamin share features of entangled solutions in the presence of cofilin (Figure 6.1). First, cross-linked networks polymerized in the presence of cofilin, profilin and formin display enhanced FRAP recovery, comparable to that observed for entangled solutions. This suggests that the capacity of cofilin to catalyze filament turnover and local reorganization is maintained in lightly cross-linked, isotropic networks. Notably, imaging-induced photobleaching is more pronounced in cross-linked networks than entangled solutions, presumably because diffusion of filaments into and out of the field of view is strongly attenuated by the cross-links. The data shown in Fig 6.1 B, like all processed FRAP data in this thesis, are corrected for the photobleaching which results from acquisition of fluorescence images.

Second, passive one-point microrheology of the same networks shows markedly different mechanics. The network formed in the presence of formin, profilin, and filamin, but without cofilin, displays an elastic plateau on timescales between 1 and 100 s, indicative of gel-like mechanics on these timescales. In contrast, networks formed in the presence of cofilin as well as formin, profilin, and filamin exhibit predominantly fluid-like mechanics over the entire frequency range probed. These observations are in line with expectations from the fluidization of

entangled solutions by cofilin. Note that the magnitude of the modulii of this cross-linked network is comparable to that of entangled solutions in the absence of cofilin because the cross-link density was chosen to be equivalent to the entanglement length. From this, the contributions of the cross-links themselves to the mechanics are expected to be nearly equivalent to that of the entanglements, so the magnitude of the modulii are not expected to be elevated significantly. Taken together, these preliminary observations suggest that non-equilibrium cofilin-mediated turnover may also be sufficient to fluidize lightly cross-linked networks of actin filaments. Given reports that high concentrations of cross-linkers reduce the efficiency cofilin-mediated disassembly (Schmoller et al., 2011), future measurements of network mechanics in the presence of cofilin over a range of cross-linker concentrations higher than those used here will be informative. In particular, it will be important to disentangle the effects of 1) filament bundling, 2) suppression of transverse filament bending fluctuations by a reduction in the distance between cross-links, and 3) the reduction in available cofilin binding sites along the filament lattice, all of which are exacerbated at high crosslink concentrations.

Additionally, the results presented in Chapter 4 pertaining to the 2D simulations of passive, cross-linked actin networks presence of turnover but absence of motors provides further supporting evidence that increasing the rate of actin turnover reduces the long-time effective viscosity of cross-linked networks.

Distance from equilibrium

In some sense, all measurements of mechanics of actin in ATP are non-equilibrium, because the actin is turning over. In the absence of regulatory proteins which specifically accelerate turnover, this process happens to be very, very slow. Non-equilibrium turnover of purified actin alone at

steady-state is sufficiently slow, in fact, that breakage of the Fluctuation Dissipation Theorem (FDT), which formally holds only in equilibrium, is typically neglected in actin solutions (Gardel et al., 2003; Liu et al., 2006) and networks (Stuhrmann et al., 2012) unless motor proteins are present (Mizuno et al., 2007; Stuhrmann et al., 2012). In principle, one could argue that use of the FDT should properly be restricted to truly equilibrium systems, which for actin would necessitate polymerization in the presence of ADP. However, the good agreement between microrheology measurements and bulk macrorheology for entangled actin solutions in the prescence of ATP (Liu et al., 2006) suggests that the FDT holds sufficiently well at least for some "weak" forms of non-equilibrium activity. An important issue going forward will be to understand, in a generic sense, how far from equilibrium a given system is, and in particular, how badly broken the Fluctuation Dissipation Theorem is (for instance, in terms of percent error).

Here, we've accelerated turnover, and coupled it to funny filament dynamics rules. But how far from equilibrium is the system? How broken is FDT? We see white fluctuation spectra, but central limit theorem may be taking over. Estimate of filament elongation rate compared to diffusion suggests that filament pushing is not relevant in the regime probed here, though it could become important at much higher densities. Two-point measurements could be informative. It would also be interesting to look at whether the solutions drive non-equilibrium currents in the motions of the probe particles.

Section 6.2 REACTION REGULATION BY PHYSICO-CHEMICAL PROPERTIES OF CONDENSED PHASE MICROENVIRONMENTS

In vivo relevance

The high local concentrations generated by partitioning provides, in principle, for an elegant means to both spatially localize biochemical reactions and efficiently control reaction rates. For instance, if proper physiological function requires a high rate of a particular cytoplasmically-localized reaction, first-order kinetics suggest that high concentrations of the participating molecules are needed. Since the absolute number of molecules which need to be synthesized to reach a given concentration scales with cell volume, ~1000-fold more molecules would required to reach the same global cytoplasmic concentration for a reaction in E. coli versus a typical mammalian cell. Spontaneous partitioning to a condensed liquid-like phase, however, substantially reduces the volume at which the high concentration is required, potentially back to that in an E. coli-sized cell.

An additional consequence is that if the partition coefficients can be dynamically controlled, then tuning of reaction rates can be achieved with no new protein synthesis required. This could be a particularly sensitive way to spatially localized reactions with threshold-like kinetics, like a self-assembly reaction, where product only forms above a minimum local concentration. In this case, having a low-level in the cytoplasm gives no global production, but upon partitioning, gives rapid, tunable production. Partitioning could be controlled either by modulating the client, e.g. by phosphorylation (Aumiller, Pak), or in principle by altering the properties of the condensed phase itself.

Section 6.3 REFERENCES

Alberts, B., Johnson, A., Lewis, J., Raff, M., Roberts, K., and Walter, P. (2007). Molecular Biology of the Cell (New York, NY: Garland Science).

Berro, J., Sirotkin, V., and Pollard, T.D. (2010). Mathematical Modeling of Endocytic Actin Patch Kinetics in Fission Yeast: Disassembly Requires Release of Actin Filament Fragments. Mol. Biol. Cell *21*, 2905–2915.

Brieher, W. (2013). Mechanisms of actin disassembly. Mol. Biol. Cell *24*, 2299–2302.

Carlier, M.-F., Laurent, V., Santolini, J., Melki, R., Didry, D., Xia, G.-X., Hong, Y., Chua, N.-H., and Pantaloni, D. (1997). Actin Depolymerizing Factor (ADF/Cofilin) Enhances the Rate of Filament Turnover: Implication in Actin-based Motility. J. Cell Biol. *136*, 1307–1322.

Cates, M.E. (1987). Reptation of living polymers: dynamics of entangled polymers in the presence of reversible chain-scission reactions. Macromolecules *20*, 2289–2296.

Chaudhry, F., Breitsprecher, D., Little, K., Sharov, G., Sokolova, O., and Goode, B.L. (2012). Srv2/CAP (cyclase-associated protein) forms hexameric shurikens that directly catalyze actin filament severing by cofilin. Mol. Biol. Cell mbc.E12-08-0589.

Courtemanche, N., and Pollard, T.D. (2013). Interaction of Profilin with the Barbed End of Actin Filaments. Biochemistry (Mosc.) *52*, 6456–6466.

De La Cruz, E.M. (2005). Cofilin Binding to Muscle and Non-muscle Actin Filaments: Isoform-dependent Cooperative Interactions. J. Mol. Biol. *346*, 557–564.

De La Cruz, E.M. (2009). How cofilin severs an actin filament. Biophys. Rev. *1*, 51–59.

De La Cruz, E.M., Martiel, J.-L., and Blanchoin, L. (2015). Mechanical Heterogeneity Favors Fragmentation of Strained Actin Filaments. Biophys. J. *108*, 2270–2281.

Doi, M., and Edwards, S.F. (1986). The Theory of Polymer Dynamics (New York, NY: Oxford University Press).

Fritzsche, M., Erlenkämper, C., Moeendarbary, E., Charras, G., and Kruse, K. (2016). Actin kinetics shapes cortical network structure and mechanics. Sci. Adv. *2*, e1501337.

Fujiwara, I., Vavylonis, D., and Pollard, T.D. (2007). Polymerization kinetics of ADP- and ADP-Pi-actin determined by fluorescence microscopy. Proc. Natl. Acad. Sci. *104*, 8827–8832.

Gardel, M.L., Valentine, M.T., Crocker, J.C., Bausch, A.R., and Weitz, D.A. (2003). Microrheology of Entangled F-Actin Solutions. Phys. Rev. Lett. *91*, 158302.

de Gennes, P.-G. (1979). Scaling Concepts in Polymer Physics (Ithaca, NY: Cornell University Press).

Isambert, H., and Maggs, A.C. (1996). Dynamics and Rheology of Actin Solutions. Macromolecules *29*, 1036–1040.

Jansen, S., Collins, A., Chin, S.M., Ydenberg, C.A., Gelles, J., and Goode, B.L. (2015). Single-molecule imaging of a three-component ordered actin disassembly mechanism. Nat. Commun. *6*, 7202.

Jégou, A., Niedermayer, T., Orbán, J., Didry, D., Lipowsky, R., Carlier, M.-F., and Romet-Lemonne, G. (2011). Individual Actin Filaments in a Microfluidic Flow Reveal the Mechanism of ATP Hydrolysis and Give Insight Into the Properties of Profilin. PLOS Biol. *9*, e1001161.

Johnston, A.B., Collins, A., and Goode, B.L. (2015). High-speed depolymerization at actin filament ends jointly catalysed by Twinfilin and Srv2/CAP. Nat. Cell Biol. *17*, 1504–1511.

Koestler, S.A., Rottner, K., Lai, F., Block, J., Vinzenz, M., and Small, J.V. (2009). F- and G-Actin Concentrations in Lamellipodia of Moving Cells. PLOS ONE *4*, e4810.

Liu, J., Gardel, M.L., Kroy, K., Frey, E., Hoffman, B.D., Crocker, J.C., Bausch, A.R., and Weitz, D.A. (2006). Microrheology Probes Length Scale Dependent Rheology. Phys. Rev. Lett. *96*, 118104.

Loisel, T.P., Boujemaa, R., Pantaloni, D., and Carlier, M.-F. (1999). Reconstitution of actin-based motility of Listeria and Shigella using pure proteins. Nature *401*, 613–616.

McCullough, B.R., Grintsevich, E.E., Chen, C.K., Kang, H., Hutchison, A.L., Henn, A., Cao, W., Suarez, C., Martiel, J.-L., Blanchoin, L., et al. (2011). Cofilin-Linked Changes in Actin Filament Flexibility Promote Severing. Biophys. J. *101*, 151–159.

Michelot, A., Berro, J., Guérin, C., Boujemaa-Paterski, R., Staiger, C.J., Martiel, J.-L., and Blanchoin, L. (2007). Actin-Filament Stochastic Dynamics Mediated by ADF/Cofilin. Curr. Biol. *17*, 825–833.

Mizuno, D., Tardin, C., Schmidt, C.F., and MacKintosh, F.C. (2007). Nonequilibrium Mechanics of Active Cytoskeletal Networks. Science *315*, 370–373.

Morse, D.C. (1998a). Viscoelasticity of Concentrated Isotropic Solutions of Semiflexible Polymers. 1. Model and Stress Tensor. Macromolecules *31*, 7030–7043.

Morse, D.C. (1998b). Viscoelasticity of Concentrated Isotropic Solutions of Semiflexible Polymers. 2. Linear Response. Macromolecules *31*, 7044–7067.

Mullins, R.D., Heuser, J.A., and Pollard, T.D. (1998). The interaction of Arp2/3 complex with actin: Nucleation, high affinity pointed end capping, and formation of branching networks of filaments. Proc. Natl. Acad. Sci. *95*, 6181–6186.

Nadkarni, A.V., and Brieher, W.M. (2014). Aip1 Destabilizes Cofilin-Saturated Actin Filaments by Severing and Accelerating Monomer Dissociation from Ends. Curr. Biol. *24*, 2749–2757.

Normoyle, K.P.M., and Brieher, W.M. (2012). Cyclase-associated Protein (CAP) Acts Directly on F-actin to Accelerate Cofilin-mediated Actin Severing across the Range of Physiological pH. J. Biol. Chem. *287*, 35722–35732.

P G de Gennes, and Leger, and L. (1982). Dynamics of Entangled Polymer Chains. Annu. Rev. Phys. Chem. *33*, 49–61.

Pavlov, D., Muhlrad, A., Cooper, J., Wear, M., and Reisler, E. (2007). ACTIN FILAMENT SEVERING BY COFILIN. J. Mol. Biol. *365*, 1350–1358.

Phillips, R., Kondev, J., and Theriot, J. (2008). Physical Biology of the Cell (New York, NY: Garland Science).

Pollard, T.D. (1986). Rate constants for the reactions of ATP- and ADP-actin with the ends of actin filaments. J. Cell Biol. *103*, 2747–2754.

Pollard, T.D., and Borisy, G.G. (2003). Cellular Motility Driven by Assembly and Disassembly of Actin Filaments. Cell *112*, 453–465.

Ponti, A., Matov, A., Adams, M., Gupton, S., Waterman-Storer, C.M., and Danuser, G. (2005). Periodic Patterns of Actin Turnover in Lamellipodia and Lamellae of Migrating Epithelial Cells Analyzed by Quantitative Fluorescent Speckle Microscopy. Biophys. J. *89*, 3456–3469.

Schaus, T.E., Taylor, E.W., and Borisy, G.G. (2007). Self-organization of actin filament orientation in the dendritic-nucleation/array-treadmilling model. Proc. Natl. Acad. Sci. *104*, 7086–7091.

Schmoller, K.M., Semmrich, C., and Bausch, A.R. (2011). Slow down of actin depolymerization by cross-linking molecules. J. Struct. Biol. *173*, 350–357.

Sirotkin, V., Berro, J., Macmillan, K., Zhao, L., and Pollard, T.D. (2010). Quantitative Analysis of the Mechanism of Endocytic Actin Patch Assembly and Disassembly in Fission Yeast. Mol. Biol. Cell *21*, 2894–2904.

Skau, C.T., Neidt, E.M., and Kovar, D.R. (2009). Role of Tropomyosin in Formin-mediated Contractile Ring Assembly in Fission Yeast. Mol. Biol. Cell *20*, 2160–2173.

Stuhrmann, B., Soares e Silva, M., Depken, M., MacKintosh, F.C., and Koenderink, G.H. (2012). Nonequilibrium fluctuations of a remodeling in vitro cytoskeleton. Phys. Rev. E *86*, 020901.

Suarez, C., Roland, J., Boujemaa-Paterski, R., Kang, H., McCullough, B.R., Reymann, A.-C., Guérin, C., Martiel, J.-L., De La Cruz, E.M., and Blanchoin, L. (2011). Cofilin Tunes the Nucleotide State of Actin Filaments and Severs at Bare and Decorated Segment Boundaries. Curr. Biol. *21*, 862–868.

Svitkina, T.M., and Borisy, G.G. (1999). Arp2/3 Complex and Actin Depolymerizing Factor/Cofilin in Dendritic Organization and Treadmilling of Actin Filament Array in Lamellipodia. J. Cell Biol. *145*, 1009–1026.

Theriot, J.A., and Mitchison, T.J. (1991). Actin microfilament dynamics in locomoting cells. Nature *352*, 126–131.

Theriot, J.A., and Mitchison, T.J. (1992). Comparison of actin and cell surface dynamics in motile fibroblasts. J. Cell Biol. *119*, 367–377.

Wegner, A. (1976). Head to tail polymerization of actin. J. Mol. Biol. *108*, 139–150.